READOUT CONCEPTS FOR LABEL-FREE BIOMOLECULE DETECTION WITH ADVANCED ISFET AND SILICON NANOWIRE BIOSENSORS

"AUSLESEKONZEPTE FÜR DEN MARKIERUNGSFREIEN BIOMOLEKÜL-NACHWEIS MIT MODERNEN ISFET UND SILIZIUM-NANODRAHT BIOSENSOREN"

vom

Fachbereich Elektrotechnik und Informationstechnik
der Technischen Universität Kaiserslautern
zur Verleihung des akademischen Grades

**Doktor der Ingenieurwissenschaften (Dr.-Ing.)**

genehmigte Dissertation

von

Thanh Chien Nguyen, M.Sc.

geb. in Nghe An (Vietnam)

D 386

Eingereicht am:	23. Oktober 2017
Tag der mündlichen Prüfung:	18. Dezember 2017
Dekan des Fachbereichs:	Prof. Dr.-Ing. Ralph Urbansky

Promotionskommission

Vorsitzender:	Jun.-Prof. Dr.-Ing. Daniel Görges
Berichterstattende:	Prof. Dr.-Ing. Andreas König
	Prof. Dr. Sven Ingebrandt
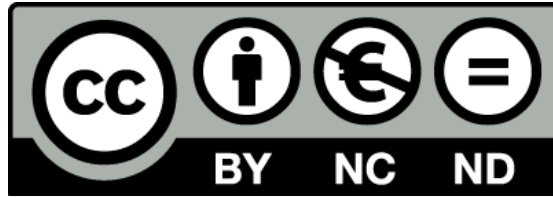
Namensnennung - Nicht kommerziell - Keine Bearbeitungen 4.0 International

Sie dürfen:

Teilen — das Material in jedwedem Format oder Medium vervielfältigen und weiterverbreiten

Unter folgenden Bedingungen:

Namensnennung — Sie müssen angemessene Urheber- und Rechteangaben machen, einen Link zur Lizenz beifügen und angeben, ob Änderungen vorgenommen wurden. Diese Angaben dürfen in jeder angemessenen Art und Weise gemacht werden, allerdings nicht so, dass der Eindruck entsteht, der Lizenzgeber unterstütze gerade Sie oder Ihre Nutzung besonders.

Nicht kommerziell — Sie dürfen das Material nicht für kommerzielle Zwecke nutzen.
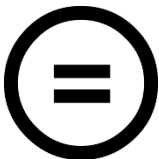
Keine Bearbeitungen — Wenn Sie das Material remixen, verändern oder darauf anderweitig direkt aufbauen, dürfen Sie die bearbeitete Fassung des Materials nicht verbreiten.

Keine weiteren Einschränkungen — Sie dürfen keine zusätzlichen Klauseln oder technische Verfahren einsetzen, die anderen rechtlich irgendetwas untersagen, was die Lizenz erlaubt.

Erklärung

Hiermit versichere ich, dass ich die vorliegende Arbeit selbst angefertigt und verfasst habe und alle benutzen Hilfsmittel in der Arbeit angegeben habe. Die vorliegende Dissertation oder Teile hiervon wurden noch nicht als Prüfungsarbeit für eine staatliche oder andere wissenschaftliche Prüfung eingereicht.

Kaiserslautern, 12.03.2018

M.Sc. Thanh Chien Nguyen

Abstract

Field-effect transistor (FET) sensors and in particular their nanoscale variant of silicon nanowire transistors are very promising technology platforms for label-free biosensor applications. These devices directly detect the intrinsic electrical charge of biomolecules at the sensor's liquid-solid interface. The maturity of micro fabrication techniques enables very large FET sensor arrays for massive multiplex detection. However, the direct detection of charged molecules in liquids faces a significant limitation due to a charge screening effect in physiological solutions, which inhibits the realization of point-of-care applications. As an alternative, impedance spectroscopy with FET devices has the potential to enable measurements in physiological samples. Even though promising studies were published in the field, impedimetric detection with silicon FET devices is not well understood.

The first goal of this thesis was to understand the device performances and to relate the effects seen in biosensing experiments to device and biomolecule types. A model approach should help to understand the capability and limitations of the impedimetric measurement method with FET biosensors. In addition, to obtain experimental results, a high precision readout device was needed. Consequently, the second goal was to build up multi-channel, highly accurate amplifier systems that would also enable future multi-parameter handheld devices.

A PSPICE FET model for potentiometric and impedimetric detection was adapted to the experiments and further expanded to investigate the sensing mechanism, the working principle, and effects of side parameters for the biosensor experiments. For potentiometric experiments, the pH sensitivity of the sensors was also included in this modelling approach. For impedimetric experiments, solutions of different conductivity were used to validate the suggested theories and assumptions. The impedance spectra showed two pronounced frequency domains: a low-pass characteristic at lower frequencies and a resonance effect at higher frequencies. The former can be interpreted as a contribution of the source and double layer capacitances. The latter can be interpreted as a combined effect of the drain capacitance with the operational amplifier in the transimpedance circuit.

Two readout systems, one as a laboratory system and one as a point-of-care demonstrator, were developed and used for several chemical and biosensing experiments. The PSPICE model applied to the sensors and circuits were utilized to optimize the systems and to explain the sensor responses. The systems as well as the developed modelling approach were a significant step towards portable instruments with combined transducer principles in future healthcare applications.

Kurzfassung[1]

Biosensoren sind leistungsstake Diagnosewerkzeuge zur quantitativen Erkennung einer Vielzahl von verschiedenen Biomolekülen. Der Bedarf an solchen kostengünstigen und tragbaren aber zugleich auch hochsensiven und zuverlässigen „point-of-care" Biosensoren steigt heutzutage rasant an. Dabei ermöglichen markierungsfreie Biosensoren eine schnellere Detektion und eine wesentliche Kostenminimierung, da der Schritt zur Biomarker-Modifikation der Zielmoleküle vermieden wird und zugleich eventuelle Artefakte bei der Biomarkierung vermieden werden. Neben vielen verschiedenen Biosensorarten sind die auf Feldeffekt-Transistoren (FET) basierenden Sensoren einer der aussichtsreichsten Sensortypen. Die FET-basierten Biosensoren ermöglichen eine direkte Erfassung der natürlichen elektrischen Ladung eines Biomoleküls durch die Bindung an die Sensoroberfläche. Durch die rasante Entwicklung der Mikroelekronik-Industrie in den letzten Jahrzehnten wurde es möglich, hochintegrierte Sensoren-Arrays mit kleineren Sensorgrößen zur gleichzeitigen und selektiven Detektion vieler verschiedener Molekülarten herzustellen.

In den letzten zwanzig Jahren ist die selektive und parallele Echtzeitdetektion von mehreren Biomarkern von sehr großem Interesse in der Biosensor Community. Durch einen bekannten Ladungsabschirmungseffekt in physiologischen Elektrolyten, stellt die direkte, selektive Erfassung geladener Biomoleküle in einer Testflüssigkeit eine große Herausforderung dar, wodurch eine direkte Analyse in Blutserum schwierig wird. Als Teillösung des Problems kann eine Impedanzspektroskopie-Methode mittels FET-Sensoren eingesetzt werden, die im Vergleich zur klassischen, potentiometrischen Methode auch eine Messung in Blutserum ermöglicht. Trotz der bisher durchgeführten, experimentellen Arbeiten in diesem Bereich ist der Mechanismus zur impedimetrischen Analyse bisher noch nicht komplett verstanden.

Für die Experimente, die in dieser Arbeit präsentiert werden, wurden verschiedene Typen von Silizium FET Sensoren benutzt. Diese Sensoren wurden von früheren Mitgliedern der Arbeitsgruppe in speziellen Prozessen entwickelt, wobei eine Hochschule-Reinraum Umgebung und nicht standardisierte Protokolle genutzt wurden. Im Wesentlichen wurden zwei Sensortypen verwendet: Silizium ionen-sensitive FETs (ISFETs) im Mikrometermaßstab und Silizium-Nanodraht Transistoren (SiNW FETs) im Nanometermaßstab. Deren Designs waren unterschiedlich in Dotierung, Kanalgeometrie und Gateoxid Dicke. Im Wesentlichen aber hatten sie unterschiedliche parasitäre Eigenschaften durch die verwendeten Verkapselungsmethoden.

Aus dieser Situation abgeleitet war das erste Ziel dieser Arbeit ein deutlich verbessertes Verständnis von Messungen mit den Sensoren und eine Erklärung der Effekte, die in den Biosensorik Experimenten in Bezug auf genutzte Sensoren und bekannte Biomolekül Parametern beobachtet werden. Ein Modellansatz sollte dabei helfen, die Möglichkeiten und Limitierungen der Impedanzspektroskopie mittels FET-basierten Biosensoren zu verstehen. Darüber hinaus, um gute

---

[1] (laut Promotionsordnung des Fachbereichs Elektrotechnik und Informationstechnik der Technischen Universität Kaiserslautern von 29.07.2013)

experimentelle Resultate mit robusten Sensoren und definierten chemischen Oberflächen der Sensoren zu erhalten, war ein hochpräziser Verstärker notwendig. Deshalb war ein zweites Ziel dieser Arbeit die Entwicklung, der Aufbau und die Charakterisierung eines impedimetrischen, tragbaren und hochpräzisen Mehrkanal Ausleseystems.

Als praktische Experimente wurden die potentiometrischen und impedimetrischen Messmethoden basierend auf der bekannten Biotin-Streptavidin Biomolekülbindung verglichen. Die Biotin-Moleküle besitzen nur wenig Ladung und die starke Ladung der Streptavidin-Moleküle ist vom pH-Wert der umgebenden Lösung abhängig. Aus diesem Grund kann eine Sensorreaktion direkt nach der spezifischen Bindung präzise ausgewertet und verglichen werden. Die Messungen zeigten, dass es nicht möglich ist, potentiometrisch die ladungsfreie Biotin-Bindung zu erfassen. Jedoch konnten mit der Impedanzspektroskopie-Methode beide Biomolekülarten deutlich und selektiv nachgewiesen werden.

Um den Detektionsmechanismus, das Funktionsprinzip sowie verschiedene Einflussparameter für die Impedanzmessungen zu verstehen, wurde in der Arbeit ein PSPICE FET Model zur Erklärung der impedimetrischen Auslesemethode entwickelt. Für die potentiometrischen Experimente, konnte die pH Sensitivität der Sensoren durch diesen Modellansatz ebenfalls erklärt werden. Die Impedanz-Spektren zeigen zwei deutlich hervorgehobene Frequenzanteile im Niederfrequenz- bzw. Hochfrequenzbereich, die entsprechend auf kapazitive Beiträge zurückzuführen sind. Dabei spielen die Kapazität auf dem Source-Kontakt für den Niederfrequenzbereich und die Kapazität auf dem Drain-Kontakt für den Hochfrequenzbereich eine große Rolle.

Im Verlauf der Arbeit wurde ein 32-Kanal Verstärkersystem mit acht auswählbaren Verstärkungsbereichen entwickelt und hergestellt, womit potentiometrische und impedimetrische Messungen an verschiedenen Bio-FET Sensoren durchgeführt wurden. Darüber hinaus wurde ein tragbarer, Microcontroller (MCU) gesteuerter, frei konfigurierbarer 4-Kanal Verstärker für potentiometrische und zeitaufgelöste Auslesemodi hergestellt. Die ausgiebige Charakterisierung beider Verstärker zeigte, dass die entwickelten Auslesegeräte reproduzierbar über eine gute Messgenauigkeit verfügen, die verglichen mit einem professionellen und teuren Parameter-Analyzer nur unbedeutend (5%) kleiner waren. Anschließend wurden die Auslesegeräte zur Signal-zu-Rausch Analyse von vielen Bio-FET Sensoren eingesetzt, wobei die Anwendbarkeit der Messverfahren mittels pH-Messungen sowie mit DNS-Messungen erfolgreich demonstriert werden konnte. Dabei betrug die pH-Empfindlichkeit typische 34 mV/pH auf den SiO_2 Sensoroberflächen. Durch die Oberflächenbehandlung mit einer Amino-Silanschicht mittels eines Gasphasenprozesses konnte eine höhere pH-Empfindlichkeit von 45 mV/pH verbunden mit einer besseren Sensorlinearität erreicht werden. Durch eine Erweiterung des SiNW FET Modells mit einer schon früher in der Literatur beschriebenen Methode zur Modellierung des elektrochemischen Verhaltens der Sensoroberfläche konnten diese Unterschiede auch erklärt werden. Bei den Biomolekül-Experimenten verschob sich die charakteristische Transfer-Kurve der FET Sensoren reproduzierbar nach rechts in Richtung kleinerem Strom, wie es für die Oberflächenbindung von negativ geladenen DNS-Molekülen zu erwarten ist.

Jedoch konnten zum Ende dieser Arbeit zwei Fragen noch nicht beantwortet werden: 1. Gibt es beim impedimetrischen Messverfahren auch einen Signalanteil durch die Ladung der bindenden Moleküle? Die Frage könnte zukünftig geklärt werden, indem die Streptavidin-Biotin Bindung in Lösungen gleicher Leifähigkeit aber mit unterschiedlichen pH-Werten untersucht wird. Leider waren während dieser Arbeit nicht ausreichend Sensoren vorhanden, um robuste, statistische Aussagen abzuleiten. In den Impedanzmessungen, die PSPICE nachvollzogen wurden, waren die stärksten Effekte durch die parasitären Parameter wie z.B. die Leitfähigkeit der Messlösung beeinflusst. 2. Der Messnachweis von nicht elektrisch geladenen Molekülen konnte nur mit den Si-Nanodraht FETs realisiert werden jedoch nicht mit den ISFET Sensoren mit größeren Messflächen im Mikrometerbereich. Die zweite offene Frage ist, ob und warum Nanotransistoren eine höhere Empfindlichkeit ermöglichen.

Zum Schluss dieser Arbeit, führte der Modellierungsansatz mit den verfügbaren Tools in PSPICE zu wichtigen Erkenntnissen über den Einfluss der parasitären Parameter der Sensoren und Verstärker, jedoch konnte das Modell die bei den Biotin-Streptavidin Experimenten beobachteten, impedimetrischen Spektren noch nicht erklären. Es kann daher geschlussfolgert werden, dass das momentane Modell die Effekte am Biosensoreingang noch nicht vollständig erklärt und ein besser geeignetes BSIM-SOI Modell für die SINW FET Sensoren verwendet werden sollte, um Spektren zu simulieren. Nichtsdestotrotz hilft das tiefere Verständnis der impedimetrischen Messungen in dieser Arbeit nun enorm bei Verbesserungen von zukünftigen Sensordesigns. Die neuartigen Verstärkerkonzepte und Ausleseverfahren, die in dieser Arbeit beschrieben werden, zeigen auch die Notwendigkeit für präzisere, tragbare Sensorsysteme, um eine kombinierte impedimetrische und potentiometrische Auslese zu ermöglichen. Die in dieser Arbeit beschriebenen Methoden und Auslesekonzepte könnten zukünftig für robustere Point-of-Care Auslesesysteme für mehrere Zielmolekültypen mit SiNW-FETs genutzt werden.

Acknowledgements

Dedicated to Kim Ngoc and Thanh Truc

"Twenty years from now you will be more disappointed by the things that you didn't do than by the ones you did do. So throw off the bowlines. Sail away from the safe harbor. Catch the trade winds in your sails. Explore. Dream. Discover."

Mark Twain 1835-1910

Contents

1. Introduction

1.1 Label-Free Biosensor Concepts

The ability to detect and to quantify the presence of an analyte such as antigens or single-stranded deoxyribonucleic acid (ssDNA) molecules in a biological sample has a significant impact in life science research, clinical and medical diagnosis [1–3], food/water safety, and pharmaceutical testing [4–7]. Biosensors are analytical tools that convert the reaction of a biorecognition element and its analyte into quantifiable signals. The potential for biosensors in qualitative and quantitative detection is very broad, including antigens, ssDNA, organisms, tissues, cells, organelles, membranes, enzymes, receptors, antibodies, and nucleic acids [8]. There is an emerging demand to build low cost point-of-care biosensors that are portable, wearable, and able to perform multiplexing analysis of a panel of analytes simultaneously. A biosensor device in general consists of three main components: bioreceptor, transducer, and readout system, as described in Figure 1-1 [9]. The bioreceptor is typically a biomolecule that recognizes the specific analyte of interest. Enzymes, antibodies, and nucleic acids are among the most common biorecognition substances used for highly selective detection. The transducer should be able to convert the biorecognition event into a measurable signal [10] using optical, mechanical, thermal, or electrical principles. The readout system provides necessary conditions for the transducer and measures its outputs and converts them into readable, meaningful values such as color change or digital display of a value. A more detailed overview of the field of biosensors can be found in several textbooks [8–11] and review articles [12–16].

In a real biosensing measurement, a biorecognition element that possesses a specific affinity to the analyte of interest (for example antigen-antibody binding, DNA hybridization, receptor-ligand attachment) is immobilized on the surface of the transducer. The measurement solution will be washed over the sensor surface and if it contains the analyte of interest, it will bind to the surface of the sensor. In a label-based detection scheme, these recognition reactions are marked by a label (reporter molecule) which has fluorescent, luminescent, radiometric, or colorimetric properties [17]. The label is selected such that it can be easily detected by its color or its capability to generate photons at a wavelength. A wide range of molecules for widespread use can be sensed in reporter-based schemes such as ELISA (enzyme-linked immunosorbent assay) and PCR (polymerase chain reaction) [18]. However, there are several intrinsic problems with label-based sensing. In practice, a high degree of development is required for label-based assays to assure that the label does not alter important active sides on the target molecule [19]. It is difficult to control the labeling yield, which introduces additional variability in the detection. In drug testing, an incorrect use of a label may result in inaccurate assessments of the potency of a drug interaction with its target protein receptor. This approach also demands a lengthy period of preparing and training personnel [11,20].
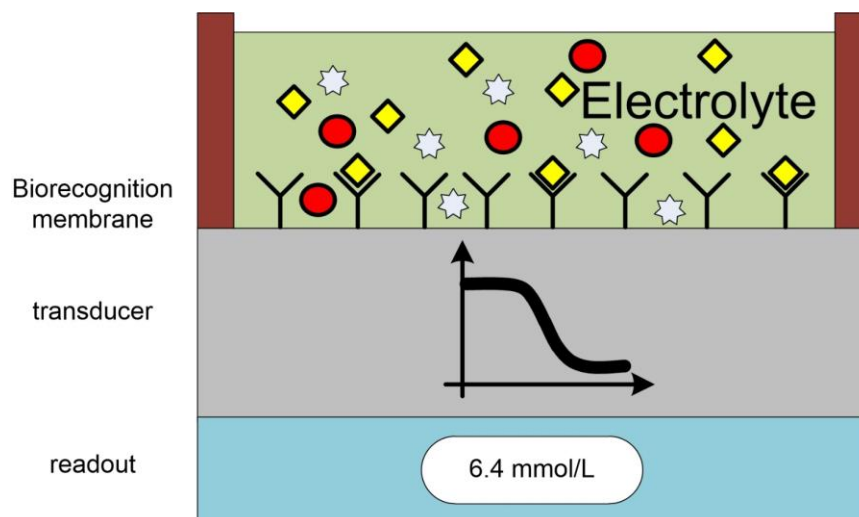
Figure 1-1 Schematic diagram of the three main components of a biosensor devices (adapted from [9])

The label-free approach, as its name implies, allows the detection of biological analytes without reporter molecules [11]. This mainly involves a transducer that can measure directly some physical properties of the analyte. For example, all biochemical molecules have finite mass, volume, viscoelasticity, dielectric permittivity, conductivity, and some of them carry an electrical charge that can be used to detect their presence or absence using an appropriate sensor. Label-free detection eliminates the labeling preparation step, which helps to minimize the cost in time and resources, while removing experimental artifacts from quenching, shelf life, and background fluorescence as well as the effect of the label on the molecular interaction. In addition, most of the labeling methods are limited to only end-point measurements, in contrast to more favorable direct, continuous, and real-time label-free detection.

Until recently, there were only a few label-free systems available on the market. The most famous among them are Quartz Crystal Microbalance (QCM) [21,22] and Surface Plasmon Resonance (SPR) [11,23,24]. The QCM sensor consists of a thin quartz disk with electrodes deposited on it. QCM is piezoelectric, and an acoustic wave is generated by an oscillating electrical field that is applied across the disk. A resonance oscillation appears when the frequency of the electrical stimulation is near the fundamental frequency of the crystal. This fundamental frequency depends on several parameters such as the thickness of the disk, its chemical structure, and its shape and mass. Among those only the mass changes when the analyte is binding to the receptor immobilized on the surface of the electrodes. SPR is an optical phenomenon that is sensitive to the alteration in optical properties of a metal-liquid interface. An SPR setup typically consists of a polarized monochromatic light source, a glass prism, a thin metal film in contact with the base of the prism, and a photodetector [11]. SPR measures changes in the refractive index in the immediate vicinity of the surface of the metal film, which depends on the binding of analytes to the immobilized receptors on the surface. These two devices can be utilized for many assays to measure the

absorption mass on the device's surface with a sensitivity of about one nanogram per square centimeter (this is in a range of nanomolar (nM) in the case of DNA molecules) [25]. Both systems also offer real-time and label-free detection, however it is very challenging to miniaturize these sensors as point-of-care detection as multi-parameter sensors and handheld devices. It is also difficult to create an array of QCM sensors with simple readout devices, and the optical detection component of SPR makes it problematic for miniaturization.

1.2 Field-Effect Sensor Concept and Literature Review

As most molecules carry charges when being in a liquid, an alternative approach in label-free detection is to measure these charges by a silicon-based, ion-sensitive field-effect transistor (ISFET). A field-effect sensor structure is analogous to a metal-oxide-semiconductor FET where the metal gate electrode is replaced by a measurement solution and a reference electrode. The binding of molecules of interest to receptors immobilized on the surface of FET devices modulates the current through the sensor. It therefore acts as a potentiometer that measures the surface potential at the insulator-electrolyte interface. The rapid development of micro fabrication techniques in recent decades has enabled ISFET sensors to become multiplex arrays, to scale down in size and to increase the array density. The established, high-yield industrial complementary metal-oxide-semiconductor (CMOS) processes enable the fabrication of hundreds of sensors per silicon wafer and greatly reduce the cost of fabrication. In addition, these sensors offer the capability of real-time, quantitative, and concentration-sensitive detection without any labeling step. The development of compact, integrated sensor systems allows the decentralized point-of-care diagnostics where current label-dependent or available label-free systems would be difficult to use.

The ISFET sensors were firstly developed in the 1970s by Bergveld [26,27] and were the first miniaturized silicon-based sensor. In these two pioneering papers, Bergveld suggested the structure without using a reference electrode. Instead of a reference electrode in the liquid, a feedback circuit to substrate is used to stabilize the amplifier. Later publication showed that having a reference electrode plays an important role in stabilizing the measurement as well as clarifying the working principle of devices [28]. The typical insulator materials at the gate of ISFETs are silicon dioxide, silicon nitride, aluminum oxide or tantalum oxide that respond to pH change without further surface modification because the insulator membrane possesses the capability of protonation and deprotonation [29,30]. The pH sensitivity of ISFETs allows their application for detection of cell metabolism and extracellular action potential measurements. The monitoring of cell metabolism is based on the acidification rate of a group of cells (10^5-10^6 cells on a sensor chip) that reacts differently with different stimulation (for example in drug testing) [31,32]. The second type of cell-based ISFET measurements is applied to several electrogenic cells such as neuronal cells [26,33], muscle cells [34] or cell networks [35]. Electrogenic cells, produce spontaneous action potentials (transient changes of their membrane potential) that can be detected by an ISFET chip lying

underneath. The local potassium concentration within the narrow gap between transistor and cell (~50 nm) during channel activation may adjust the electrical double layer in front of the gate oxide that effects the transistor signal [36]. In addition, ISFET can be used for other applications: combining enzymes and ISFET for chemical sensor (EnFET) (Glucose, Urease [37], Penicillin [38] etc.); ImmunoFET for detection of antibody-antigen interaction [39]; or GenFET for detection of DNA hybridization [40]. More detail about ISFET and its applications can be found in the review article [35].

The ISFET sensor is normally in the range of micrometers in width and length dimensions and therefore requires a large total number of molecules, that bind to the surface in order to achieve measurable signals [41]. The introduction of silicon nanowire (SiNW) in 2001 by Cui et al. [42] offers two main advantages over the standard ISFET [43]. First, the width of SiNW is in the order of 10 nm, which is comparable in dimension or even smaller than most of biological entities such as nucleic acid, protein, cells, viruses, etc. This leads to a smaller total number of molecules needed to bind to the chip surface to produce a detectable signal. The surface potential changes, however, is proportional to the surface density of binding molecules. Therefore, FET and SiNW sensors should record signal amplitudes of similar sizes. However, SiNW could in principle achieve higher sensitivity or a lower detection limit if all molecules to be detected would bind to the sensor surface only. Second, nano-scale SiNWs possess new physical and chemical properties arising from their size. The high surface-to-volume ratio allows the surface atoms to play an important role in defining the physical, chemical, and electronic properties of the device. In addition, the working current of SiNW is approximately 1000 times less than that of ISFET. Therefore, the power consumption of the multiplexed sensors, once implemented, will be significantly reduced. This is favorable for portable or implantable devices where continuous monitoring might be necessary.

Since the SiNW FET was introduced, the field of semiconductor nanowire has become one of the most active research areas in the nanoscience community [44], where the number of publications have increased exponentially for more than ten years. It covers a wide range of applications in biosensor technology. It can detect in real time, label-free proteins downs to 10 picomolar [45–47], DNA down to 1-10 fM [48–50]. The SiNW FET is also used for drug testing [46] and cell measurements [51–53].

There are two approaches in fabricating SiNW: bottom-up and top-down. SiNW employing the bottom-up method is typically grown with a vapor-liquid-solid mechanism with metal nanoclusters as catalysts [54]. The nanowire has a diameter from several nanometers to 100 nm while maintaining high surface quality. However, this approach experiences two major drawbacks: it is difficult to integrate a high-density sensor array because of the complexity in alignment and contacting the grown nanowires [55]. And the diameter of nanowire has large variance that leads to differences in electrical characteristics [56]. The top-down approach utilizes conventional micro-fabrication processes on wafer scale to create a nanowire-like structure on a thin silicon-on-insulator (SOI) wafer. SiNW structure is defined in the active silicon layer by electron beam

lithography [57], deep UV (ultraviolet) lithography [48,58] or nanoimprint lithography [59,60]. Subsequently, the final SiNW size is determined by etching processes: wet etching [57,61] or dry etching reactive-ion etching (RIE) [62,63] or combinations of them. SiNW FET sensors in this work are 28×2 array chips that are fabricated by combining high throughput nanoimprint lithography and wet tetramethylammonium hydroxide (TMAH) etching. It showed good electric performances and improved sensitivity of sensors. The fabrication processes and characterization of the SiNW FETs were described in detail in another earlier work [64].

1.3 Challenges and Open Issues

Even though SiNWs offer several advantages compared to standard ISFETs, they share the same detection mechanism: the electrical field of charged molecules binding to the surface modulates the drain-source current or characteristics of the sensors. In liquid, near a (for example) negatively charged species there is an accumulation of counterions (ions of opposite charge) and a depletion of coions because of electrostatic interactions [65]. At a certain length from the surface (called the Debye length), the counterions will balance the electrical field of the charged molecules. Therefore, FET sensors can only detect the charge inside the Debye length from the chip surface. For aqueous solution, this length depends on the ionic strength of the measurement solution by the following equation [66]:

$$\lambda_D = \sqrt{\frac{\varepsilon \varepsilon_0 kT}{e^2 \sum c_i Z_i^2}} \tag{1}$$

where ε is relative dielectric permittivity of the solvent (in most of the case is the water: ~ 80 at t = 20°C, ~78 at t = 25°C); ε_0 is the vacuum permittivity; k is the Boltzmann constant; T is Kelvin temperature; e is the elementary charge; c_i the ion concentration; Z_i is the valence of the ith ion.

Using above equation, the dependence of Debye length on the concentration of measurement solutions can be plotted as in Figure 1-2. In a moderate buffer solution (biological condition), this length is on the order of 1 nm, meaning beyond this distance from the chip surface, no electronic charge can be detectable. Therefore, detecting large molecules such as longer DNA sequences or protein in blood samples is not possible with FET devices. In other words, developing these devices for point-of-care applications in the potentiometric readout mode is far from attainable. The Debye screening effect was reported for both ISFET [67,68] and SiNW FET [69–71] sensors in the literature.

A different approach is to employ the powerful technique of electrochemical impedance spectroscopy with FET devices. The idea is that when there are bindings of analytes to receptors immobilized on the chip surface, not only the drain-source current of FET devices changes but also the whole impedance of the system including the nanowire surface is also modified. The experimental approaches of the frequency response measurement in ISFET-based biosensor applications were described in Refs. [72–75] and showed a stable operation of the sensor against

many side-parameters such as temperature drift, sensor drift, or pH value variations of the solution [76]. This detection method depends on the impedance alteration; therefore, it has the potential to implement measurements in a direct blood sample that is not achievable with a potentiometric approach. Even though reported experimentally successful, the understanding of the detection mechanism and the effects of side parameters (such as the drain, source contact line capacitances, and solution's concentration) are not clear.
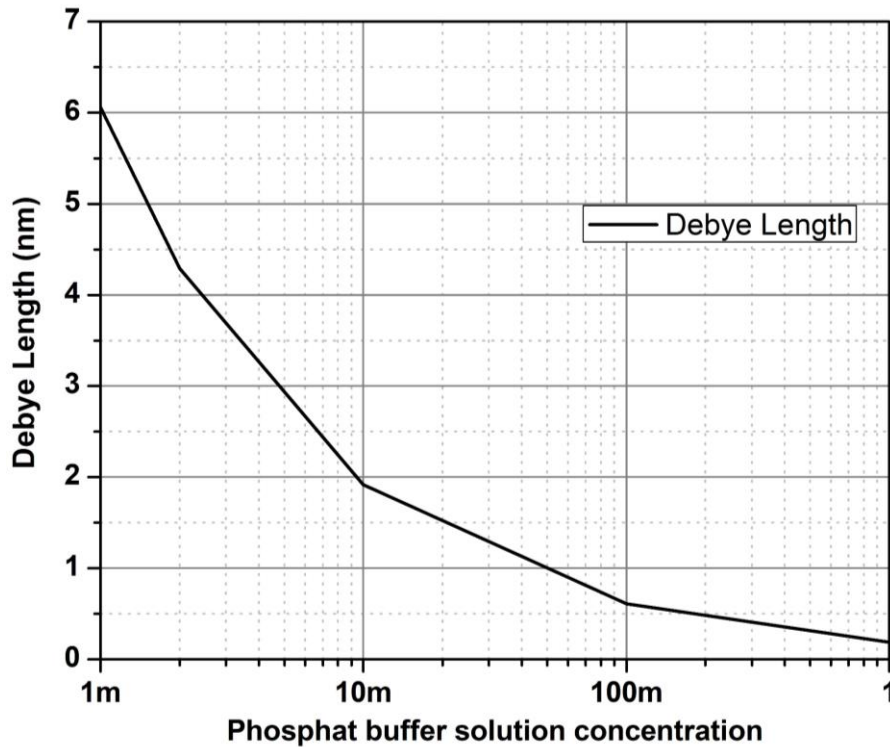
Figure 1-2 Dependence of Debye length on measurement solution concentration

The other main problem that inhibits the development of FET-based array sensors is the reference electrode. As mentioned before, having a well-defined reference electrode in measurement solutions is necessary in all potentiometric measurements. To obtain a micro system, it is recommended that the reference electrode has a comparable dimension to the transistor. The main problem here is the miniaturization of the electrode [77]. Even though there have been many efforts to miniaturize reference electrode [78–81], no way has been found to fabricate "micro-reference electrodes" in large numbers that fulfill basic requirements: stability, reproducibility, and reversibility.

An FET-based biosensor also has three main components like any other biosensor (Figure 1-1). To use the devices reliably, the readout part is equally important. The binding of a small number of molecules to the chip surface normally generates little potential signal (range of only a few mV). To obtain an adequate signal-to-noise ratio (SNR), it is crucial to keep the noise as low as possible to distinguish the signal from noise. Most of the time, such devices are measured by a high accuracy

semiconductor parameter analyzer or dedicated system [82–84]. These are either big and expensive or lack the necessary accuracy, portability, and multiplicity.

Besides many efforts to develop chemical processes and biological procedures for surface modification and specific assay developments (not mentioned here), this section described two main challenges and an open issue that constrains the development of an FET-based point-of-care handheld biosensor:

- The measurement of static charges in a liquid environment is limited by the Debye length, which depends on the ionic strength of the solution. This prevents the detection of large molecules in blood samples and therefore inhibits the creation of point-of-care devices.

- A reference electrode is necessary in all potentiometric measurements. A method to fabricate a "micro-reference electrode" in large numbers that fulfill basic requirements – stable, reproducible, and reversible – is currently not available.

- A detailed work on the development of a readout system, especially a portable/handheld one, is missing in the literature.

1.4 Aims of the Thesis

This work is motivated by the aim of bringing an affordable system to everybody that helps them to monitor certain health parameters without involvement of centralized laboratories. To realize this with an FET-based biosensor, the two challenges and one open issue mentioned above need to be solved. In this work, a macroscopic commercial reference electrode will be used. The present approach is to:

- Contribute to understanding the mechanism and working principle of impedance spectroscopy measurements with FET devices.

- Create a readout system that can implement both potentiometric and impedimetric measurements with an array of FET sensors for comparison the Debye screening effect on both methods.

- Create a high accuracy, portable/handheld readout device.

1.5 Organization of the Thesis

The format of this thesis is as follows:

- Chapter 1 introduces the general concepts and terminologies of a biosensor. The idea of label-free detection with FET devices is discussed. Then the limitation of potentiometric detection and the motivation of the work toward the impedimetric detection and the goals of the thesis are described.

- Chapter 2 describes the background of the impedance spectroscopy method and discusses the state of the art of impedimetric measurement with ISFETs.

- Chapter 3 discusses the theoretical background of field-effect-transistor based biosensors. The working principle of ISFET as well as SiNW FET, together with two measurement approaches: potentiometric and impedimetric will be explained.

- Chapter 4 explains transducer fabrication. FET-sensor chips encapsulation and electric characterization are also described.

- Chapter 5 focuses on measurement setups. Two different readout systems (32-channel and 4-channel handheld) are designed and developed. Measurements with the developed systems and a standard parameter analyzer are compared. The noise power spectrum and signal to noise ratio will be evaluated.

- Chapter 6 deals with different biosensor applications. It will be started with pH sensing and then DNA measurements, and finally a proof of concept of impedimetric measurement with the setup for different buffer concentrations is implemented.

- Chapter 7 investigates the simulation for SiNW FETs. At first the characteristic measurements of SiNW FET are simulated by both level2 FET and level7 (BSIM 3v3) for comparison. Later, this model is used to examine factors that affect the impedimetric measurements with SiNW FETs.

- Chapter 8 conclusions are provided, and possible further developments of SiNW FET based biosensors are proposed.

- The Appendix contains a more detailed description of the fabrication process for ISFET and SiNW FET devices, and a PSPICE source-code for the simulation.

2. State-of-the-Art of Impedance Spectroscopy with FET Devices

2.1 Electrochemical Impedance Spectroscopy-Background

Electrochemical Impedance Spectroscopy (EIS) is a powerful technique for the analysis of interfacial property changes of modified electrodes upon biorecognition events happening at the surface [85]. The advantage of EIS is that, with a single experimental procedure covering enough frequencies, the influence of the governing physical and chemical phenomena can be distinguished and isolated at a given applied potential [86]. Impedance measurements supply detailed information on capacitance/resistance variation taking place at sensors' surfaces. Therefore, it has long been used to characterize biomaterial films associated with electronic elements [87–89].

EIS can be classified as Faradaic or non-Faradaic impedance spectroscopy based on the magnitude of a DC current flowing through the interface [90]. If there is no DC current, the frequency scanning is referred to as non-Faradaic impedance spectroscopy. In this case, the measurement results in capacitive sensing and the capacitance of the interface plays an important role in determining the impedance response. If there is a DC current flowing through the interface, the measurement is referred to as Faradaic impedance spectroscopy. It allows analysis of kinetics and the mechanism of bioelectrocatalytic reaction, providing information for the development of amperometric biosensors and biofuel cells [85].

Fundamental purpose of EIS is to apply a small amplitude sinusoidal excitation signal to an electrochemical cell and to measure the resulting response. Figure 2-1 shows a non-linear I-V curve of a theoretical electrochemical system. A small amplitude wave – $\Delta V\sin(\omega t)$ – is applied to the working polarization voltage, V. This induces a current response of $\Delta I\sin(\omega t + \psi)$ superimposed on the DC current, I. The Taylor series expansion is as follows:

$$\Delta I = \left(\frac{dI}{dV}\right)_{V,I} \Delta V + \frac{1}{2!}\left(\frac{d^2I}{dV^2}\right)_{V,I} \Delta V^2 + \frac{1}{3!}\left(\frac{d^2I}{dV^2}\right)_{V,I} \Delta V^2 + \ldots \qquad (2)$$

If the magnitude of the sinusoidal amplitude signal ΔV is small enough, the higher order terms in equation (2) can be neglected. The impedance of the system can then be calculated using Ohm's law:

$$Z(\omega) = \left(\frac{dV}{dI}\right)_{V,I} \approx \frac{\Delta V(\omega)}{\Delta I(\omega)} \qquad (3)$$

The impedance spectrum of the system can be obtained by varying the frequency of the applied signal. Typically, a frequency range of 0.1 Hz – 100 kHz is scanned in the measurement with an electrochemical system. There are two ways of data representation: the real part of impedance versus the imaginary part (Nyquist Plot); the magnitude of impedance and the phase shifts against frequency in two different plots (Bode Plot).

9

Impedance spectroscopy can be implemented in the potentiostatic or galvanostatic mode [91]. In the potentiostatic mode, experiments are implemented at a fixed DC voltage. A stimulation sinusoidal voltage is superimposed on the DC potential and applied to the system. The response current is measured to calculate the impedance of the system. On the other hand, in the galvanostatic mode, experiments are conducted at a fixed DC current. A stimulation sinusoidal current is superimposed on the DC current and applied to the system. The response voltage is measured to calculate the impedance of the system. Normally, impedance spectroscopy is done under the potentiostatic mode. In some cases, e.g. battery research, impedance experiments can be implemented in the galvanostatic mode.
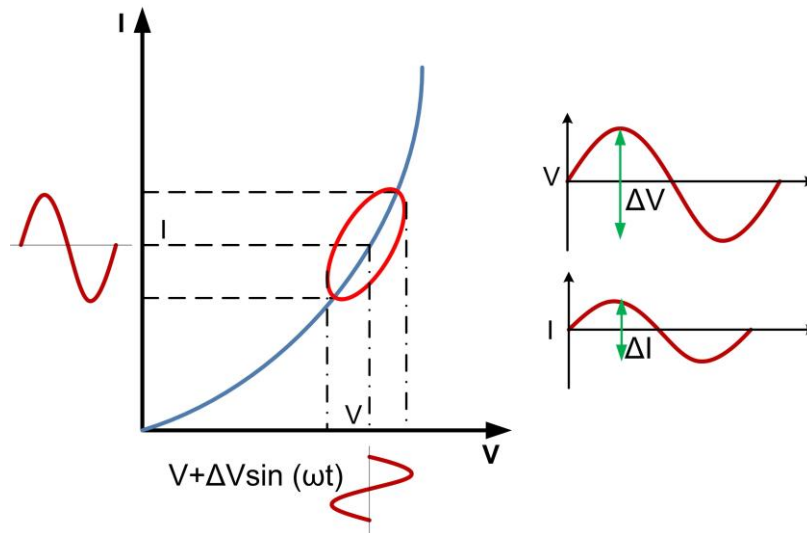
Figure 2-1 Principle of EIS measurement (adapted from [86])

In order to provide impedance measurement the system under analysis needs to satisfy the following conditions [92]:

- Linearity: this condition is fulfilled when the applied stimulation sinusoidal signal is small enough such that the selected state of the system is unchanged.

- Steady state: the measurement should be independent from the moment of the measurement. This applies to all frequencies of interest.

- Finiteness: the real and imaginary parts of the impedance should have finite values at all frequencies of interest.

- No memory properties: the measurement should be independent from the sequence of measurements.

A typical setup to measure impedance spectrum consists of a cell (the system under interest), a potentiostat/galvanostat, and a frequency response analyzer (FRA). The FRA stimulates the cell with a signal and measures the response from potentiostat/galvanostat to calculate the impedance at the frequency of the applied signal.

To interpret the experimental data, it is common to use equivalent circuit models. These models normally consist of well-known passive elements such as: resistor, capacitor, inductor, constant phase element and Warburg impedance (Table 2-1). These elements can be connected in series and/or parallel to fit the best the impedance spectrum.

Circuit Element	Impedance
R, Resistance	R
C, capacitance	$Z = \dfrac{1}{j\omega C}$
L, Inductance	$Z = j\omega L$
CPE, Constant Phase Element: Y_0 is the admittance of an ideal capacitance and α is an empirical constant, ranging from 0 to 1.	$Z = \dfrac{1}{Y_0(j\omega)^\alpha}$
W, Warburg impedance under the assumption of semi-infinite diffusion layer: Y_0 is the diffusion admittance	$Z = \dfrac{1}{Y_0\sqrt{j\omega}}$
W, Warburg impedance under the assumption of a finite diffusion layer thickness: Y_0 the diffusion admittance, δ is the diffusion layer thickness and D is the diffusion coefficient	$Z = \dfrac{1}{Y_0}\tanh\left(B\sqrt{j\omega\tau}\right);$ $B = \dfrac{\delta}{\sqrt{D}}$

Table 2-1 Summary of equivalent circuit elements (adapted from [93])

The main advantages of EIS can be described as follows [90,94]:

- Simple and high sensitivity: The impedance spectroscopy is becoming a popular analytical tool in biosensor research because it involves a relatively simple electrical measurement whose results can be used to investigate properties of sensing membranes. It is highly sensitive to the bioevents happening close to the sensor surface. Utilizing short self-assembly-monolayer for immobilization and low buffer strength solutions can improve sensitivity.

- Label-free: the EIS does not require reporter molecules because it depends on the inherent properties of molecules. It is therefore suitable for sensing proteins which are difficult to label.

- Real-time detection: a common approach that at first experiments are implemented with *ex situ* detection, that the whole frequency spectrum is obtained. However, once a specific frequency range is found where the biorecognition events are clearly distinguished, the detection can be done at a chosen frequency and the impedance can be measured with biomolecular interactions as a function of time.

- Ease of integration: the EIS is fully electronic in nature, therefore it has great chance to facilitate handheld point of care applications by using standard electronic integration circuits.

Though enjoying many advantages compared to conventional label detections and other label-free methods, EIS has its disadvantages, such as:

- Blocking and surface cleaning: the short-immobilized monolayer normally has low surface coverage, which permits non-specific attachment. In many cases, it requires a blocking step to reduce detection errors, especially if the sample contains a large percentage of interfering molecules. In addition, the cleaning procedure also needs to be carefully monitored to minimize the cross-talk between channels.

- One of the disadvantages of EIS is primarily related to possible ambiguities in results interpretation. Which specific equivalent circuit should be used if one is necessary? An equivalent circuit containing too many circuit elements can often be rearranged in different ways and still result in the same impedance spectra.

Through this section, it can be seen that EIS is highly sensitive to bio recognition events occurring close to the sensor surface, and can be used as label-free, point-of-care array platform. Despite its shortcomings, EIS is still a very promising alternative to some commercially label-free detection systems such as SPR and QCM.

2.2 Review of Impedance Spectroscopy Measurements with FET Devices

Schasfoort et al, [95,96] proposed the impedance spectra measurement with an ISFET to detect the charge redistribution of an (human serum albumin) HSA-antiHSA complex (a precipitate) formed on top of the sensor. The measurement setup is described in Figure 2-2. A function generator applied a 20 mV (peak-peak) sinusoidal signal to the calomel reference electrode (a reference electrode that is based on the reaction between mercury Hg and mercury chloride Hg_2Cl_2). To reduce the impedance of the reference electrode at all frequencies, a Pt wire in series with a 1 µF capacitor was connected in parallel to the electrode. The drain-source current was converted to the voltage by an I-V converter. Authors stated that only the magnitude of the transfer function is sufficient to characterize the existence of the antigen-antibody complex; the phase shift does not provide additional information. It was observed that the cut-off frequency of the impedance spectrum of an ISFET with the complex was noticeably higher than that of the bare ISFET. Noting the similar effect in measurements with different buffer concentrations, this work suggested that the ions present in the immunocomplex layer diffuse out of the layer after immersing the sensor into the electrolyte. Since the layer closest to the surface of the gate area contributes the largest part of the total resistance from the reference electrode to the chip's surface, this resistor is influenced heavily by the diffusion of ions out of the complex. As the results demonstrated, after dipping the ISFET into the solution the cut-off frequency decreased as a function of time. Once

this diffusion stopped, the total resistance of ISFET with the immunocomplex was still significantly higher than that of the bare ISFET, therefore the cut-off frequency of the impedance spectrum of a ISFET with the complex was higher than that of the bare ISFET. The papers claimed that the capacitive effect of the protein can be neglected. Kruise et al., [97] further worked on this question with experiments with cross-linked lysozyme. He learned that the membrane resistance is inversely proportional to the fixed charge density.
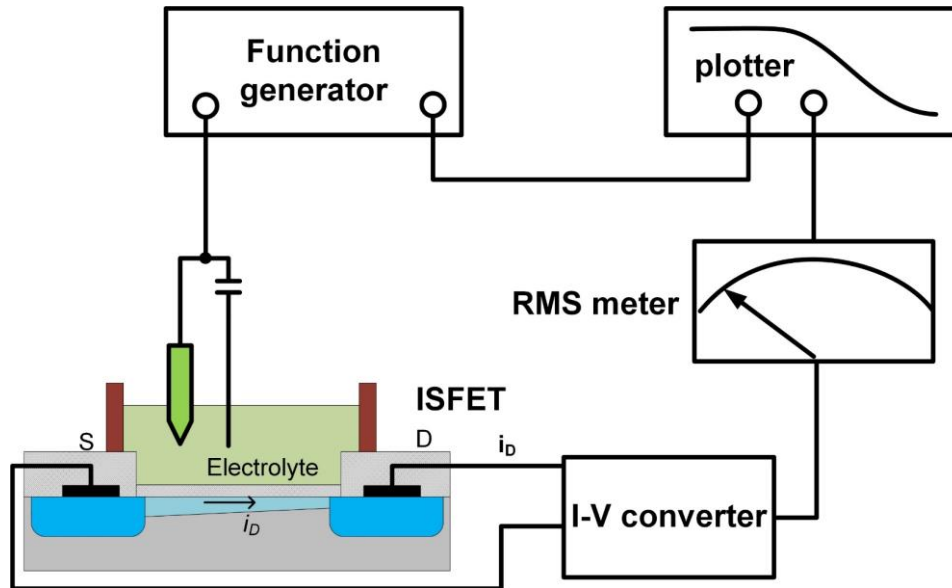

Figure 2-2 Block diagram of AC measurement (adapted from [95])

Antonisse et al., [72] utilized the impedance spectroscopy to characterize an ion selective ISFET (CHEMFET) and the influence of polymer membranes on ISFET (MEMFET), respectively. In these studies, the ISFET with adhered membrane was depicted by an equivalent electronic circuit, as in Figure 2-3. In this model, the membrane impedance is modeled as a sum of a membrane bulk and an oxide-liquid interface impedance. The membrane bulk impedance is represented by a resistor (R_{mem}) and a capacitor (C_{mem}) in parallel. The oxide-liquid interface part is described by the double-layer capacitance (C_{DL}), the resistance of the charge transfer at the interface (R_{CT}), and a contribution from the diffusion of ions, which are represented by a Warburg element (W). The interfacial effect on the membrane is generally detectable at low frequencies. However, according to the authors, the rapid exchange of the ions at the interface results in a charge transfer resistance, which is too small to be observed. The impedance contribution of the ISFET to the whole sensor is modeled by the silicon-electrode resistance (R_{Si}) in series with a space-charge capacitance (C_{SC}), and the oxide layer capacitance (C_{ox}). The space-charge capacitance is negligible compared to the oxide layer capacitance when the ISFET is working in inversion mode. Also, the electrode resistance and the resistance of the electrolyte solution (R_{sol}) are small (100 Ω or less) compared with the membrane resistance (~10^5 Ω) and can also be neglected. The equivalent circuit therefore can be simplified as in Figure 2-4.
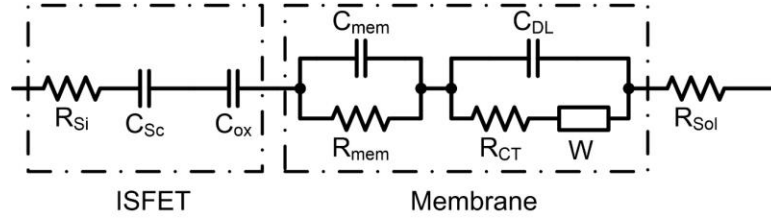
Figure 2-3 Equivalent circuit of a membrane-coated ISFET (MEMFET) (adapted from [72])
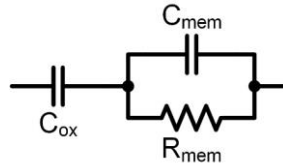
Figure 2-4 Simplified equivalent circuit of a membrane-coated ISFET

Utilizing the measurement setup in Figure 2-5, the drain-source current variation (i_D) can be measured as a function of sinusoidal signal applied at the gate electrode (v_{GS}). The voltage after the transimpedance amplifier v_{out} is calculated from i_{DS}, v_{GS}, and g_m as given by equation (4)
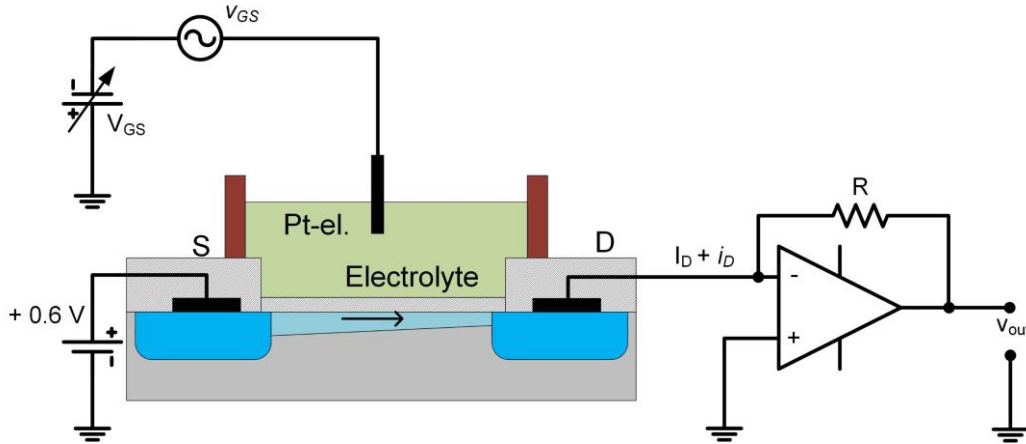
Figure 2-5 Measurement setup for ISFET transconductance measurement (adapted from [72])

$$v_{out} = -Ri_{DS} = -Rg_m v_{GS} \tag{4}$$

The applied gate voltage v_{GS} is divided over the membrane and the oxide when there is a biological layer deposited on top of the gate oxide of the ISFET. The relationship between the effective gate voltage and the applied voltage can be described by a transfer function $H(j\omega)$. From the simplified equivalent circuit in Figure 2-4, the transfer function can be defined as follows:

$$H(j\omega) = \frac{1 + j\omega R_{mem} C_{mem}}{1 + j\omega R_{mem}(C_{mem} + C_{ox})} \tag{5}$$

The output voltage after the amplifier stage:

$$v_{out} = -Rg_m H(j\omega)v_{GS} \tag{6}$$
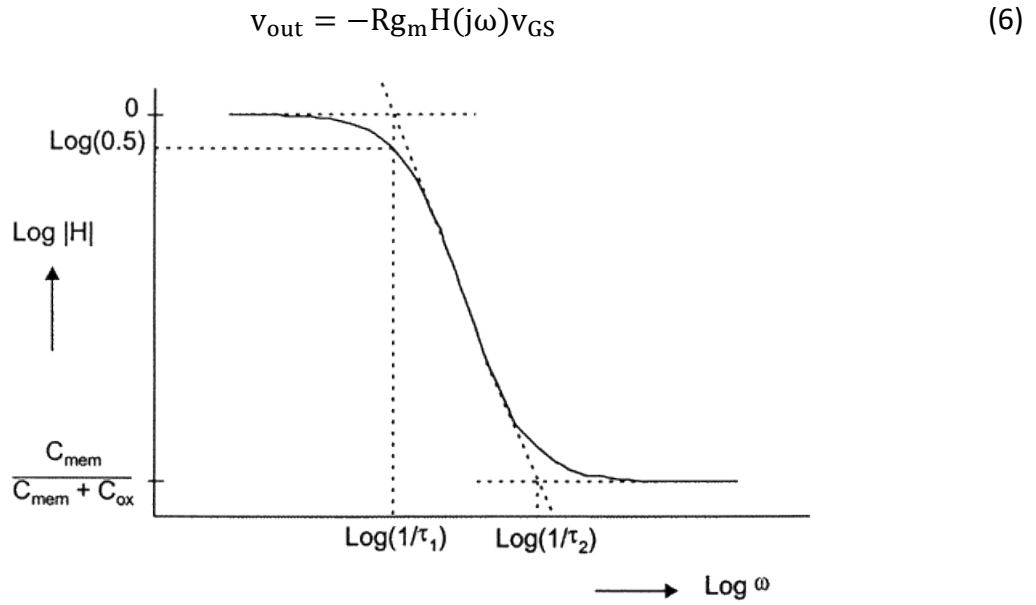
Figure 2-6 Theoretical transfer function $|H(j\omega)|$, reprinted with permission from [72]. Copyright 2000 American Chemical Society

The relation between the transfer function and the frequency is illustrated in Figure 2-6. The time constants corresponding to the pole and zero points can be calculated in equation (7) and equation (8). If the capacitance of the surface oxide is known, by obtaining these two constants, the evaluation of membrane properties through R_{mem} and C_{mem} is possible.

$$\tau_1 = R_{mem}(C_{mem} + C_{ox}) \tag{7}$$

$$\tau_2 = R_{mem}C_{mem} \tag{8}$$

Kharitonov et al., [73] employed the theory from Antonisse et al., to study the thickness of layered protein assemblies on the gate interface. In addition, authors stated that one crucial prerequisite needs to be satisfied to use the impedance spectroscopy with the ISFET sensor. That is, the protein layer(s) should be significantly thinner compared to the thickness of the oxide-layer or the membrane associated with the gate surface. The work reported the characterization of layered assemblies consisting of glucose oxidase and of biotin-cross-linked avidin. Additionally, Zayats et al., [98] compared the thickness measurement on ISFET with complementary surface plasmon resonance and found similar film thicknesses of the biomaterial and comparable detection limits. In this work, a dinitrophenyl (DNP) antigen layer is immobilized as a receptor for the sensing of anti-dinitrophenyl antibody (anti-DNP-Ab). The detection sensitivity of anti-DNP-Ab corresponds to 0.1 μgmL^{-1}. Based on the impedance spectrum of the measurements, authors claimed that the association of the anti-DNP-Ab to the anti-antibody to the functional interface mainly alters the capacitance of the membrane. This work also described the cholera toxin (CT) sensing

15

measurement. The binding of the CT and anti-CT, which is immobilized on the chip surface, was monitored by the impedance spectroscopy. The detection limit for sensing CT was 10 fM.

Ingebrandt et al., [99] proposed a differential impedance readout (also was named AC readout to distinguish from the potential (DC) readout method) on FET microarrays for the detection of DNA hybridization (a short description of a DNA structure and DNA-DNA hybridization can be found in the section 6.2). The work also described the comparison between the AC and DC measurement methods in terms of selectivity and reliability using the same FET devices. The DC measurement method can achieve a selectivity of only two mismatches in 20 base pair (bp) sequences, although the target DNA concentration was very high (3 µM in a standard Tris-EDTA (TE) buffer solution). The ionic strength of the buffer solution must be kept low during the potentiometric detection of DNA hybridization to avoid charge screening. This leads to a long hybridization time, from 10 minutes to hours. Practically, the DC detection is easily varied by side effects such as sensor drift, temperature drift, changes in electrolyte composition, pH value, influence of the reference electrode, etc. The work claimed that the differential impedance measurement method provides stable operation of the sensor against these parameters.

Figure 2-7 depicts results of a DNA hybridization experiment with impedimetric detection. After hybridization, the time constants of the impedance spectrum measurements change relied upon the probability of the target DNA to bind to the receptor layer on the transistor gate. The perfect match (PM) channel showed the largest change. The differences between fully mismatch (FMM), 1 mismatch (1MM) and perfect match (PM) are clearly discriminated. The selectivity of the transfer function method could resolve the detection of single polymorphisms (SNPs), which is superior compared to the DC *in situ* readout. Authors claimed that the differential transfer function method has three advantages over the fluorescence techniques: first, it is label-free detection; second, it reduces unspecific binding if these bindings occur at different spots; and third, this detection method is not modified by any background signal as is the case for the fluorescence method. Author explained that as the binding of the target DNA to the probe DNA happened, the resulting double stranded DNA led to difficulty with protonation and deprotonation processes. As a result, the resistance of the membrane increased. Consequently, this led to higher time constant τ_1. Additionally, the double stranded DNA will be denser compared to the single stranded DNA that causes the increase of the membrane capacitance, which changes the time constant τ_2. In other words, the authors stated that the membrane formed by the complex of the single stranded probe DNA and the target DNA induced not only a change in the membrane resistance, but also in the membrane capacitance.
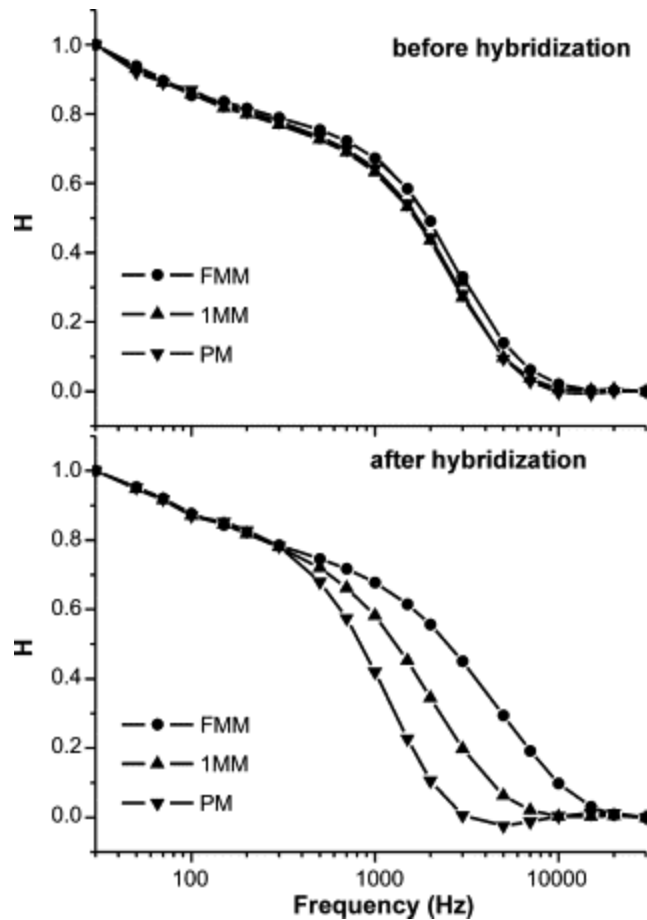
Figure 2-7 Impedimetric *ex situ* detection of the hybridization by readout of the transfer function for each channel. After immobilization of the different probe DNA sequences, the time constants for the low pass of the three channels were almost identical. After hybridization, the differences between FMM, 1 MM and PM can be clearly distinguished. Reprinted from [99], Copyright (2007), with permission from Elsevier.

Further, Susloparova et al., [100] described the utilization of impedance spectroscopy with ISFET to study the adhesion status of human embryonic kidney (HEK293) and human lung adenocarcinoma epithelial (H441) cancer cells at a single cell level. Real-time impedance measurement at 200 kHz resulted in 20% change in the amplitude of the impedance spectra as a result of the introduction of a well-known chemotherapeutic drug, topotecan hydro-chloride, to the cells. The experimental results were interpreted with an equivalent electronic circuit to evaluate the influence of the system parameters. The authors claimed that the developed method could be employed to analyze the specificity and efficiency of novel anti-cancer drugs in cancer therapy research on a single cell level in parallelized measurements. Similarly, Law et al., [101] reported the monitoring of human T cells (human CD8^{+} T) migration on a FET-based sensor using the same method. The real-time impedance measurement at a fixed frequency was used to trace individually migrating T cells. The authors were very confident that the system can be adapted to other cellular

models such as migrating cells during wound healing or single neuron migrations during brain development.

In summary, since the first introduction of the impedance spectroscopy with an ISFET in 1989, there have been several publications that described different applications with this method: from DNA sequencing to immunosensor and cell adhesion measurements. It was claimed that this method is superior compared to the potentiometric detection method and can be more immune to some side effects that compromise both the potentiometric measurement and fluorescence method. To interpret the molecular detection experimental results, it is commonly assumed that the complex of receptors and target molecules forms an ion permeable membrane on the gate surface of ISFETs. This membrane will have either resistive or capacitive, or both effects, on the impedance spectra measurement. All the impedance spectra presented was only to describe the sensor itself. The coupling of sensors and the readout system and effect of other parasitic parameters such as drain, source capacitances were left out of consideration in many of the previous works.

3. Theoretical Considerations

3.1 From MOSFET to ISFET and SiNW

MOSFET

The metal oxide semiconductor field-effect transistor (MOSFET) is the most widely used electronic device, especially in the design of integrated circuits (ICs). The enhancement-type MOSFET is the key element in multiple applications from signal amplification to digital logic and memory [102,103]. The physical structure of a p-type MOSFET is shown in Figure 3-1. It includes two highly p-doped regions (p+ source and p+ drain) in an n-type semiconductor substrate and therefore fits the definition of a pnp structure. A thin layer of silicon dioxide (SiO_2) of thickness t_{ox} (typically 1 nm to 10 nm) is grown on top of the substrate between the source and drain regions, which functions as an excellent electrical insulator. Metal is deposited on oxide as well as on the source, drain regions, and the substrate (also known as the body). Therefore, MOSFET has four terminals: the gate terminal (G), the source terminal (S), the drain terminal (D) and the substrate or body terminal (B). In most MOSFET operations, the body terminal is connected to the source terminal and to the Ground (GND). Thus, the substrate terminal can be considered as having no effect on the device's characteristics. Commonly, the MOSFET will be regarded as a three-terminal device: gate (G), drain (D) and source (S).
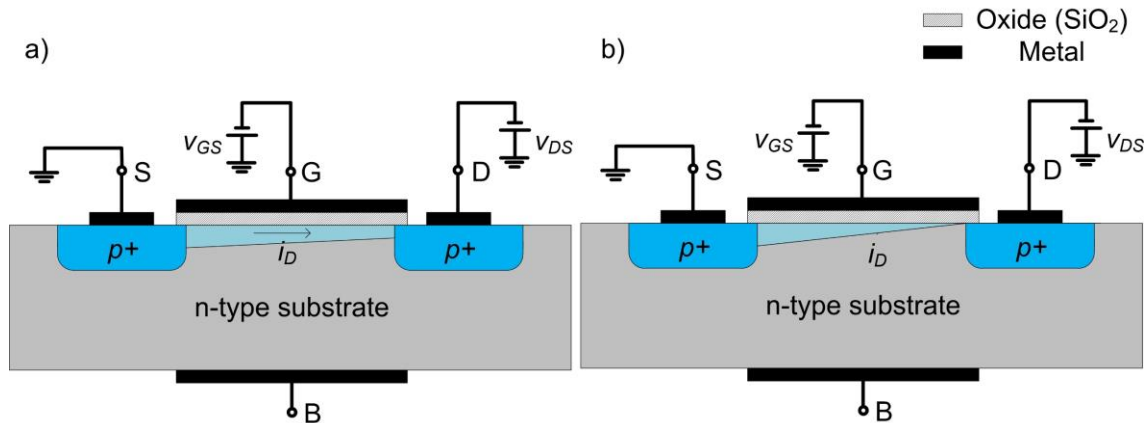

Figure 3-1 Physical structure of the PMOS transistor with two operation modes (adapted from [102]), *a) linear mode; b) saturation mode*

In the following, all statements refer to p-channel devices if not otherwise indicated, because they are the kind of device that were mainly used in the scope of this thesis. However, concepts can also apply to an n-type transistor by analogy.

The voltage applied to the Gate will control the current flows between the Source and Drain (or the conductance of the transistor). A negative voltage on the Gate attracts more holes into the region between oxide and semiconductor. Once this voltage magnitude is greater than the magnitude of

the threshold voltage, a p channel is created as in Figure 3-1. The threshold voltage is the most important parameter and is defined as [103,104]:

$$V_{TH} = \Phi_{ms} - \frac{Q_{ox} + Q_{ss} + Q_D}{C_{ox}} + 2\Psi_B \tag{9}$$

Where Φ_{ms} is the work-function difference between the gate material (metal/polysilicon) and semiconductor; Q_{ox} represents the sum of charges in the oxide; Q_{ss} is the charge at the oxide-semiconductor interface; Q_D refers to the silicon depletion charge, and $2\Psi_B$ is the sum of voltages across the semiconductor.

It can be imagined that the size and number of charge carries is proportional to the excess gate voltage (V_{GS}-V_{TH}). A negative voltage V_{DS} will induce a current flowing from the Source to the Drain terminal. There are two different modes of operation:

- The linear mode: a small value of magnitude voltage of V_{DS} ($|V_{DS}| < |V_{GS} - V_{TH}|$) is applied between the Drain and Source terminals. This is called the linear mode because the MOSFET operates as a linear resistance whose value is controlled by the Gate-Source voltage. The I_{DS}-V_{DS} relationship can be derived in the following equation:

$$I_{DS} = \frac{1}{2}\mu_P C_{ox} \frac{W}{L}[2(V_{GS} - V_{TH})V_{DS} - V_{DS}^2] \tag{10}$$

  with I_{DS} being the electrical current between the Drain and Source electrodes, μ_P the mobility of the hole carriers, C_{ox} the capacitance per unit gate area, W the channel width, and L the channel length. This is nonlinear relationship, however for even smaller value of V_{DS} ($V_{DS} \ll 2(V_{GS} - V_{TH})$), the equation (10) can be rewritten:

$$I_{DS} = \mu_P C_{ox} \frac{W}{L}(V_{GS} - V_{TH})V_{DS} \tag{11}$$

  For a given voltage of V_{GS}, the I_{DS}-V_{DS} relationship is linear (that is why it is called the linear mode).

- The saturation mode: at a higher magnitude of V_{DS} ($|V_{DS}| > |V_{OV}| = |V_{GS} - V_{TH}|$), the channel reaches the term "channel pinch-off" at the drain (Figure 3-1 b). Increasing the magnitude of $|V_{DS}|$ above the $|V_{OV}|$ has no effect on the Drain-Source current; this current remains almost constant. This saturated current can be obtained by replacing $V_{DS} = V_{OV}$ in the equation (10):

$$I_{DS} = \frac{1}{2}\mu_P C_{ox} \frac{W}{L}(V_{GS} - V_{TH})^2 \tag{12}$$

In the following sections, working points of ISFET/SiNW FET sensors in real-time measurements (I_{DS} vs time) will be always in the linear mode. But during the characteristic (I-V curve) experiments there are some time they will go to the saturation mode. However, the lengths of

ISFET/SiNW are above 5 µm. Therefore, the channel-length modulation phenomenon can be neglected in this work.
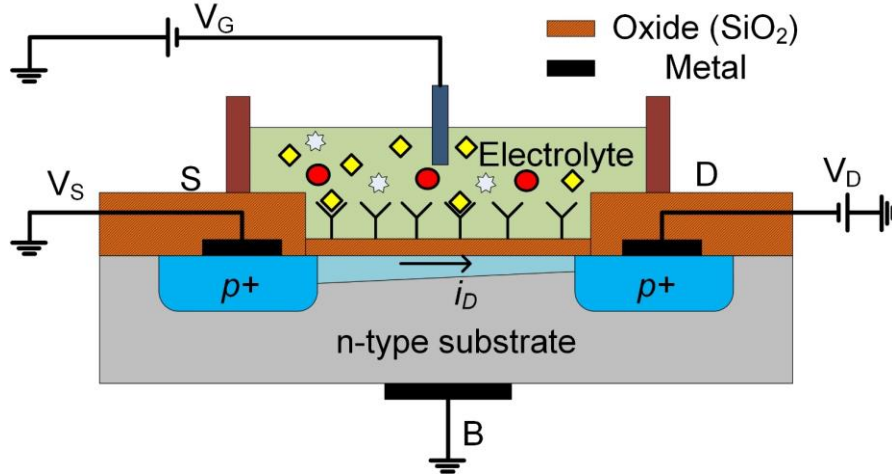
ISFET

Figure 3-2 Sketch of an ISFET configuration

Figure 3-2 illustrates the structure of an ion-sensitive field-effect transistor (ISFET). The ISFET discovered by Bergveld and others [27] is basically a MOSFET where the metal (or polysilicon) gate is replaced by a liquid solution and the channel conductance is controlled by the voltage of a reference electrode immersed in the analytic solution. To avoid the leakage currents between the Gate electrode through the liquid to the Drain and Source terminals, thick layers of insulator cover the contact lines of these electrodes. The gate oxide in direct contact with the solution has the hydroxyl groups at the surface that can take or give away protons. Therefore, the simplest application of ISFETs is a pH sensor. Moreover, different chemical processes induce sensing layers on the top of the gate dielectric, which enable the ISFET to detect chemical or biological species.

The basic working principle of an ISFET is that the binding and unbinding of ion molecules in the analytic solution to sensing layer alter the surface potential of the layer and thus modify the threshold voltage of the device. The V_{TH} equation of a MOSFET now can be rewritten for an ISFET as [105]:

$$V_{TH} = \mathrm{E}_{ref} + \chi_{sol} - \Psi_0 - \frac{\Psi_s}{q} - \frac{Q_{ox} + Q_{ss} + Q_D}{C_{ox}} + 2\Psi_B \qquad (13)$$

with the potential of the reference electrode to vacuum E_{ref}. In the liquid environment, this potential is defined by the surface dipole potential of the solution χ_{sol}; Ψ_s is the working function of the semiconductor and Ψ_0 is the surface potential which depends on the chemical composition of the electrolyte and the gate surface material. The potential drop from the reference electrode to the transducer is depicted in Figure 3-3. It has been shown that having an electrochemical reference

21

electrode immersed in the electrolyte is crucial in maintaining the working reliability of ISFETs [64].

In the ideal case, only Ψ_0 is the varying parameter in equation (13) upon changes in the electrolyte composition. Thus, $\Delta V_{TH} = -\Delta\Psi_0$. The only question left is how Ψ_0 is related to the electrolyte composition. In the simplest application, pH sensing, this relation is described by the double layers (Gouy-Chapmann-Stern) theory [106–110] and the site-binding mode [111], which will be discussed in detail in the next section.
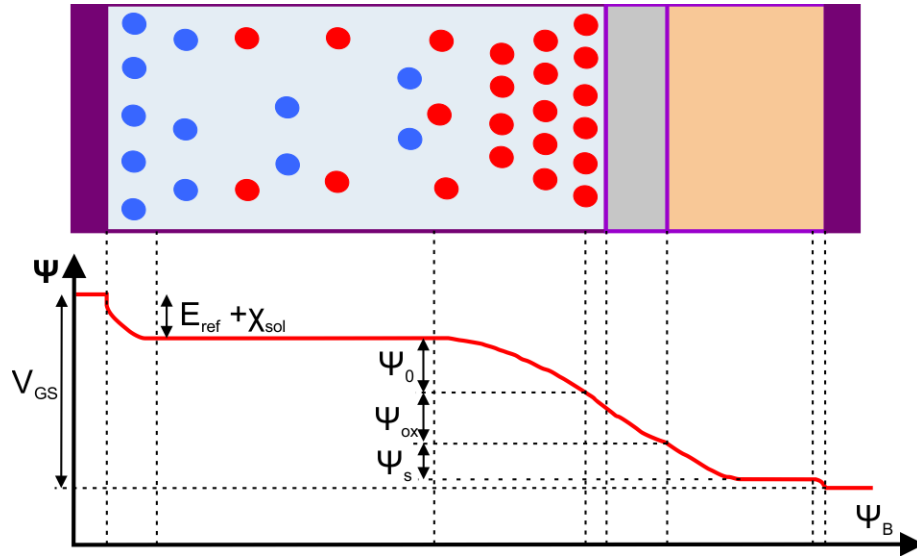

Figure 3-3 Potential drops along the ISFET structure with liquid gate (adapted from [112])

The transconductance (g_m) of an ISFET is the characteristic that reflects the change in the Drain-Source current upon the variation of the Gate-Source voltage. It is another important criterion of an ISFET device because it hints at how sensitive the sensor is. In the real-time measurement mode, the working point where the g_m is at maximum is selected to monitor the variation of the I_{DS} upon the binding of molecules of interest to the sensing layer of ISFET devices. Figure 3-4 depicts an example of transfer characteristics of an ISFET and its transconductance value. Having the relationship between I_{DS}-V_{GS} in equation (11) and (12), the transconductance can be determined by taking the derivative of those equations:

$$g_m = \frac{\partial i_{DS}}{\partial v_{GS}} = \begin{cases} \mu_P C_{ox} \dfrac{W}{L} V_{DS} & \text{Linear mode} \\ \mu_P C_{ox} \dfrac{W}{L} (V_{GS} - V_{TH}) & \text{Saturation mode} \end{cases} \tag{14}$$
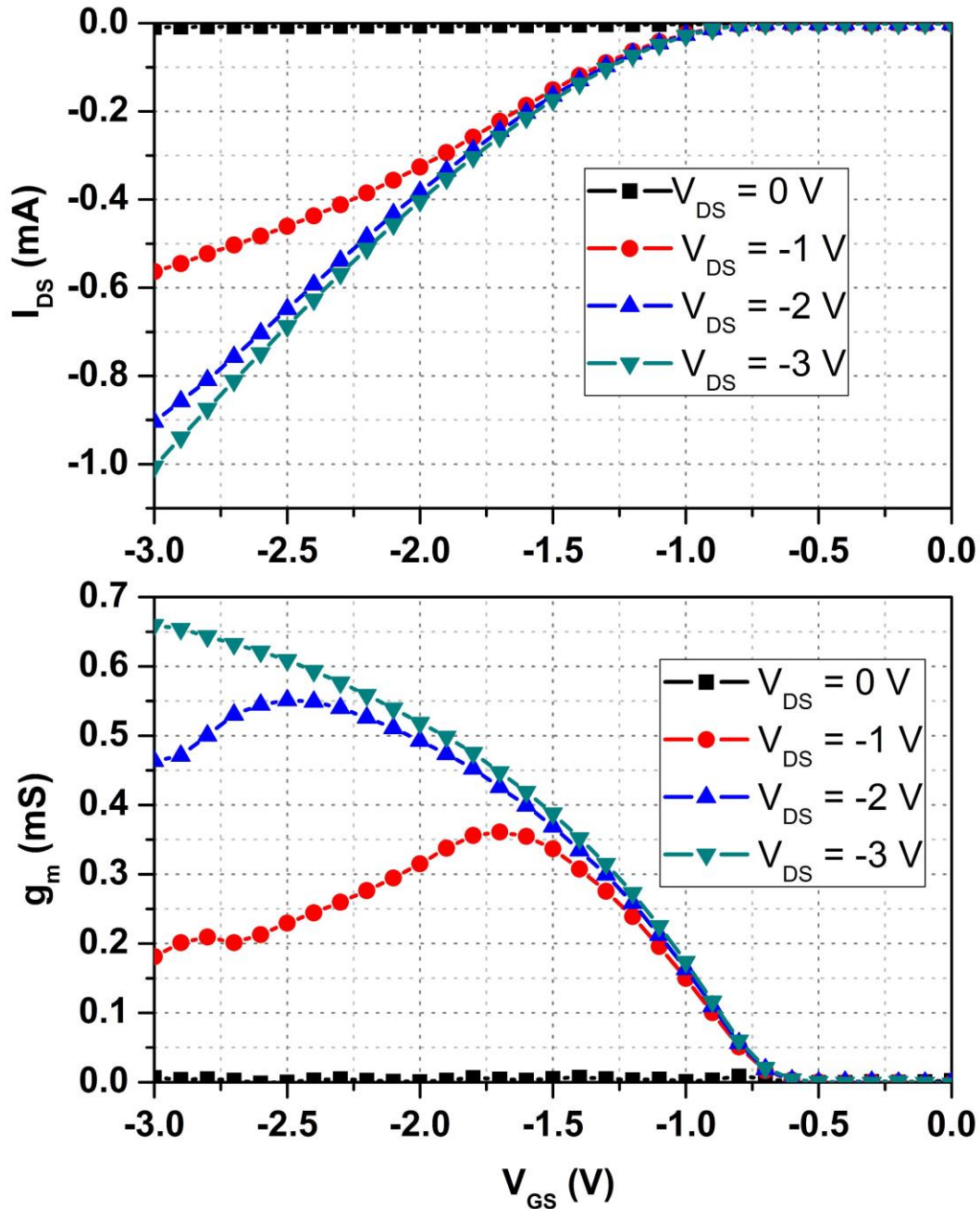
Figure 3-4 Transfer characteristic of an ISFET and the transconductance value

SiNW FET

It is important to understand the working principle of a Silicon nanowire (SiNW) based sensor to evaluate its potential as well as to overcome its constraints. A SiNW-based sensor fundamentally shares the same working principle as the conventional ISFET in the way that it transfers the change of the surface potential on the nanowire to the wire conductance variation. However, there are also differences. SiNWs were fabricated on Silicon on insulator wafers (SOI) and an oxide layer isolates

the whole channel from the substrate. SiNW FET is smaller and so are its transconductance values. A SiNW FET structure includes a low p-doped nanowire between two highly p-doped silicon regions functioning as the source and drain contact lines (Figure 3-5). Differing from planar ISFET, SiNW FET has a multigate (or multiple-gate) structure [113] (shown in the Figure 3-5b) and the wire itself is the conductance channel [114]. The device therefore has a much higher surface-to-volume ratio compared to conventional planar ISFET. In addition, because the size of SiNWs is comparable with the size of biomolecules, a small total number of biomolecules attached to the surface of the nanowire will induce a detectable variation of the device's conductance. Thus, SiNW FET has higher sensitivity compared to micro-sized ISFET devices. The reported sensitivity of a SiNW FET sensor varies from nanomolar to femtomolar of analyte concentration [115,116]. Because of its significantly high surface-to-volume ratio and its high sensitivity detection capability, the detection mechanism of SiNW FET based sensors is still under discussion. However, many theoretical considerations for ISFET are also relevant to SiNW FET cases.
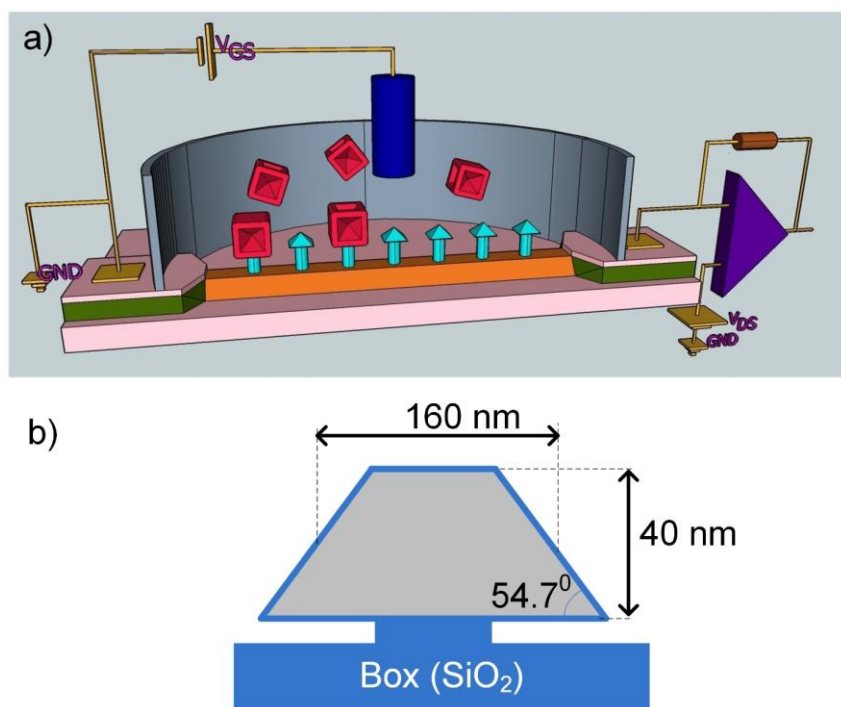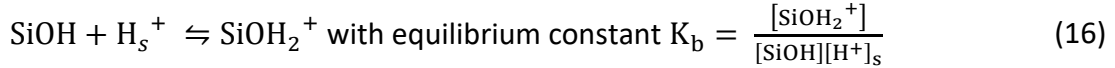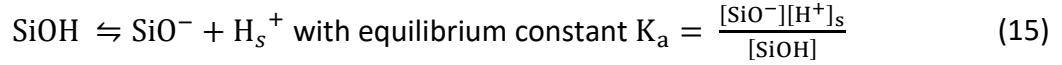

Figure 3-5 a) Structure of a SiNW FET based sensor; b) Cross section of a single SiNW

3.2 pH Sensing

Field-effect transistor sensors, because of their real-time readout capability, are well-suited to pH sensing, which is fast and reversible. Applications of pH sensing include metabolic studies on large and small number of cells [18]. It is generally considered that the dominating surface charging mechanism of pH sensing with FET devices is the protonation and deprotonation of the hydroxyl groups of the silicon oxide surface (SiOH). Therefore, the surface potential and hence the threshold voltage V_{TH} of the sensor are modulated by the pH of the measurement solution [30,111,117,118]

which was well described by the Site-binding theory. The following equations 15 – 38 will investigate the dependence of surface potential Ψ_0 at the electrolyte-insulator interface upon pH of the bulk solution following [30,118]. Among those the equations 21-26 and 35-37 were derived from this work for better understanding the final conclusion of the dependence. The assumption of the site-binding theory is that there are discrete sites located on the chip's surface which are considered as amphoteric binding sites (can be both proton donor and acceptor) Figure 3-6 :

$$\text{SiOH} \leftrightarrows \text{SiO}^- + \text{H}_s^+ \text{ with equilibrium constant } K_a = \frac{[\text{SiO}^-][\text{H}^+]_s}{[\text{SiOH}]} \tag{15}$$

$$\text{SiOH} + \text{H}_s^+ \leftrightarrows \text{SiOH}_2^+ \text{ with equilibrium constant } K_b = \frac{[\text{SiOH}_2^+]}{[\text{SiOH}][\text{H}^+]_s} \tag{16}$$

Where Ka and Kb are dimensionless equilibrium constants and $[\text{H}^+]_s$ is the concentration of H^+ ion on the chip surface, which is related to bulk $[\text{H}^+]$ by the Boltzmann equation:

$$[\text{H}^+]_s = [\text{H}^+] \exp(\frac{-q\Psi_0}{kT}) \tag{17}$$

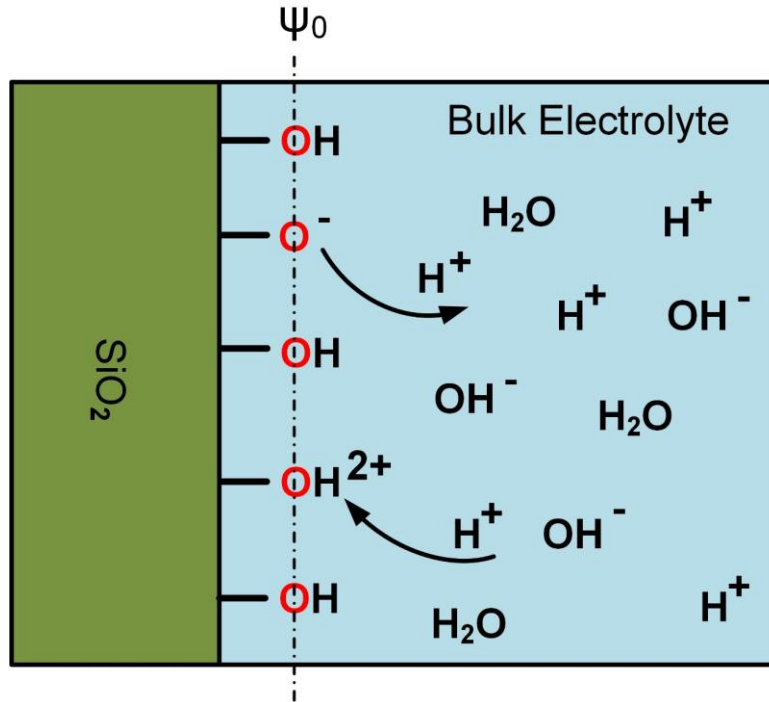q is electron charge, k is Boltzmann constant, T is Kelvin temperature.

Figure 3-6 Hydroxyl group on the oxide surface can function as amphoteric binding sites (can be both proton donor and acceptor)

Replacing $[\text{H}^+]_s$ from equation (15) and (16) to (17):

$$[\text{H}^+] = \sqrt{\frac{K_a}{K_b}} \exp(y_0) \sqrt{\frac{[\text{SiOH}_2^+]}{[\text{SiO}^-]}} \tag{18}$$

Where $y_0 = \dfrac{q\Psi_0}{kT}$

A variable is defined as: $x = \sqrt{\dfrac{[SiOH_2^+]}{[SiO^-]}} \rightarrow [SiOH_2^+] = x^2[SiO^-]$

Two other equations can describe the surface species concentration:

Number of surface sites:

$$N_s = [SiOH] + [SiO^-] + [SiOH_2^+] \tag{19}$$

And the surface charge density:

$$\sigma_0 = q([SiOH_2^+] - [SiO^-]) \tag{20}$$

To calculate x the following equations can be extracted:

$$[SiO^-] = \frac{\sigma_0}{q(x^2 - 1)} \tag{21}$$

$$[SiOH_2^+] = \frac{x^2\sigma_0}{q(x^2 - 1)} \tag{22}$$

Multiple (15) and (16):

$$[SiOH] = \frac{\sigma_0}{q\sqrt{K_aK_b}} \frac{x}{(x^2 - 1)} \tag{23}$$

Replacing (21), (22) and (23) to equation (19):

$$N_s = \frac{\sigma_0}{q(x^2 - 1)} + \frac{\sigma_0}{q\sqrt{K_aK_b}} \frac{x}{(x^2 - 1)} + \frac{x^2\sigma_0}{q(x^2 - 1)} \tag{24}$$

The parameters α_0 is defined as: $\alpha_0 = \dfrac{\sigma_0}{qN_s}$; $\delta = 2\sqrt{K_aK_b}$

Then (24) can be rewritten as follows:

$$(1 - \alpha_0)x^2 - 2\frac{\alpha_0}{\delta}x - (1 + \alpha_0) \tag{25}$$

Solving the equation (25), the value of x can be obtained:

$$x = \frac{\dfrac{\alpha_0}{\delta} + \sqrt{\left(1 + \left(\dfrac{\alpha_0}{\delta}\right)^2 (1 - \delta^2)\right)}}{(1 - \alpha_0)} \tag{26}$$

The concentration of $[H^+]$ in (18) can be described as follows:

$$[H^+] = \sqrt{\frac{K_a}{K_b}} \exp(y_0) \frac{\frac{\propto_0}{\delta} + \sqrt{\left(1 + \left(\frac{\propto_0}{\delta}\right)^2 (1 - \delta^2)\right)}}{(1 - \propto_0)} \tag{27}$$

It is assumed that $\delta^2 \ll 1$ for inorganic insulators such as silicon dioxide. The pH value which is needed to neutralize the surface potential (no net surface charge) of a certain insulator material is called the point of zero charge pH_{pzc}. The value of pH_{pzc} of silicon oxide has been reported between pH 1.5 to pH 3.7 [30]. The neutrality of surface charge leads to $y_0 = 0$ and $\propto_0 = 0$:

$$pH_{pzc} = -\log_{10}([H^+]) = -\log_{10}\left(\sqrt{\frac{K_a}{K_b}}\right) \tag{28}$$

The parameter ϑ is proportional to the difference between the pH and the pH_{pzc}:

$$\vartheta = \ln[H^+] - \ln\sqrt{\frac{K_a}{K_b}} = 2.303 \left(pH_{pzc} - pH\right) \tag{29}$$

Equations (27) and (29) give the basic relation between pH and the surface potential:

$$\vartheta = y_0 + \ln\left(\frac{\propto_0}{\delta} + \sqrt{1 + \left(\frac{\propto_0}{\delta}\right)^2}\right) - \ln(1 - \propto_0)$$
$$= y_0 + \sinh^{-1}\left(\frac{\propto_0}{\delta}\right) - \ln(1 - \propto_0) \tag{30}$$

To achieve the relation of pH/Ψ_0 the model of Gouy-Chapman-Stern for an electrical double layer is used, in which Ψ_0 is the sum of potential of the diffusion and the Stern capacitance.

The surface charges induce an electric field. This electric field brings counter ions to the surface [66]. The layer of surface charges and the counter ions is called "electrical double layer" which is modeled by the Gouy-Chapman and Stern theories. As its name suggests, the electrical double layer consists of two layers: the inner layer of counter ion absorbed on the oxide surface is called the Stern layer; the outer layer is formed by diffused counter ions from the inner layer to the bulk of the solution, which is called the Gouy-Chapman layer. A potential drop over these two layers is depicted in Figure 3-7.

Calculation of Stern capacitance (C_{St}) uses the simple equation for a plate capacitor. The two plates are formed by the absorbed ions and the oxide surface. If R_{ion} is the radius of the hydrated ions (ions at Outer Helmholtz plane: OHP), the radius is in the order of $R_{ion}/2 \approx 2$ Å. The Stern capacitance per unit area is defined as following:

$$C_{St} = \frac{2\varepsilon_{St}\varepsilon_0}{R_{ion}} \tag{31}$$

where ε_{St}: the permittivity at the surface is reduced and typically of the order of $\varepsilon_{St} \sim 6\ldots32$ for water.
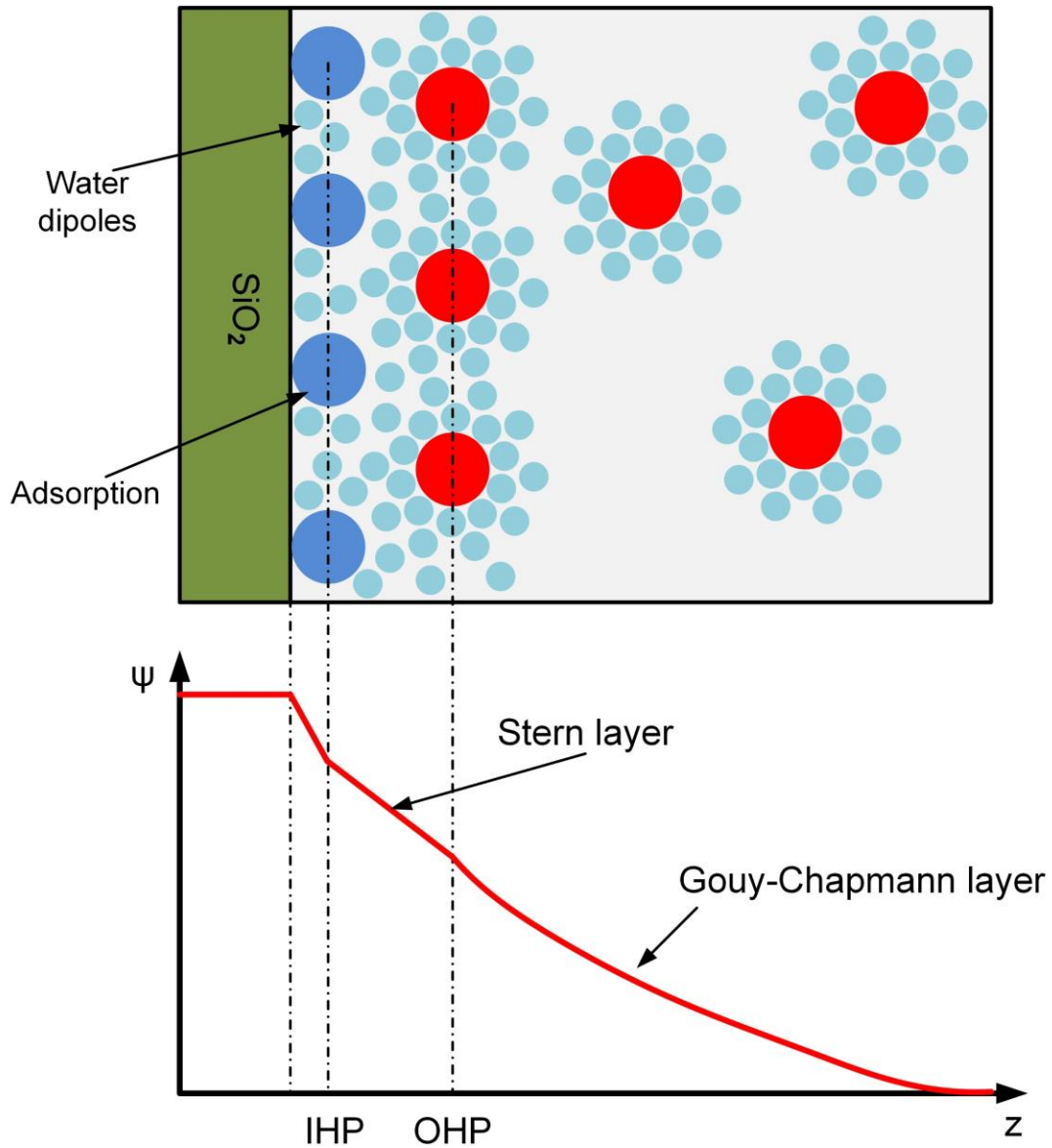

Figure 3-7 Gouy-Chapman-Stern model of oxide-liquid interface and the potential drop over them

Gouy-Chapman capacitance is calculated:

$$C_{GC} = \frac{\sqrt{8\varepsilon\varepsilon_0 kTc}}{2kT/q} \qquad (32)$$

where ε is the dielectric constant for water, and c is the concentration of the electrolyte in ion pairs/cm³.

The equivalent capacitance of Gouy-Chapman capacitor in series with Stern capacitor then can be described as follows:

$$\frac{1}{C_{eq}} = \frac{1}{C_{GC}} + \frac{1}{C_{Stern}} \tag{33}$$

It is assumed that the charge neutrality condition is correct: the surface charge density on the silicon oxide surface is compensated by the charge density over double layers in the electrolyte:

$$\sigma_0 = -\sigma_{dl} = \psi_0 C_{eq} \tag{34}$$

Replace (34) into (30):

$$\vartheta = y_0 + \sinh^{-1}\left(\frac{\Psi_0 C_{eq}}{q N_s \delta}\right) - \ln(1 - \propto_0) = y_0 + \sinh^{-1}\left(\frac{y_0}{\beta}\right) - \ln(1 - \propto_0) \tag{35}$$

$$\beta = \frac{q^2 N_s \delta}{C_{eq} kT} \tag{36}$$

The parameter β is dimensionless and can be considered as the ratio of a voltage value (a voltage related to double layer and thermal voltage kT/q).

It can be assumed that the surface of silicon oxide is far from saturated for the pH measurement ($\propto_0 \ll 1$), and $\sinh^{-1}\left(\frac{y_0}{\beta}\right) \sim \left(\frac{y_0}{\beta}\right)$, the equation (35) can be rewritten as following:

$$2.303 \left(pH_{pzc} - pH\right) = y_0 \left(\frac{\beta}{\beta + 1}\right) = \frac{q\Psi_0}{kT}\left(\frac{\beta}{\beta + 1}\right) \tag{37}$$

The variation of surface potential $\Delta\psi_0$ induced by a change in the pH value of the bulk solution, can be described by the following equation:

$$\Delta\Psi_0 = -2.303 \frac{kT}{q} \frac{\beta}{\beta + 1} \Delta pH \tag{38}$$

This Boltzmann distribution leads to the conclusion that the maximum pH sensitivity is $2.3 * \frac{kT}{q}$ (V/pH) (~ 60 mV/pH at 27 °C), the so-called Nernstian limitation.

3.3 Detection of Biomolecules

As mentioned before, the basic working principle of ISFET devices is detecting the change of the surface potential upon the binding of charged molecules to the dielectric gate surface. The experiments are conducted in electrolytic solutions that have many dissolved ions such as K^+, Na^+, Cl^-, etc. In an interface between electrolyte and electrode, counter ions will accumulate on the surface of an electrode and form a diffuse electric double layer [66]. Therefore, if a potential is

applied to an electrode, it will experience an electrostatic potential drop along the distance to the electrode. At the distance beyond what is called Debye length λ_D, counter ions screen the potential.

An analogous model of pH sensing can be used to explain biomolecules detection with FET devices. It differs from ion detection where the hydroxyl group and ions are close to the surface, within the Debye length, for most electrolyte concentrations used. However, when detecting biomolecules, the sensor's surface needs to be modified and coated with specific receptors that are about 10 nm or longer. In this case, careful selection of buffer solution needs to be done for optimal Debye length [119]. This length is given by the equation (1) [66].

In equation (1), c_i is given in particles per m^3, which is not very common in practice. The ionic strength of the solution is given as: $I_c = \frac{1}{2}\sum c_i Z_i^2$; where c_i is the ion concentration given in mM, and Z_i is the valence of the ith ion sort. Then the equation can be rewritten as follows:

$$\lambda_D = \sqrt{\frac{\varepsilon\varepsilon_0 kT}{2N_A e^2 \sum c_i Z_i^2}} \tag{39}$$

where N_A is the Avogadro constant and the concentration c_i in equation (39) is given in mM.

For example: human blood plasma – that is blood without red and white blood cells and without thrombocytes – contains 143 mM Na^+, 5 mM K^+, 2.5 mM Ca^{2+}, 1 mM Mg^{2+}, 103 mM Cl^-, 27 mM HCO_3^-, 1 mM HPO_4^{2-} and 0.5 mM SO_4^{2-}. At 36°C the water permittivity $\varepsilon = 74.5$, the Debye length is 0.78 nm. This length is around two times the length of one base pair in a DNA molecule (0.34 nm).

It is obvious that detecting the intrinsic charge of proteins and DNA strands in the physiological conditions (where $\lambda_D < 1$ nm) with ISFET faces significant difficulty. Proteins and DNA strands are large molecules and easily longer than one nm. The problem has been indicated in several publications [120–123]. Several approaches were proposed to overcome the Debye screening effect, such as measuring at high frequency [124], differential readout using transfer function [99], or surface modification with polymers [125]. However, the most common way of minimizing the screening effect is conducting measurements in diluted buffer solutions. In experiments, different phosphate buffer solutions (PBS) were used that include monosodium phosphate and disodium phosphate. The Debye lengths calculated in this work for different PBS are given in Table 3-1. The table shows that to detect macro molecules, experiments need to run in low ionic strength solution (1 mM PBS or less). This will increase the sensitivity of the system; however, it might not be a practical technique. It is preferable to study the molecular interactions at physiologically relevant and compatible ionic concentration, because the interactions can be different at lower concentrations. In addition, certain bio-molecules like DNA tend to alter their structure under reduced buffer concentration [90].

Concentration	Debye length (nm)
1 M PBS	0.19
100 mM PBS	0.61
10 mM PBS	1.92
2 mM PBS	4.29
1 mM PBS	6.06

Table 3-1 Calculated Debye screening lengths for different PBS concentrations

Assuming a charge Q has a distance d away from the chip surface, then the equivalent surface charge that affects the device as described in pH sensing case can be calculated as:

$$Q_{eff} = Q\exp(\frac{-d}{\lambda_D}) \tag{40}$$

This is just a single point charge effect; the binding of receptor and biomolecules of interest involves many charge points and the physical model is quite complex if the effect of diffusion, mass-transportation, non-specific binding, multiple binding sites, etc. are included. A more detailed explanation of bio-molecular membrane layer can be found in [126,127].

3.4 Impedimetric Measurements with FET Devices

The potentiometric sensing presented in the previous sections relies on the surface potential variations of the interface between the ISFET oxide and the liquid, which depends on the biomolecular binding happening at the surface. This method has several advantages such that it does not require redox molecules or enzymes to perform measurement. The leakage currents through the interface are in the range of pA, therefore there is almost no risk of material corrosion during measurement [90]. The disadvantage is the Debye screening effect: the measurements need to be done in low buffer concentrations, so the point-of-care solution is not available for this method. Moreover, the surface potential needs to be kept at a defined value, otherwise the system will be susceptible to drift and the change in the buffer solution. Thus in order to obtain precise experimental results, a bulky and expensive reference electrode is required [105].

The Electrochemical Impedance Spectroscopy (EIS) described before is a powerful method capable of characterizing many of the electrical properties of materials and their interface with electronically conducting electrodes [94]. A single-frequency voltage or current is applied to the interface, and the resulting current or voltage phase shift and amplitude (or real and imaginary part) are measured using either analog circuit or fast Fourier transform (FFT) analysis. Normally, the measurement is done at different frequencies, which results in an impedance spectrum in a wide range of frequencies. The EIS based biosensors use the impedance change in response to receptor-

analyte binding at the electrode-electrolyte interface [85] (Figure 3-8). One of the following mechanisms can explain the impedance change as the bio-event happens on the surface [90]:

- The analyte-receptor binding induces the reduction of the double layer capacitance (C_{DL}) where the thickness of the double layer is increased and the permittivity constant near the interface is decreased (e.g., permittivity of water is around 80 and permittivity of organic molecules is around 2-3). In addition, the macro molecules hinder the charge transfer at the interface, which induce the increment of R_{CT} [20,128,129].

- When the charged biomolecules bind to the surface, they can repel or attract charged molecules around them. This affects the charge transfer near the surface, leading to changes in R_{CT} [20]. Moreover, the ionization of the surface causes the change in charge density profile of the electrode-electrolyte interface [130], therefore alters the double capacitance.
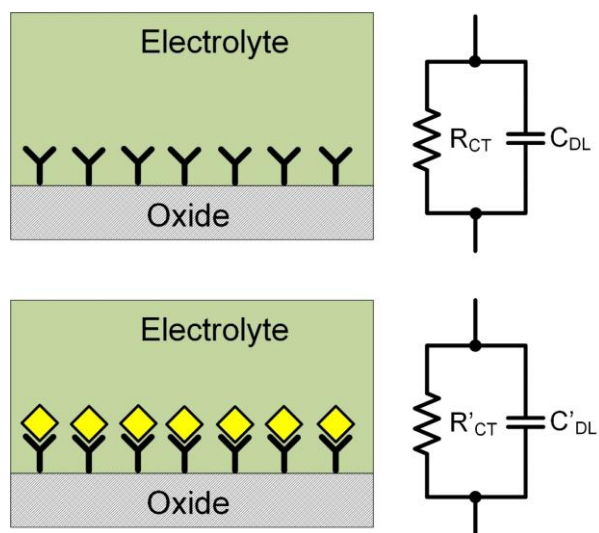

Figure 3-8 Impedance variations upon the binding of biomolecules: C_{DL} is double capacitance, R_{CT} is resistance of charge transfer at the interface

The EIS, compared to potentiometric detection with ISFET, provides much more information about electrode-electrolyte interfaces at a variety of frequencies. If one can combine ISFET chip fabrication technologies and the EIS measurement technique, the result would be very promising. One problem is that the EIS can only work with an electrically conducting electrode (the applied voltage will induce a response current through the interface) where ISFET is three-electrode configuration and there is no current flow through the oxide-liquid interface. Therefore, the transfer function technique needs to be introduced.

The transfer function is a commonly used mathematical representation to describe the input-output relationship of a linear, time-invariant, differential equation system. It is defined as the ratio of the Laplace transform of the output (response function) to the Laplace transform of the input (driving function) under the assumption that all initial conditions are zero [131]. In this work, FET sensors are studied by frequency-response method, in which the frequency of the input sinusoidal signal is

varied, and the transfer functions are obtained. The advantage of the frequency-response method is that the data measured from the physical system can be used without deriving its mathematical model. The frequency-response is characterized by its magnitude and phase angle with frequency as the parameter. There are two commonly used graphical representations of the frequency response: Bode plot and Nyquist plot.

The binding of biomolecules to the receptor on the surface of ISFET does not only change the drain source current but also changes the impedance of the oxide-liquid interface layer. The ISFET transfer function is used to study this change of impedance. The published literature showed that the binding of DNA hybridization or protein interaction altered the impedance spectrum of ISFET sensors [40,72,96,99,132]. In this section, the transfer function of an ISFET sensor and the lock-in amplifier technique to obtain the frequency response of the system will be discussed.

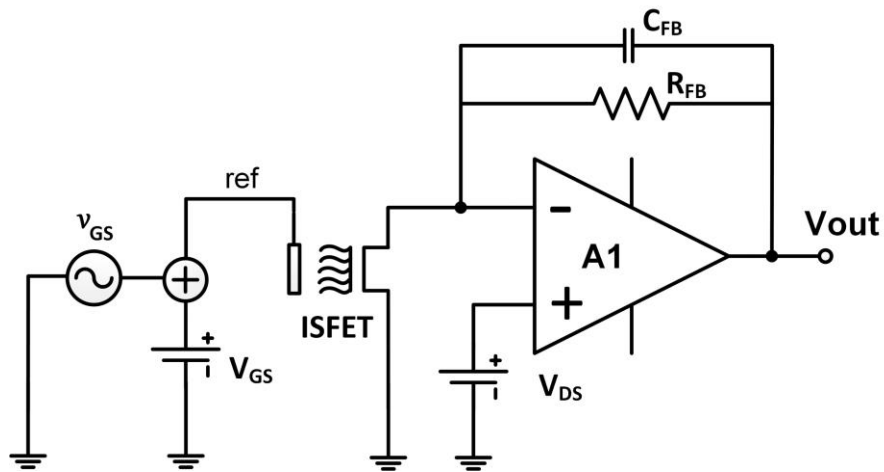### 3.4.1 Transfer Function of a SiNW FET/ISFET Sensor

Figure 3-9 Schematic of frequency response measurement with ISFET sensor

To obtain the frequency response of a SiNW FET/ISFET sensor system, the device is biased at a working point (fixed value of V_{DS} and V_{GS}) (Figure 3-9). A sinusoidal voltage is superimposed on the gate electrode at various frequencies. The output voltage response after the transimpedance amplifier is recorded and the transfer function of the output/input is calculated. In this case, the commonly accepted explanation is that the transconductance g_m becomes frequency dependent [84]:

$$g_m = \frac{\partial I_{DS}}{\partial V_{G*S}}\bigg|_{V_{DS}=const} = \frac{i_{DS}}{v_{G*S}} \tag{41}$$

where i_{DS} being the 'AC drain-source current' and v_{G*S} being 'AC effective gate-source voltage'.

Figure 3-10 shows the schematics of the equivalent circuit for an ISFET sensor, which includes the oxide/liquid interface and the modified FET model. This circuit can be used for pH and conductivity measurements with FET sensors. To describe the impedance response, parasitic

parameters need to be included in the model as well. C_{PD} and C_{PS} are the capacitances of the drain and source contact lines (equation 42), respectively, caused by the SiO_2 passivation layer.

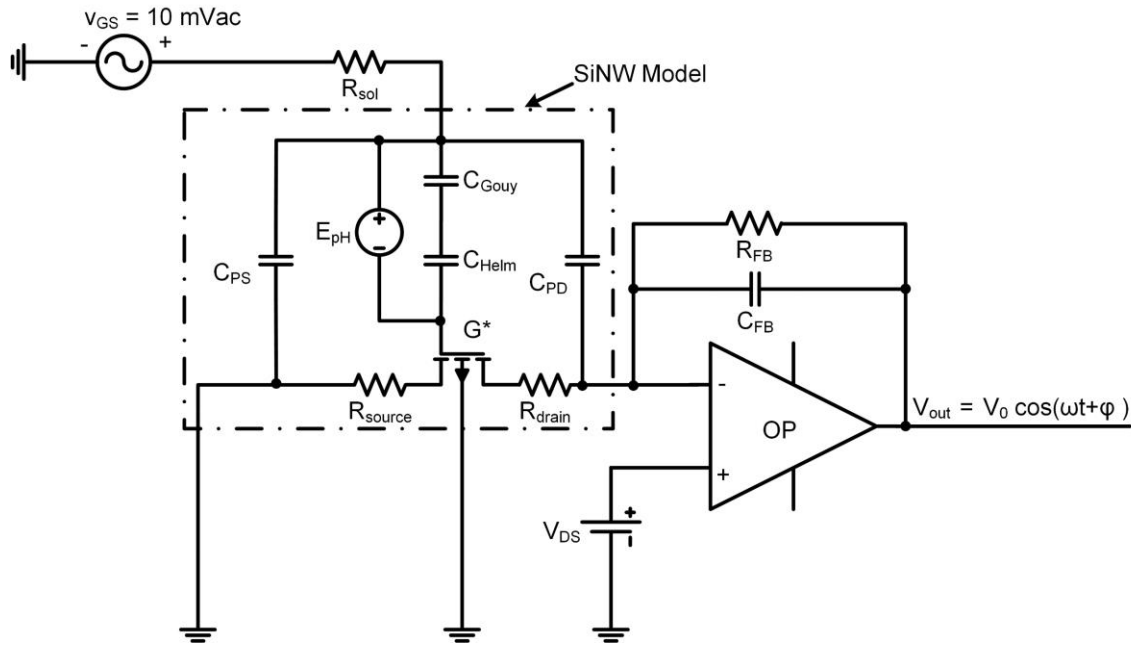$$C = \frac{\varepsilon_0 \varepsilon_{SiO_2} A}{d} \tag{42}$$

Figure 3-10 Schematic of the equivalent circuit for a SiNW FET/ISFET sensor in frequency response method [84]

Where ε_0 is the electric constant, ε_{SiO_2} is the relative permittivity of SiO_2, d is the thickness of SiO_2 passivation layer and A is the area of passivation layer at the drain or source electrode in contact with the electrolyte solution.

R_{drain} and R_{source} are the resistance values at the contact lines of the drain and source electrodes. E_{pH} is a voltage source representing the potential variation at the electrolyte-insulator interface. The AC signal of the output voltage after the first amplifier v_{out} can be derived by the following equation:

$$v_{out} = -Z_{FB}i_{DS} = -\frac{R_{FB}}{1 + j\omega R_{FB}C_{FB}} g_m v_{G^*S} \tag{43}$$

where R_{FB}, C_{FB} and Z_{FB} are feedback resistance, feedback capacitance, and feedback impedance of the transimpedance amplifier, respectively, and ω is the angular frequency. The 'AC gate-source voltage' v_{G^*S} is dependent on the transistor, oxide/liquid interface, capacitances and resistances at the source and drain electrodes and the resistance of the solution R_{sol} (here the distance from the reference electrode to the SiNW FET plays an important role [97] especially in diluted electrolytes

and is kept constant during all measurements). It is assumed that a complex function $f(j\omega)$ can describe these dependences. The AC gate-source voltage v_{G^*S} can then be defined by the following equation:

$$v_{G^*S} = f(j\omega)v_{GS} \tag{44}$$

From (42), (43) and (44) the transfer function $H(j\omega)$ of sensor and readout system will be:

$$H(j\omega) = \frac{v_{out}}{v_{GS}} = -\frac{R_{FB}}{1 + j\omega R_{FB}C_{FB}}g_m f(j\omega) \tag{45}$$

Here the stimulation signal v_{GS} is the input and v_{out} is the output voltage. In simulations, the v_{out} is considered as the output value for the following reasons: According to equation (43), the relationship between i_{DS} and v_{out} depends on the frequency. In impedimetric measurements, if i_{DS} and v_{out} are calculated similarly to what is done in the potentiometric measurements, this frequency dependency would be unintentionally eliminated. Moreover, the coupling between C_{PD} and C_{PS} with the feedback capacitance (C_{FB}) and the transimpedance amplifier plays an important role in the frequency response measurement. The C_{PD} and C_{PS} are capacitance of passivation layers at the drain and source contact lines, respectively. In this work, the output capacitance C'_{DS} consisting mostly of the two p-n junction capacitances connected in series through the semiconductor bulk is not took into account because of its trivial effect in the impedance spectra measurement [103]. The above-mentioned coupling prevents a precise calculation of i_{DS} from v_{out} in impedimetric measurements. Therefore, utilizing v_{out} is necessary for impedimetric measurement. The resulting transfer function should then represent effects of the solid-liquid interface, the FET characteristics – including on chip parasitic – and the transimpedance of the amplifier. Any change at the oxide/liquid interface or in the solution will be included in this function.

3.4.2 Lock-in Amplifier Technique

There are two main ways to measure the frequency response of a system: Frequency Response Analyzer (FRA) and fast Fourier transform [94,133]. The FRA or single sine method is better in terms of accuracy and bandwidth. Stimulation of a low amplitude pure sinusoidal voltage or current waveform at a known frequency is applied to the cell. The impedance of the cell at that frequency is calculated from measuring the results of the current or voltage AC response. This method only provides the impedance result of one frequency at a time. To obtain the impedance spectrum, the frequency of the stimulus is swept across the frequencies of interest. The most common method to implement this approach is the lock-in amplifier method. The frequency response analyzer gives accurate experimental results but is limited in terms of the speed of the measurement. However, with the fast development of the digital signal processor (DSP) technology, this is becoming less of a limitation at high frequencies. At low frequencies, it is still a constraint because at least one cycle of the waveform needs to be implemented. The FFT (Fast Fourier Transform) technique can provide an alternative method of the frequency analysis where a stimulus waveform consists of

multiple frequency components (for example a multi-sine or a random noise), and then the impedance is calculated from obtaining the voltage and current in time domain. This method includes performing FFT computations to transform time-domain to frequency domain. It is not necessary to sweep at different frequencies, therefore the FFT method can perform much faster than the FRA method. With the development of DSP, very fast measurements can be performed. The advantages of this method are fast, multifrequency analysis, fewer problems when measuring time variant systems, and a consistent set of data because all frequencies are measured at the same time. The main disadvantages are the limited dynamic range, especially when measuring over several decades of frequencies. ADCs (Analog to Digital Converters) are very limited in their maximum sampling rate, and even if a high sampling rate can be achieved, the data processing is restricted by the high computational requirement. It is more sensitive to noise and has problems with aliasing of frequencies. Moreover, this method requires high computing power for data processing, intensive hardware, and can be expensive. In this work, only the frequency analysis based on the lock-in amplifier technique was utilized.

The key feature of a Lock-in amplifier is its capability of measuring a very small signal (down to a few nanovolts) even when it is obscured by noise sources many thousands of times larger [134,135]. A sinusoidal signal at a frequency of interest stimulates the device under test (DUT). If the system is linear and time invariant, the response signal will have the same frequency but at different amplitude and phase. However, the DUT normally carries noise that can be much higher than the signal. To detect the signal, the Lock-in amplifiers use a technique known as phase-sensitive detection (PSD) that passes only the frequency of interest and reject the remaining parts of the spectrum.
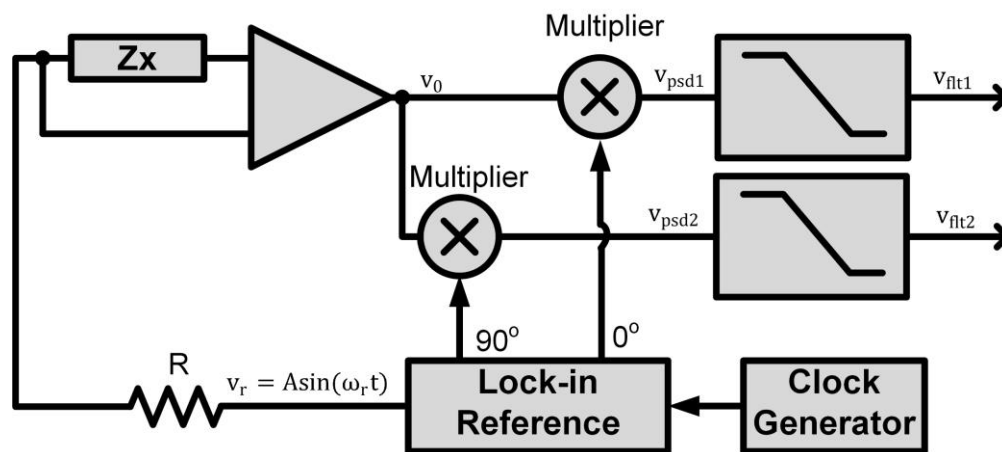

Figure 3-11 The principle schematic of the lock-in amplifier technique (adapted from[136])

Figure 3-11 depicts a simplified lock-in based Frequency Response Analyzer. A sinusoidal voltage stimulates an unknown impedance system Z_x:

$$v_r = A\sin(\omega_r t) \tag{46}$$

where A is the amplitude and ω_r is a reference angular frequency of the stimulation signal. This stimulation voltage will induce an AC current through the system, and after the transimpedance amplifier the resulting voltage v_0:

$$v_0 = A_0\sin(\omega t + \theta) \tag{47}$$

with A_0, ω, θ are the amplitude, angular frequency, and phase of the resulting voltage output.

The stimulation signal is known. To calculate the unknown impedance Z_x, the amplitude and phase of the response signal need to be measured. The lock-in technique calculates those values by multiplying the output signal with in phase (0°) and 90-degree out-of-phase component of the reference signal.

$$\begin{aligned} v_{psd1} &= A_0 A\sin(\omega_r t)\sin(\omega t + \theta) \\ &= \frac{1}{2}A_0 A\cos\big((\omega_r - \omega)t + \theta\big) - \frac{1}{2}A_0 A\cos\big((\omega_r + \omega)t + \theta\big) \end{aligned} \tag{48}$$

$$\begin{aligned} v_{psd2} &= A_0 A\sin\left(\omega_r t + \frac{\pi}{2}\right)\sin(\omega t + \theta) \\ &= \frac{1}{2}A_0 A\sin\big((\omega_r - \omega)t + \theta\big) - \frac{1}{2}A_0 A\sin\big((\omega_r + \omega)t + \theta\big) \end{aligned} \tag{49}$$

These PSD signals are directed through low pass filters, and the AC components are filtered out. In general, all AC part of the resulting signal v_0 are removed except the frequency $\omega = \omega_r$. The filter of the PSD output will then be:

$$v_{flt1} = \frac{1}{2}A_0 A\cos(\theta) \tag{50}$$

$$v_{flt2} = \frac{1}{2}A_0 A\sin(\theta) \tag{51}$$

The amplitude and phase shift of v_0 are calculated in the following:

$$A_0 = \frac{2}{A}\sqrt{v_{flt1}{}^2 + v_{flt2}{}^2} \tag{52}$$

$$\theta = \text{atan}\left(\frac{v_{flt2}}{v_{flt1}}\right) \tag{53}$$

The Z_x at the frequency of stimulation ω_r can be described by its amplitude and the phase shift as:

$$Z_x(\omega_r) = \frac{A}{A_0 A_{TI}}\angle(\theta - \theta_{TI}) \tag{54}$$

where A_{TI}, θ_{TI} are the amplifier factor and phase shift of the transimpedance stage respectively.

There are different methods in implementing the multiplications and filters in the Figure 3-11 in different type of Lock-in amplifiers. Conventionally, the signal and reference are analog voltage signals. The analog multiplier implements the multiplication of the response signal with the reference voltage and one or more stage of RC low pass filter will filter out the AC components of the multiplication [137]. Most of analog-based lock-in devices have limited bandwidth (up to hundred kHz), problems with output offsets, and harmonic rejection [136]. In digital lock-in amplifiers such as SR830, SR850 of Stanford Research System, Inc. or HF2LI of the Zurich Instruments AG, the signal and reference are generated by sequences of numbers, and a digital signal processing (DSP) chip implements the multiplication and filter mathematically. In this work, the lock-in amplifier tasks were performed by the HF2LI (Figure 3-12). The HF2LI combines the analog front-end for signal sampling and DSP for filter and demodulation. It has high-frequency outputs with the range from DC to 50 MHz. Its advantages are zero drift, precise phase shift, and high reserve [138].
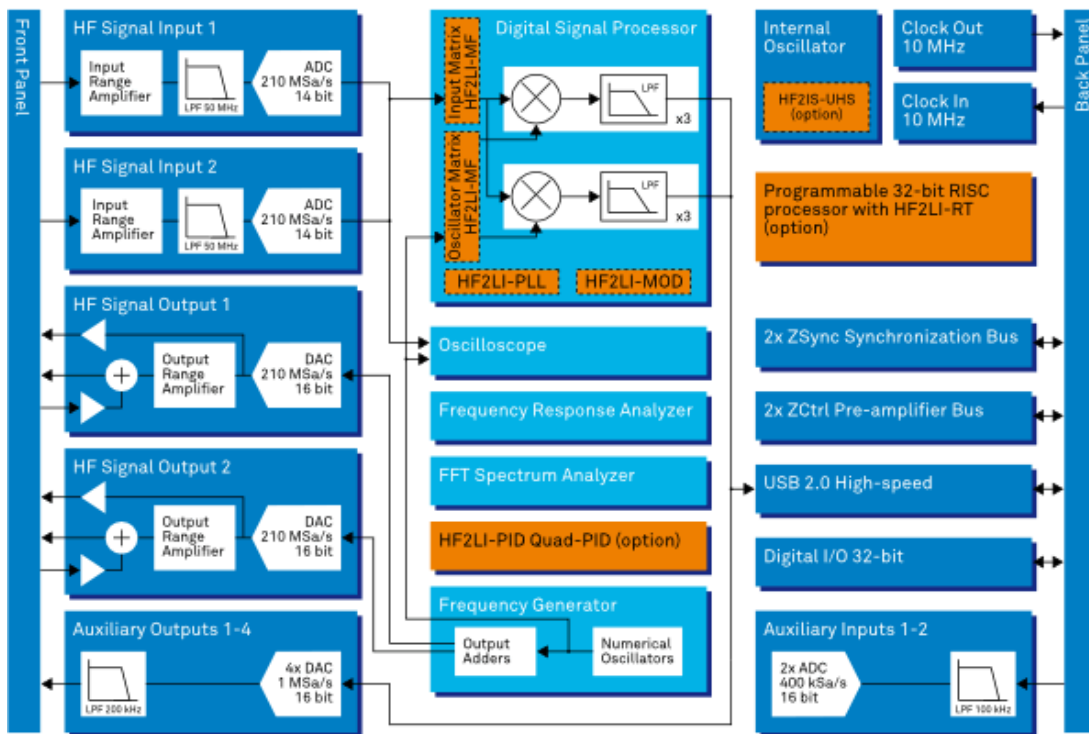
Figure 3-12 HF2LI functional diagram, reprinted with permission from [138]. Copyright 2016 Zurich Instrument AG

4. Sensor Chip Fabrication, Encapsulation, and Characterization

4.1 ISFET Sensor Arrays

The microsized FET devices used in this study were developed and described in previous works [139–141]. The transistor array arranged as a 4×4 matrix with the spacing of 200 µm includes 16 measurement points on a 5×5 mm^2 silicon die (Figure 4-1). The transistor array has a common source layout, while individual drain contacts can be used to address each channel. The gate oxide consisted of a thermally grown SiO_2 layer of 8-10 nm thickness and the gate dimensions of 16 µm $\times$ 7 µm (width to length – mask measures) were mainly used in this work. The transconductance g_m of the FET chips was about 0.3 mS. These sensor devices were fabricated in an earlier project at Fraunhofer ICT-IMM (previously Institute for Microtechnique, Mainz). A new chip generation, in which the fabrication processes were modified for better cell adhesion measurements, was fabricated at the University of Applied Sciences Kaiserslautern, in Zweibrücken, Germany [142]. In this process, a stronger contact line implantation was utilized to reduce the resistance at drain and source electrodes. Furthermore, instead of employing silicon oxide / silicon nitride / silicon oxide stack (ONO-stack), only silicon oxide was used for the isolation of the contact lines from measurement solutions. This resulted in an almost flat chip surface and, hence, in a better cell adhesion in cell-based bioassays [142]. From this new design, 16-channel ISFETs with gate dimensions of 12 µm $\times$ 4 µm and 25 µm $\times$ 5 µm (mask measures) were used in this thesis. More detail can be found in Appendix A.
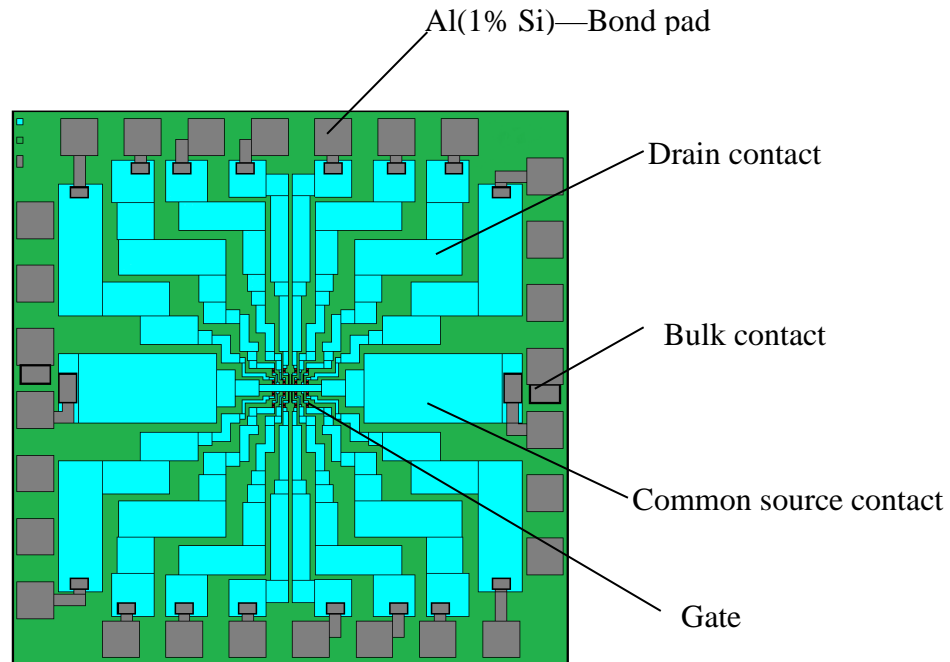

Figure 4-1 Layout of 4×4 FET array

The chip encapsulation protocols were also reported before [143,144]. The 5×5 mm^2 FET chips were cleaned by acetone/isopropanol in an ultrasonic bath to remove the protective layer. Chips were then fixed onto a chip socket: 68 pin LCC6832 (Global Chip Materials, LLC, USA) (Figure 4-3 c), or custom made printed circuit boards (PCB) 68/12 pins (Figure 4-3) by two-components glue (EPO-TEK H20E-175, Epoxy Technology Inc., USA) for different measurement systems. The wire bonding from chip sockets to the FET chip with a 25 µm aluminum wire (AlSi 1%) (Heraeus Germany) was done using an ultrasonic bonding machine (Westbond, USA). The liquid reservoir to contain measurement solutions were provided by gluing a glass ring (d = 16 mm, h = 3 mm) onto the chip socket and a funnel onto the silicon chip. The funnel was made of Polydimethylsiloxane (PDMS) from molding techniques (SYLGARD 182, Dow Corning Germany). The gap between the funnel and glass ring was filled with the PDMS glue (SYGARD 96-083, Dow Corning, Germany) to isolate measurement solutions from the wire bonding. The result is a free gate area of around 7 mm^2 (3 mm in diameter) of the FET chips and the total bath volume is about 700 µl. Figure 4-2 shows a gate area of a used ISFET chip and its zoom in image of a gate electrode. Different encapsulated FET chips are shown in Figure 4-3.
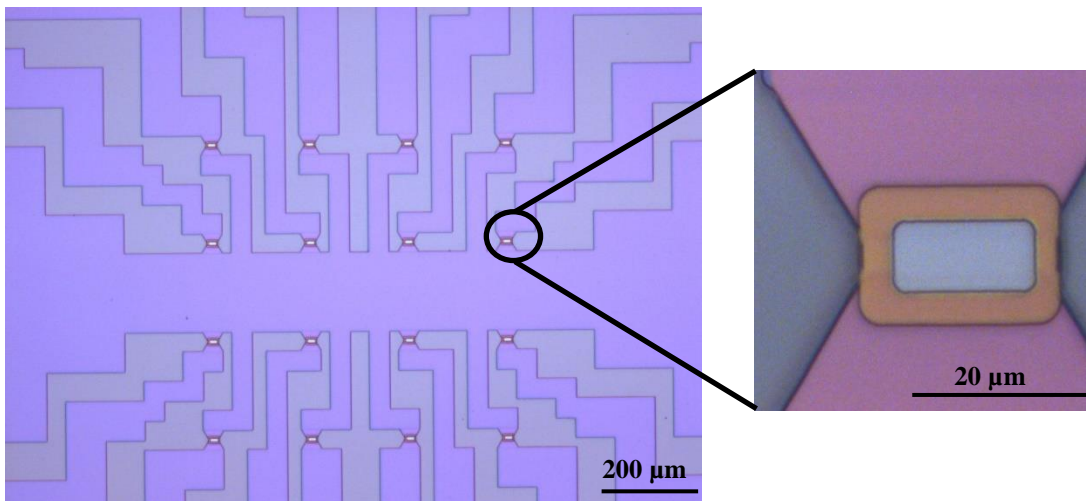
Figure 4-2 Layout of a used FET-arrays in the gate area (left side) (DIC-microscope picture). On the right side, the detailed view of a single gate structure is shown

Characterization of FET-chips

The characterization of FET chips was done by a standard parameter analyzer system Keithley 4200 SCS (Tektronix, Inc.) with the electrical contact to the FET chip, as in Figure 4-4. The output characteristics $I_{DS}(V_{DS})$ at constant V_{GS} and the transfer characteristics $I_{DS}(V_{GS})$ at constant V_{DS} were implemented. The transconductance graph was calculated by differentiating the transfer curve.
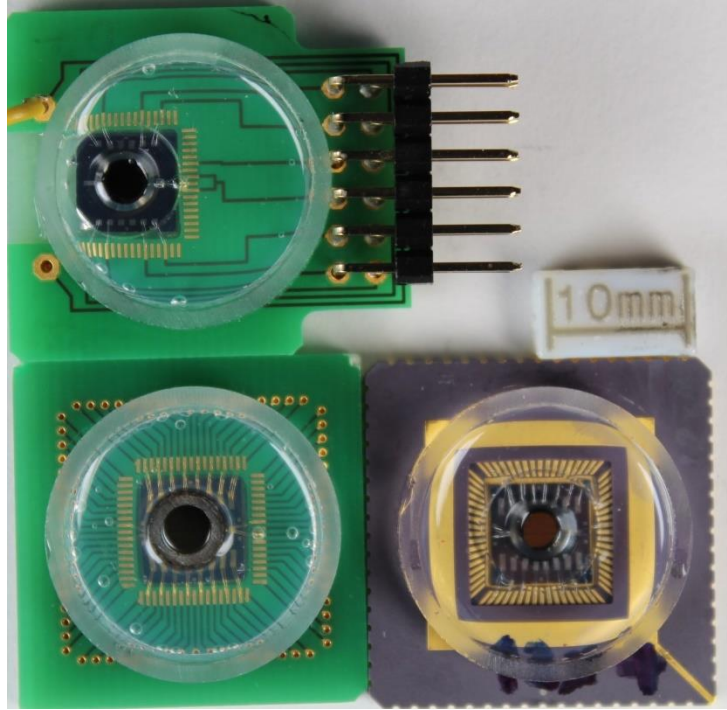
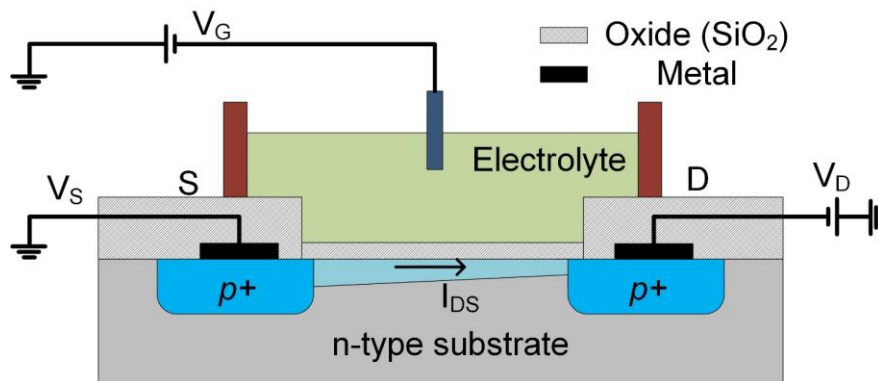Figure 4-3 Encapsulated FET chips for different measurement systems

Figure 4-4 Electrical contacts for FET chip characterization measurement

Figure 4-5 represents the characterization of a p-channel FET array with a gate size of 25×5 µm (width × length) and a gate silicon dioxide thickness of 8 nm. The transfer characteristics (top graph) show the dependences $I_{DS}(V_{GS})$ in the range of V_{GS} from 0 to -3 V (step -0.1V) at constant V_{DS} from 0 to -3V (step -1V). In this graph, the leaking current through the reference gate electrode also was measured. For good quality devices, this current was in the range of 1 million times less than the current between the drain and source electrode of the sensors. The middle graph depicts the numerical derivative of the first graph and is called the transconductance of the transistor. The higher the transconductance value, the higher the amplifier factor of the sensor as the change happened at the gate surface. At certain drain source voltage, there is a value of V_{GS} where the transconductance is maximum, which is the ideal working point for the device. In the bottom graph

is the output characteristics of the sensor. The device is an enhancement mode transistor, as a gate-source voltage must be applied to open the conductance channel.
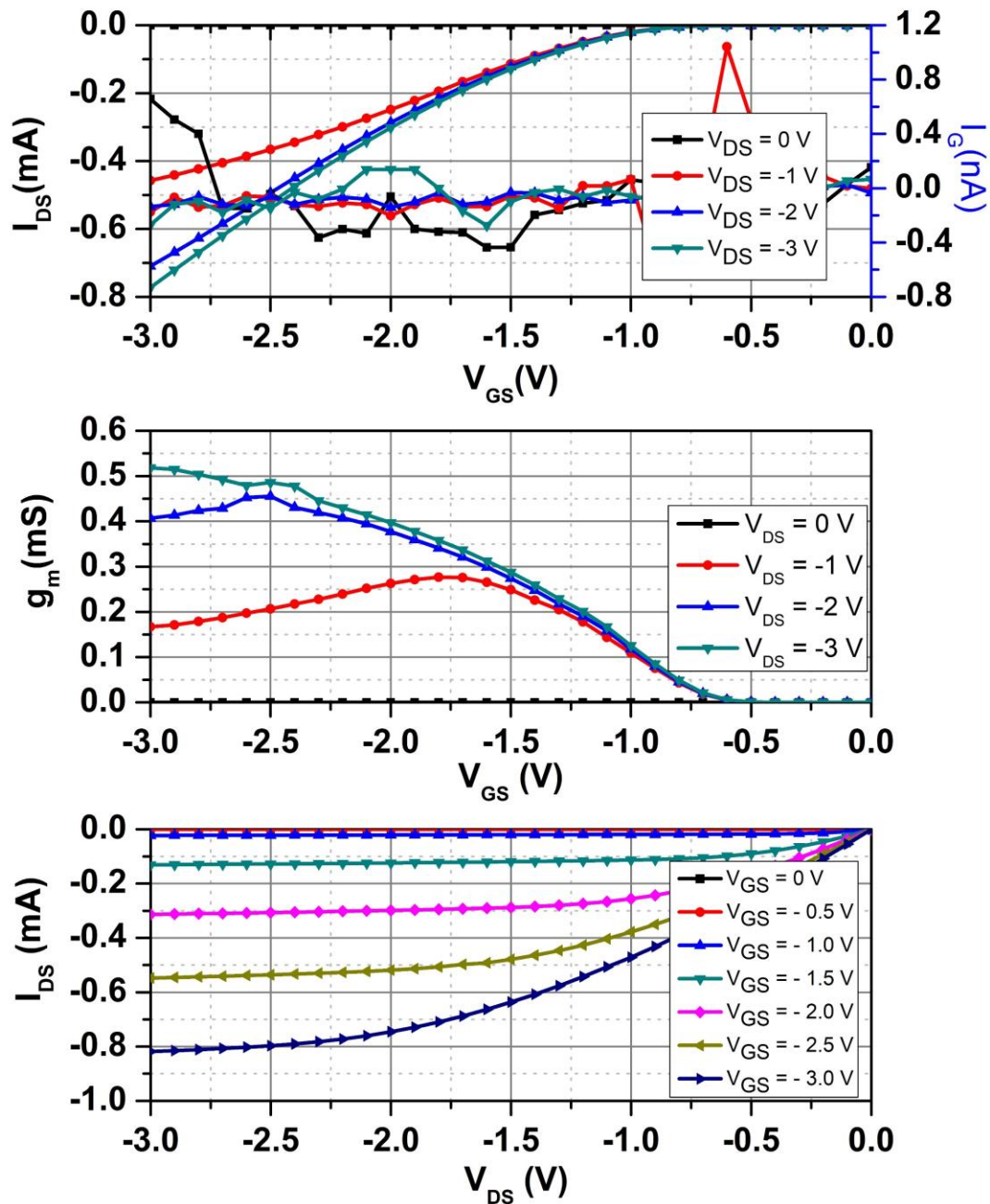

Figure 4-5 Characterization of a p-channel 25×5 ISFET sensor: The top graph traces the transfer characteristics; the middle graph traces the transconductance; and the bottom graph traces the output characteristic as shown.

4.2 Silicon Nanowire Sensor Arrays

Silicon nanowire sensors can be fabricated by either "top-down" or "bottom-up" method. In the bottom-up approach, SiNW FET is accomplished by taking advantage of ideas from vapor–liquid–solid (VLS) growth [45] that involves two main steps: 1) the formation of a small liquid metal droplet and 2) the alloying, nucleation, and growth of the NW [145]. SiNW FET sensors arrays in this work were fabricated by the top-down approach. The fabrication of silicon nanowire (SiNW) devices was previously accomplished and described in another work [64]. The sensors have a layout of 28×2 channels with a common source electrode. The lateral gate length of SiNW FETs was varied (10 µm, 20 µm, and 40 µm), while the width was either 200 nm or 400 nm, depending on the design (mask measures). In short, SiNW FET arrays were fabricated with the top-down approach on a 4" silicon-on-insulator (SOI) wafer (SOITEC, France). The active silicon layer was first thinned out to 50 nm of thickness. Then the structure of SiNW FET and the drain/source contact lines were defined by combining nanoimprint lithography and wet anisotropic etching with tetra methyl ammonium hydroxide (TMAH). This combination helps in obtaining robustness, mass production and reproducibility of the devices [59,144]. While the SiNW FET doping level was retained as almost intrinsic (14 - 22 Ω-cm) the conducting lines were heavily doped to reduce the drain and source line resistances. The advantages of this were high charge carrier mobility inside the SiNW FETs, while keeping low conducting resistances of the drain and source electrodes. Chips were passivated by a 300 nm SiO_2 layer (low-pressure chemical vapor deposition (LPCVD)). As gate oxide of the SiNW FETs, a thin thermal SiO_2 (6 - 8 nm) was grown by a dry oxidation process, which serves as an input dielectric. More detailed information of the SiNW FET fabrication processes can be found in Appendix B. The result of the wafer-scale, top-down approach was the uniformity of electrical characteristics of SiNW FET arrays in compared with the bottom-up method, that enable differential readout between differently coated sensors.

The SiNW FET chip encapsulation was the same as that of the ISFET sensor. The sensors were first washed by acetone/isopropanol solutions and rinsed under running DI water to remove residual lithography resist. The chip is fixed on a 68 pin LCC6832 chip socket (Global Chip Materials, LLC, USA) using epoxy glue (EPO-TEK H20E-175, Epoxy Technology Inc., USA) and wire bonded from the socket to the chip by a wedge-wedge wire-bonder (West Bond Inc., USA). A custom-made silicone funnel made of PDMS (SYLGARD 182, Dow Corning Germany) from molding techniques was put in the center of the SiNW FET chip with a silicone adhesive (SYLGARD 96-083 silicone adhesive kit, Dow Corning, Germany), that does not cover the gate area of SiNW FETs. To form a reservoir for the measurement solution, a glass ring was glued on to the socket with silicone adhesive. The space between the silicone funnel and the glass ring was filled with silicone adhesive to isolate the liquid with the electrical contact between sensors and the socket. Figure 4-7 d represents an encapsulated SiNW FET chip with a volume of reservoir liquid of around 700 µl.

Aluminum Bond pad

Drain contacts

Common Source contact
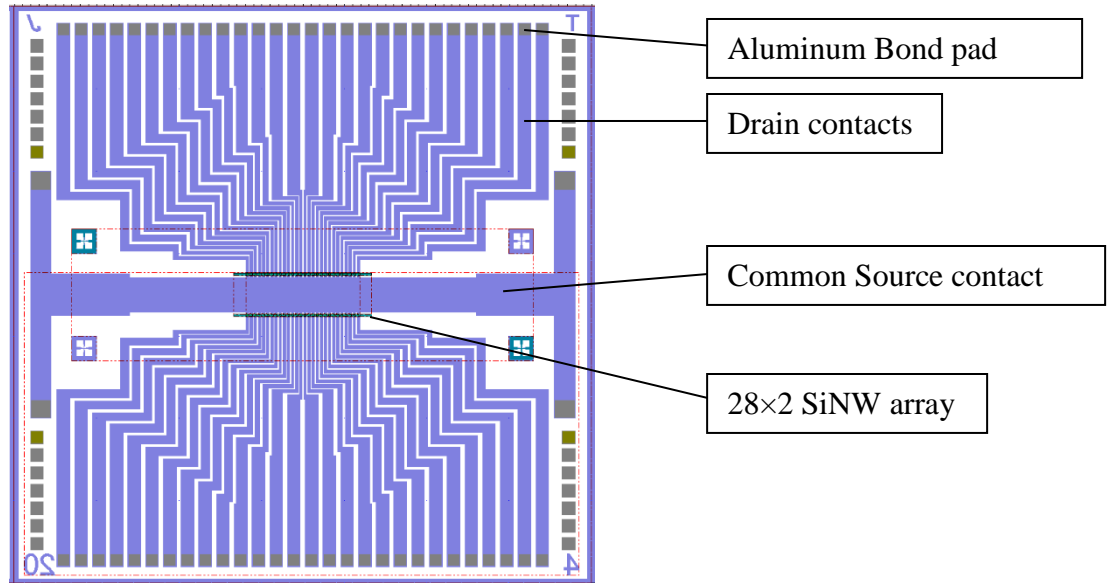
28×2 SiNW array

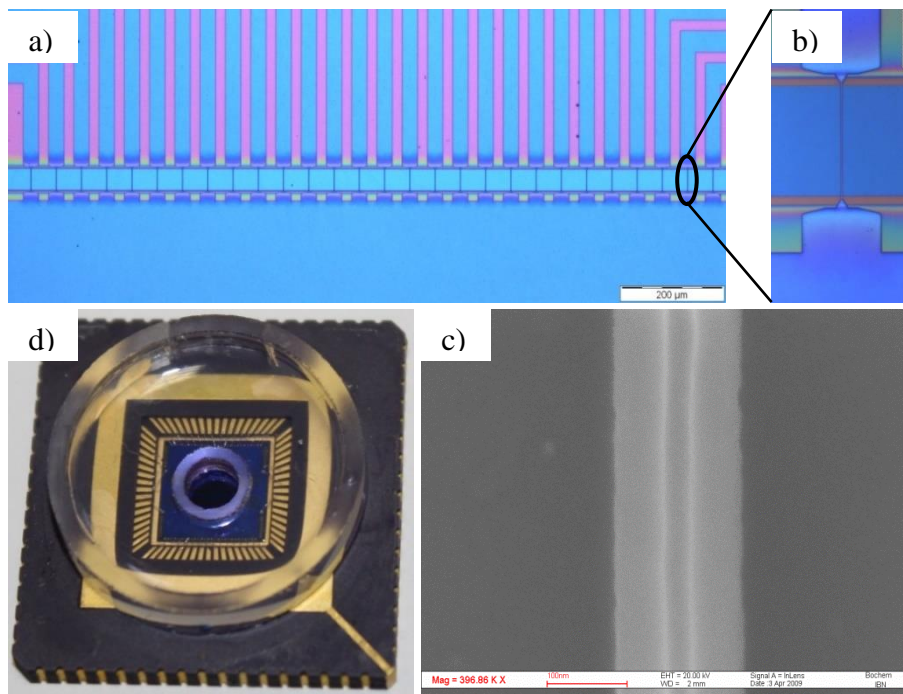Figure 4-6 Layout of the 28×2 SiNW FET-arrays

Figure 4-7 a) DIC image of a half of 28×2 SiNW FET arrays; b) A zoom in on a single SiNW FET channel; c) A SEM image of a SiNW FET; d) An encapsulated SiNW FET sensor

The setup for SiNW FET chip characterization is the same as for ISFET chip with the standard parameter analyzer system Keithley 4200 SCS (Tektronix, Inc.) with the electrical contact to the FET chip as in Figure 4-4. The output characteristics $I_{DS}(V_{DS})$ at constant V_{GS} and the transfer characteristics $I_{DS}(V_{GS})$ at constant V_{DS} were also implemented. The transconductance graph was calculated by differentiating the transfer curve. Figure 4-8 represents the characterization of a

typical SiNW FET device with wire size of 4×10 (400 nm width × 10 µm length) and a gate silicon dioxide thickness of 8 nm. The transfer characteristics (top graph) show the dependences $I_{DS}(V_{GS})$ in the range of V_{GS} from 0 to -3V (step -0.1V) at constant V_{DS} from 0 to -2V (step -0.5V). The drain-source current of SiNW FET is in the range of microampere while the leaking current through the gate electrode is small like it is the case for the ISFET sensor. Figure 4-9 shows the output characteristic of the SiNW FET sensor. The device is an enhancement mode transistor as a gate-source voltage must be applied to open the conductance channel.
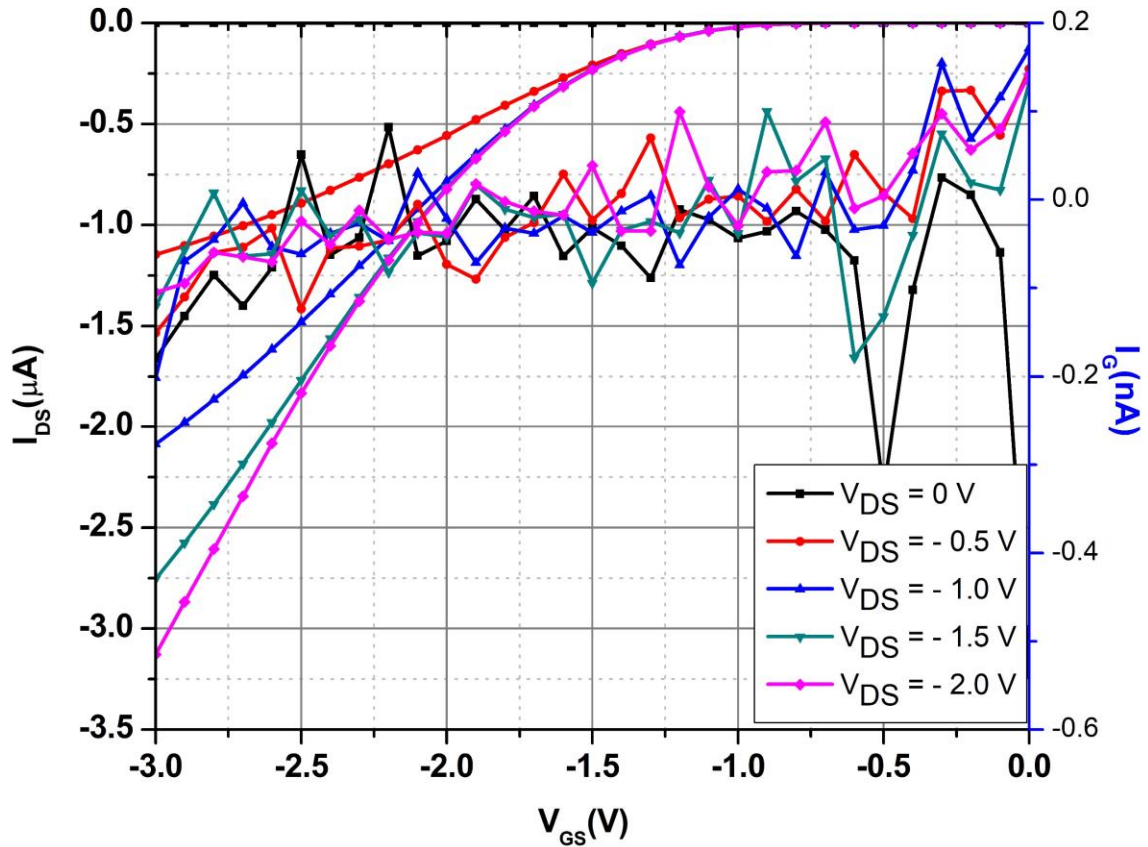
Figure 4-8 Transfer characteristics of a 4×10 SiNW
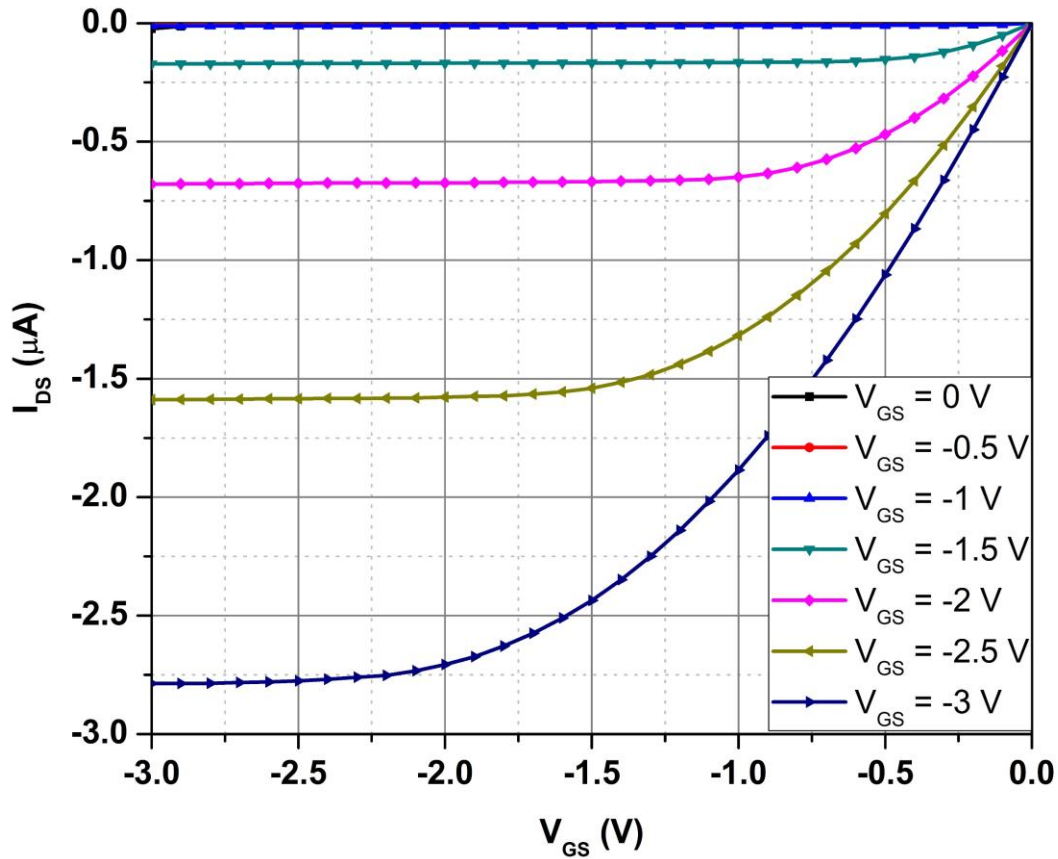
Figure 4-9 Output characteristics of a 4×10 SiNW FET

ISFET and SiNW FET sensors in this work can be reused after experiments by implementing proper cleaning procedures. However, these cleaning steps induce the sensitivity degradation of the device after each use. The wearing out phenomenon is mainly dependent on the quality of the thermal growth gate oxide, cleaning procedures and encapsulation methods, that is beyond the scope of this thesis. In the following sections, sensing experiments are done only with fresh/newly encapsulated chips.

5. Readout System: Design, Fabrication, and Characterization

In general, one needs to connect an analog circuit to an ISFET or SiNW FET sensor in order to collect a measuring signal. The sensor converts the variation of the surface potential into its conductivity, which manifests itself as the drain-source current change, as the drain-source voltage stays the same. All this transition can be tracked back as the variation of the threshold voltage of the transistor. In this chapter, some existing readout configurations will be reviewed. The summary provided here is by no means complete, but only considers setups that are suitable for the available microsized ISFET and SiNW FET sensors. A more thorough review can be found in [146]. Two measurement readout systems (32-channel multiplexer and 4-channel handheld) were then described and utilized to characterize electrical properties and the noise power spectrum of the ISFET and SiNW FET sensors. pH sensing and DNA measurements in the next chapter also were done by using these readout setups. The description of the handheld system and different biosensor applications were summarized and published as a peer-reviewed paper [147].

5.1 Analysis of Possible Amplifier Concepts for FET Devices

5.1.1 Source and Drain Follower

The source and drain follower setup is presented in Figure 5-1 [148]. The system is powered by a current source I_1 and a variable reference voltage V_{ref}. The amplifier circuit includes an instrumentation amplifier and an operational amplifier. The input to the instrumentation amplifier as well as the biasing voltage between the Drain and Source electrodes of the ISFET are kept constant ($V_{input} = V_{DS} = I_1 * R_1$), while the amplification factor depends on the resistance of ISFET in the following equation:

$$\text{Gain} = \left(1 + \frac{2R_3}{R_{ISFET}}\right)\frac{R_5}{R_4} \tag{55}$$

The operational amplifier A4 magnifies the difference between the output of the instrumentation amplifier and the reference voltage V_{ref}. This voltage then injects another current to R_2 to define the final biasing on the Drain and Source of the FET sensor. If the open-loop amplification of the interface circuit (including the instrumentation amplifier and the open-loop operational amplifier A4) is high enough the output voltage can be defined:

$$\Delta V_0 = \frac{R_6}{R_2}\Delta V_{TH} \tag{56}$$

This configuration has some advantages. It reduces the effect of decreasing sensitivity owing to internal source and drain series resistors [148], and the dependence of the measurement signals and the change of V_{TH} is linear. By adjusting the V_{ref} and R_6, one can manipulate the sensitivity of the experiments. However, this setup is limited in only detecting real-time measurement and a fine adjustment needs to be done for each device under test.
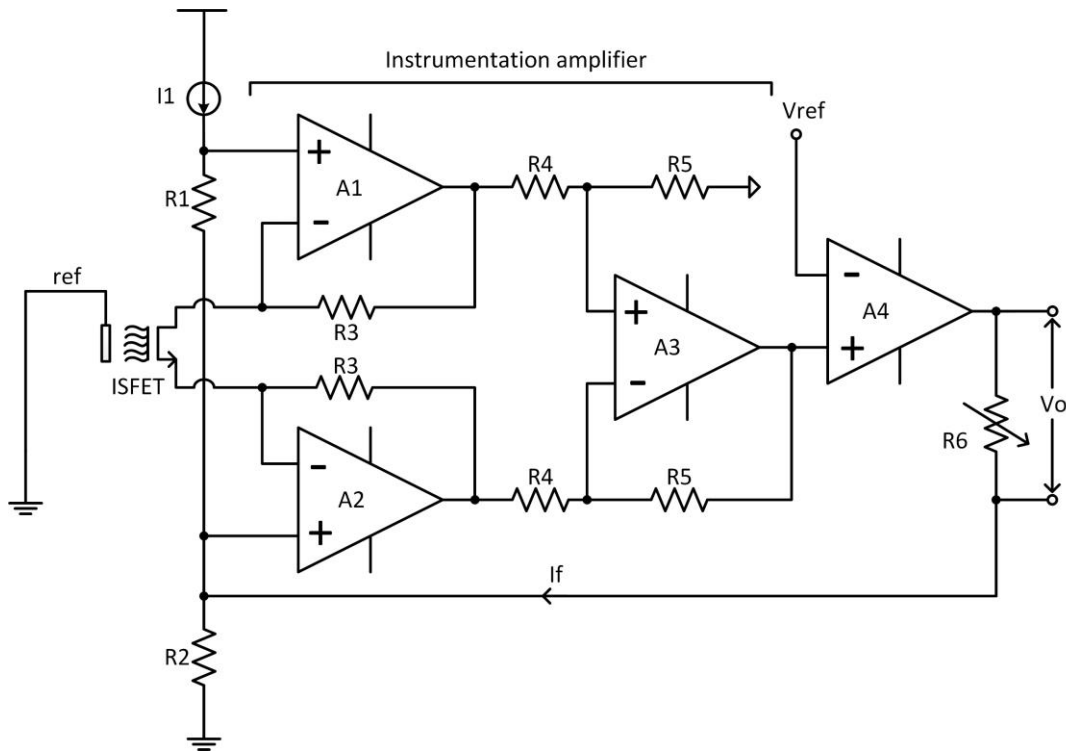
Figure 5-1 Source and drain follower

5.1.2 Constant Current Driver

The constant current driver which has a similar fundamental principle to the source and drain follower setup is presented Figure 5-2 [149]. The setup utilizes two op amps and two current sources. The current $I_1 = I$ goes through resistor R_1 and drops a voltage $V_{DS} = I * R$ between the Drain and Source electrodes of the ISFET via an op amp A_1. A chip that provides two constant current sources to the upper (I) and lower end ($2 * I$) of the setup was used. The sensor's drain-source current is kept constant as the difference between these two current sources (in this case it is I). The changing of the threshold voltage of the sensor is reflected in the voltage of the source electrode and can be measured at the output pin of the second op amp A2.

Although sharing a similar principle with the source and drain follower, the constant current driver setup reduces the complexity while keeping the advantages of the setup. However, this is also only limited in real-time measurements, and not flexible enough when measuring different kinds of devices.
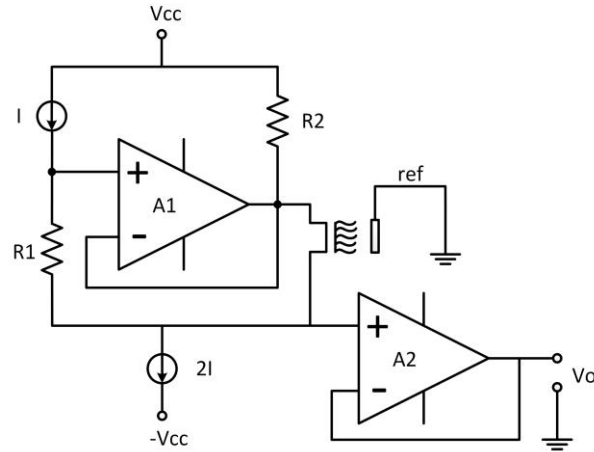
Figure 5-2 A constant-current driver provides the basis for a chemical-concentration test system

5.1.3 Readout-Circuit without Feedback Loop

A simpler configuration without feedback is shown in Figure 5-3. The sensor is biased at different controllable Drain-Source and Gate-Source voltages while the Source is at the GND. The current of the sensor is measured after a transimpedance amplifier:

$$V_o = V_{DS} - I_{DS} * R \tag{57}$$

$$I_{DS} = \frac{1}{2} \mu C_{ox} \frac{W}{L} [2(V_{GS} - V_{TH})V_{DS} - V_{DS}^2] \tag{58}$$

This configuration has some disadvantages: measuring signals and V_{TH} are not directly related, and some fitting procedure needs to be done to monitor the chemical effects. In real-time measurement, the drifting of semiconductor sensors leads to variation of I_{DS}. However, by software calculation and careful controlling of biasing voltage, these drawbacks can be overcome. Moreover, this configuration enables both characteristic and real-time measurement without changing any hardware. Therefore this was employed in some publications before [64,141,150]. For these reasons, the simple configuration without feedback was used in this thesis as well.
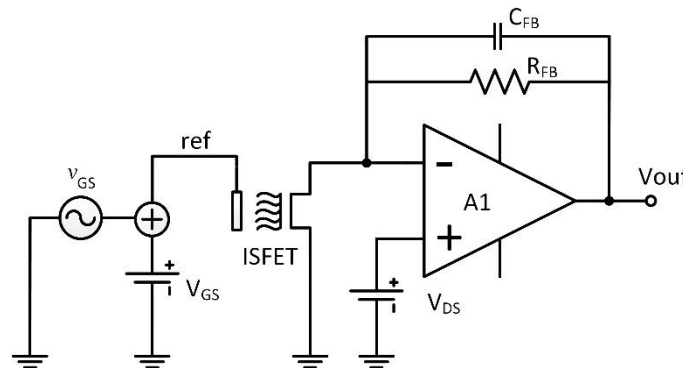
Figure 5-3 Readout circuit without feedback configuration

49

5.2 Available Measurement Setups and Commercial Solutions

5.2.1 Available Measurement Setups in the Laboratory

Figure 5-4 Available measurement setups: Agilent 4156C Precision Semiconductor Parameter Analyzer (http://www.keysight.com) (left), TTF box (right)

There were two systems already available to measure ISFETs in the Biomedical Instrumentation research group at the University of Applied Sciences Kaiserslautern before this work was started. The first is Agilent 4156C Precision Semiconductor Parameter Analyzer for advanced device characterization. It has 1 fA and 0.2 µV measurement resolution. The device can work as a stand-alone system or with Desktop EasyEXPERT software for PC-based GUI instrument control (Figure 5-4 (left)). Second is a dedicated 16-channel system called Transistor Transfer Function box (TTF box) which contains a preamplifier, a main amplifier and a microprocessor [99]. The system can implement both potentiometric (dc) and impedimetric measurement modes with a frequency range from 1 Hz to 100 kHz. The measurement system is operated by a microcontroller, and data is transferred via a USB connection and can be recorded by a dedicated software written in Borland Delphi 5.0.

5.2.2 Commercial Semiconductor Chip Based Sequencing

In 2011, Ion Torrent^{TM} (now Thermo Fisher Scientific Inc.) began the distribution of the Ion Torrent Personal Genome Machine (PGM), which can be considered as a successful commercialization of ISFET sensors [151]. This is the first DNA sequencing platform that measures changes in pH rather than light to detect polymerization event. The principle is straightforward: DNA is fragmented, ligated to adapters, and adaptor-ligated libraries are clonally amplified onto beads. These beads are then captured in microwells [152]. Then unmodified nucleotides are floated across the wells, once at a time. When the nucleotide is incorporated into the growing strand, one net liberation of a single proton is released into the solution for each nucleotide, which is detected by the ISFET sensor underneath.
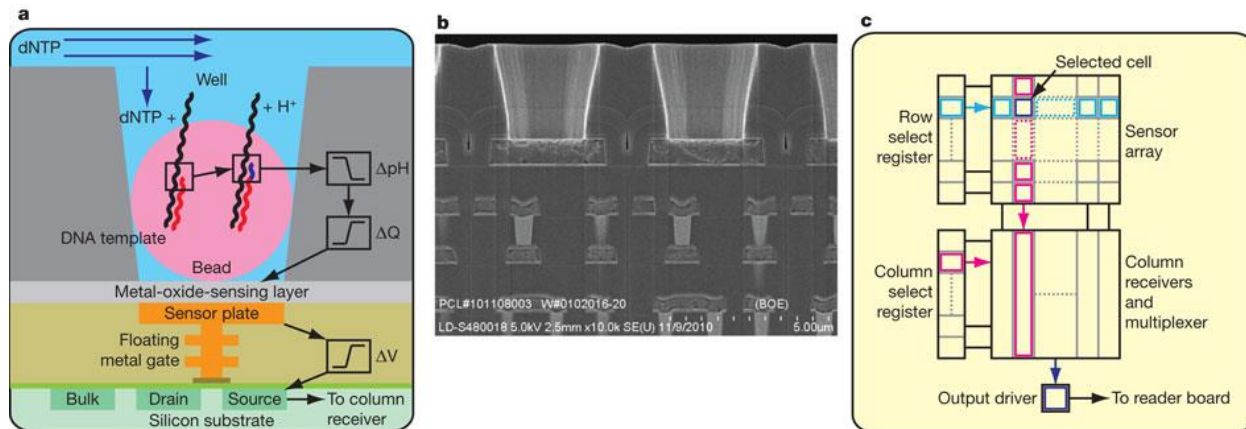
Figure 5-5 Sensor, well and chip architecture. a) A simplified drawing of a well, a bead containing DNA template, and the underlying sensor and electronics. Protons (H$^+$) are released when nucleotide (dNTP) are incorporated on the growing DNA strands, changing the pH of the well (ΔpH). This induces a change in surface potential of the metal-oxide-sensing layer, and a change in potential ($\Delta\Psi_0$) of the source terminal of the underlying field-effect transistor. b) Electron micrograph showing alignment of the well over the ISFET metal sensor plate and the underlying electronic layer. c) Sensor are arranged in a two-dimension array. A row select register enable one row of sensors at a time, causing each sensor to drive its source voltage onto a column. A column select register selects one of the columns for output to external electronics, reprinted with permission from [152]. Available under a Creative Commons license (Attribution-Noncommercial).

The fact that Ion Torrent^{TM} does not need optics allowed them to rapidly expand the output from their system approximately 10-fold every six months [153]. This fast improvement, along with quick run of about 20 hours and relatively inexpensive instrument has made Ion Torrent^{TM} a benchtop machine that may put medium-size sequencing projects within reach for almost every laboratory. The Ion Torrent's PGM has a price of approximately $50k and individual runs cost in the range of $300 to $750. Given its output capability (currently up to 1 Gigabase) and speed of runs (2 hours), it is being targeted towards smaller genomes and targeted sequencing [153]. Other models of Ion Torrent allow for larger chips with higher densities needed for exome and whole genome sequencing.

5.3 Design, Fabrication, and Characterization

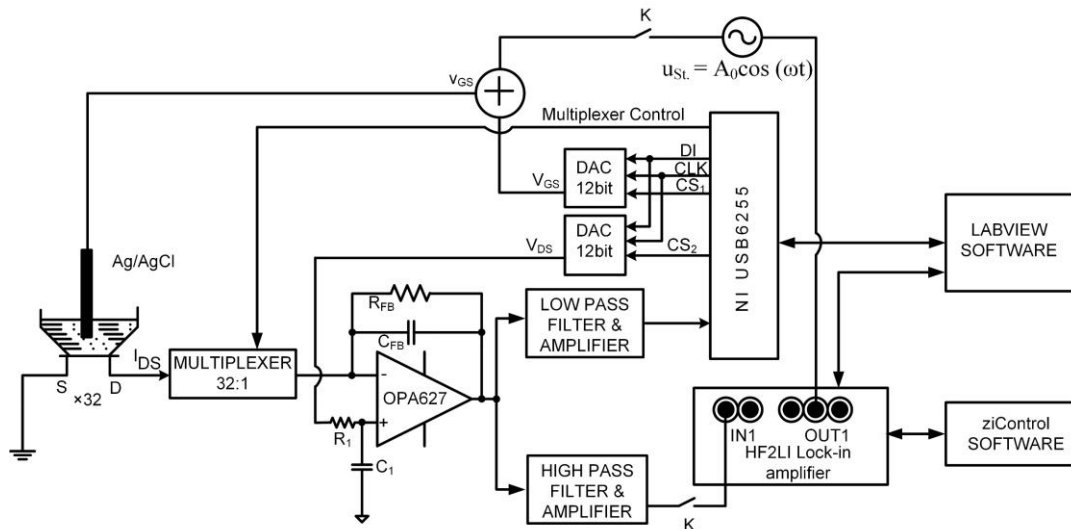### 5.3.1 32-Channel Readout System (T-Box)

Figure 5-6 Amplifier system for FET sensors for both potentiometric and impedimetric measurement modes

Figure 5-6 describes a schematic design of a single channel readout system for FET sensors that was designed in this thesis for both potentiometric and impedimetric measurements. The drain-source current is first converted to a voltage signal using an operational amplifier, feedback resistances (R_{FB}) and a feedback capacitance (C_{FB}). The reason that a current amplifier is used here instead of terminating the drain-source current with a resistor and amplifying the resulting voltage with a voltage amplifier is explained in the following. Large resistors are needed to get a large voltage from a small current. In the presence of cable and other stray capacitance, this can lead to unacceptable error in frequency response and phase accuracy. Trans impedance amplifiers have much better amplitude and phase in combination with stray capacitance [154].This impedance amplifier stage is very important in determining the noise and the accuracy of the measurements. Several op amps were simulated for this purpose the best op amp was the OPA627 (Texas Instruments, USA), which had very low bias current (5 pA max) and reasonable voltage offset (100 µV max) [155]. Here 8 amplification options were included that enable the measurement of different types of FET devices from µA to mA drain source currents. Then the voltage signal is separated into two different parts: low frequency (DC to 33 Hz) for DC characteristics and high frequency (10 Hz to 1 MHz) for impedance spectra measurements. The system utilizes a data acquisition device (USB-6255, National Instruments (NI), USA) to control the circuit and record the data. The USB-6255 has 80 single ended analog inputs with ADC resolution of 16 bits, no missing codes guaranteed, absolute accuracy is 1010 µV (input range ± 5 V) while the sampling rate can go up to 1.25 MS/s for single channel [156]. The device also has 24 digital input output (DIO) channels that are individually programmable. To set the devices to different working points

of gate-source and drain-source voltages, the NI card was used to generate serial peripheral interface (SPI) signals through its DIO pins. Two 12-bit Digital-to-Analog-Converter (DAC) chips (LTC1451, Linear Technology, USA), that have reliable built-in reference voltages ($\pm\,0.1$ LSB/ºC), differential nonlinearity (DNL) of $\pm\,0.5$ LSB max, integral nonlinearity (INL) of $\pm\,0.5$ LSB max and offset error of $\pm\,18$ mV were used to generate stable and precise bias voltages. [157] To obtain 32-channel readout in one measurement a 32-1 software controllable multiplexer between the setup and the sensors is included. This 32-channel setup was called Transistor box (T-box).

The internal components of the T-box are described in Figure 5-7. The power supply board provides four DC voltages: $+$ 12 V, $-$ 12 V, $+$ 5 V and GND. The amplifier board included transimpedance amplifier, signal separations and second voltage amplifier stages. The biasing board uses two LTC1451 in combination with a shifting circuit can provide a wide bipolar output swing of -4.096 V to 4.096 V. With this output swing 1 LSB = 2 mV. The multiplexer board added multi-channel functionality to the box where each channel on the sensors could be addressed and measured one by one. The DAQ interface was the connector to the USB-6255 to record ADC signal and control multiplexer and the Serial Peripheral Interface (SPI) as well. The Lock-in amplifier interface (BNC connectors) allows the box to measure in combination with a commercial lock-in amplifier.

Figure 5-8 shows the T-box as a complete measurement solution: on the topside is the chip socket IC51-0684-390-1 Plastic Lead Chip Carrier (PLCC) (Yamaichi electronics Co., Ltd) with a custom-made lid that fits to the chip encapsulation methods. On the backside is the connector to the power supply, while on the front side is the SCSI 68 connector to the DAQ card. The left side connectors provide interface to a lock-in amplifier circuit as well as monitor devices to debug the system. The system also provides a pin to hook up with a reference electrode to dip into measurement solutions.

In DC (potentiometric) readout mode (switch K in Figure 5-6 opened), the FET chip was biased at a working point where it had the maximum transconductance value g_m (real-time measurement). At this working point, the amplification factor of a FET sensor that converts variation of the surface charge potential into change of the drain-source current is maximum. Alternatively, the chip could be biased at different values of drain-source and gate-source voltages for characterization. The DC signals in the low frequency part of the setup are measured by employing the analogue inputs of the NI device using a LabVIEW program (LabVIEW 2011, National Instruments, USA). This software version based on the state-machine-programming method was developed, the flowchart of which is depicted in Figure 5-9. This method is not only suitable in programing medium size LabVIEW software but also adaptable to upscale to more channels multiplexer. At first, the program initialized the biasing and other protocols ready for measurements, and then it waited until users clicked the start button. Once started, the program automatically set channels, measured, and displayed experimental results on the GUI and saved data into a log file until it finished the predefined number of channels that it was measuring. Two versions of the software were

developed: 16-channels software for microsized ISFET and a 32-channel one for SiNW FET chips. Figure 5-10 shows exemplary results of two kinds of devices (microsized ISFET and SiNW). Both devices were p-type transistors; however, the system has been adapted to measure n-type devices and even bi-polar chips from graphene materials. Although capable of implementing both characteristic and real-time measurements, the system only could measure 32-channels in characteristics mode. Using the real-time option, it only could measure one channel that can be selected by the software (Figure 5-11). The resolution of ADCs of the USB-6255 is 1mV, therefore theoretically the device can measure in the accuracy of 1 nA and 1 µA for the case $R_{FB} = 1$ MΩ ± 0.1% and $R_{FB} = 1$ kΩ ± 0.1% respectively, however the resolution observed during experiments are 5 nA and 5 µA. This is because the noise contribution of other discrete components and sensors are added onto the noise level of ADCs.
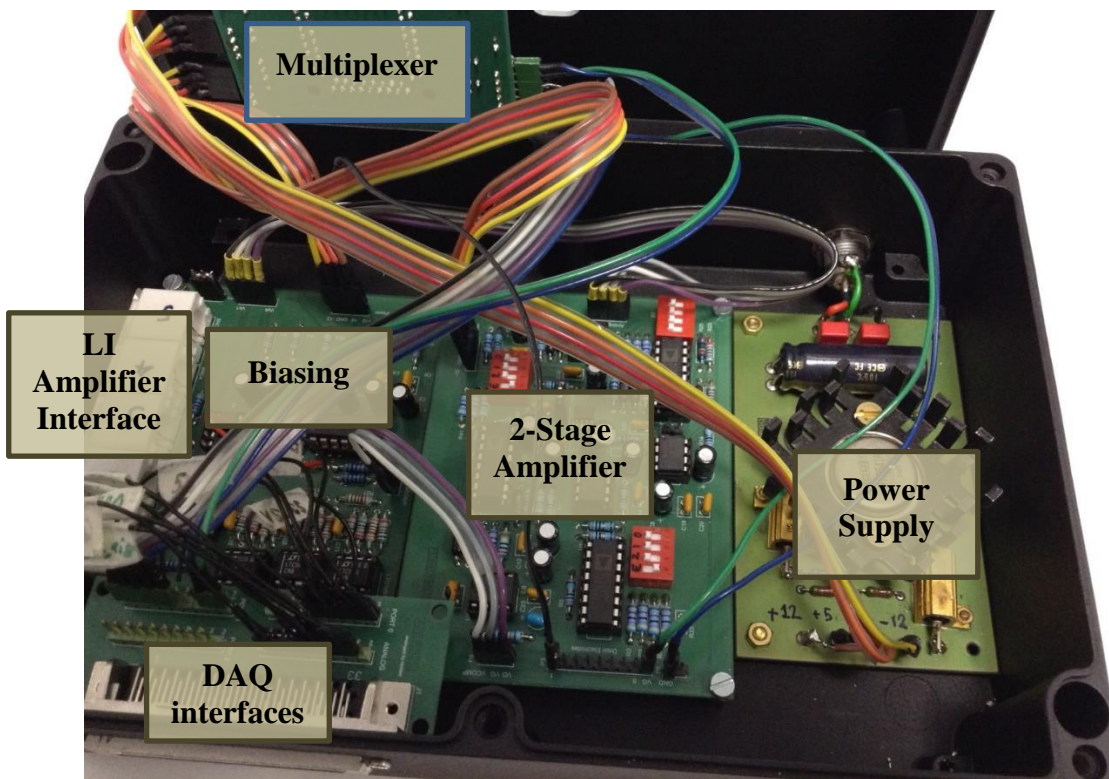
Figure 5-7 Internal setup of the T-box readout system

Figure 5-8 T-box as a measurement setup
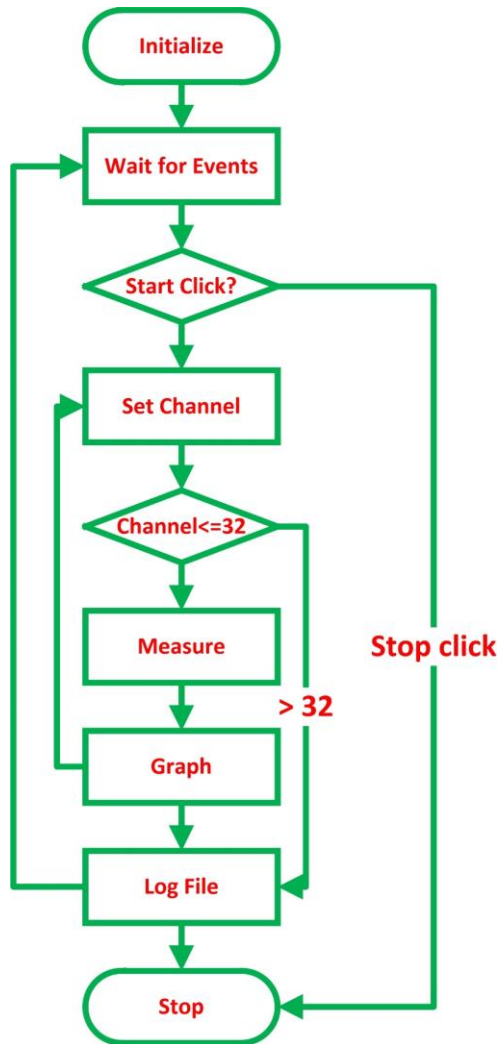
Figure 5-9 Software flowchart for 32-channel measurement
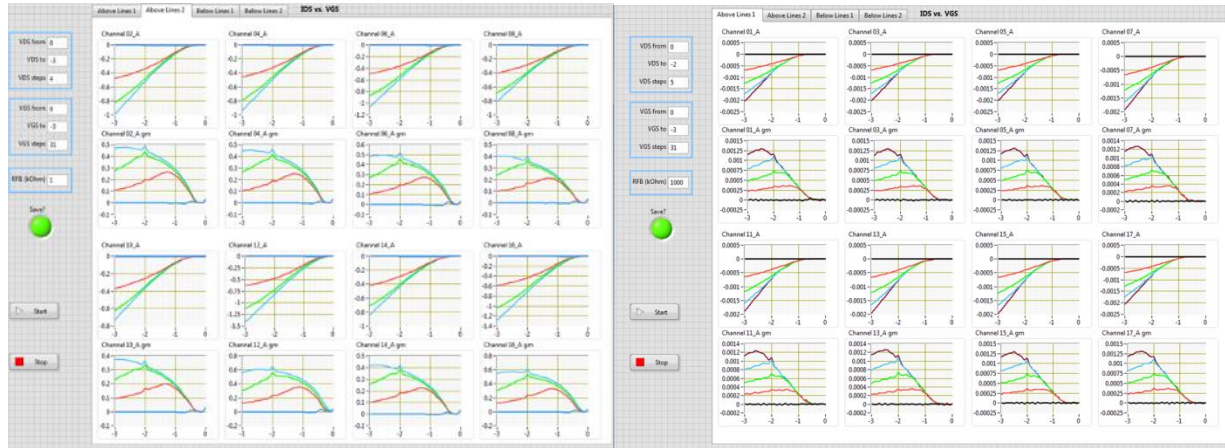
Figure 5-10 DC measurement examples (microsized ISFET (left), SiNW FET (right))
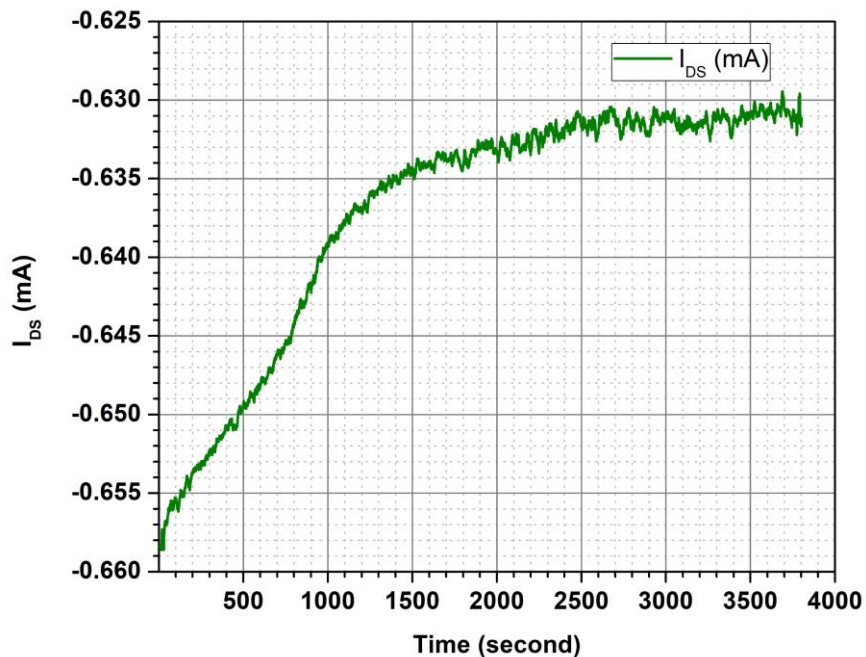
Figure 5-11 Exemplary real-time measurement with T-box

In AC readout mode (switch K in Figure 5-6 closed), the above-mentioned setup was utilized to bias devices. To record the impedance spectra, a fast lock-in amplifier (HF2LI, Zürich Instruments, Switzerland) was used to generate a stimulation signal of 10 mV amplitude in a frequency range from 10 Hz to 2 MHz superimposed on the biasing signal at a reference electrode (Ag/AgCl Dri-Ref DRIREF-2SH, World Precision Instruments, Germany). The high-frequency signal part after amplification was fed into the input channel of the HF2LI device and the spectra was recorded (Figure 5-12). The HF2LI goes with a GUI software called ZiControl that has many functionalities, however using this software limits the experiments to analyzing a single channel at a time. The channel selection, parameters adjustment, as well as saving and organizing recording datum, consume a lot of time. In this work, a program to implement those procedures automatically was

developed as well. In that case, the LabVIEW program, also written based on the state machine programming method, needed to synchronize the T-box and the HF2LI: initializing both devices, using T-box for selecting channels, setting up biasing voltages and amplifying signal. Then it set up some parameters ready for measurement of HF2LI and went into a loop of sending command of current measuring frequency to the device, getting data, displaying it in real-time on a monitor and until it finished the current channel, and then it saved the measurement data into a log file. After that, it went back to selecting channels and measuring again until finishing a pre-defined number of channels. An exemplary experimental result of impedance analyzing of a (microsized) ISFET can be found in Figure 5-13.
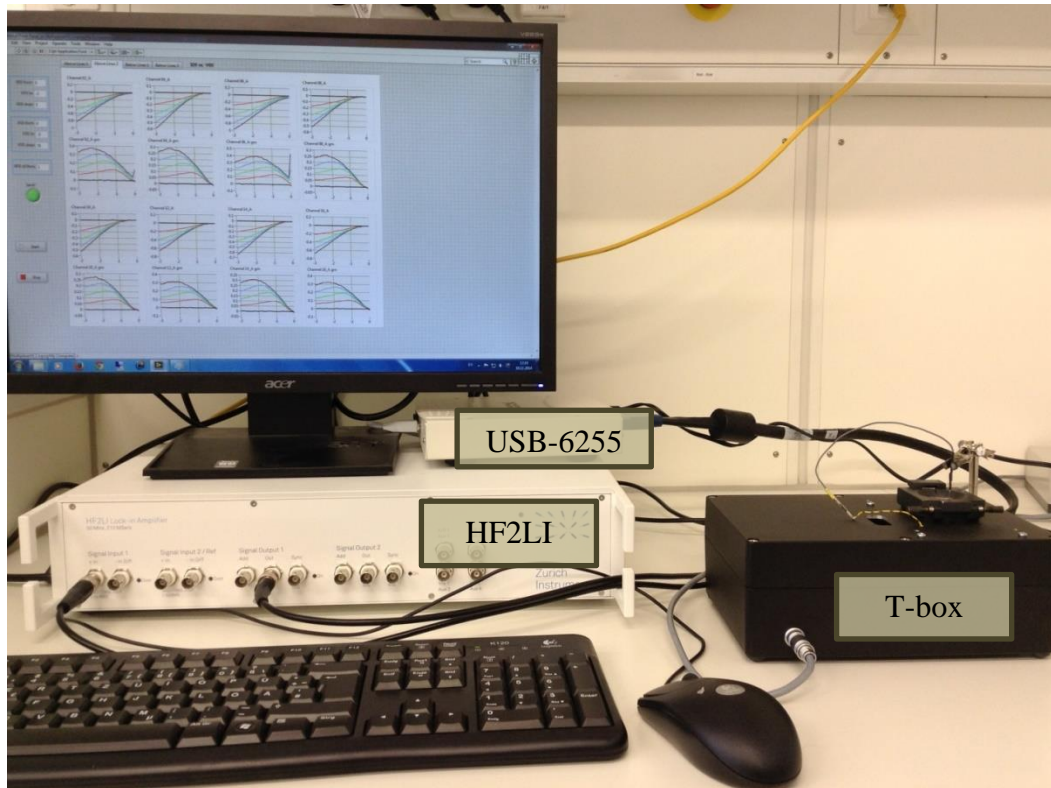
Figure 5-12 T-box setup in combination with a Lock-in amplifier
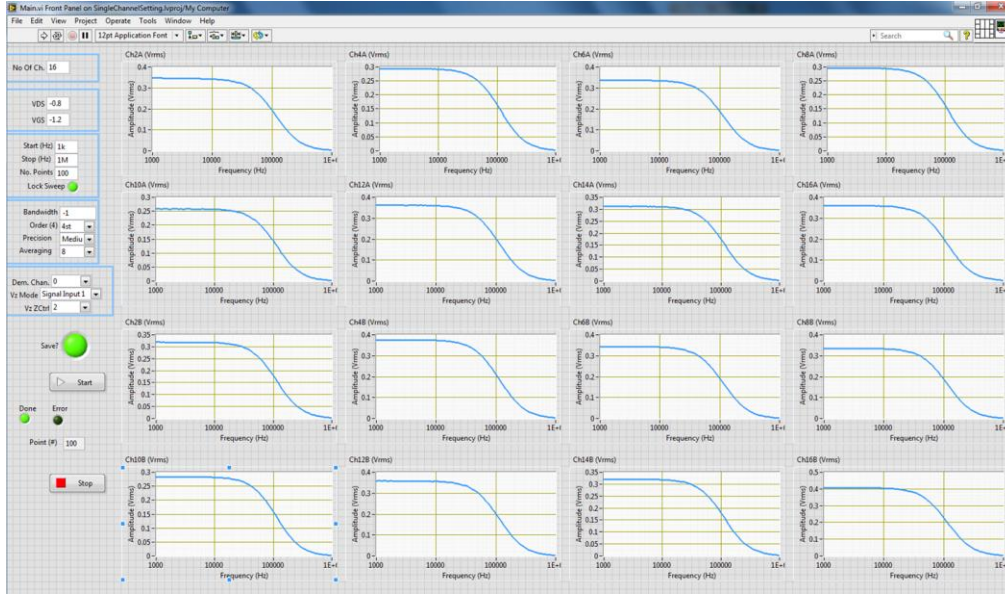
Figure 5-13 An exemplary impedance analyzing of a microsized ISFET

5.3.2 4-Channel Handheld Readout System
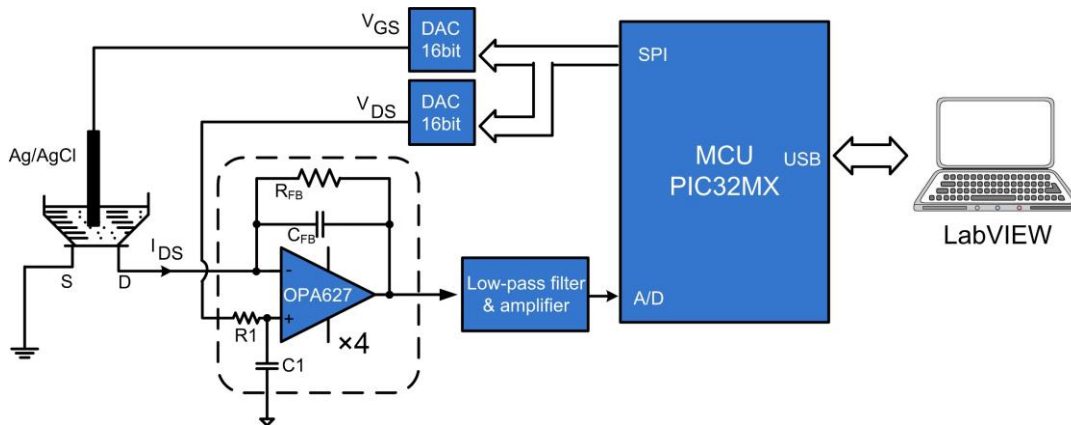
Figure 5-14 Block diagram of the handheld box

T-box provides a laboratory-based readout system for different types of FET sensor up to 32-channel; however, it lacks portability and can only measure in real-time mode one channel at a time. To build a system for point of care applications, more channels and handheld devices need to be developed. Figure 5-14 shows the block design of a 4-channel handheld readout system developed in this work. The biasing of the devices at different drain-source voltages (V_{DS}) and gate-source voltages (V_{GS}) was done by two 16-bit Digital-to-Analog Converter (DAC) chips (LTC1655, Linear Technology, USA) that have typical DNL of $\pm$ 0.3 LSB, INL of $\pm$ 8 LSB and offset error of $\pm$ 0.5 mV [158], which ensured precise and stable voltages. That differs from the previous setup [84], where the Serial Peripheral Interface (SPI) signals to these DAC chips were from a data acquisition device (USB-6255, National Instruments, USA). a microcontroller PIC 32MX695F512H (Microchip Technology Inc., USA) was utilized, which offers a miniaturization

of the readout system. This is a 32-bit microcontroller that has enhanced features and performance, which are suitable for not only the current application but also for a future multiple-channel readout version. It contains a 32-bit Reduced Instruction Set Computer (RISC) MIPS32 M4K core (MIPS Technologies, USA) with a maximum execution speed of 80 MIPS (Microprocessor without Interlocked Pipeline Stages), 512 KB of flash memory, and full speed USB 2.0 capabilities. In addition, it includes 16 10-bit Analog-to-Digital Converter (ADC), 3 SPI and offers a low-power consumption operation mode [159]. On the analog side of the readout unit, the drain-source current (I_{DS}) was converted into a voltage by a transimpedance amplifier which included an operational amplifier (OPA 627, Texas Instruments, USA), a feedback resistance (R_{FB}) and a feedback capacitance (C_{FB}). A $R_{FB} = 6$ kΩ $\pm 0.1\%$ was used for measuring microsized ISFET, while $R_{FB} = 1$ MΩ $\pm 0.1\%$ was used in the case of measuring the silicon nanowire chips. The voltage after the first amplifier resulted from the biasing voltage V_{DS} and the amplified signal of I_{DS}. To achieve a high precision and a wide dynamic range of the measurement current, the biasing voltage was subtracted before feeding the voltages to 4 analog channels of the microcontroller. Figure 5-15 exposes 4-channels handheld box: on the left side is the plug for dip-chip like carrier, on the right side is the Universal Serial Bus (USB) connector, in the front is plug for power supply (it can be either 9V adapter from the 220V power line or 9V from a battery).

Figure 5-15 Housing of the handheld measurement device

The firmware for the microcontroller was written in C/C++ in the Integrated Development Environment (IDE) MPLAB 8.9 (Microchip Technology Inc., USA). It controlled two DACs to sweep V_{GS} and V_{DS} voltages applied to the sensor chips. Then it recorded the corresponding voltages at the ADC pins and sent these values via the USB HID communication protocol to the measurement PC. On the computer side, a software programmed in LabVIEW 2012 was used to set the sweeping range and the steps of the biasing voltages during device characterization. It received the I_{DS} current signals from the microcontroller to plot the characteristic curves and to calculate the transconductance values of all channels. Recorded data can be saved inside a text file for further analysis. The device can measure both characteristics and real-time 4-channel chips, simultaneously (Figure 5-16 and Figure 5-17).
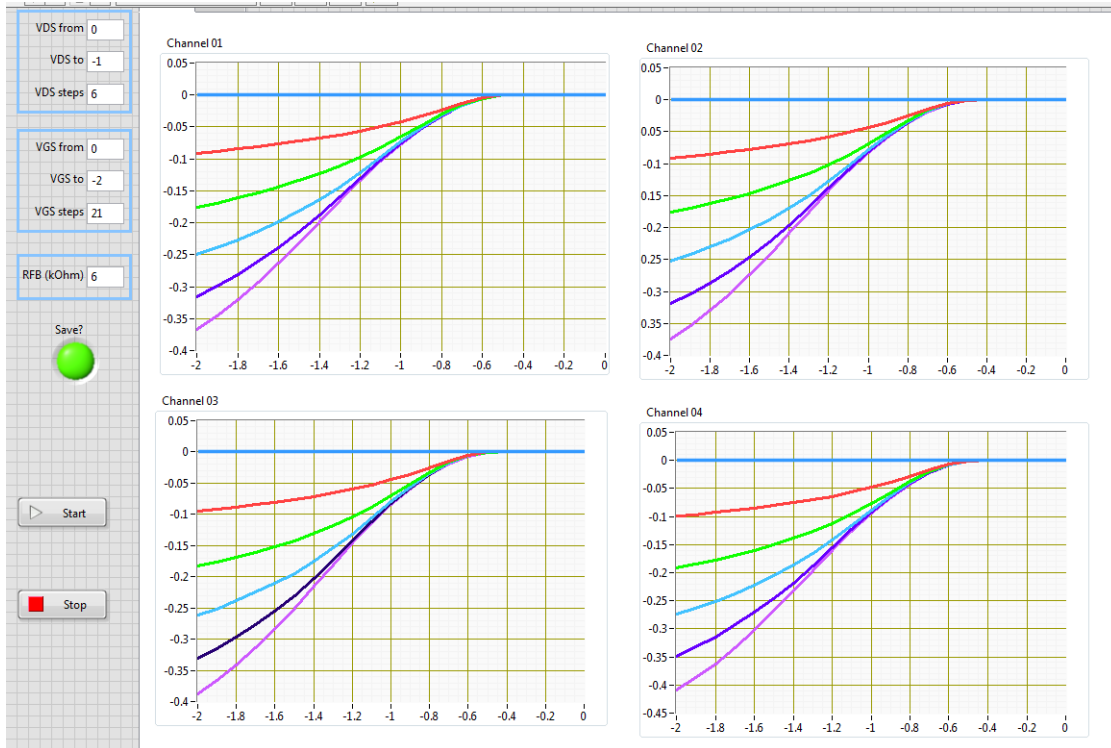
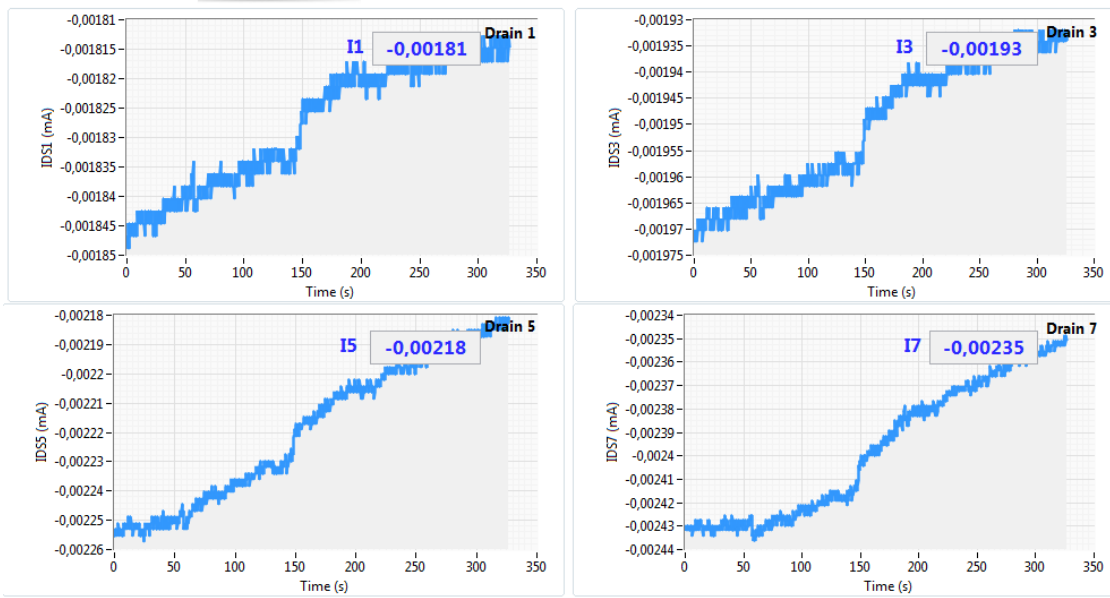Figure 5-16 Exemplary characteristic measurement of a ISFET chip

Figure 5-17 Exemplary real-time measurement of a SiNW FET chip

5.3.3 Miniaturization AC Readout with Monolithic Impedance Analyzer Chip AD5933
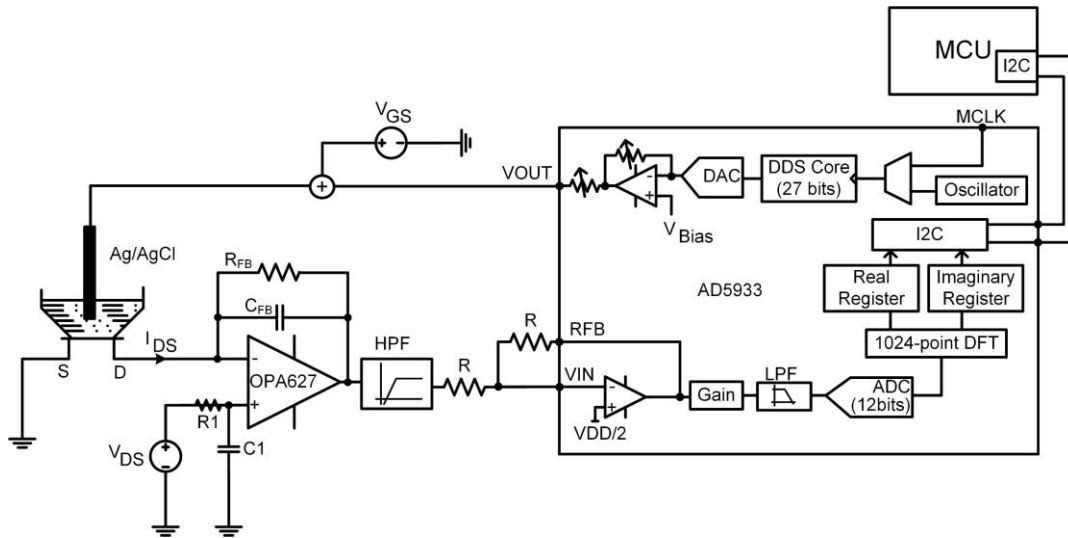

Figure 5-18 Miniaturized impedance readout diagram (the operational circuit diagram of AD5933 was adapted from [160])

The handheld device enabled FET-based sensors testing in remote areas, however it still lacks the capability in implementing impedimetric measurements. In the design of the second version of the handheld device, an impedance converter, system on chip AD5933 from Analog Device, Inc. was used to simplify measurement procedures and make it possible to have a handheld equipment for both potentiometric and impedimetric testing. The AD5933 is an impedance converter chip with a built-in signal generator. The excitation signal can be applied to an external complex impedance at a known frequency and the response signal will be sampled by a 12-bit, 1 MSPS, ADC. A discrete Fourier transform (DFT) is performed which returns a real (R) and imaginary (I) data to calculate impedance and phase shift at each output frequency [160]. The AD5933 has impedance measurement range from 1 kΩ to 10 MΩ with the frequency spectrum up to 100 kHz and the frequency resolution of 27 bits (< 0.1 Hz). In the direction of realizing a functional application-specific integrated circuit (ASIC) design, AD5933 represents a step in the middle. It is therefore interesting to look into its application capabilities and drawbacks.

The operational circuit diagram of the AD5933 is shown in Figure 5-18. It has a 27-bit direct digital synthesizer (DDS) core that generates the output excitation signal at a particular frequency (sub hertz resolution). Table 5-1 provides four options of output peak-to-peak voltages and their corresponding DC bias levels for 3.3 V power supply. To obtain a frequency spectrum, the AD5933 supports the frequency sweep feature that can be programmed with the three parameters: the start frequency, the frequency increment, and the number of increments. The response current from an external complex impedance after applying an output excitation voltage is fed into a current-to-voltage amplifier. It is then followed by a programmable gain amplifier (PGA), antialiasing filter, and ADC. The first stage of current-to-voltage amplifier configuration means that VIN is at the

virtual ground with the DC bias of VDD/2. The gain of this amplifier is defined by a user-selectable feedback resistor connected between Pin 4 (RFT) and Pin 5 (VIN). At each frequency point, the AD5933 DFT algorithm is calculated over 1024 samples that generates the real and imaginary component of the result.

Table 5-1 Output peak-to-peak voltage levels and respective bias levels for 3.3 V supply [160]

Range	Output voltage amplitude	DC bias level
1	1.98 V p-p	1.48 V
2	0.97 V p-p	0.76 V
3	383 mV p-p	0.31 V
4	198 mV p-p	0.173 V

When utilizing the AD5933 for FET-based biosensors, it has a drawback that the AD5933 was developed for a two-electrode impedance measurement setup while a FET is a three-electrode configuration. The configuration using the AD5933 that can implement impedimetric measurements with FET-based biosensors is shown in Figure 5-18. The excitation signal from the AD5933 is summed up with an DAC to generate stimulation and biasing signals at the reference electrode. The drain electrode of sensors also needs a specific working point and an additional current-to-voltage amplifier is used, such that both potentiometric and impedimetric measurements are possible. Because the input to the AD5933 must be a current, two identical nominal resistance R were utilized, and the first amplifier stage of the chip is a unity gain amplifier.

The schematic design and layout for the second version of the handheld device was accomplished, however there are several firmware and software packages (such as fast USB communication protocol, I2C etc.) were not done. It is therefore not able to test the capabilities and shortcomings of the AD5933 in impedimetric measurements with FET-based sensors. Nevertheless, the design and hardware in this work established a foundation for a future work of testing AD5933 as well as realizing a functional (ASIC) design.

5.3.4 System Calibration and Measurement Accuracy

To calibrate the system, a resistor (10 kΩ nominal value $\pm$ 0.1%, $\pm$ 15ppm/^{o}C) was utilized that was connected to the drains and the source pins of the chip socket. The V_{DS} voltage applied to all channels simultaneously was varied from 0 V to - 2 V with steps of - 0.5 V. In this case, the I_{DS} current was not affected by V_{GS} and, hence, the characteristic curves were parallel to the horizontal axis. In this case the relation between V_{DS} and I_{DS} is linear. After calibrating, there was a minor error between the calibration measurement and the theoretical curve (Figure 5-19) visible.

To evaluate performances of the setup, two ISFET (16×7 μm^2 gate dimension of the old design with in total 7 working channels) were measured with 0.1× PBS solution of pH 7.2 with both the handheld system and the standard parameter analyzer (Agilent 4156C). The mean error of seven

ISFET channels of the setup evaluated in these measurements was 3.9 ± 0.7 % and individual values were always less than 5% for each channel compared to the high-accuracy system (Figure 5-20).
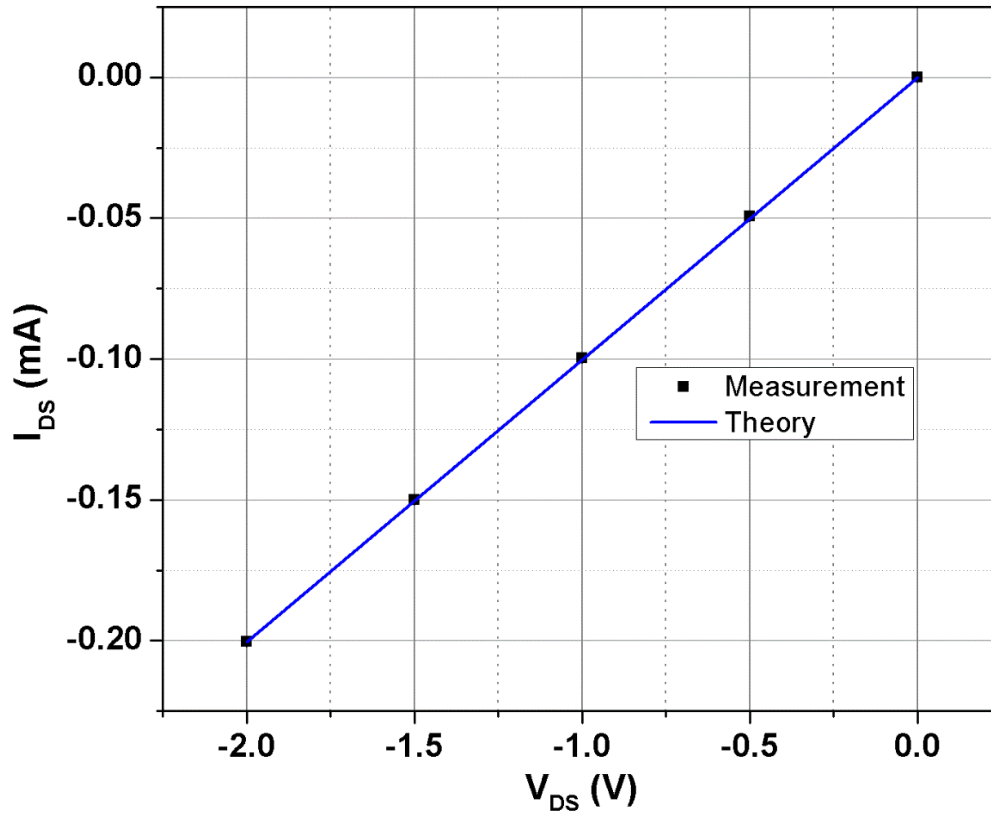

Figure 5-19 A calibration curve when a 10 kΩ (nominal value) resistor was connected between the drain and source pins
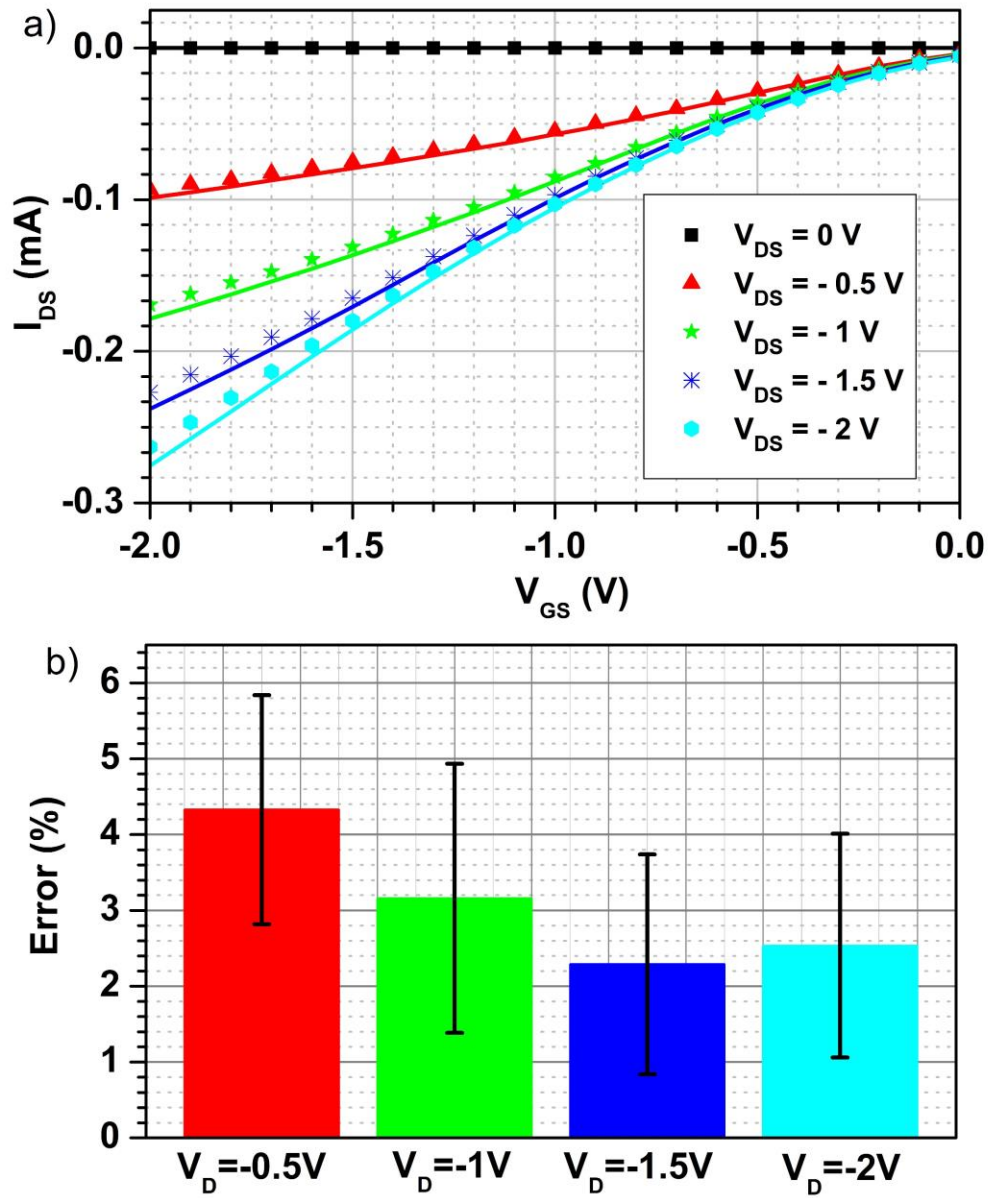
Figure 5-20 An exemplary comparison between the developed handheld setup and the Agilent 4156C measurement: a) characteristics measurement (handheld: scattering, Agilent 4156C (line); b) error calculation

5.3.5 Noise Features of the Developed Readout Systems

The detection membrane of the sensor is SiO_2, which has long-term drift due to its electrochemical instability when immersed in liquid [29]. In addition, the sensors show a high noise level due to the capture and de-capture of carriers to and from trap states of the interface between oxide layer and silicon itself [161]. Thus, this inhibits the detection of small biomolecules concentrations inside the solutions.

Considering noise analysis, it is always instructive to view it in both the time and frequency domain. In this chapter, the noise theory is reviewed [143,162,163], two fundamental theories (the Parseval's theorem and the Wiener-Khinchin theorem) that link the two domains are introduced, and the noise measurement of the ISFET and SiNW FET chips in combination with the readout system are measured.

5.3.5.1　Description of Noise in Time-Domain

In the following, it is considered that the data $A(t)$ as a time-dependent measuring data and will concentrate on how to characterize noise component from it. To simplify, $A(t)$ is measured in volts. If the data $A(t)$ carries both noise and signal of interest, the needed value cannot precisely be measured. However, the average value of the signal can always be calculated:

$$\bar{A} = \frac{1}{N}\sum_i A_i \tag{59}$$

The deviation of $A(t)$ from the average value is given by:

$$a(t) = A(t) - \bar{A} \tag{60}$$

A standard function in noise theory is the calculation of the variance (or square of the root-mean-square), which is a measure of the spread in the data.

$$rms^2 = \sigma^2 = \frac{1}{N}\sum_i (A_i - \bar{A})^2 \tag{61}$$

5.3.5.2　Power Spectral Density

The power spectral density describes the distribution of variance amongst the different frequencies. The power spectral density is basically the square of magnitude of the Fourier transform of $a(t)$:

$$N(f) = \int_{-\infty}^{+\infty} a(t)e^{i2\pi ft}\,dt \tag{62}$$

$N(f)$ is a complex quantity and the magnitude square of it:

$$P(f) = |N(f)|^2 + |N(-f)|^2 \qquad (63)$$

$P(f)$ is the power spectral density and it describes the variance at each frequency.

Parseval's theorem states that the total power in the time domain is the same as the total power in the frequency domain:

$$\text{Total power} = \frac{1}{T}\int_0^T a(t)^2\,dt = \int_0^{f_N} P(f)df \qquad (64)$$

5.3.5.3   Auto-Correlation Function and Its Relationship with Power Spectral Density

If a certain signal at time t_1 is well known, what is the prediction of the value at the time $t_2 = t_1 + \tau$. The function which describes how much the fluctuation functions at time t_2 and t_1 are correlated is called the auto-correlation function.

$$A(\tau) = \int_{-\infty}^{+\infty} a(t)a(t+\tau)dt \qquad (65)$$

The Wiener-Khinchin theorem says that the Fourier transformation of the power spectral density is the auto-correlation function.

$$A(\tau) = \int_{-\infty}^{+\infty} P(f)e^{-i2\pi f\tau}\,df \qquad (66)$$

5.3.5.4   Noise Measurement

A noise measurement of the FET sensor setup at the room temperature (20ºC) is shown in Figure 5-21, which shows the basic measuring procedure. Sensors were biased at the working point (where the highest transconductance is), and the signal output was sampled for 5 seconds at the speed of 10 kSamples/s with ADC resolution of 16 bits, no missing codes guaranteed, absolute accuracy is 1010 µV (input range ± 5 V) [156]. Figure 5-22 represents the auto-correlation function calculation of the data fluctuation. According to Wiener-Khinchin theorem: by calculating the Fast Fourier Transformations of this auto-correlation function, the noise power spectrum can be achieved. Figure 5-23 displays a noise power spectrum of a $12{\times}4\ \mu m^2$ ISFET: it shows the 1/f well-known noise figure of transistor devices. At high frequencies, the noise spectrum slowly goes to white noise region. Figure 5-24 also describes a noise spectrum of a 400 nm $\times$ 20 µm SiNW FET. It can be seen that because of a better fabrication technology, which was utilized for SiNW FET fabrication, the 1/f noise region is reduced compared with ISFET. However, the white noise is higher because of using higher value resistance feedback. The noise spectra in Figure 5-23 and Figure 5-24 are composed of both the noise of the FET sensors and readout device. In the future, with the help of a Vector Network Analyzer the noise feature of the FET sensors and readout system can be characterized separately. Obviously, compared with other FET readout system [143], the noise level of the setup is still high (both1/f noise and white noise level). There is still a lot of

room for optimization. Concerning readout design, more careful design and components selection are needed. In addition, careful layout and power supply design would also help in reducing the noise level of the whole system. The noise level in this chapter can only be evaluated with the T-box. The handheld device noise level was not able to achieve because the sampling speed was limited in the generic USB human interface device (HID) protocol.
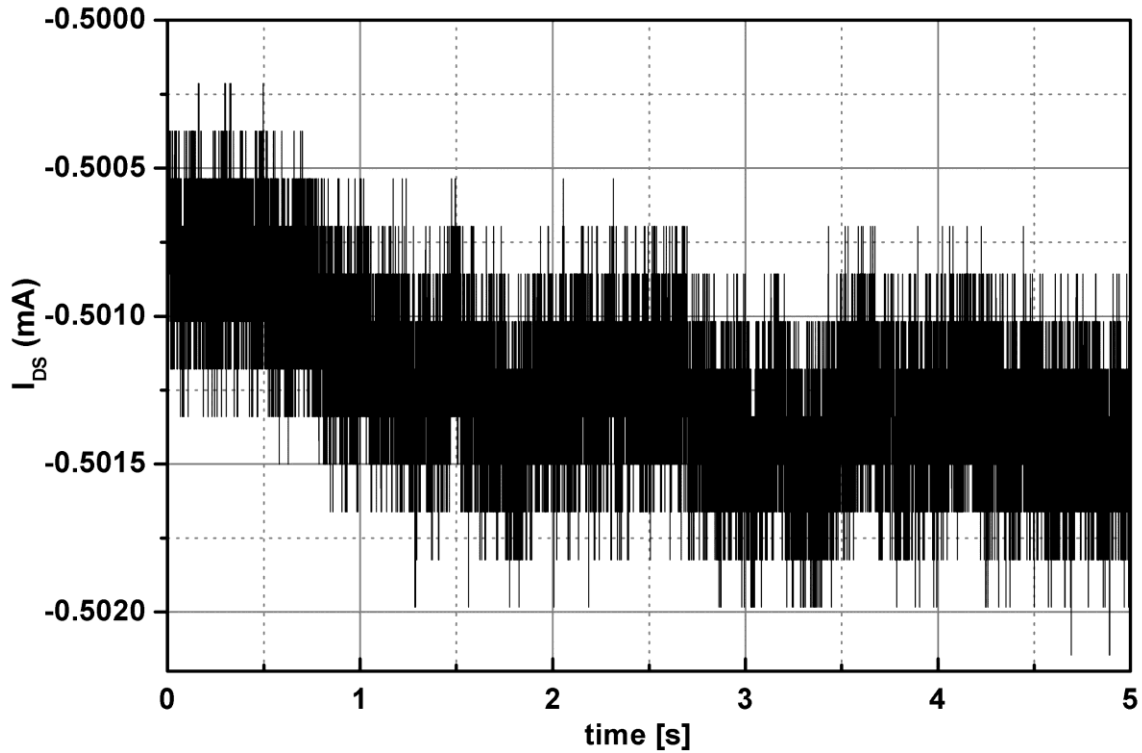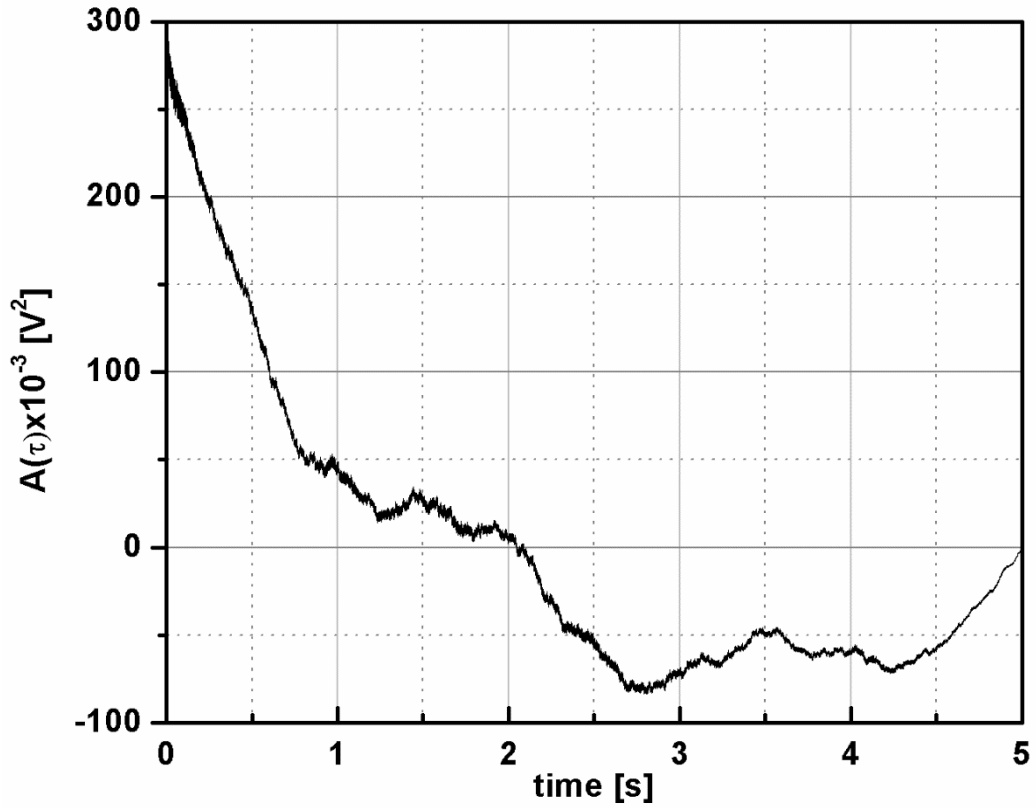

Figure 5-21 Noise raw data of the ISFET setup

Figure 5-22 Autocorrelation function of the signal fluctuation
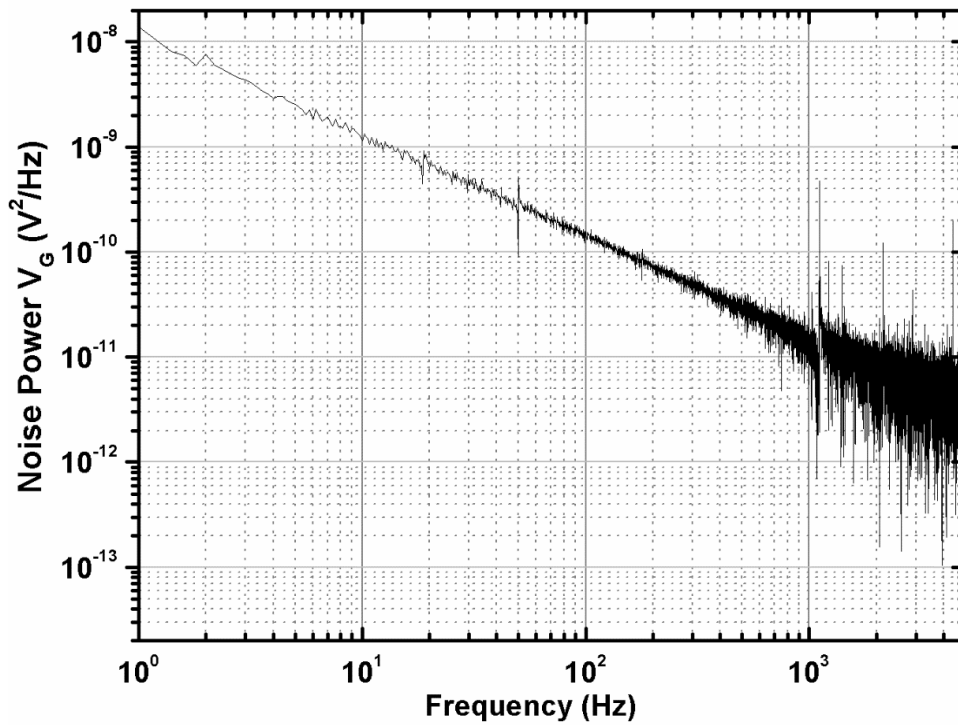
Figure 5-23 Noise power spectral of a 12×4 (12 µm width × 4 µm length) ISFET
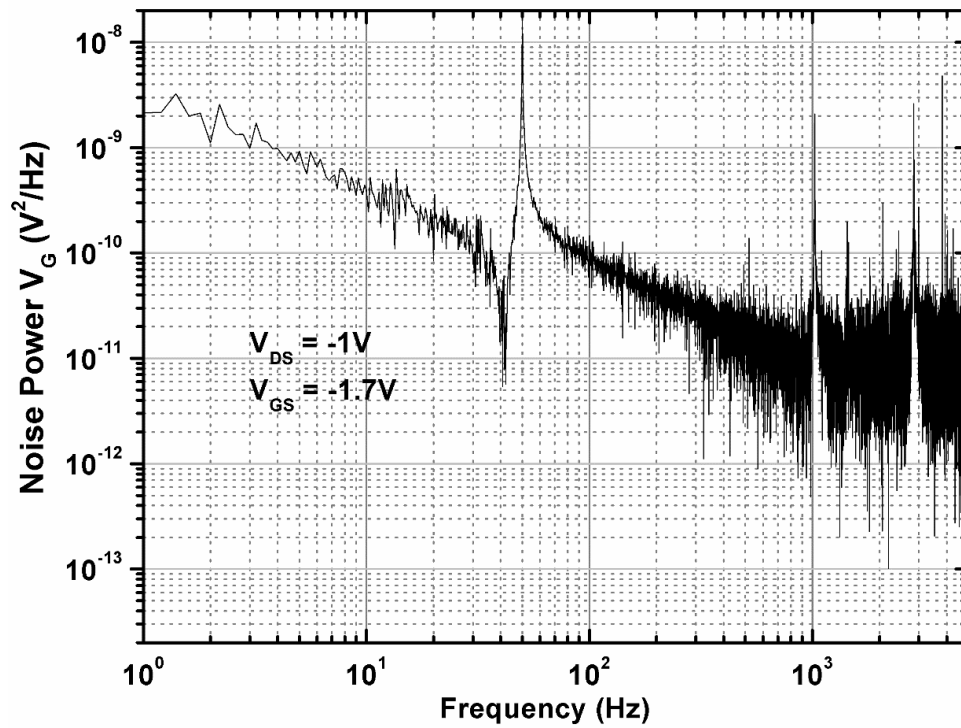
Figure 5-24 Noise power spectral of a 4×20 (400 nm width × 20 µm length) SiNW FET

6. Experiments and Results

This chapter will discuss proof-of-concept experiments with the sensors and the different amplifier systems, which were developed in this thesis. Both T-box and handheld systems can implement potentiometric measurements. However the following data of pH and DNA sensing were obtained from the handheld readout as they were reported in the publication [147]. On the other hand, impedimetric measurements can only be done by the T-box setup. These measurements will be the basis for the circuit simulation models based on SPICE including parameters and circuit elements from the biomolecules under test, which are then discussed in the next chapter. It will be started by discussing the detection of hydrogen in liquid with FET devices.

6.1 pH Sensing
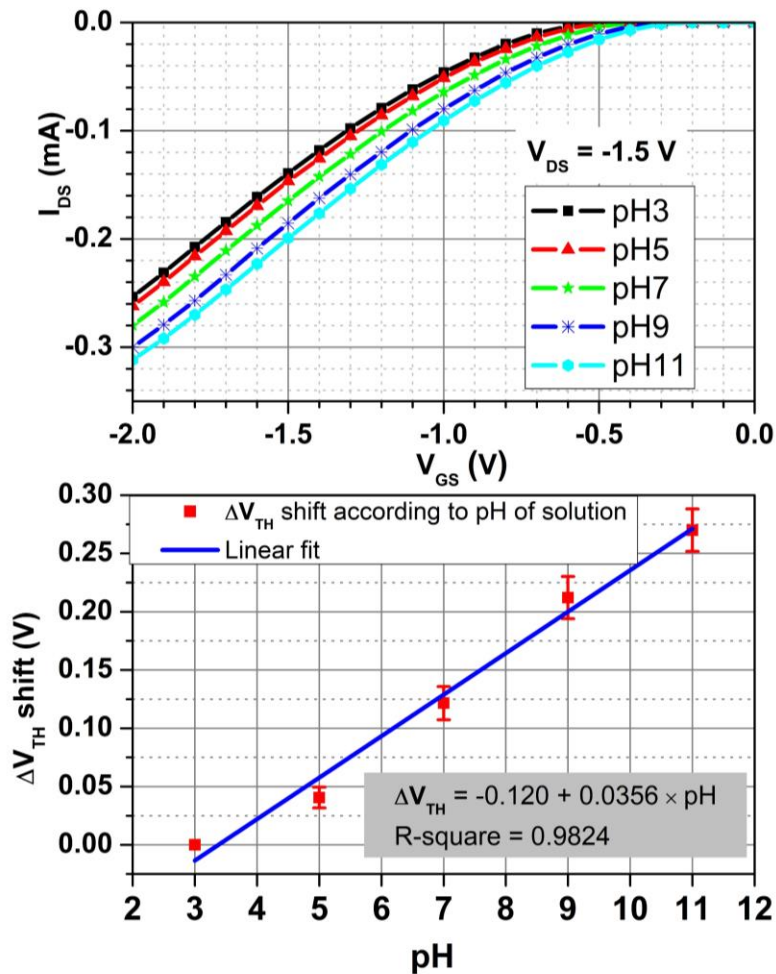
Figure 6-1 a) Typical transfer characteristic measurements for pH sensing on a bare SiO_2 FET chip. b) Shift of threshold voltage of bare chips caused by the variation of pH

The first pH measurements with microsized FET were introduced by Bergveld in 1972 [164]. Meanwhile there is a vast amount of literature available in the field. The most common, i.e. the easiest experiments are pH sensing with FET devices. In literature, also nanosized (nanowire) FET devices were used in many publications, such as Y. Cui et al. (2001) [45] and Y. L. Bunimovich (2006) [116], to only name two examples. In many cases the sensing membrane is silicon oxide, however it is not an ideal material for pH sensing, and other oxides such as Al_2O_3 [30] and Ta_2O_5 [165] show a better sensitivity and stability. The site-binding theory describing the detection mechanism for proton concentration was already mentioned in chapter 3.

In this work, the pH measurements were carried out either with bare SiO_2 surfaces or after surface treatment with APTES. Five different pH solutions (pH3, pH5, pH7, pH9 and pH11 obtained from Merck KGaA, Darmstadt, Germany) were measured with ISFET chips for characteristic curves to investigate the shift of the flat band voltage upon the pH variation of the solutions. Measurements with a standard pH and conductivity meter (SvenMultiTM, Mettler Toledo, Switzerland) were implemented in parallel as the controls for the experiments. The chip surface was cleaned and activated by piranha solution (H_2O_2:H_2SO_4 = 1:2) for 10 min at 60°C to obtain a high density of –OH group. After rinsing with deionized water and drying with nitrogen, the chip was gas phase silanized under vacuum conditions. The silanization was performed with aminosilane (3-aminopropyl) triethoxysilane (APTES) in a glove box. The encapsulated sensor chips can be reused by applying proper cleaning steps; however, the sensitivity of the device might degrade after each use. Therefore, only fresh chips were used for pH sensitivity sensing. In this experiment, four 16×7 μm^2 (width $\times$ length) ISFETs were utilized, where two chips (8 channels) were treated with amino silane under gas phase conditions. The measurements were implemented from low to high pH buffer solutions or vice versa with the handheld readout system. To obtain the equilibrium condition, after each step pH buffer solutions were exchanged several times before implementing next characteristic measurements.

According to the site-binding model, the variation of surface potential ($\Delta\Psi_0$) induced by a change in pH value of the bulk solution can be described by the following equation:

$$\Delta\Psi_0 = -2.303 \frac{kT}{q} \frac{\beta}{\beta + 1} \Delta pH \tag{67}$$

The Nernst equation (67) shows that an increase of the solution pH leads to a decrease of the surface potential, thereby inducing a higher flat band voltage of the ISFET device [105]. Thus, the characteristic curve of the p-type ISFET shifted to the right as the increment of the pH from 3 to 11 (Figure 6-1 b). In an ideal case, the surface potential variation upon the change of pH value is close to 59.3 mV per pH. In the measurement, the average pH sensitivity of bare SiO_2 devices was 34 ± 2 mV/pH of V_{TH} shift and the linearity of the fitted mean values is only 0.9824 (Figure 6-1a). The pH sensitivity is in good agreement with previous publications, where the sensitivity of bare silicon oxide surfaces was 30-40 mV/pH [166]. The low linearity and the sensitivity depend on

several factors, such as the pH_{pzc} of the surface, the density of surface sites, and the equilibrium constants for protonation and deprotonation of the surface as discussed in chapter 2.
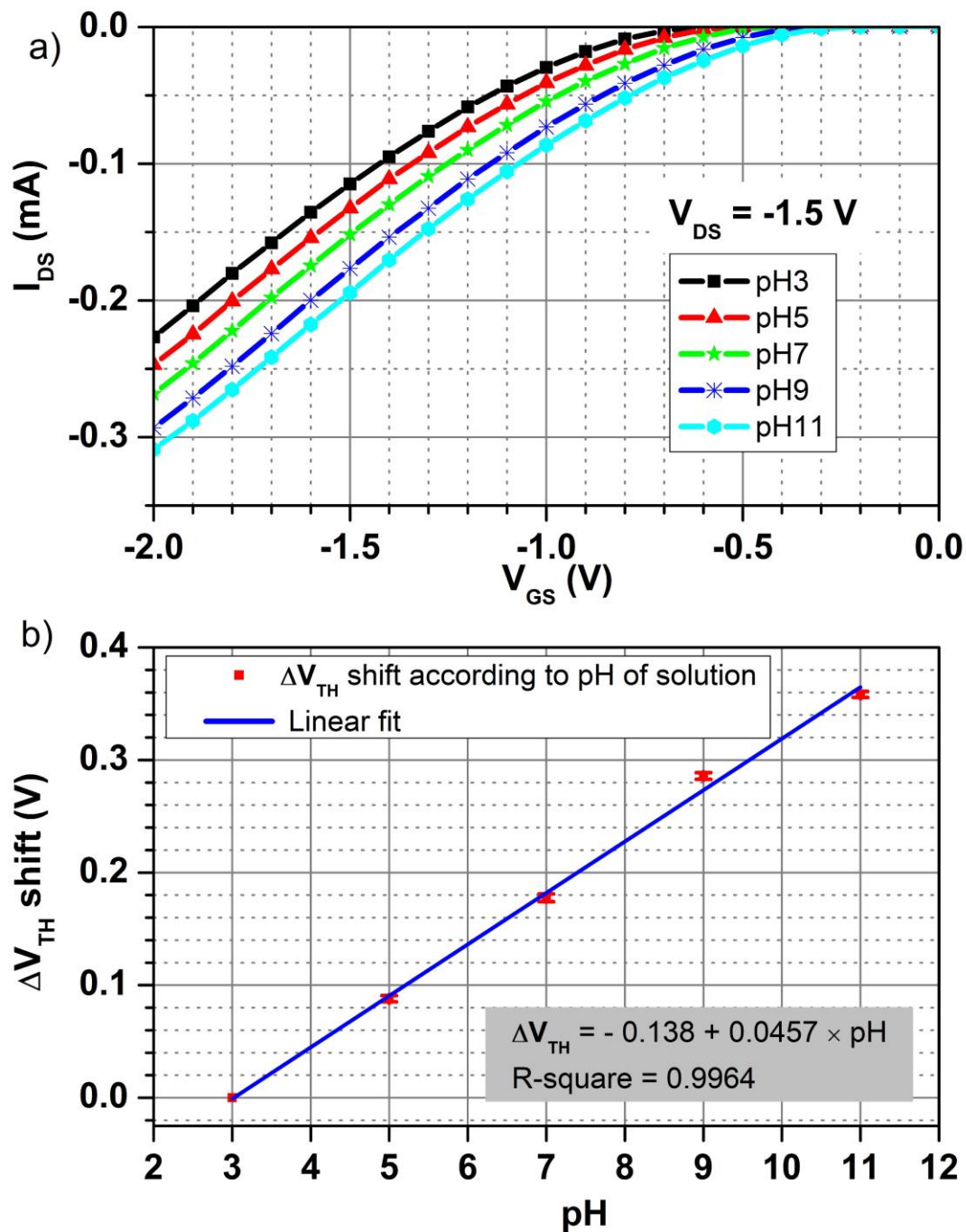

Figure 6-2 a) Typical characteristic measurement of pH sensing of a silanized (APTES) chip. b) Shift of threshold voltage of silanized chips.

To increase sensitivity and linearity of these ISFET sensors, the chip surface was treated with aminosilane in gas phase conditions. The sensitivity then increased to 45 ± 0.3 mV/pH and the

linearity improved to 0.9964 (Figure 6-2). This can be explained by the change of surface chemistry of the modified ISFET, in which covalent binding of aminosilane to silicon dioxide surface leads to the presence of both $-NH_2$ and SiOH groups. These groups have different equivalent constants. At low pH, the amino group is protonated to $-NH_3^+$, while at high pH, SiOH is deprotonated to $-SiO^-$ [45]. This result shifts the pH_{pzc} outside of the measurement range and hence increases the linearity of detection.

6.2 DNA Sensing

Deoxyribonucleic acid (DNA) is the storage of all genetic information in all cells, that regulates cells' specifications and the construction of proteins and ribonucleic acid (RNA) molecules [167,168]. DNA molecules are polymers (polynucleotides) consisting of monomer nucleotides. Nucleotides themselves are built from three different parts:

- A deoxyribose sugar (5-carbon sugar)

- A nitrogenous base: adenine (A) and guanine (G) (double-ring structure), or cytosine (C) and thymine (T) (single-ring structure).

- A phosphate group: consisting of a phosphorous atom bonded with four oxygen atoms. At neutral pH level, they are negatively charged and therefore give the nucleotide and hence the DNA molecules a negative charge.

Because the carbon atoms in both the nitrogenous base and sugar are numbered, the sugar atoms have prime (´) to distinguish them, making sugar atoms such as 1´, 2´, 3´, 4´ and 5´. A nucleotide is formed such that the phosphate group attaches to the 5´ atom of the sugar while the nitrogenous base binds to the 1´ atom of the sugar (Figure 6-3).

Cellular DNA molecules have two polynucleotide chains twisted around an imaginary axis, forming a double helix (Figure 6-4). The two sugar-phosphate backbones run in opposite 5´→ 3´directions from each other and are *antiparallel*. The nitrogenous base of two strands join by hydrogen bonds in the way that adenine (A) always pairs with thymine (T), and guanine (G) always fits with cytosine (C). It also can be said that A is complementary to T and C is complementary to G. When two strands are matched up in terms of their base sequences, they are called complementary stranded DNA.

In its natural form, DNA is then a double-stranded molecule or a double helix. The base pairs are only stabilized by hydrogen bridge bonding. At neutral pH and at physiological buffer concentration the hydrogen bridge binding overcomes the electrostatic repellence of the two negatively-charged single strands. This binding is highly specific depending on the base pair sequence and the binding reaction is called hybridization.

When heating above a critical temperature (melting temperature) the thermal energy overcomes the bonding force and the double strands detach (de-hybridization or denaturation)
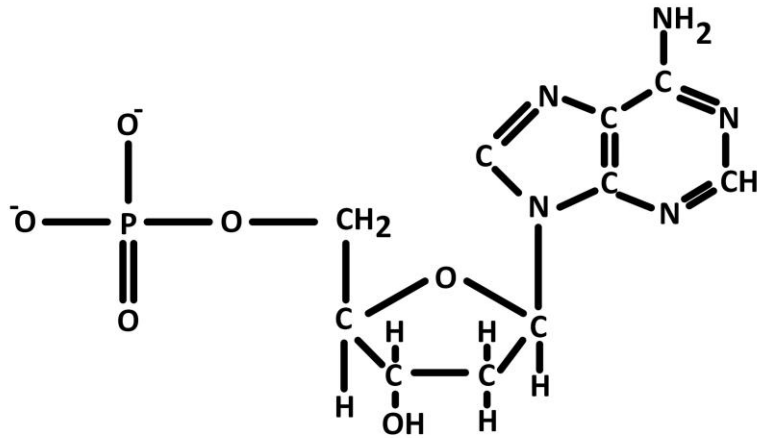
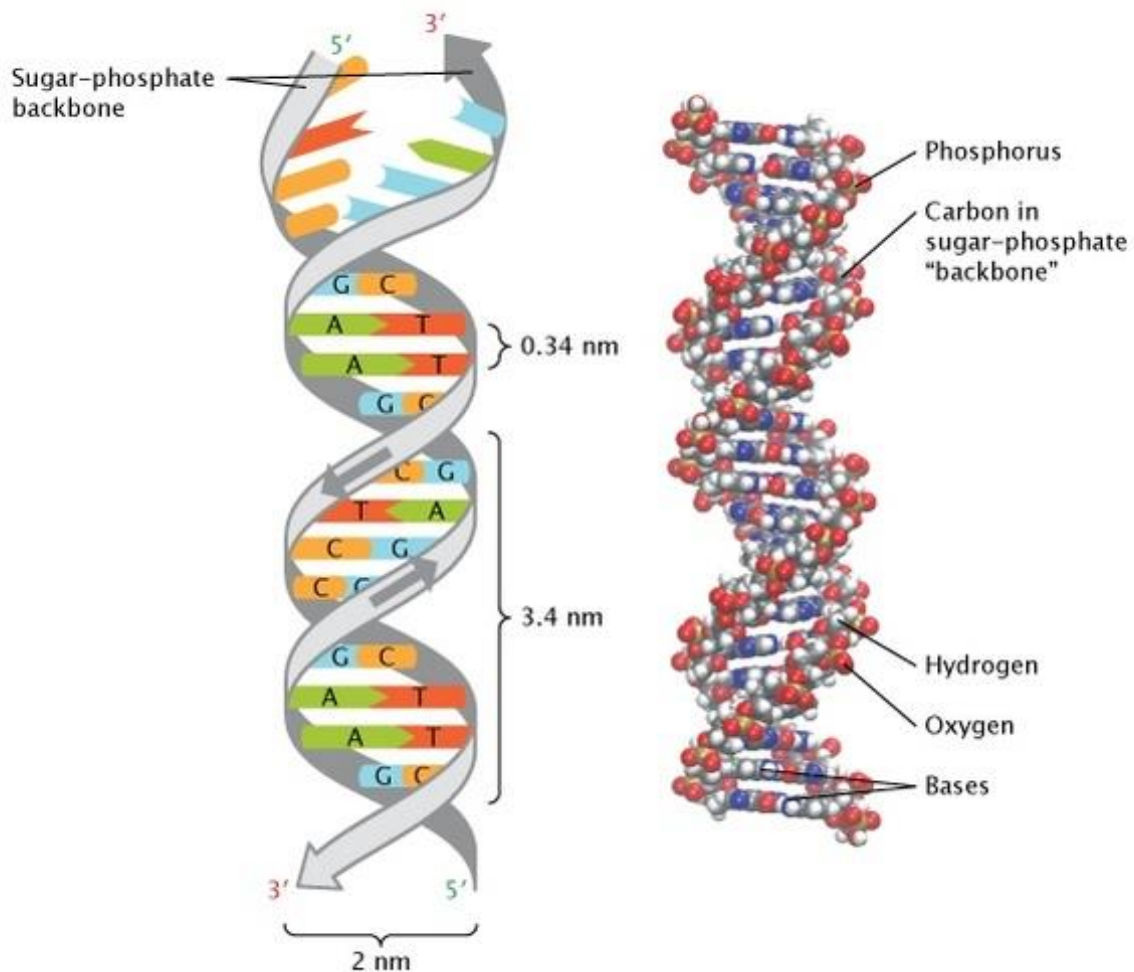Figure 6-3 The components of nucleotide (adenosine monophosphate)

Figure 6-4 Double helix structure of DNA reprinted with permission from [169] © 2013 Nature Education

DNA sequencing, which determines the physical order of nucleotides in a DNA strand, plays a crucial role in clinical diagnostics such as early detection of genetic diseases (cystic fibrosis, sickle-cell anemia, Huntington's disease, breast cancer), pharmacogenetics and parental testing. Most DNA sequencing today is *cycle sequencing*, which combines the original chain-termination method (developed by Fredrick Sanger and coworkers in 1977) with the heating and cooling cycle of polymerase chain reaction (PCR). To begin cycle sequencing, the DNA to be sequenced, primers that target the DNA at a specific position, a DNA polymerase (Taq polymerase), many typical nucleotides (dNTPs), and lots of dideoxyribonucleotides (ddDTPs) are put into the solution. The dideoxyribonucleotide does not have a 3´ hydroxyl group, therefore inhibits the DNA elongation once it is on the chain. Then the basic cycle of PCR is repeated, producing many copies of variant length of the gene to be sequenced. As the partial sequence passes through a gel electrophoresis which separates DNA strands based on their size and electrical charge, a laser is used to read the fluorescent tag on each ddNTP. Each tag has a different color so that a computer can read and calculate the sequence of the DNA strand. This method provides a result with 99.9% accuracy; however, it is time-consuming, not cost-effective, requires trained personnel, and therefore limits the realization of point-of-care applications.

Field-effect transistor (FET) devices offer an alternative approach for label-free, rapid biomolecule detection, in which a transistor amplifier is utilized as a miniature transducer for the detection and measurement of potentiometric signals, which are produced by binding events happening on the gate of the FET [40,64,83,116,170–177]. DNA detection with SiNW FET can achieve the level of sub-femtomolar concentration and can distinguish DNA strands with one- and five-base-mismatches from hybridization [177]. The basic working principle is that a single stranded probe DNA is immobilized on the surface of FET chips. Once there are complementary strands of DNA in the measurement solution, the hybridization of complementary DNA strands happens on the surface of the chip. The hybridization is highly specific, and DNA is highly charged with uniform distribution—each base has a single excess negative charge along the sugar-phosphate backbone. Highly integrated measurement channels can be achieved by using standard CMOS processes. Moreover, biosensors based on FET devices were proposed as a handheld point-of-care diagnostic tools more than a decade ago [178]. On the other hand, detecting the static charge of a DNA strand with an ISFET device faces significant difficulties where the static charges are screened in electrolyte solution. Thus, measurements in low ionic strength solution are needed in these experiments (1.5 mM phosphate buffer). The reason a low ionic strength measurement solution was selected in this work for proof-of-concept experiments, similar to what was reported in earlier works [70,118]. However, at low ionic strength the repulsion between two complementary DNA strands is strong as well. Consequently, the hybridization probability will be reduced and extended time for hybridization will be required [179,180]. To deal with this problem, *ex situ* hybridization was done at high ionic strength, and then the detection measurements were done in a much lower ionic strength solution.

Measurements with DNA immobilization and hybridization were implemented on two ISFET chips (16×7 and 12×4) as a proof-of-principle demonstration of the biomolecule detection capability of the setup. Miriam Schwartz developed the following procedure of DNA immobilization and hybridization. She helped with the experimental work with the handheld device and the results were published in a co-first authors paper [147]. At first the chips were cleaned, activated, and then gas phase silanized with (3-Glycidyloxypropyl) trimethoxysilane (GPTES). Amino-modified single-stranded probe DNA (pDNA) (5'AC6-ATGAACACTGCATGTAGTCA-3'; AC6 = amino-modifier) was employed for the DNA immobilization. The probe molecules were diluted in 150 mM phosphate buffer at pH 8.5, consisting of NaH_2PO_4 and Na_2HPO_4. At a pH value of 8.5 – 9, the epoxy ring of the GPTES opens and the amino-modified group of the pDNA can covalently bind to the opened ring [181]. The capture sequence was site-specifically immobilized on certain gates of the ISFETs by using a microspotter (sciFLEXARRAYER S3, Scienion AG, Germany). Three drops of the probe molecule solution with a volume of 200 pl were spotted on each channel. To prevent evaporation of the solution, a humidity of 70 % was adjusted in the closed housing of the microspotting system. The immobilization proceeded overnight at 37 °C in an incubator with a humidity of around 65%. Afterwards, the chip was cleaned thoroughly with 4× saline sodium citrate buffer (SSC), 1× SCC, and deionized water to remove unspecific bound pDNA. Subsequently, a blocking step with 1 % Bovine Serum Albumin (BSA) diluted in 1× PBS pH 7.2 (137 mM NaCl, 2.7 mM KCl, 8.1 mM Na_2HPO_4 and 1.47 mM KH_2PO_4) was performed for 3 h to avoid unspecific binding of the target molecules. Before the hybridization with complementary target DNA (cDNA) (5'-TGACTACATGCAGTGTTCAT-3'), the chip was rinsed with 4× SSC, 1× SSC and deionized water. Hybridization was allowed for 2 h at 37 °C in an incubator with a humidity of 65 %. Denaturation experiments were carried out by putting the chips in deionized water at 90°C for 3 minutes. Subsequently the chips were cleaned with 4× SSC, 1× SSC and deionized water. The applied DNA sequences were purchased and synthesized by Eurofins MWG Operon, Germany, and had a length of 20 base pairs. The immobilization and hybridization procedures were double checked with a fluorescent microscope [181]. After assay optimization, only the experiments with the electronic detection method were further implemented.

After each step (silanization, immobilization, blocking, hybridization and denaturation), the characteristics were measured in 1.5 mM phosphate buffer pH 7.2, consisting of NaH_2PO_4 and Na_2HPO_4 (Figure 6-5a). At this pH, pDNA, BSA and cDNA are negatively charged, therefore the characteristic curve shifts to the right side upon the binding of these molecules on the chip surface. When considering the curve after silanization as a base line, the variations of V_{TH} upon 1µM pDNA, 1% BSA and 1 µM cDNA was 29 mV, 42 mV and 55 mV, respectively. After DNA denaturation, the voltage shifted back to 28 mV, which was the starting value of V_{TH} after DNA immobilization (Figure 6-5b).

Several publications have discussed the underlying detection principle of DNA with FET devices [127,178,182,183]. In a first approximation, according to Debye-Hückel theory, the surface potential Ψ_0 can be calculated from the surface charge density by using the Grahame equation [65]:

$$\Psi_0 = \frac{2kT}{e} \sinh^{-1}\left(\frac{\sigma_0}{\sqrt{8\varepsilon_w\varepsilon_0 kTn_0}}\right) \tag{68}$$

ε_0 is the permittivity of free space, ε_w is the dielectric constant of the measurement electrolyte, and n_0 is the buffer ionic strength.

The attachment of DNA molecules to the surface induced the change in the surface charge density σ_{DNA}. Therefore the shift of V_{TH} can be calculated in the following equation [141]:

$$\Delta V_{TH} = \frac{2kT}{e}\left(\sinh^{-1}\left(\frac{\sigma_0}{\sqrt{8\varepsilon_w\varepsilon_0 kTn_0}}\right) - \sinh^{-1}\left(\frac{\sigma_0 - \sigma_{DNA}}{\sqrt{8\varepsilon_w\varepsilon_0 kTn_0}}\right)\right) \tag{69}$$

It is well known that the electrostatic effect in the solution is screened outside of the Debye length, which depends on the ionic strength of the solution:

$$\lambda_D = \sqrt{\frac{kT\varepsilon\varepsilon_0}{2z^2e^2n_0}} \tag{70}$$

with z the valance of the ions in the electrolyte.

Therefore, the DNA experiments were measured with a low ionic strength buffer solution (~ 2 mM), which results a Debye length of 6.8 nm. This is comparable with the length of 20 base pair DNA double stranded molecules.
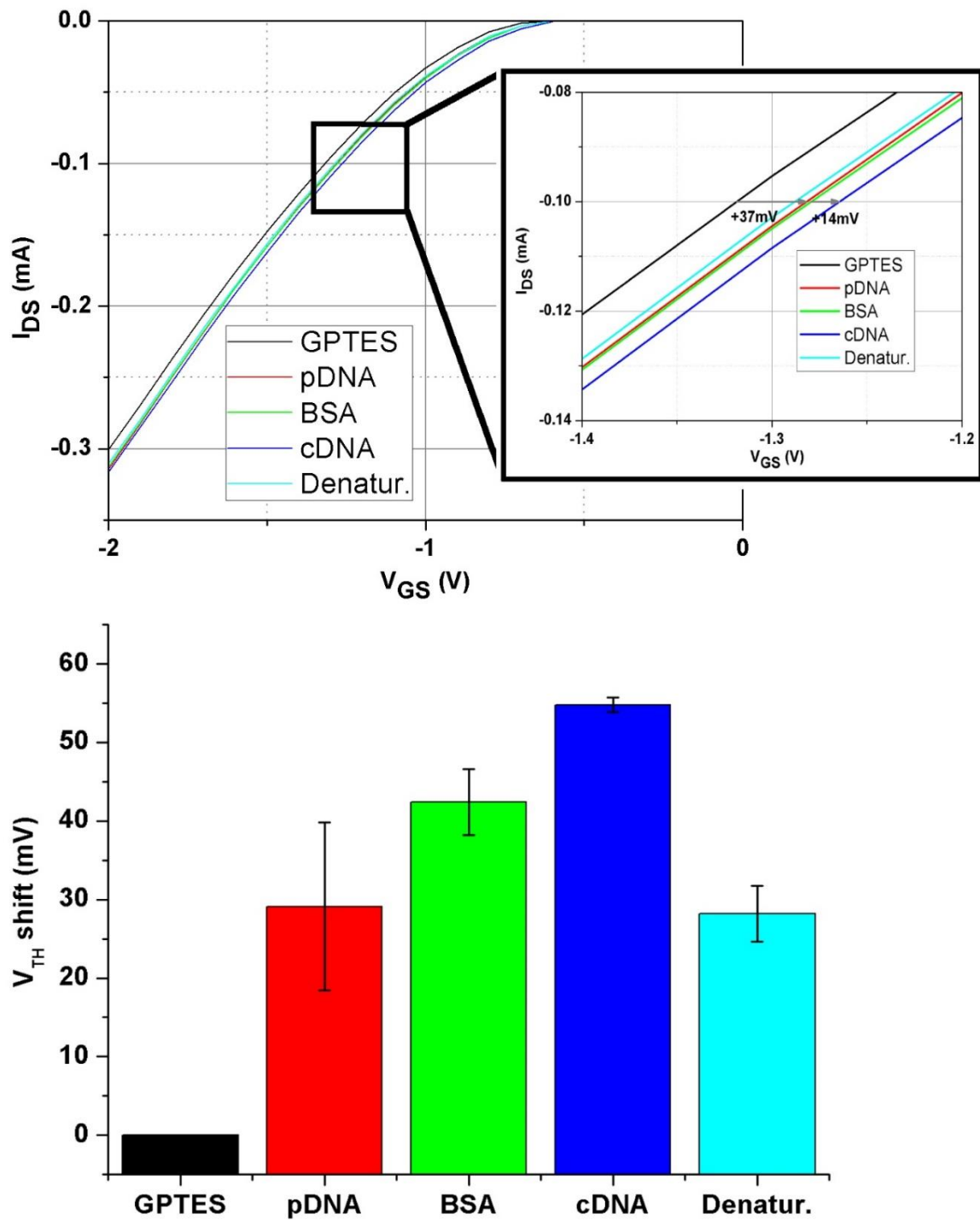
Figure 6-5 a) Transfer characteristics of an ISFET device after each step; b) The shift of V_{TH} extracted from characteristic curves

If the maximum surface charges density σ_0 of 0.8 C/m^2 can be achieved (which is in real case is not possible), from equations (68) and (69) the following values can be calculated:

$$\Psi_0 = 294 \ (mV) \tag{71}$$

$$\Delta V_{TH} = 29 \ (mV) \rightarrow \ \sigma_{DNA} = 0.346 \ (\frac{C}{m^2}) \tag{72}$$

If one 20-base oligonucleotide can contribute a maximum 20 electron charges to the surface charge density, then the density of DNA is 1 strand per 9.25 nm^2. This corresponds to ~ 10^{13} strands DNA per cm^2. The surface density of the immobilized oligonucleotide on silicon dioxide/silicon nitride has been reported to be from 10^9 to 10^{13} /cm^2 [184–186], which depends on the substrate material and immobilization method. In this case, the surface charge density after GPTES treatment was considered to be the maximum value of silicon dioxide surface. The non-perfect surface and the silanization with GPTES lead to a smaller value of σ_0. Therefore, the density of immobilized DNA will be less than the calculated value.

6.3 Impedimetric Measurements with Solutions of Different Conductivity

To understand the working principle of the impedance measurements with FET devices as well as the effects of parasitic parameters (the drain and source insulation capacitors), the measurement with both ISFET and SiNW FET in AC-mode was implemented at different PBS buffer concentrations while keeping the pH values constant. Here, the frequency shift of the cut-off frequency of measurement spectra was observed for ISFETs, while the amplitudes at resonance frequency was monitored in case of the SiNW.

At first, several phosphate buffer solutions (PBS) with different concentrations (1 mM, 2 mM, 10 mM, 100 mM, 500 mM, and 1 M) at the same pH were prepared. The conductivity and the pH values were measured and controlled by a standard pH and conductivity meter (SevenMultiTM, Mettler Toledo, Switzerland). Then, the impedance spectrum of SiNW FET and ISFET channels were obtained by the T-box setup and the Lock-In amplifier (chapter 5.3.1) with frequencies up to 2 MHz.

Figure 6-6 describes exemplary impedance measurements of an ISFET channel with different buffer concentrations. As the conductivity of the solution increases (increasing the concentration of the PBS solutions) the cut-off frequency of the spectra shifted to the right side (greater frequency region). This showed the low-pass filter response with resistance (combined resistance of reference electrode and electrolyte solution) and capacitance (gate oxide and contact line insulator) which were described well in some earlier publications [73,95]. It was found from these experiments that the cut-off frequency is linear with the concentration of the measurement buffer concentrations (Figure 6-8)
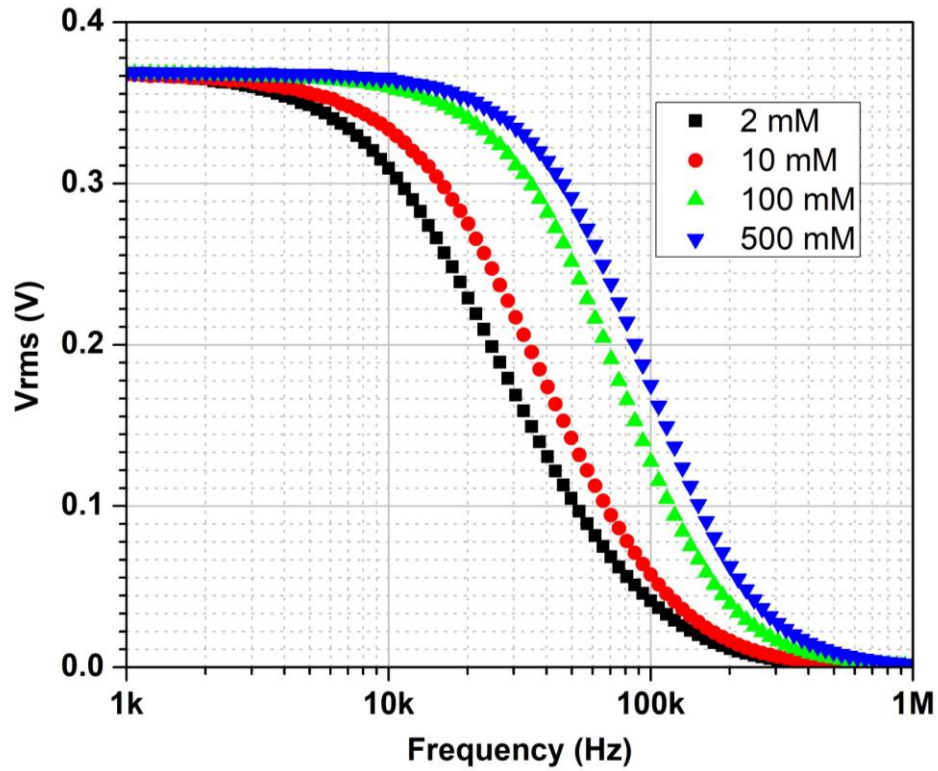
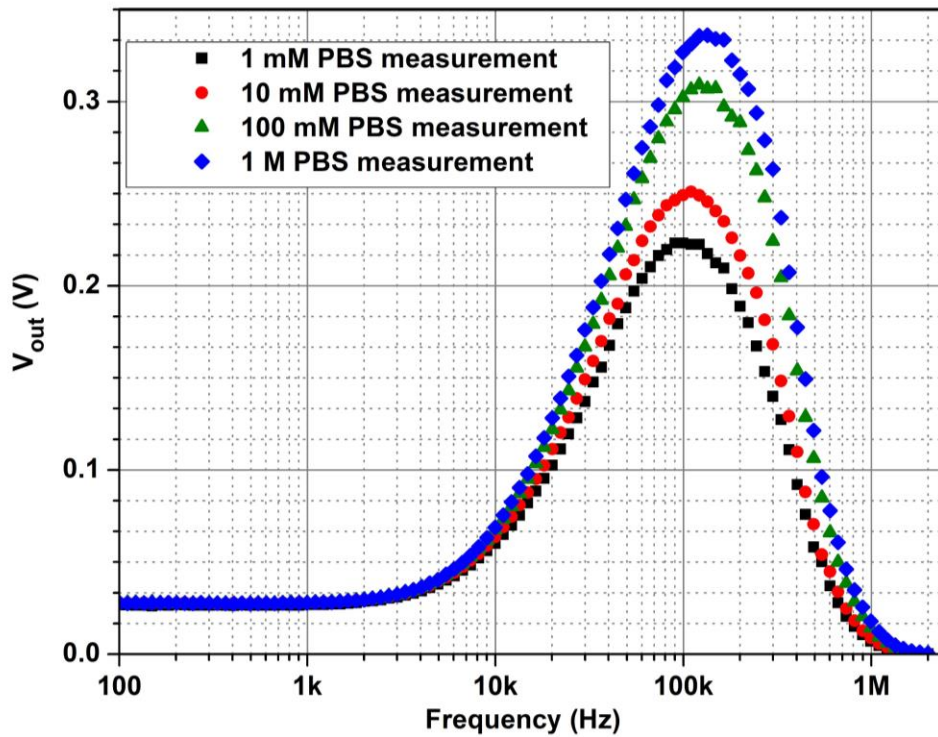Figure 6-6 Impedance spectra of an ISFET channels

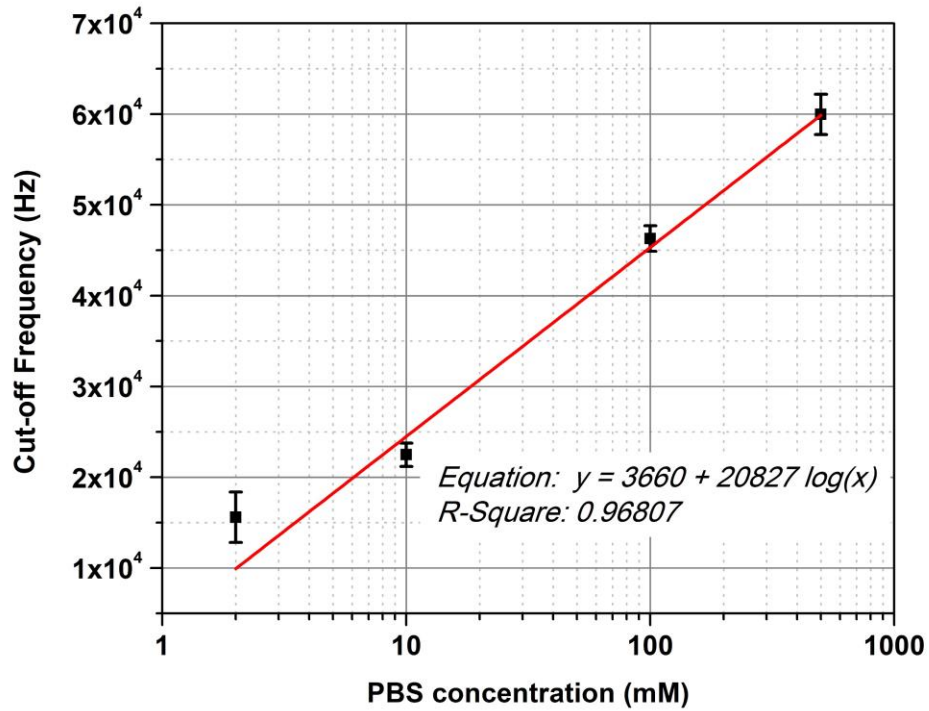Figure 6-7 Impedance spectra of a SiNW FET channel

Figure 6-8 Dependence of the cut-off frequency of ISFET spectrum on the concentration of measurement buffers
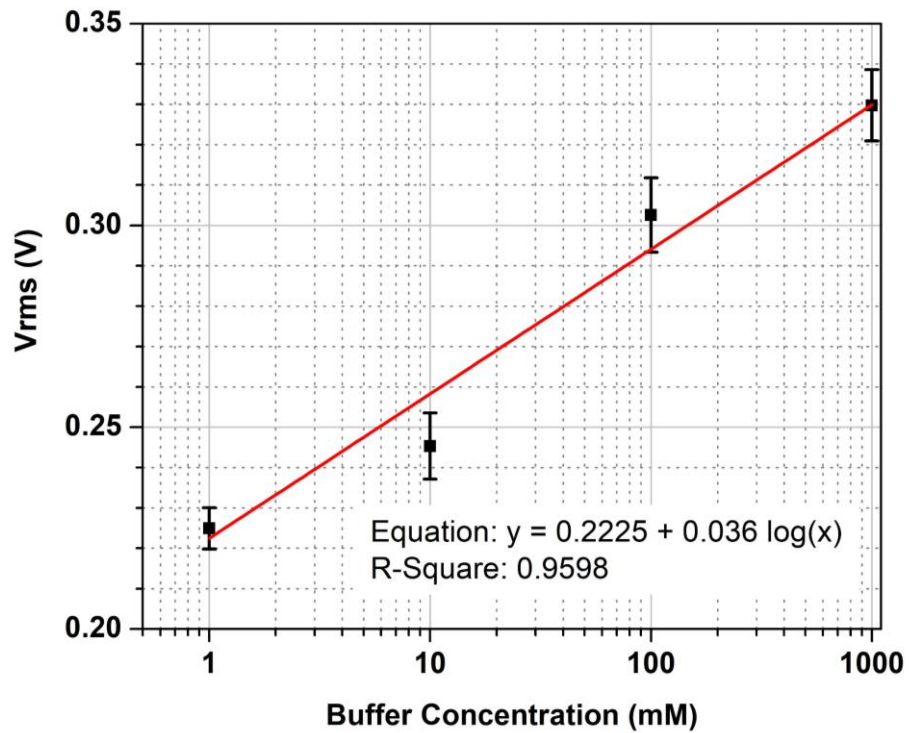

Figure 6-9 Dependence of the resonance amplitude of SiNW FET spectrum on the concentration of measurement buffers

The response of the impedance spectrum of SiNW FET channels to the variation of solution conductivities is different from those of ISFET sensors. The clear difference interestingly happens at a certain frequency and only the pitch point varies as the concentration changes. The reason may be that the coupling between the SiNW FET and the first amplifier stage of the transimpedance creates a resonance at a certain frequency that does not depend on the conductivity of the buffer solution. The low pass-filter effect is still there in the spectrum; however, it is hidden and leads to different amplitudes of the pitch point at the resonance frequency. In general, as it can also be seen from Figure 6-8 and Figure 6-9, this effect could be exploited in sensor applications when the solution conductivity should be tested.

The AC experiments in this work were done by obtaining the whole impedance spectra (from 100 Hz to 2 MHz) to find the most interesting frequency range. However, once it is found, only this range is investigated with a miniaturized impedance analyzer for a certain application. In addition, a simple platinum reference electrode was sufficient to implement AC measurements at even high conductivity solutions. These will open a big opportunity to realize point-of-care devices for rapid, mobile era with integrated reference electrode.

6.4 Protein Interaction Detection Using SiNW FETs

Many biological signal cascades include proteins and protein interactions and these are also important in many practical applications such as pathogen detection, environment monitoring, medical diagnostics and biomedical research [187]. As a proof-of-principle demonstration of the protein detection capability of the setup in both impedimetric and potentiometric methods, biotin-streptavidin binding experiments were implemented. Streptavidin is 52.8kDa protein that is composed of four identical units. It is purified from the bacterium Streptomyces avidinii [188]. Biotin is a water-soluble, small molecule with the weight of 244.3Da that is also called B vitamin. Biotin is important for many biological processes, including cell growth, the production of fatty acids, the metabolism of fats, amino acids, and glucose [189]. It is therefore essential to maintain a healthy digestive and cardiovascular function. Biotin can be found in most foods and biotin deficiencies are rare. The binding of streptavidin and biotin is the strongest non-covalent interactions known in nature. Each streptavidin has four binding sides for biotins. The streptavidin-biotin interaction is highly specific and has a rapid on-rate. In addition, it is resistant to changes in temperature or pH, and to the presence of organic solvents such as DMSO [190]. This makes it an ideal model for demonstration of protein sensing applications.

Figure 6-10 shows the individual steps of implementing the biotin-streptavidin experiments. At first, SiNW FET sensors are cleaned and activated by Piranha acid to obtain a high density of hydroxyl groups on the silicon dioxide surface. Then the chips are put under a vacuum condition (0.6 mPa) with the evaporation of (3-Aminopropyl) triethoxysilane (APTES) at 70ºC in two hours to form a thin amino silane layer on SiNW surface. These amino groups will covalently bond to a linker molecule (Sulfo-NHS-LC-LC-Biotin (Thermo Fisher Scientific Inc.)) during the

immobilization process. Streptavidin proteins (Sigma-Aldrich Inc.) will then bind to the biotin. The biotin molecules are not charged at neutral pH of the solution. Streptavidin is a protein that has an isoelectric point (pI) of 6.4-7. At a pH below the pI, streptavidin carries a net positive charge; above the pI it carries a net negative charge. In the much larger biomolecule, the charges are unevenly distributed.
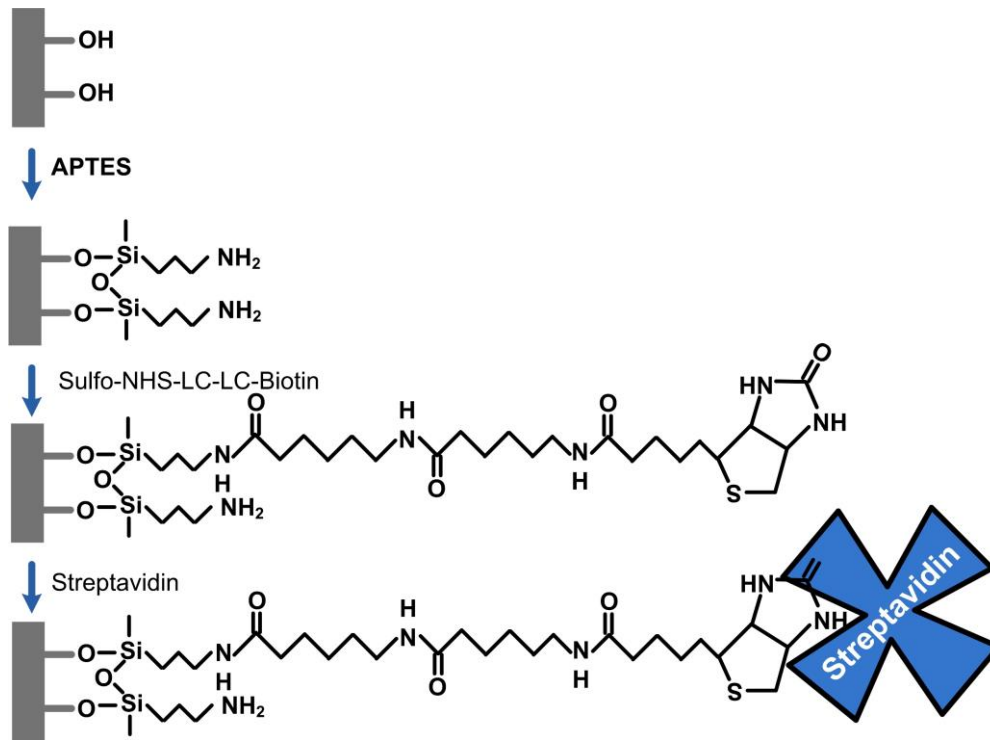
Figure 6-10 Biotin-streptavidin experimental procedures

The transfer characteristics of the devices were measured after the silanization, biotinylation and streptavidin binding. All measurements were implemented with the 0.001× PBS solution at pH 7.5. In this case, streptavidin is negatively charged, and biotin is not charged (Figure 6-11). After immobilization of biotin, the characteristics curve is almost not changed, while after streptavidin binding the curves move to the right side. This is caused by the negative charges of the streptavidin molecules on the p-type FET devices.

To further investigate the effect of the Debye screening, the measurements with different ionic strength solutions (1 mM, 10 mM, 100 mM and 1000 mM PBS solutions) were implemented. As the ionic strength of the buffer solution increases, the Debye length decrease. Therefore, the effect of streptavidin on the device characteristics is reduced and the curve moves to the higher absolute threshold region (Figure 6-12).
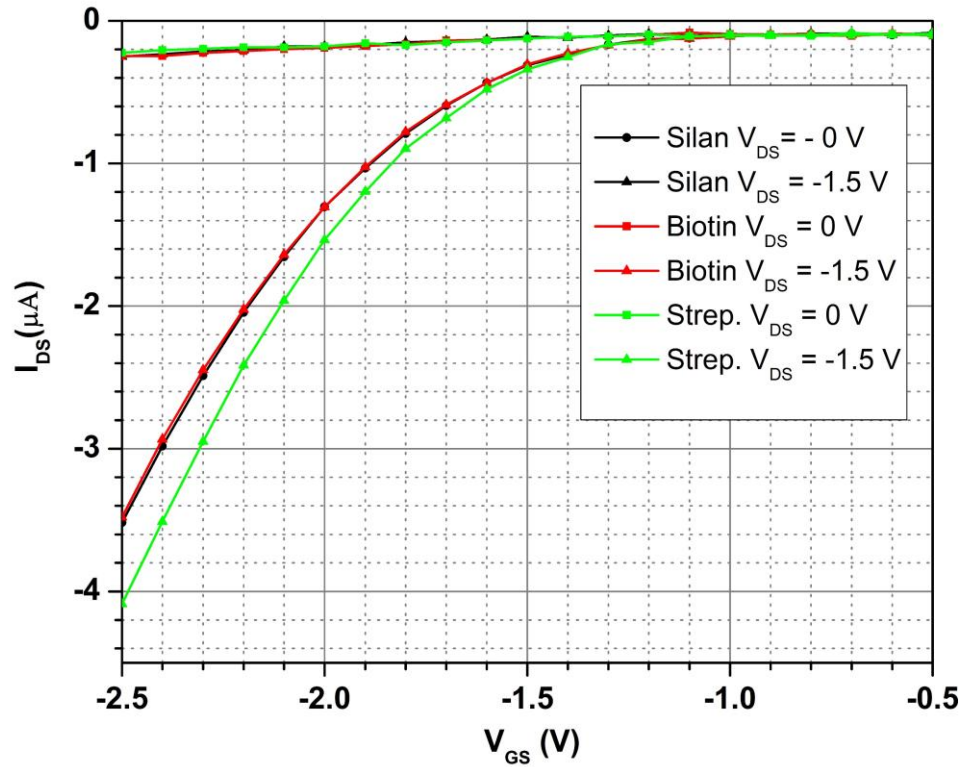
Figure 6-11 Biotin-streptavidin measurement with SiNW FETs in potentiometric mode
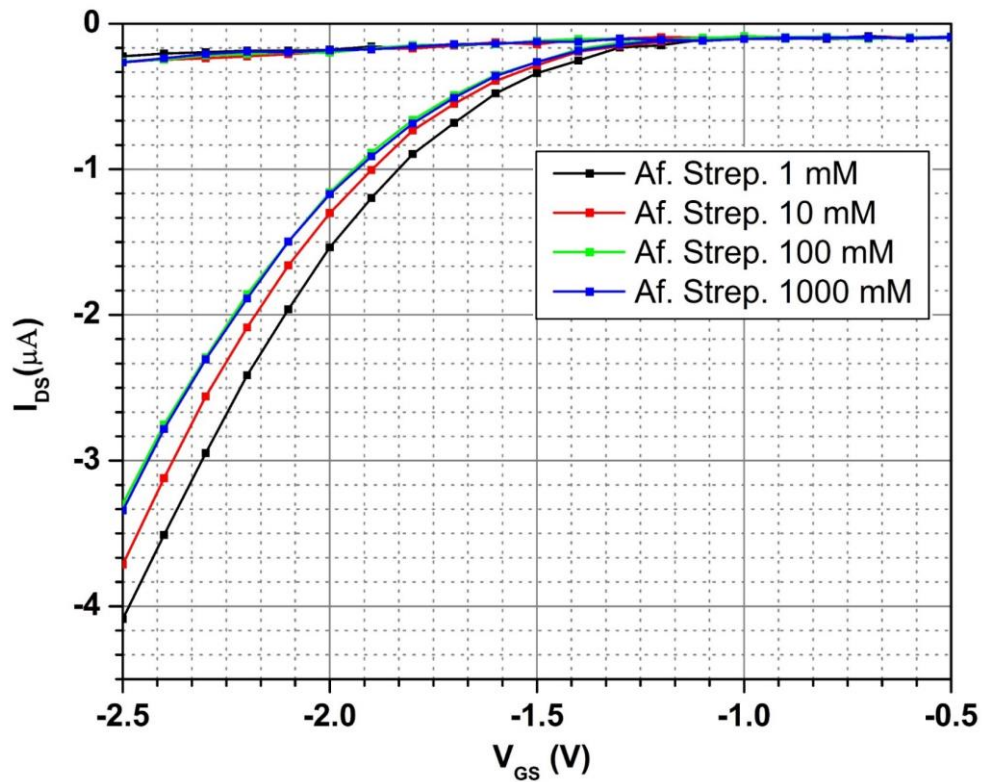
Figure 6-12 Effect of Debye screening on DC measurements with biotin-streptavidin binding

Similarly, to the potentiometric measurements, after silanization, biotinylation and streptavidin the impedance spectra were obtained for evaluation. The biotin molecules are not charged and therefore it was not possible to detect them by the potentiometric method. However, they are clearly detectable by the impedimetric method (Figure 6-13). After biotinylation, the resonance point in the impedance spectrum increases, while after streptavidin binding this point decreases. Even though biotin does not carry static charge in liquid, the binding to the chip surface modify the sensing membrane or the effective oxide capacitance. This leads to a change in the impedance spectrum in the Figure 6-13. The experiment shows the advantage of the impedimetric mode compared to the potentiometric mode in detecting non-charge molecules in bio sensing applications.
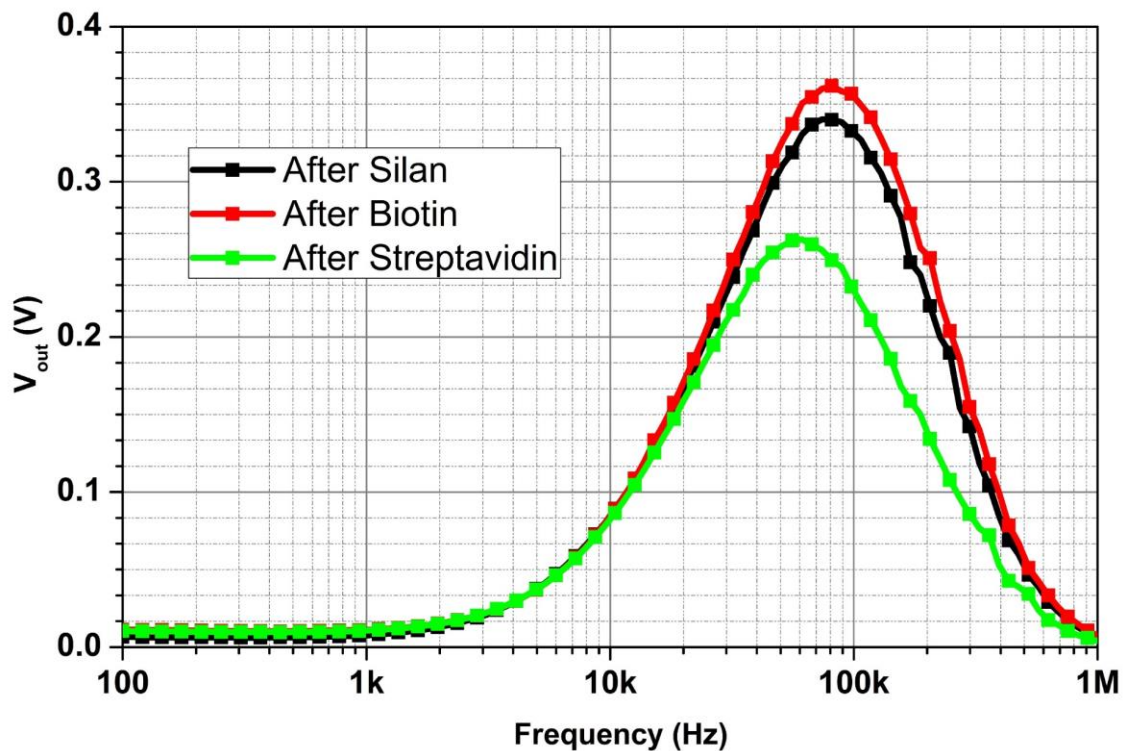
Figure 6-13 Detection of biomolecules by the impedance spectra method (with 1 mM $\times$ PBS solution at pH 7.5)

7. SPICE Model for SiNW FET Sensors

In this chapter, a PSPICE simulation model for SiNW FET sensors was developed with the help of former models for microsized ISFET available in literature. It was possible to adapt the model for the SiNW FETs. In the model in this thesis – as opposed to the available models – also parasitic parameters and device variations resulting from the in-house processes of the available devices were considered. The SiNW FET model was structured as a combination of two separate stages: an electronic stage and an electrochemical stage, which will be discussed in detail in the following sections. The model simulated successfully the pH experiments as they were discussed in chapter 6 and it was further used to investigate the effect of different parasitic parameters for impedance recording with SiNW FETs.

7.1 SiNW FET-Based Macro Model
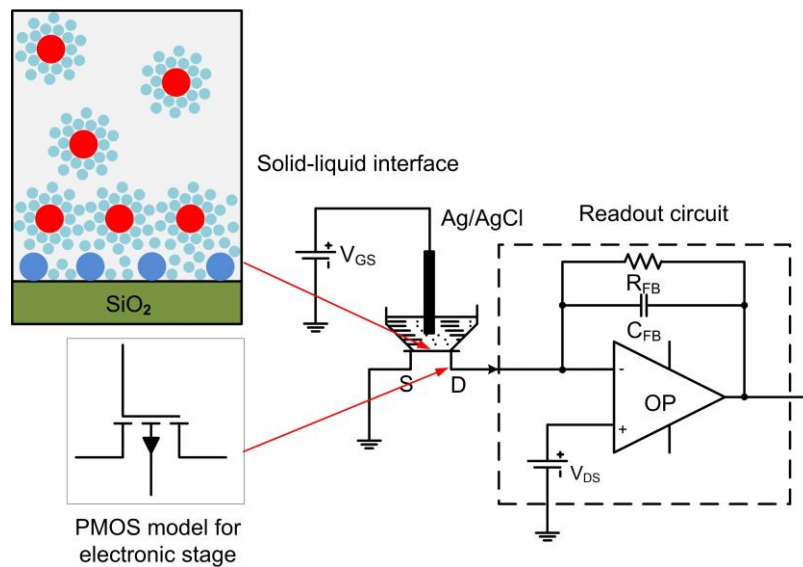
Figure 7-1 The SiNW FET sensor model was divided into two stages: an electrochemical stage for the electrolyte-insulator interface and a PMOS model for the electronic stage

The development of FET-based biosensors requires the knowledge from multi-disciplinary research fields that include solid-state physics, biology, electrochemistry, electronics, and modeling. It is very important in many biosensor applications to apply an accurate model of the device in combination with an additional model part for the electrolyte-electrode interface. Thus, the optimization and improvement of the complete biosensors performances can be accomplished. Many previous publications are describing models for microsized FET sensors [191–194]. This chapter will focus on the simulation of SiNW FET biosensors. Although various approaches to fabrication and application of SiNW sensors were published [45,57,59,83,144,195], a general model for biosensor applications still needs to be developed to fully describe the performance of SiNW FET-based biosensors. In this thesis, a behavioral PSPICE model was applied, which was

also suitable to simulate the frequency domain electrical measurements. The basic model is divided into two main stages: an electrochemical stage for the electrolyte-insulator interface at the gate input and an electronic stage as a MOSFET, which represents the starting structure of the SiNW FET sensor.

7.1.1 PMOS Model for the Electronic Stage

All sensors utilized in this thesis show a p-channel FET characteristic. Figure 7-2 displays a cross section of a SiNW FET-based sensor and the SiNW itself. As described in chapter 4, the FET devices have around 40 nm thickness of active Si layer and 400 nm thickness of the buried oxide (BOX) on a silicon-on-insulator (SOI) wafer. A gate voltage V_{GS} is applied to the sensor via a commercial Ag/AgCl reference electrode that is dipped into the electrolyte. A 6-nm thick dry thermal silicon oxide at the sensing gate is isolating the active Si from the electrolyte.
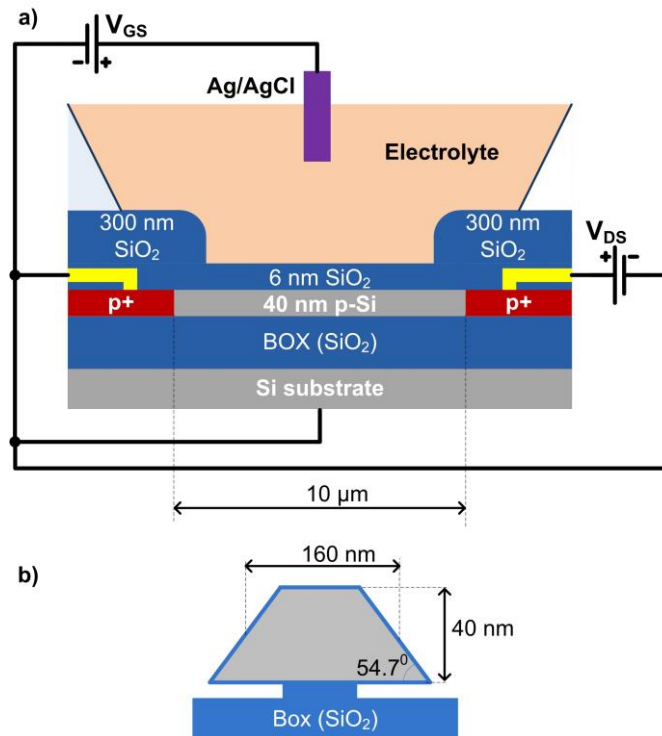
Figure 7-2 (a) Schematic showing the cross section of SiNW FET biosensor. (b) Cross section of a single SiNW (width = 160 nm, wire thickness = 40 nm, length = 10 µm)

The first approach for the SiNW FET modeling developed in this thesis was based on the standard MOS FET model level2 in PSPICE with some modifications for the SiNW FET case. The reason of firstly using the level2 model was that it was previously developed for an earlier generation of ISFET sensors [143]. Using this much simpler model might not be the best choice, however, it helped for basic investigations in the beginning of this thesis work. It is included here, since it was also the basis of a first publication in the framework of this thesis [84]. In addition, since the SiNW FET sensors can be regarded as long channel FET devices, which do not suffer from short channel effects, the simple FET model level2 (the Grove-Frohman model [196,197]) is an appropriate

approach. Moreover, one can take advantage of ISFET models including descriptions of the solid-liquid interface already built in other publications [126,193]. The basic level2 model for the SiNW FET devices was composed such that it inherited from previous models for ISFET devices [143,198] accounting for the similarities in SiNW FET and ISFET sensor fabrication processes. The following parameters were obtained only for SiNW FET cases:

- The 'effective' width to be included in the FET model should combine the whole surface of the nano wire in contact with the liquid. For example, a single nanowire with a lateral width of 160 nm (Figure 7-2 b) has then an 'effective' width of about 330 nm.

- Because of the differences in contact line dimensions, in the highly doped drain and source contacts and in the formation of ohmic contacts between the metal aluminum and the doped silicon, drain and source resistances were added accordingly.

- The thermal oxidation process led to a thinner oxide layer and therefore the threshold voltage was smaller compared to the ISFET case. The threshold voltage in the simulation model was obtained from transfer characteristics measurements of the sensors with the standard measurement devices.
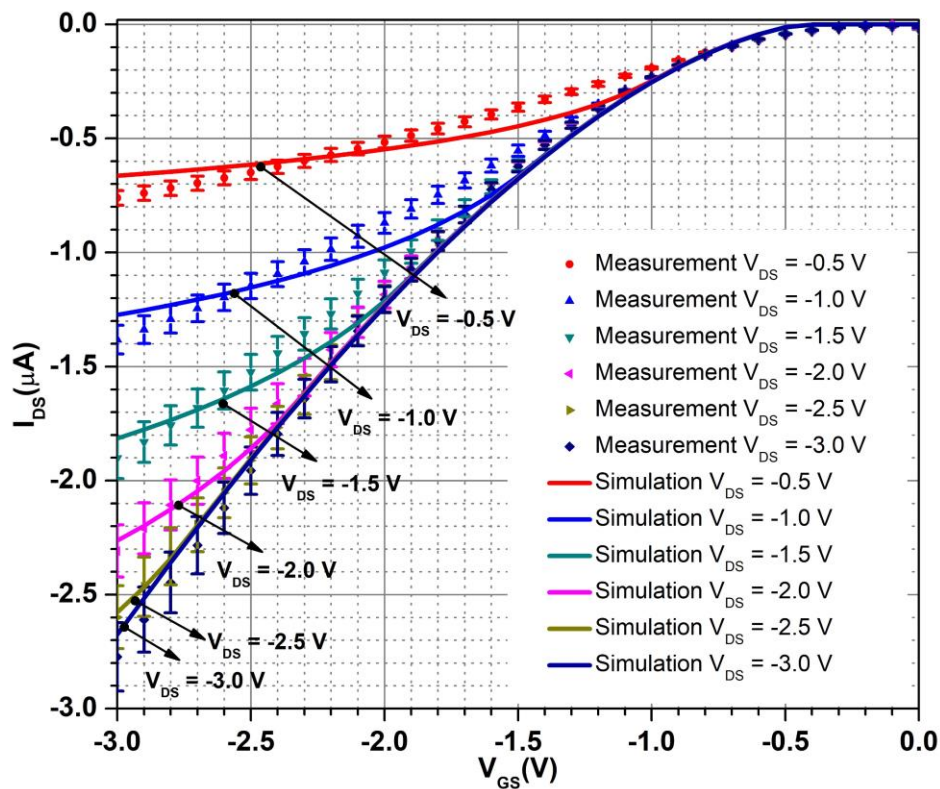
Figure 7-3 Characterization measurements and simulation of a SiNW FET transfer characteristics (symbol plots: experimental data as average from n = 3 devices, solid plots: PSPICE simulation data) [84].

The level2 model was implemented for characterization measurements with 2×10 SiNW: 200 nm width, 10 µm length. Figure 7-3 shows the measurements of the 2×10 SiNW FET sensors and the respective simulation results at 20°C. The channels were biased at the drain-source (V$_{DS}$) and gate-source (V$_{GS}$) voltages from 0 V to -3 V with steps of -0.5 V and -0.1 V, respectively. Figure 7-3 shows a difference between experimental and simulation data. The cumulated error between the simulation results and the experimental data was quite high with 12.4% [84]. This error was calculated by averaging the differences in percentage between simulation and experimental results of the sensors characteristics. The error might come from the reason that the level2 MOSFET is not a perfect choice for the SiNW FET simulation. In this model, the mobility was assumed to be constant with the applied voltage, which does not agree with the experimental data; a reduction in mobility with an increase in the gate voltage is observed [197].

A more precise approach in simulation of the SiNWs is to utilize a more sophisticated FET model (the BSIM3v3 MOSFET level7 in PSPICE), that is based on physical parameters of fabrication processes such as gate oxide thickness, junction depth, and doping concentration, etc. Today, most advanced semiconductor foundries and integrated device manufacturers utilize a professional software such as the Integrated Circuit Characterization and Analysis Program (IC-CAP) for DC and RF semiconductor device modeling. It provides a complete solution from the instruments connection, measurements automation, model parameters extraction and statistical analysis tools. Because of a general limitation in accessing these tools for this thesis work, most of the parameters in the standard BSIM3v3 SiNW FET model were obtained from the IC-CAP SPICE default values for PMOS [199]. The following main parameters were then adapted to describe the SiNW FET sensors in this work:

- The widths of the SiNW FETs were mask designed of 200 nm and 400 nm, respectively. However, the actual widths were then defined by the TMAH etching process. For example, they are expected to vary in the range of 120 nm to 180 nm in the case of 200 nm mask design depending on etching times. The 'effective' width is then the combination of the whole surface of the wire in contact with the liquid leading to an almost wrapped around gate configuration (Figure 7-2 b)

- The SiNW FET channel is the whole wire (fully-depleted case), therefore the junction depth (XJ) was assumed to be the thickness of the SiNW. This thickness was defined by the thinning out process of the top silicon device layer (from 360 nm to its initial thickness down to 40 nm – 60 nm depending on the process).

- The gate oxide was obtained from the dry oxidation at high temperature (820°C) under a pure oxygen atmosphere. This process induces a slow growth of a layer of silicon dioxide with high density. The thickness of this layer varies from 5 nm – 8 nm in the applied processes. It is important to note that not only the thickness is important, but also the quality

of the oxide layer plays an important role in the device performance. In the practical work, this thickness was characterized by spectroscopic ellipsometry and TEM microscopy [64].

- With the formerly fabricated devices, in this thesis output and transfer characteristic measurements were implemented to obtain the threshold voltages of the devices. The threshold voltages varied from -0.3 V to -0.5 V for all devices used in this work.

- NCH, the peak doping concentration inside SiNW, was assumed to be homogeneous for the model and its value was acquired from the datasheet of the p-type SOI wafers of $1*10^{17}$ (atoms/cm^3). The details of the fabrication processes and corresponding characterizations can be found in another work [64].

- There are, however, several parameters, that could not be obtained with the setup available during this thesis work and were therefore estimated from an expected scaling out of the fabrication process. These parameters are related to the mobility and the maximum velocity of the carriers. The summary of the customized parameters and their tolerance ranges can be found in Table 7-1. The default parameters of the BSIM3v3 model can be found in detail in the appendix C.

Table 7-1 BSIM3v3 simulation parameters that were adapted for the SiNW FET sensor case (parameters were Gaussian-distributed ±4σ)

	Parameter	Default value	Simulation	Range	Units
1	Width	-	160E-09	140E-09 – 180E-09	m
2	XJ	150E-09	50E-09	40E-09 – 60E-09	m
3	TOX	15E-09	6E-09	4E-09 – 8E-09	m
4	VTH	-1.0	-0.4	-0.3 – -0.5	V
5	NCH	1.7E17	1.0E17	-	1/cm^3
6	U0	250	115	-	cm^2/(Vs)
7	VSAT	8.0E6	0.8E+05	-	cm/s
8	A0	1.0	-0.5	-	-
9	A2	0.08	1.08	-	-

Width	: width of the SiNWs
XJ	: Junction depth = thickness of the SiNWs
TOX	: thickness of gate oxide
VTH	: threshold voltage of the SiNW FET sensor
NCH	: doping concentration near the interface
U0	: carrier mobility
VSAT	: Saturation velocity

A0   : Bulk charge effect coefficient

A2   : Second non-saturation factor
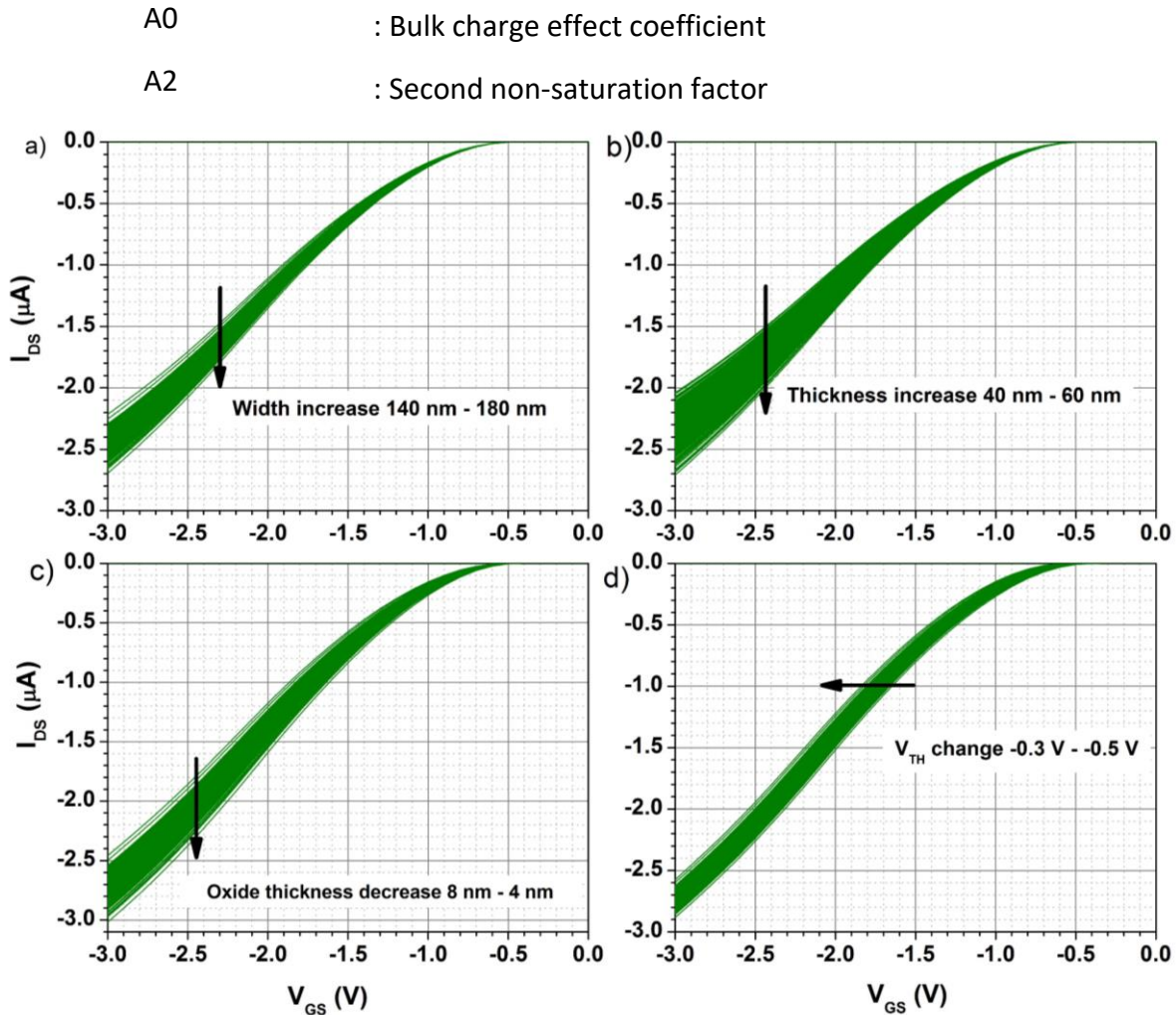
Figure 7-4 Effect of different fabrication process parameters on the transfer characteristics by simulation of SiNW FET sensors at V_{DS} = -2 V: a) SiNW width effect, b) SiNW thickness effect, c) Gate oxide effect, d) effect of the threshold voltage V_{TH}

There are four main parameters that were identified from the fabrication processes: wire width (width), wire thickness (XJ), thickness of the silicon oxide insulator on the gate surface (TOX) and threshold voltage (VTH). To see the variation in the transfer characteristics of the sensors as the parameters used in the PSPICE simulation deviate from their nominal values, a 500 runs Monte-Carlo simulation on the resulting I_{DS} was implemented. The parameters varied between their specific tolerance limits according to the Gaussian distribution. Figure 7-4 shows different effects of these four main parameters on the characteristic simulation at V_{DS} = -2 V and V_{GS} sweeps from 0 V to -3 V with the step of -0.1 V. In each simulation the parameter under investigation was varied, while others were kept constant at the nominal values. On the other hand, Figure 7-5 depicts the simulation result of the sensor characteristics when all four parameters were varied together (the grey curves). The experimental results of three typical SiNW FET channels of the dimension of

2×10 (200 nm width × 10 µm length) are ranging in the Gaussian distribution of the Monte Carlo results. One can see that thickness and width have the highest influence on the resulting I_{DS} values. These parameters are defined from the processes of the nano imprint lithography and TMAH etching. In a larger scale industrial fabrication, this variability could be significantly reduced applying other, more precise fabrication methods.
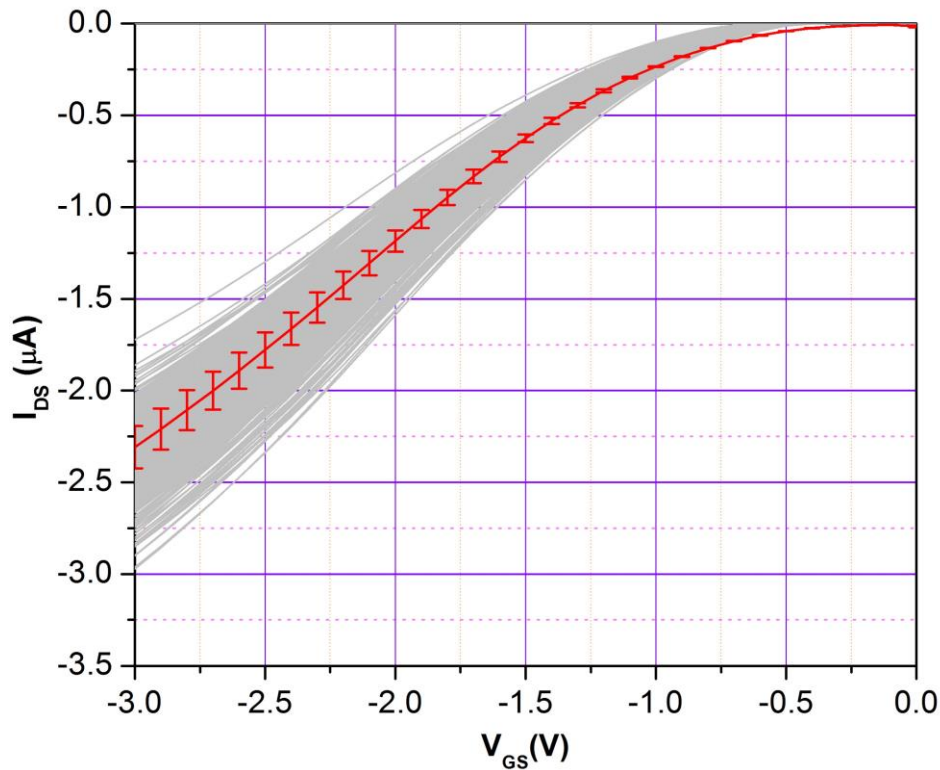
Figure 7-5 500 Monte Carlo runs to simulate the transfer characteristic curves (grey), when all four main parameters were varied within their tolerances with Gaussian distribution (±4σ). The measurement results of three channels of a typical 2×10 SiNW (red) chip are ranging within these variations (More simulation results with other SiNW dimensions can be found in the Appendix D)

[2]One additional parameter, which was found to be very important to fit the shape of the transfer characteristic curves of the SiNW FET, was the bulk charge effect parameter (A0). This parameter, which is only accessible in the level7 model, could mimic an additional change in the charge carrier concentration inside of the transistor channel. It was then utilized to account for a "steepness increase" effect for DNA experiments as discussed below [200]. In Figure 7-6, a comparison of the

---

[2] The following results were obtained in a collaborative work in the framework of this thesis together with another doctoral student [204]. Results were published, whereas the discussion of the effects are differing here due to a former confusion of the nanowire dimensions. A correction of this article was already submitted to the journal.

fitting result for the level7 and the level2 models is shown. These devices in this case can be considered as long-channel transistors and the model level 7 can represent the device characteristics more faithfully compared to the level2 model. Most importantly, this model includes narrow channel effects as well as the bulk charge effect parameter, which was used to simulate the SiNW devices. The transfer characteristics at different V_{DS} bias conditions fit much better in terms of both steepness and shape.
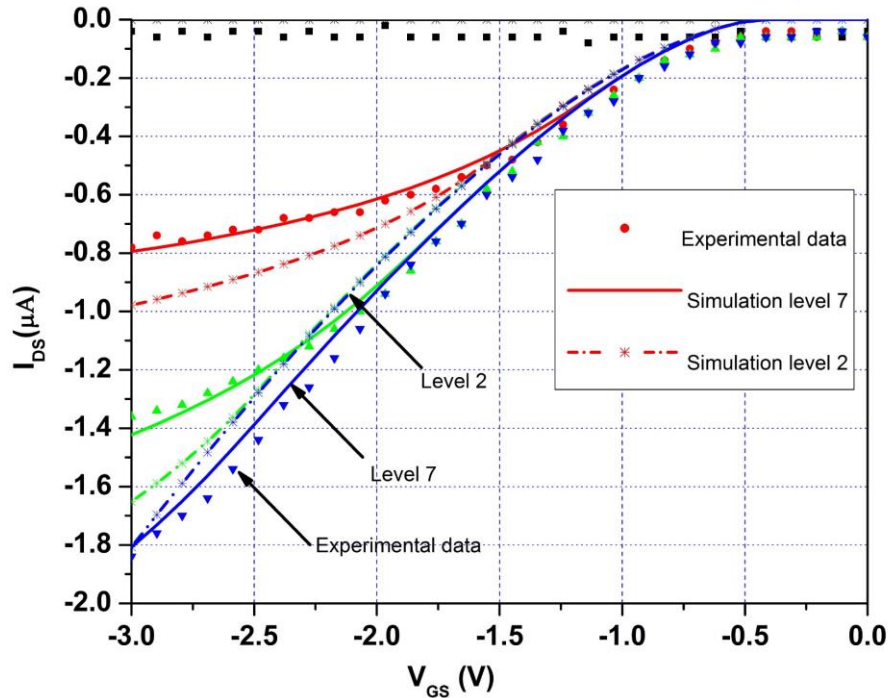
Figure 7-6 Comparison of employing two different FET models (level2 and level7) for an exemplary SiNW sensor (SiNW 200 nm × 10 µm in this case).

To clarify the impact of this bulk charge effect parameter to the transfer characteristics, a theoretical curve of a p-channel FET is qualitatively shown in Figure 7-7. When the threshold voltage is increased in the model, which is equivalent to a shift of the V_{GS} voltage (front gate/ reference electrode voltage), the transfer characteristics shifts to more positive voltage values, inducing more negative current in the device. This can be done by changing part 1 in the model, which represents the biological membrane. This would account for the traditional sensing mechanism of ISFET, which is used for pH sensing or potentiometric detection of charged biomolecules. If the effective carrier density in the transistor channel is increased in addition by varying the bulk charge effect coefficient, the slope of the curve increases, leading to even more negative currents. This parameter is only accessible in the level7 MOSFET model and is contained in the electronic stage of the new model. It was previously reported that the size [201], the surface modification on the nanowire [116], different buffer pH-value [144,202], different Debye lengths [70], as well as the distance of the charged DNA sequences to the surface of the nanowire, can all influence the field-effect, and therefore the sensitivity of the device [203].
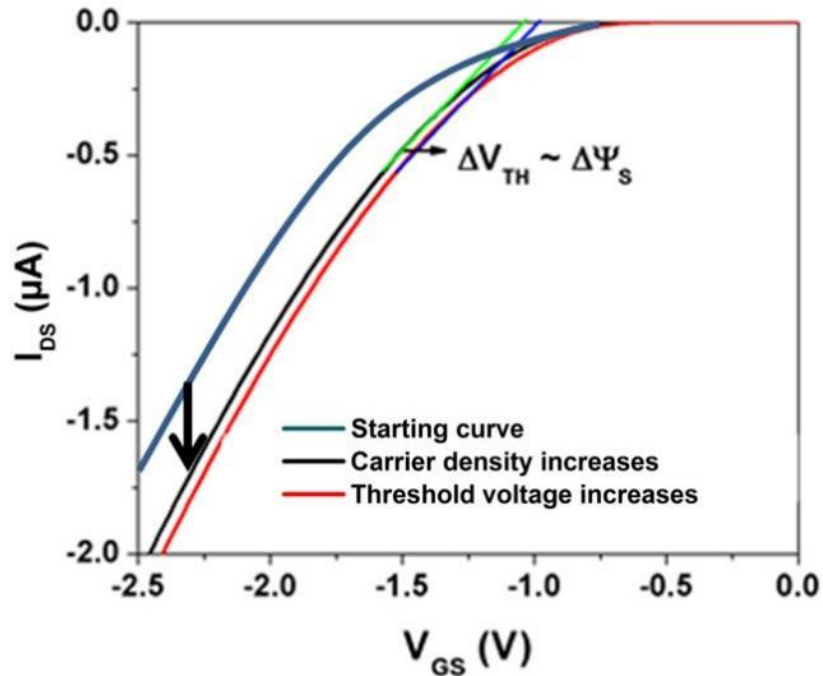
Figure 7-7 In both parts of the model the biological TC characteristics can be changed as indicated in this plot. The shift in V_{TH} is realized by the membrane effect in the model. A change in steepness of the curve can only be achieved, when the charge carrier density inside of the wire is increased in addition [200].

Experimental results are presented for the potentiometric detection of captured DNA immobilization and hybridization with complementary target DNA. The transfer characteristics (TC) of the SiNW FETs are displayed before and after the molecules are bound to the surface. In addition, the obtained signals of two different nanowire dimensions are compared. It was found that the TC characteristics after two different steps was becoming steeper in the smaller nanowire, in contrast to the wider one, where the shift of the TC characteristic was regular like in ISFETs. The influence of different buffer concentrations on the sensitivity of the SiNW FETs was also investigated, and exhibited the well-known Debye-length screening effect [200].

To explain the change in TC steepness in the assays, it is reasoned that the increase in charge carrier concentration might come from the narrow-channel effect when the nanowire gets smaller. Therefore, experiments on devices with different nanowire width were performed to compare the received signals. Unfortunately, only two different nanowire width structures – 200 nm and 400 nm – were available with the same length of 10 µm (mask width measurement). In the experimental procedure, both nanowire devices were treated in the same way. The results after the silanization and immobilization step are compared in Figure 7-8. In Figure 5-12a, the results for an exemplary measurement on a chip with nanowire width of 400 nm (4×10 chip) can be seen. In Figure 7-8 b, the TC characteristics of a smaller wire of 200 nm (2×10 chip) is presented. It can clearly be seen that the effect of immobilization of 20 bp capture DNA strands is distinctly different for the two

nanowire structures. In order, not to draw conclusions from a one-time experiment, a statistical evaluation was implemented by calculating the change in V_{TH} at two different I_{DS} values: in the smaller nanowire, the shift in V_{TH} was bigger at lower I_{DS} values than at higher I_{DS} values (Figure 7-8c). In the 4×10 chips, the change in V_{TH} was also different at different I_{DS} values, but this difference was not as high as in the smaller 2×10 nanowire devices. To make this more obvious, linear fits to these characteristics were done to emphasize the different effects.
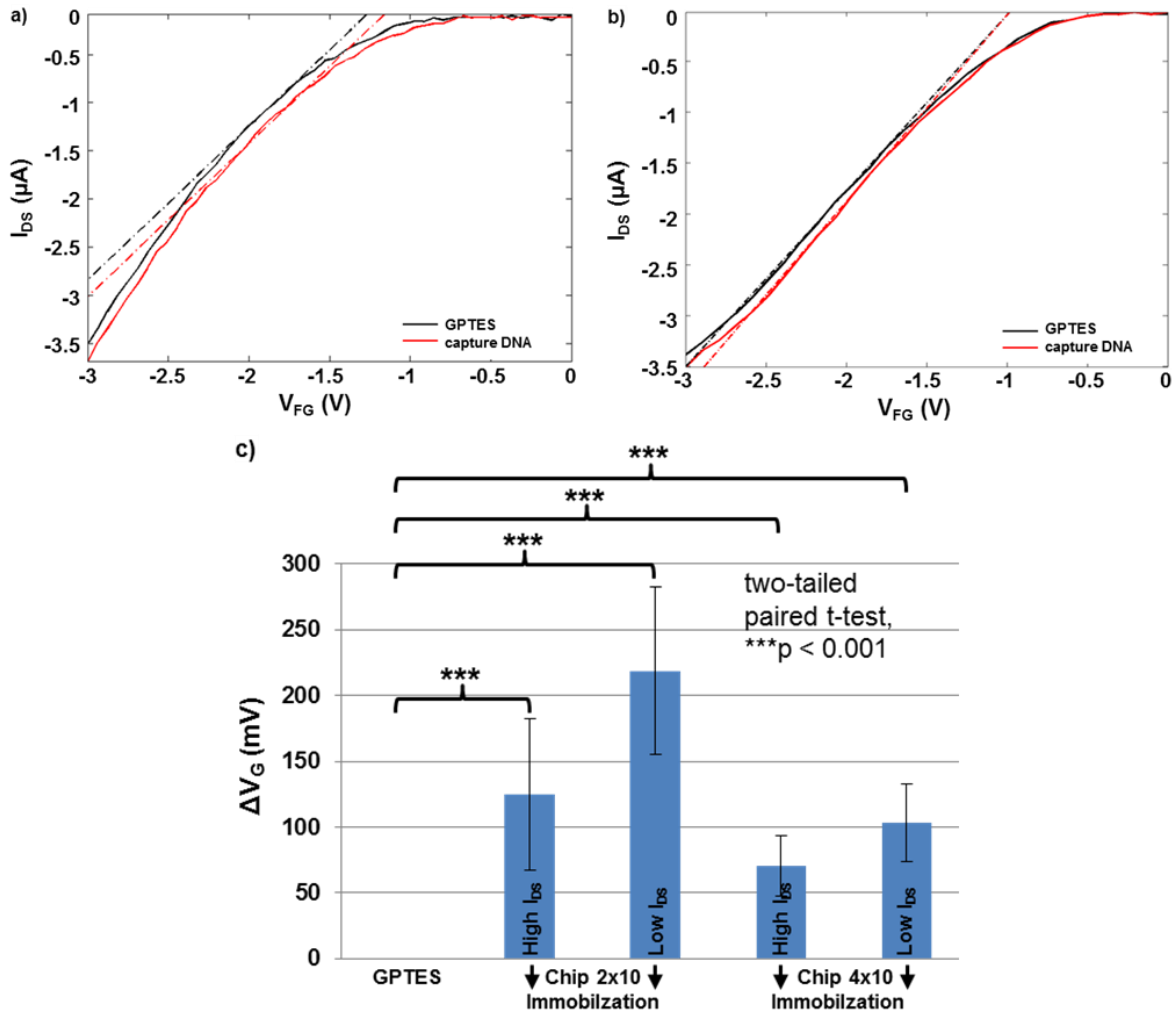
Figure 7-8 The TC characteristics obtained after silanization (black) and immobilization (red) are shown for a 4×10 chip (a) and a 2×10 chip (b). Moreover, a linear fit was done and included in the figure to emphasize the differences in TC shape. As it can be seen, the shift of the TC characteristic of a SiNW FET with wider nanowires seems to be parallel, whereas an additional steepness increase was observed, when narrower wires were used. By investigating many measurements this observation was confirmed (c) (n = 28 for chip 4×10 and n = 13 for chip 2×10) [204].

In Figure 7-9 the simulation of a narrower SiNW FET can be seen. The change in the transfer characteristics steepness upon DNA binding to the SiNW FET surface can be modelled by an artificial increase in carrier density in the structure. However, to work out this assumption, more systematic experiments need to be done with varying nanowire sizes in future works.
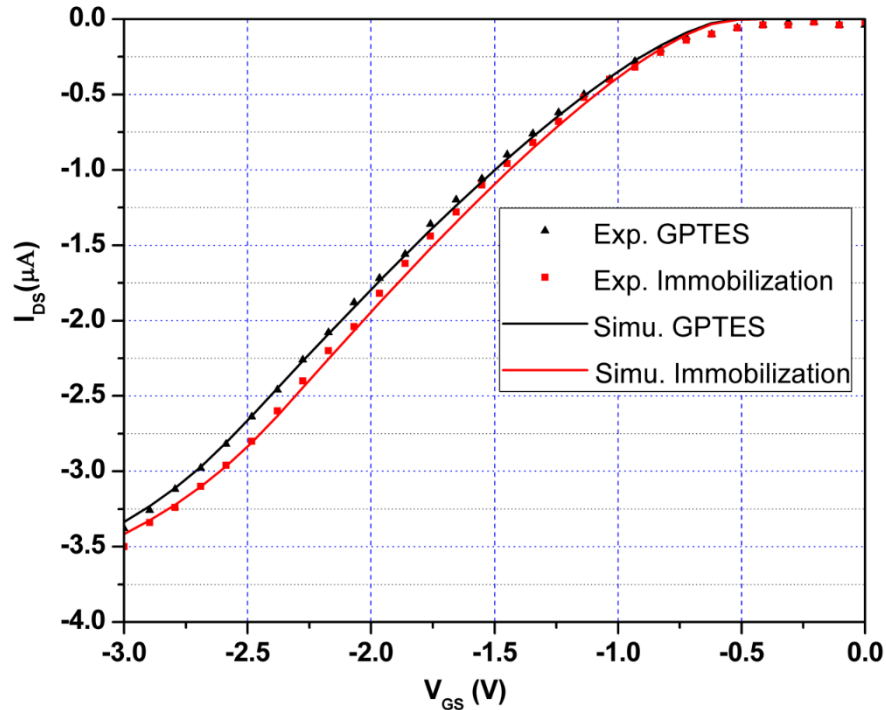
Figure 7-9 Simulation of the steepness effect in the TC characteristics. As discussed before this effect can be seen more clearly in the smaller nanowires (below 200 nm) [204].

As a conclusion of this modeling section, the BSIM3v3 level7 model in PSPICE was better suited than the level2 model, but it is still not the ideal model for the fabricated SOI SiNW FET devices. By artificially modulating the bulk charge effect parameter in the level7 model, a resulting "higher I_{DS} change" with thinner wires can be worked out. However, it would be more appropriate to use a full SOI device model such as BSIM-SOI to fully simulate the effects. Unfortunately, this simulation software was not accessible during this thesis work. The simplified simulations in the level7 model presented in this thesis are one step towards a better understanding of the detection mechanism of the devices. Eventually this additional steepness effect might also scale with even smaller nanowire width, which might be a possible explanation for the enhanced sensitivity of SiNW FETs compared to ISFET devices, which was previously reported in many publications in the field [201].

7.1.2 Electrolyte-Insulator Interface Modeling
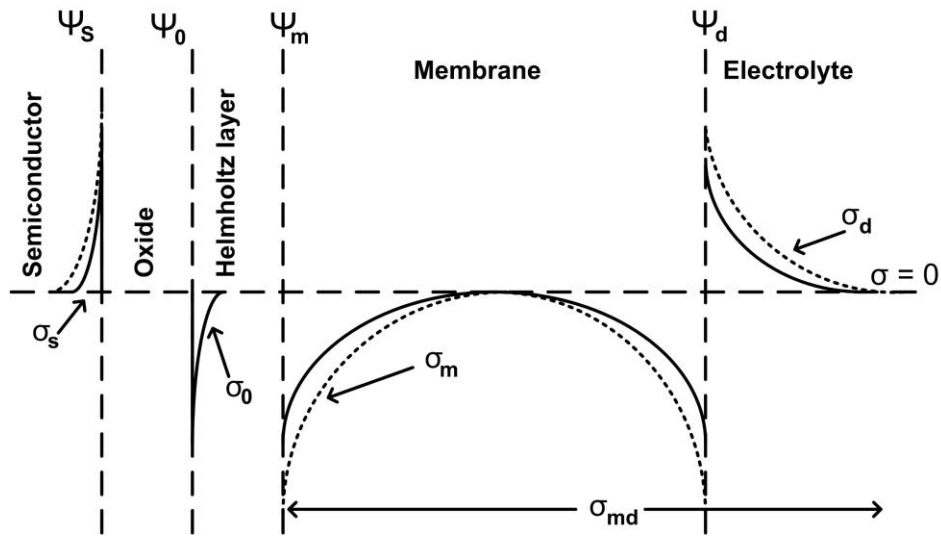
Figure 7-10 Solid lines show charges in the top channel of the FET structure and the oxide–electrolyte interface, which include the semiconductor charge σ_s, site binding charge σ_0, the charge throughout a, in this example, negatively charged membrane σ_m, and the Gouy-Chapman/diffuse layer charge σ_d at physiological pHs with applied potentials. Dashed lines show the impact of adding more charge to the membrane, which takes place after a binding event (adapted from [126])

As discussed in chapter 3, the shift controlling parameter of the ISFET and SiNW can be described in terms of the threshold voltage. From various terms in the expression of this voltage, the voltage drops at the insulator-electrolyte interface is what decides the sensitivity of the device to the analyte in the solution. The oxide-electrolyte interface includes a Helmholtz and Gouy-Chapman layer together with a membrane layer between these two. Figure 7-10 illustrates the charge distribution over the semiconductor/oxide-electrolyte interface [126]. The site-binding theory developed by Yates et al. [111], that is based on the chemical reaction of Hydrogen ions in the electrolyte and Hydroxyl groups on the surface of the oxide layer, describes the surface charge density of the oxide or site-binding charge σ_0. The second layer, that carries the charge density of σ_d, is made of mobile ions in the electrolyte forming the Gouy-Chapman or diffusion layer. The ion-permeable membrane model that is presented between these two layers was firstly introduced by Ohshima [205]. That model united two different theories of the Donnan potential and the surface potential to describe the electrical potential distribution of a charged biological membrane (σ_m) in an electrolyte solution. The membrane can be a layer of DNA or protein that binds to the oxide surface of the FET devices. A silanization process (gas phase or liquid phase) generally creates a layer of commonly used (3-aminopropyl)-triethoxysilane (APTES) or (3-Glycidyloxypropyl) trimethoxysilane (GPTES). Then a biological membrane layer attaches to this silane layer. This model gives a representation of the DNA or the protein layer in potentiometric detection mode with

FET devices, where ions in the electrolyte can enter the membrane; thereby the potential distribution undergoes a smooth transition from Donnan potential to the surface potential. In this model, the mobile charges are considered as point charges. However, this fails to explain some experimental results, where the ion sizes play an important role [206,207]. Therefore, the Landheer group developed an analytical model based on the Metropolis Monte Carlo algorithm [127,182,208–210] that gave a better agreement between the simulation results and the experimental ones.

The analytical modeling approach with the Monte Carlo method provided a deeper understanding and simulation of different processes and interactions between them [71,209]. However, these approaches contain time-consuming analytical solutions and usually require high computational power. A more detailed investigation into this direction would go a beyond the scope of this thesis. An alternative method is to utilize macromodels to simulate the response of the sensor to different bioassays. They are user-friendly and can be adapted to different models of FET devices as well as different versions of simulation software. This approach is generic and can be used for different experiments without requiring high computational power. The macro model simulation of an ISFET by SPICE [126,193] or of a SiNW FET by Verilog-A [211] was already published in the literature. These models were so far not used for simulation of impedimetric measurements and there is no SPICE model for SiNW FETs available. In the framework of this thesis the level7 BSIM3v3 model as described in the previous section was therefore used in such a generic macro model simulation and embedded into a simulation of the readout circuit to describe the effects observed in impedance recordings with SiNW FETs. For these model descriptions, basically the capacitances in the circuit play a major role.

The chemical model, describing the interface between silicon oxide and the electrolyte, is derived by the site-binding theory and electrical double-layer theory [30,111,193,212]. This model includes the Helmholtz and Gouy-Chapman capacitances (Figure 7-11) in series that are described by equations (73) and (74).

$$C_{Helm} = \frac{\varepsilon_{IHP}\varepsilon_{OHP}}{\varepsilon_{IHP}d_{OHP} + \varepsilon_{OHP}d_{IHP}} \tag{73}$$

ε and d are the symbols for the relative permittivity and the thickness of the inner Helmholtz plane (IHP) and outer Helmholtz plane (OHP), respectively.

$$C_{Gouy} \cong \frac{\sqrt{8\varepsilon_w kTc_{bulk}}}{2V_T} \tag{74}$$

where ε_w is the permittivity of the electrolyte, k is Boltzmann constant, T is the absolute temperature in Kevin, $V_T = kT/q$ is the thermal voltage with q as the electron charge.

In short, a single equivalent capacitor can represent these two capacitors with the value of:

$$C_{eq} = \frac{C_{Helm}C_{Gouy}}{C_{Helm} + C_{Gouy}} \tag{75}$$
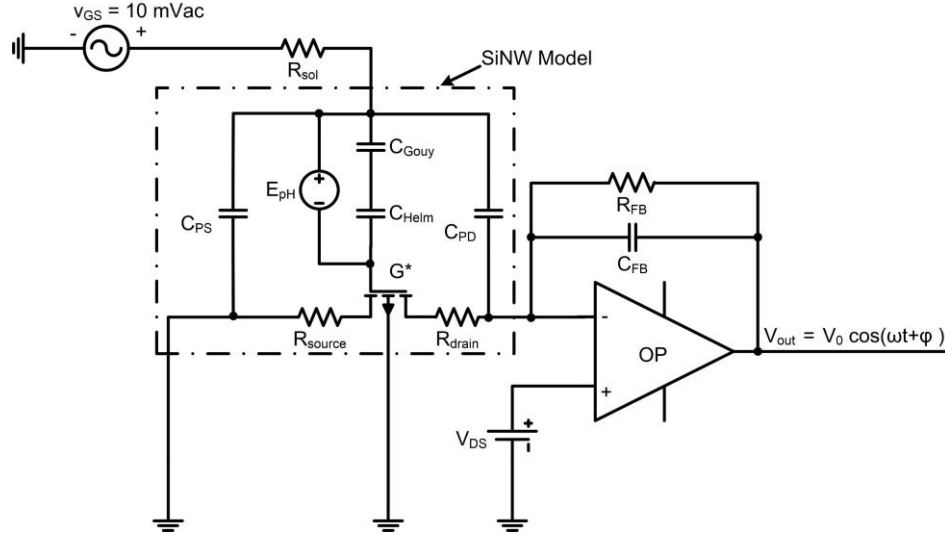
Figure 7-11 Equivalent circuits for a SiNW FET sensor and the transimpedance amplifier for pH-value and solution conductivity measurements as developed in this thesis work.

Yates et al. [111] developed the site binding theory to calculate the surface charge density σ_0 accounting for the binding site density N_{sil}, hydrogen ion concentration in the bulk solution $[H^+]$, the surface potential ψ_0 and the dissociation constants K_a and K_b of the chemical reactions, which can happen at the oxide surface:

$$\sigma_0 = qN_{sil}\left(\frac{[H^+]^2 e^{-\frac{2q\Psi_0}{kT}} - K_aK_b}{[H^+]^2 e^{-\frac{2q\Psi_0}{kT}} + K_a[H^+]^2 e^{-\frac{q\Psi_0}{kT}} + K_aK_b}\right) \tag{76}$$

From equation (75) and (76) the potential of the electrolyte-insulator interface E_{pH}, which is partially dependent on the pH value of the solution, will be:

$$E_{pH} = \frac{\sigma_0}{C_{eq}} \tag{77}$$

This potential will change accounting for the biological interface parameters at the surface of the SiNW FET devices, when operated in liquid-gate configuration.

7.1.3 Simulation Results of pH Sensing
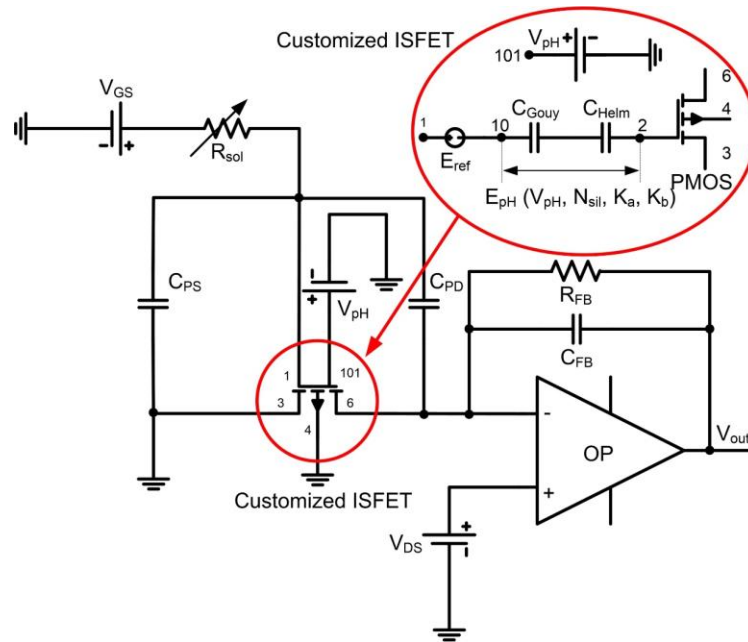
Figure 7-12 PSPICE simulation circuit that combines two stages (PMOS and electrolyte-insulator interface) of the SiNW FET sensor modeling and the readout amplifier circuit.

The developed model was tested, and the simulation results were compared with the experimental data discussed in chapter 6 of this thesis. The model was also used to study the effect of different parameters on the pH sensitivity of the device. Figure 7-12 depicts the PSPICE simulation circuit that combines two stages (PMOS and electrolyte-insulator interface) of the SiNW FET sensor modeling and the readout circuit. It can be seen in the equation (76), that the pH response of the sensor depends on the surface site density (N_{sil}) and on the positive dissociation constant (K_a) and the negative dissociation constant (K_b) of the protonation, deprotonation reaction. K_a, K_b are the surface dissociation constants that are different from the values that are measured in the bulk solution. These constants have different values in the literature and are summarized in Table 7-2. Figure 7-13 shows the simulation results of the SiNW FET sensor with a bare SiO_2 gate surface. The relevant model parameters used to obtain this result are as following: $K_a = 0.1$, $K_b = 63.1*10^{-9}$, $N_{sil} = 5*10^{18}$, t = 20°C. The linear fitted pH sensitivity of the simulation results is 36 mV/pH, which is close to the experimental results of 35.7 mV/pH. It was reported that the sensitivity of bare silicon oxide surfaces is in the range of 30-40 mV/pH [166].

Table 7-2 Literature values of N_{sil}, K_a, K_b constants of SiO_2

K_a (mol/L)	K_b (mol/L)	N_{sil} (#/m^2)	Ref.
10^{-6}	10^2	$5*10^{18}$	[118]
$2*10^{-6}$	$5*10^{-2}$	$5*10^{18}$	[146]
15.8	$63.1*10^{-9}$	$5*10^{18}$	[193]
12.4	$5*10^{-6}$	$5*10^{18}$	[113]
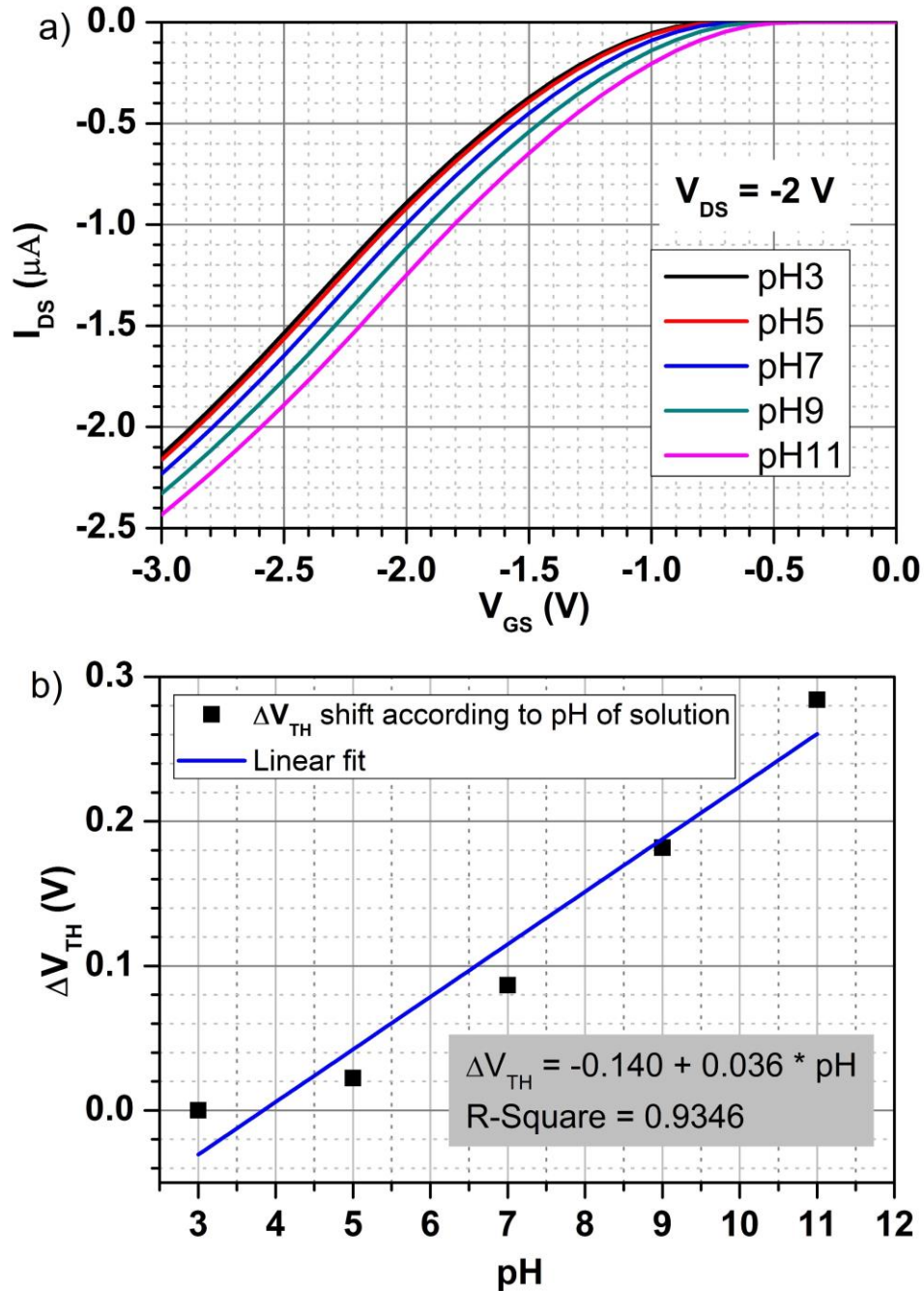
Figure 7-13 pH sensing simulation results of a SiNW FET with bare SiO_2 as gate oxide, $K_a = 0.1$, $K_b = 63.1*10^{-9}$, $N_{sil} = 5*10^{18}$, t = 20°C: a) Transfer characteristic simulation for pH from 3 to 11 at V_{DS} = -2 V. b) Shift of threshold voltage caused by the variation of pH
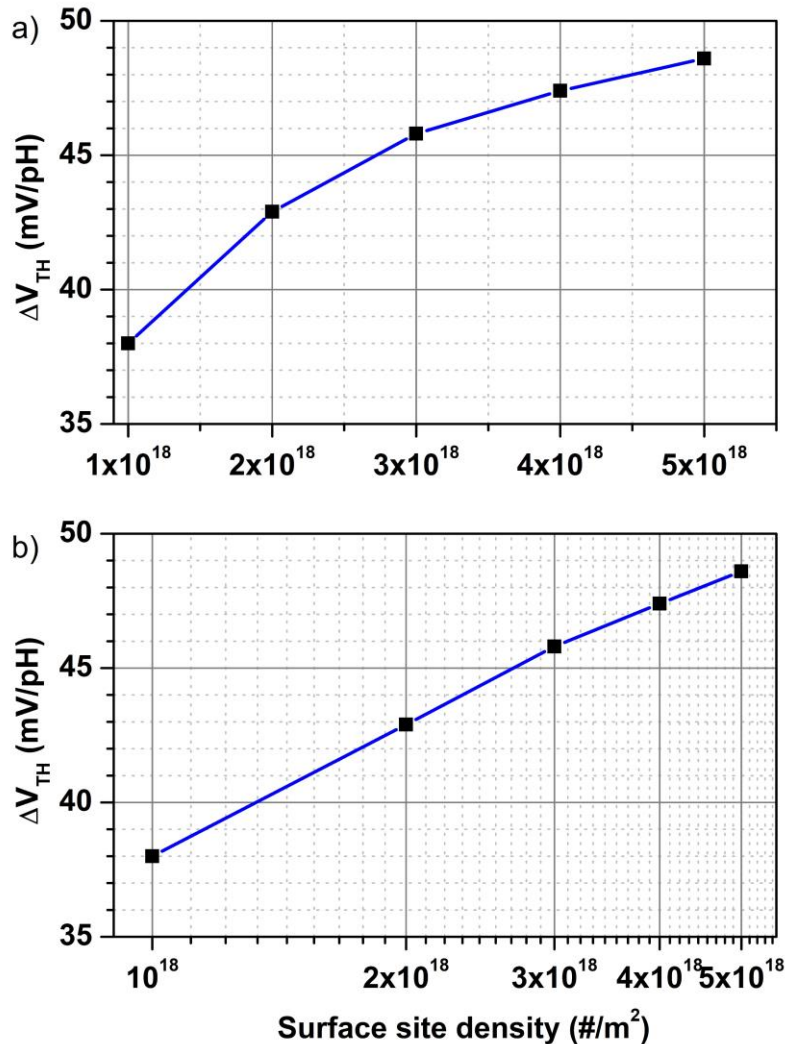
Figure 7-14 Dependence of the pH sensitivity of a SiNW FET sensor on the number of surface site density of the APTES-modified SiO_2 gate surface: a) Linear scale of the surface site density. b) Logarithmic scale of the surface site density

The second set of experiments with pH sensing was done after the treatment of the chip surfaces with (3-aminopropyl)-triethoxysilane (APTES) in gas phase conditions as described in chapter 6. The sensitivity then increased to 45 mV/pH. After the APTES deposition onto the gate oxide, NH_2 groups are added to the oxide surface, which modify the dissociation constant of the surface. A pK_a value of 3.9 ($K_a = 1.26*10^{-4}$) was estimated for the APTES modified SiO_2 surface in another work [213].

 shows the dependence of the pH sensitivity on the surface site density of a SiNW FET with APTES treatment in linear and logarithmic scale of the surface site density. As the number of surface site density increases, the sensitivity of the SiNW FET sensor also increases but slowly saturates as in the linear scale plot. This relationship, however, is almost linear in the logarithmic scale plot. In the second pH sensing experiment as discussed in this thesis in chapter 6, the pH sensitivity was

45 mV/pH, which would correspond to a lower value of $3*10^{18}$ surface sites per m^2. Simulation with this value produces a sensitivity of 45.8 mV/pH and an R-square of 0.9978 (Figure 7-15). This is in good agreement with the experimental result of 0.9964. From this simulation result, it can be concluded that the APTES treatment of the SiO_2 surface, as described in the experimental part of this thesis, leads to a change in the positive dissociation constant, but also to a reduction the total number of site density on the chip surface.
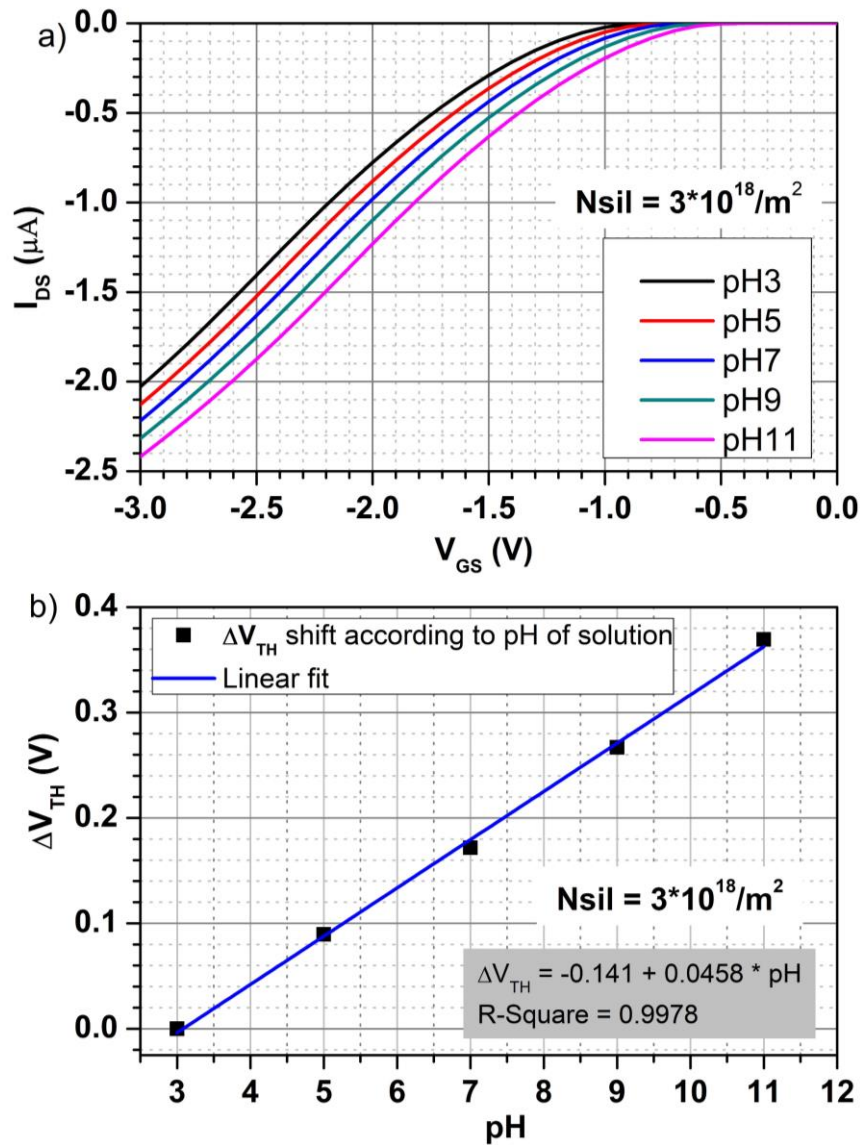
Figure 7-15 pH sensing simulation results of a SiNW FET with an APTES modified SiO_2 surface, $K_a = 1.26*10^{-4}$, $K_b = 63.1*10^{-9}$, $N_{sil} = 3*10^{18}$, $t = 20^{\circ}C$: a) Transfer characteristic simulation for pH from 3 to 11 at $V_{DS} = -2$ V. b) Shift of the threshold voltage caused by the variation of pH.

The typical gate insulators, which are widely used for pH sensing, that also have a better sensitivity and linearity than SiO_2, are Al_2O_3 and Ta_2O_5. This can be explained by the fact that these oxides possess different dissociation constants and different surface site densities. For example, Al_2O_3 has $K_a = 7.1*10^{-8}$, $K_b = 1.8*10^{-9}$ and a surface site density of $8*10^{18}$ [113]. To see how the dissociation constants effects the pH sensitivity, a simulation with Al_2O_3 was implemented with the assumption that the surface density was only $5*10^{18}$. Simulation with this value produces the sensitivity of 55.7 mV/pH at 20°C (Figure 7-16). The summary of the simulation of a SiNW FET with the two different gate materials is shown in Table 7-3. It was reported that the sensitivity of a SiNW FET with an Al_2O_3 gate oxide can be 59.4 mV/pH at 30°C that is very close to the ideal Nernstian response of 60.2 mV/pH at this temperature [113].
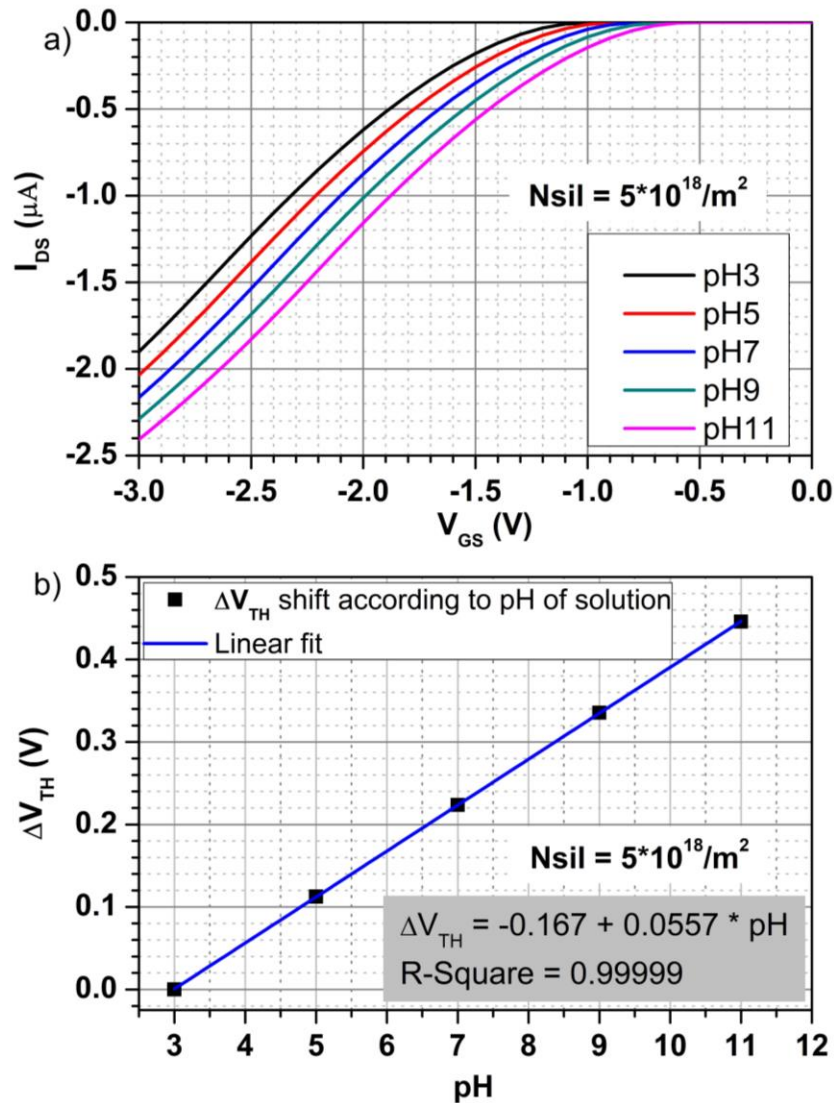
Figure 7-16 pH sensing simulation results of a SiNW FET with an Al_2O_3 gate surface, $K_a = 7.1*10^{-8}$, $K_b = 1.8*10^{-9}$, $N_{sil} = 5*10^{18}$, t = 20°C: a) Transfer characteristic simulation for pH from 3 to 11 at $V_{DS} = -2$ V. b) Shift of threshold voltage caused by the variation of pH

Table 7-3 Summary comparison between Al_2O_3 and SiO_2 + APTES gate oxide surface

	K_a (mol/L)	K_b (mol/L)	No. of site (#/m^2)	Sensitivity
SiO_2+APTES	$1.26*10^{-4}$	$63.1*10^{-9}$	$5*10^{18}$	48.6 mV/pH
Al_2O_3	$7.1*10^{-8}$	$1.8*10^{-9}$	$5*10^{18}$	55.7 mV/pH

From this electrochemical part of the model circuit, the results obtained in this thesis for pH sensing with a bare SiO_2 surface and the same surface after APTES modification can be explained. However, for an ideal pH sensor, gate oxides like Al_2O_3 or Ta_2O_5 should be used.

7.2 Impedimetric Simulation with SiNW Sensors

7.2.1 A Simplified Model for AC Measurements with SiNW FET Sensors
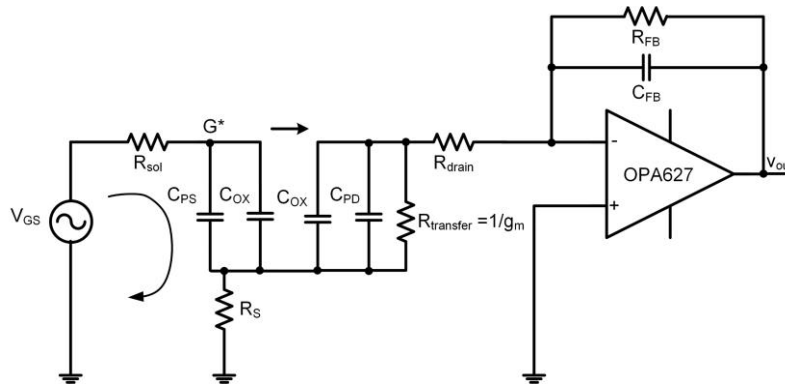
Figure 7-17 Simplified circuit for AC measurement with a SiNW FET sensor

The impedance spectra obtained from AC measurements with SiNW FETs are not well studied in this field of research. In the framework of this thesis and in a parallel PhD work [200] this technique was adapted from former works on impedance sensing with ISFETs and utilized for recordings with SiNW FETs [214]. To explain the influence of the parasitic side parameters to the spectra, the level7 model of the SiNW FET devices as discussed in section 7.1 was further combined with some additional, parasitic parameters of the solution and reference electrode resistivity value, the resistance and capacitance of the contact lines and the bandwidth of the transimpedance amplifier. By this extended circuit a complete readout circuit description can be achieved. As a first step, a simplified AC circuit model to understand the resonance effect of the coupling between the SiNW FET chip and the readout system is suggested. It can be assumed that there are two signal parts in the whole circuit. The first part is the signal that couples from the reference electrode though the measuring solution to the source electrode and to the ground (Figure 7-17). This part will determine the "effective gate voltage" (V_{G*S}) that directly modulates the drain-source current inside the SiNW FET channels:

$$V_{G*S} = V_{GS} \frac{Z_{CS} + Z_{Cox} + R_S}{Z_{CS} + Z_{Cox} + R_S + R_{sol}} \tag{78}$$

Where Z_{CS} is complex impedance of the capacitance of the passivation layers at source contact line, Z_{Cox} is impedance of the gate oxide of the SiNW FET input, R_S is resistance at the source contact line, and R_{sol} represents the resistance of the measuring solution.

The second AC signal pathway, where the remaining V_{G*S} modulates the drain-source current, couples from the source electrode through the drain to the readout circuit. When implementing AC measurements with FET devices in general, the device is biased at a certain working point that is assumed to be constant, because only a small sinusoid stimulation signal is applied (pseudo-linear range). Therefore, the transfer resistance of the SiNW FET is constant $R_{transfer} = 1/g_m$. When considering measurements in AC mode, the circuit in Figure 7-17 can be simplified into the following circuit:
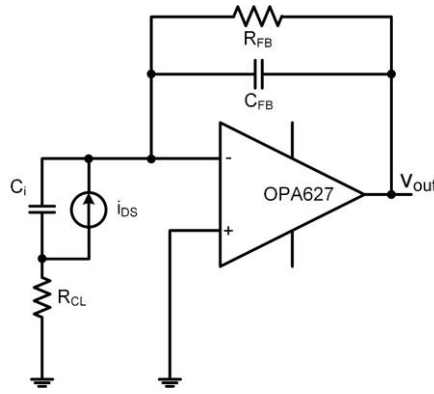
Figure 7-18 Simplified model of AC measurement with SiNW FET as a AC current source i_{DS}

Figure 7-18 describes the simplified model for AC measurements with SiNW FETs:

$$C_i = C_{ox} + C_D$$

$$R_{CL} = R_S + R_D$$

$$i_{DS} = \frac{V_{G*S}}{R_{transfer}} = g_m V_{G*S}$$

This model leads to the following equation describing the characteristics of the AC measurement with SiNW FETs:

$$BW = 1.4 * \sqrt{\frac{f_c}{2\pi R_{FB}(C_i + C_{FB})}} \tag{79}$$

BW is the bandwidth of the whole system and f_c is the gain bandwidth product of the operational amplifier.

$$V_{out} = \frac{i_{DS} * R_{FB}}{1 - \frac{\omega^2}{\omega_n^2} + j2\zeta\frac{\omega}{\omega_r}}$$

(80)

Where: $\omega_n = \sqrt{\omega_{zf}\omega_c}$

$\omega_{zf} = \frac{1}{R_{FB}(C_i+C_{FB})}$; $\omega_{pf} = \frac{1}{R_{FB}C_{FB}}$

$f_{zf} = \frac{1}{2\pi R_{FB}(C_i+C_{FB})}$; $f_{pf} = \frac{1}{2\pi R_{FB}C_{FB}}$;

The damping factor will be:

$$\zeta = \frac{1 + \frac{\omega_c}{\omega_{pf}}}{2\sqrt{\omega_c/\omega_{zf}}} = \frac{1 + f_c/f_{pf}}{2\sqrt{f_c/f_{zf}}}$$

(81)

Equation (80) presents the quadratic form of the frequency response. In this case, the C_i capacitance (10 pF – 40 pF) is much higher than the feedback capacitance C_{FB} (1 pF – 3 pF), which biases the operational amplifier. Even though a high gain bandwidth operational amplifier was selected for the readout circuit, the denominator was always higher than the numerator. Therefore, the range of ζ is $0 < \zeta < 1$, and the denominator is the product of two complex conjugate factors. Near the frequency $\omega = \omega_n$, a resonance peak happens as expected from the V_{out} equation. The damping ratio ζ determines the magnitude of this resonance peak (Figure 7-19).

Already, this simplified circuit can explain, that at a certain frequency a resonance effect at the voltage output will occur. The resonance frequency and the amplitude of V_{out} are defined by C_{FB}, R_{FB}, and C_i. The amplitude of the current source i_{DS} on the other hand is determined by the first signal pathway that goes from the reference electrode through gate oxide to the source electrode. Therefore, the impedance spectrum also carries the information of impedance on the gate surface, that might be alternated by the biomolecule binding events at the SiNW FET surface.
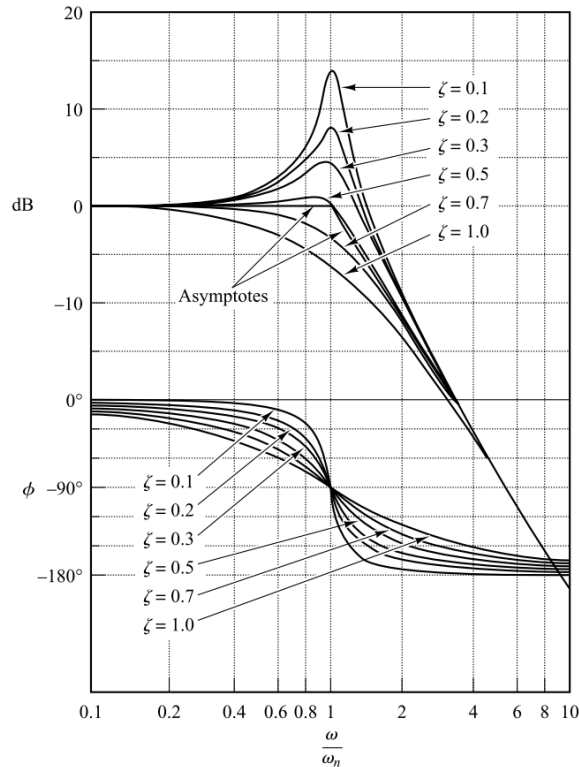
Figure 7-19 Log-magnitude and phase-angle curves of the quadratic transfer function [131]

7.2.2 Effect of the Feedback Resistance and Capacitance of the Transimpedance Amplifier

Different experimental approaches for impedance measurements with ISFET-based biosensors were described [72,132,142,215]. The technique offers a stable operation of the FET sensor against many side-parameters such as temperature drift, sensor drift, or pH value variations of the solution [99]. In some of these studies, to explain the experimental results, authors included the drain and source capacitances in their model. However, a simulation approach explaining the effects of these two capacitors as well as other parameters are missing in the literature. Utilizing the model developed in the previous section, it is now possible to study different aspects of impedance recording with SiNW FET sensors.
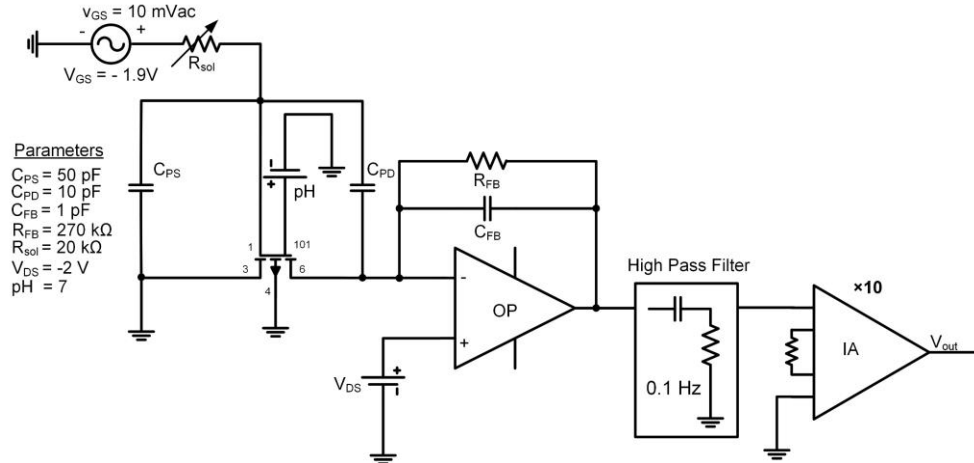
Figure 7-20 Simulation circuit for the impedance spectrum recording with SiNW FETs. The parameters used are indicated in the Table 7-1 and represent typical values

Figure 7-20 depicts the simulation circuit for the impedance recording with SiNW FET sensors. After the first transimpedance stage and a high pass filter, the signal is amplified in the second stage by 10 times or 100 times. As already explained in chapter 5, the impedance recording and signal stimulation at the reference electrode were implemented by a lock-in amplifier.

In the AC simulation, the recorded spectrum is influenced by all the components in the signal path, from the reference electrode to the output voltage, in which the first amplifier stage plays an important role. Figure 7-21 shows the effect of the feedback resistance R_{FB} to the impedance recordings: R_{FB} was varied as: 10 kΩ, 47 kΩ, 100 kΩ, 270 kΩ, 470 kΩ, 1 MΩ, and 2 MΩ. Figure 7-22 show the impedance spectrum, when the feedback capacitance C_{FB} was varied: 1 pF, 3 pF, 5 pF, 7 pF, 9 pF and 11 pF. When the parameter of interest was varied, all other parameters were kept at the default values as indicated in Figure 7-20. It can be seen from equation (80) and (81) that changing R_{FB} and C_{FB} will induce variations of resonance frequency as well as of the damping factor. On the other hand, R_{FB} also changes the amplitude of V_{out} at lower frequencies.

In the following simulations, values of R_{FB} of 270 kΩ and C_{FB} of 1 pF and the factor of the second amplifier of 10 were fixed. These are the values utilized in the amplifier settings. The reason for this selection is that higher feedback resistances induced an overload of the lock in amplifier device, that was employed in impedance recordings.
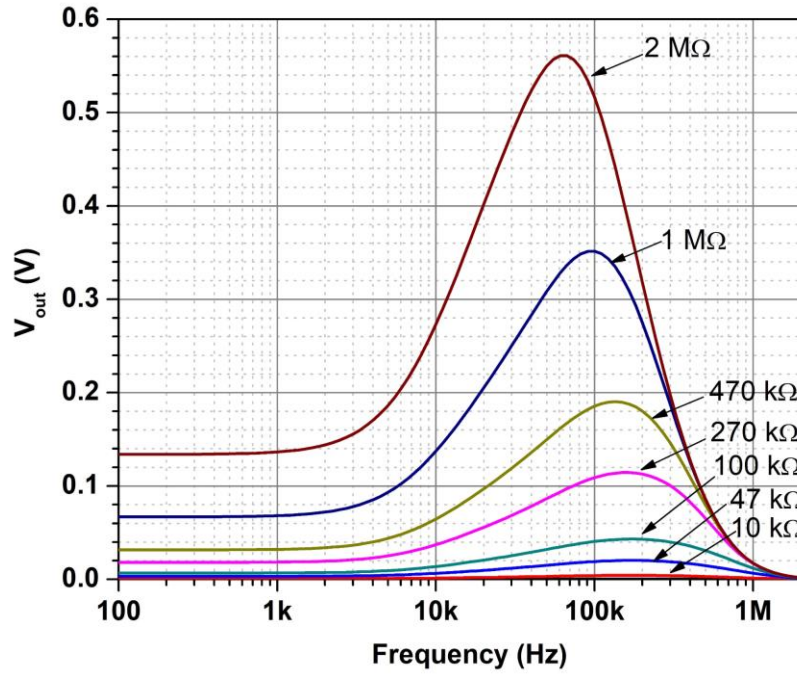
Figure 7-21 Impedance recording with SiNW 2×10 at different feedback resistances R_{FB}. With higher values of the resonance effect increases and shifts to smaller frequencies.
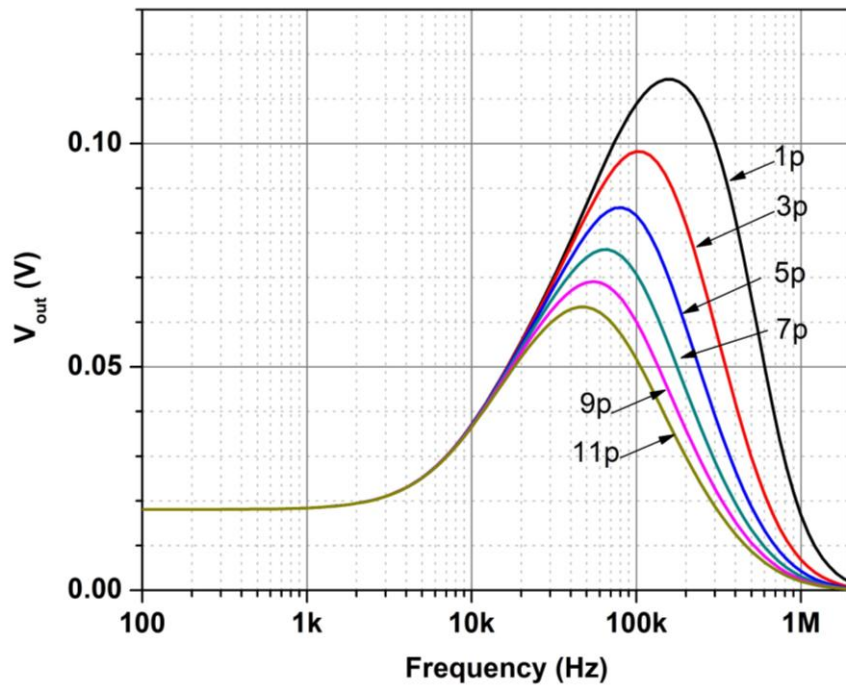
Figure 7-22 Impedance recording with SiNW 2×10 at different feedback capacitances C_{FB}. With higher values the resonance amplitude is damped and shifts to smaller frequencies as well.

7.2.3 Effect of the Solution Conductivity and of the Drain, Source Passivation Capacitances

The variation of the wire dimension and the pH value of the solution will mainly induce a change in the low frequency region of the spectrum as in the case of R_{FB} in the low frequency spectrum. (appendix D). There are three other parasitic parameters: solution conductivity R_{sol}, drain passivation capacitance (C_{PD}) and source passivation capacitance (C_{PS}) that were found to be important for the AC recordings. Their influence will be investigated in this section. The results of this section were the basis of another publication in the framework of this thesis [84]. Since this work was done in an early phase of this thesis, the simulation in this section was done with the level2 MOSFET model. However, the level7 MOSFET model also generates the same results. Figure 7-23 shows the effect of R_{sol} on the impedance spectrum, when C_{PD} and C_{PS} are the values calculated from equation (42). As the resistance increases, the pitch point (where the I_{DS} has highest amplitude: resonance point) decreases and its frequency moves to lower frequencies. To the spectrum it has a very similar influence than varying C_{FB}.
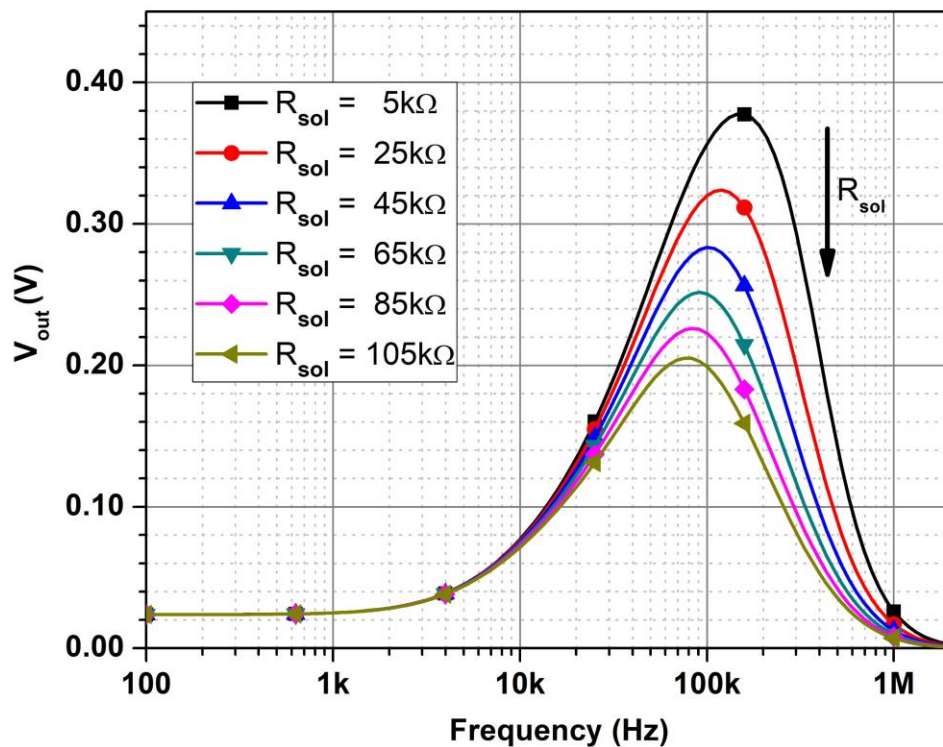
Figure 7-23 Influence of R_{sol} to the impedance spectra (when C_{PS} = 50 pF, C_{PD} = 33 pF) [84].

However, the effect of C_{PD} on the amplitude of the pitch point of the resonance is opposite to the one of R_{sol}. As the drain capacitance increases, the amplitude of the pitch point also increases almost linearly, and the resonance frequency slightly moves to lower frequencies. The coupling of R_{sol}, C_{PD} and the system including the SiNW FET sensor and the readout circuit might create an intrinsic frequency. This intrinsic frequency is inversely proportional to the multiplication of R_{sol}

and C_{PD}. When the frequency of the stimulation signal is equal to this intrinsic value, a resonance occurs in the spectra (Figure 7-24).
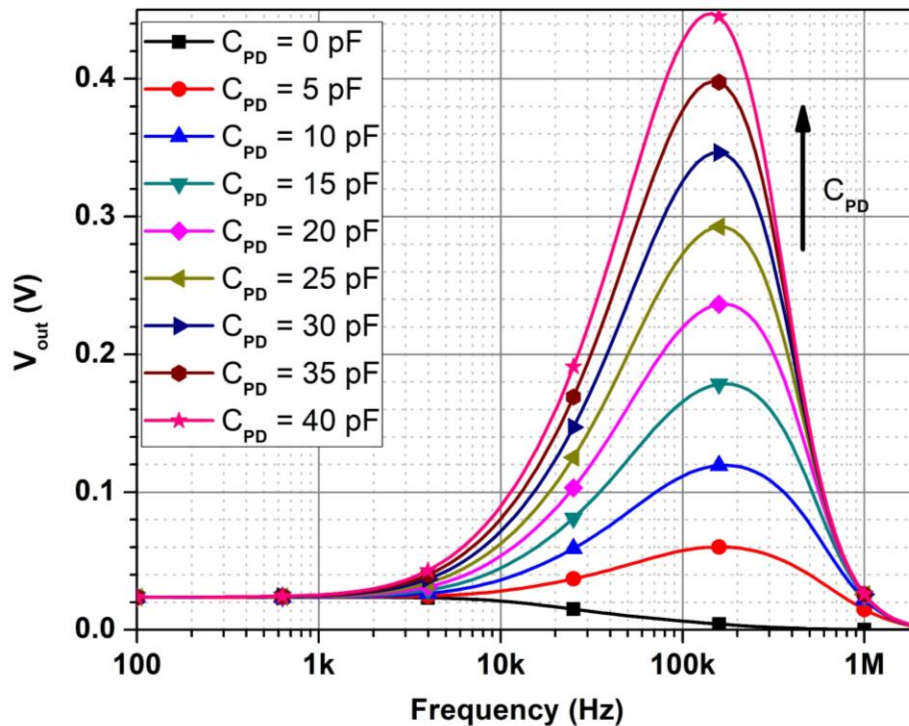
Figure 7-24 Influence of C_{PD} to the impedance spectra (when $C_{PS} = 50$ pF and $R_{sol} = 5k\Omega$) [84]

In addition, when the drain capacitance is small enough, the transfer function curve exhibits a low pass filter effect. Figure 7-25 shows the effect of the source capacitance on the impedance spectra when ($C_{PD} = 0$ F): as C_{PS} increases, the cut-off frequency decreases. Moreover, in the case of $C_{PS} = 0$ F ($C_{PD} = 0$ F), a low-pass filter effect can clearly be observed. This is either the cut-off frequency of the coupling of R_{sol} and the double layer capacitance, or the one of the transimpedance readout. However, the cut-off frequency of the transimpedance converter in the circuit is much higher than this frequency. Therefore, in this idealized case since capacitances at source and drain will never be zero, the oxide/liquid interface strongly contributes to the frequency response. This effect could eventually be exploited for biosensor assays [99]. For this, however, the design of the contact lines of the SiNW FET need to be further optimized to as small as possible parasitic capacitances.

Based on these simulation results, it can be concluded, that there might be an optimum design for SiNW FET devices for highest response to changes of the gate input impedance. In a previous work, a similar optimization process was utilized for the ISFET devices for cell impedance recordings [216]. The different conductivities will modulate the parameter R_{sol}. However, in contrast to these alternative works for impedance recording with micro scale ISFET, the fabrication for SiNW FET devices is much more tedious and requires more time. Therefore, it was not possible

to derive an optimum SiNW FET design and fabricate this based on the simulation results during the time of this thesis work.
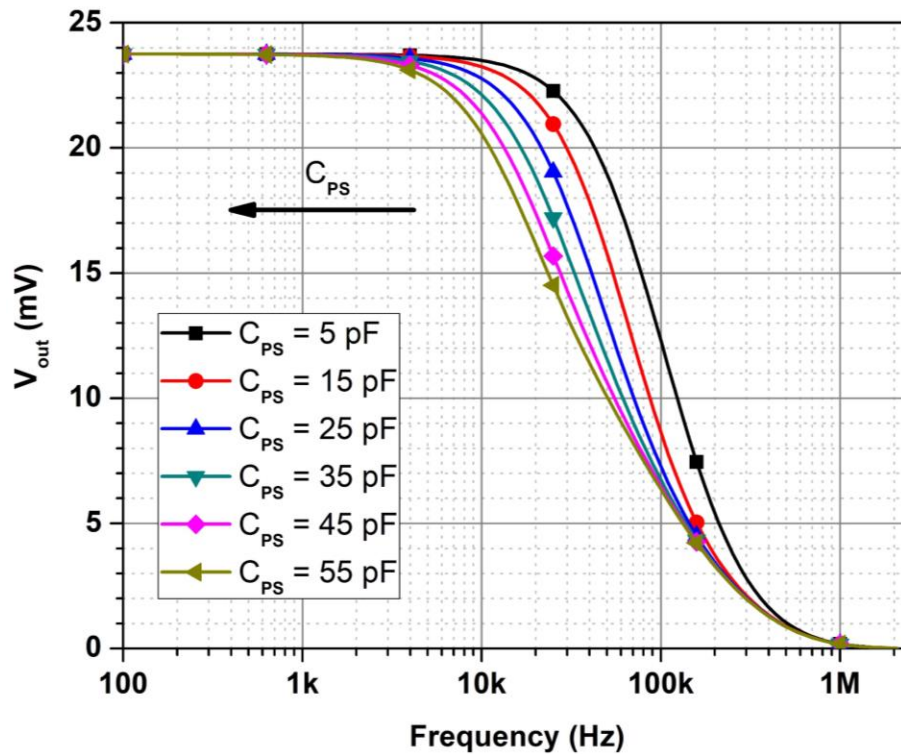
Figure 7-25 Influence of C_{PS} to the impedance spectra (when $C_{PD} = 0$ F, $R_{sol} = 5k\Omega$) [84]

7.2.4 Test of the Influence of the Solution Resistance

To confirm the above results from the simulations, frequency response measurements were done with phosphate buffer solutions (Na_2HPO_4 and NaH_2PO_4) of different concentrations (1 mM, 10 mM, 100 mM and 1 M) with identical pH values of 6.7. The measurements for this experiment were implemented with the setup described in section 5.3.1. The different conductivities will modulate the parameter R_{sol}.

The conductivities of the test solutions were firstly measured by a standard pH and conductivity meter (SevenMulti^{TM}, Mettler Toledo, Switzerland). The symbol plots in Figure 7-26 display the experimental results. It was found that the pitch points of the resonance peak did not linearly depend on the inverse value of the conductivity, but on the logarithm of it. Therefore, to simulate the spectra with accuracy, an additional parameter R_{sol} as a so-called representative resistance (Figure 7-11), by the following equation was suggested [84]:

$$R_{sol} = \alpha \log\left(\frac{1}{\sigma}\right) + K \tag{82}$$

where α is a value, which depends on the position of the reference electrode and the shape and size of the SiNW FET (constant in this simulation), σ is the conductivity of the solution, and K is a constant value depending on the resistance of the reference electrode. The simulation results using this resistance showed a very good agreement with the measurement data shown in Figure 7-26.
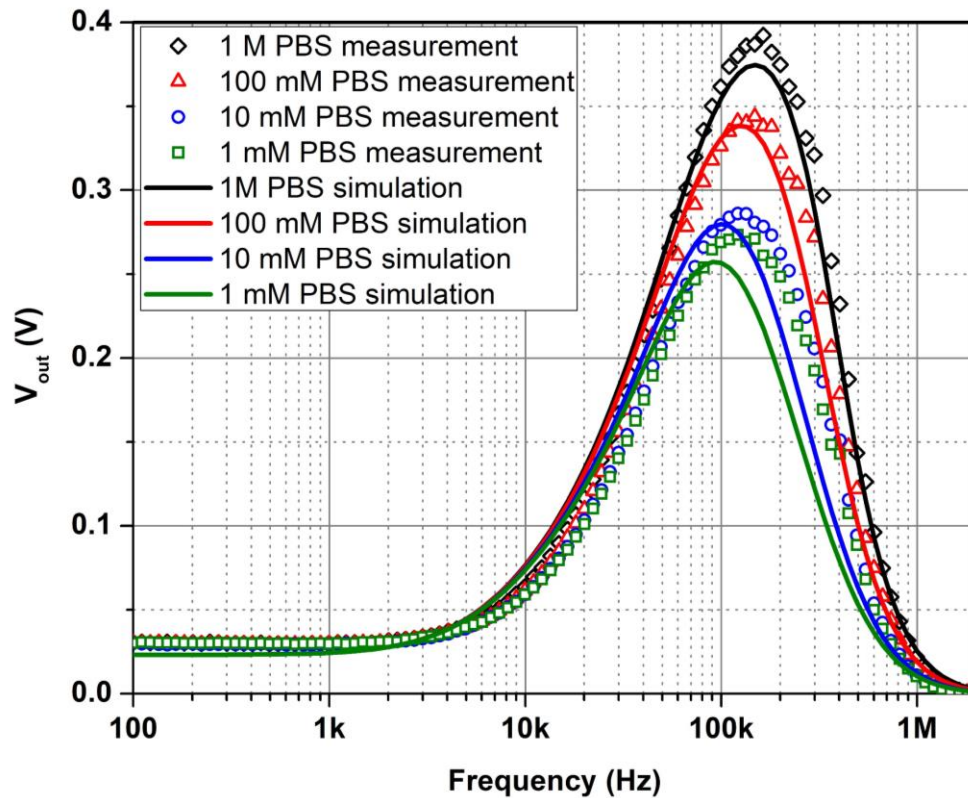
Figure 7-26 Conductivity measurements of different phosphate buffer solutions and corresponding simulation results [84].

In Figure 7-26, only the data of one 2×10 channel of an exemplary SiNW FET chip is shown. Different channels of the same chip showed only small differences in DC transfer characterization measurements, since the fabrication parameters are almost the same for the SiNW FETs in an array. However, when using these channels to measure the impedance spectra in the same phosphate buffer solutions and with the same conditions, the resulting spectra were different (especially with respect to their resonance frequencies). It can be concluded from this simulation model that the reason for this is most likely the contribution of the different passivation drain capacitances from channel to channel in the current chip design. Generally, a silicon funnel of a round shape was utilized for encapsulation of the sensor array (see Figure 4-7). Therefore, the area of the passivation layer of each channel in contact with the solution is different from channel to channel resulting in different passivation drain capacitances. Simulating these channels by the same values of R_{sol} but

using different values for the passivation drain capacitances (C_{PD}) was therefore implemented. Typical errors between simulation and experimental data for both types of SiNW FETs (for more spectra see supplementary data) were between 10 and 20%. The remaining inaccuracy of the simulated spectra can be explained by a possible inaccurate selection of the parasitic parameters inside the model. However, this part of the simulation was only done to display the qualitative effect of the parasitic parameters in the circuit.

As a general conclusion, the simulation results in this chapter confirm the correctness of the SPICE model and the influence of the drain capacitance to impedance measurements with the SiNW FET sensors. The impact of the passivation source capacitance C_{PS}, however, was less pronounced in the experiments. From the simulations the following hints for fabrication of the next-generation of SiNW FET sensors for impedimetric readout are as following:

- The measurement setup should include a microfluidic system such that only the sensitive area of the SiNW FETs is exposed to the measurement solutions. The regions of the drain and source contact lines that are open to liquids should be limited to minimize the value of C_{PS} and C_{PD}.

- The design of the SiNW FET array sensor should be considered such that the exposed area of contact lines to liquids are the same for different channels. By this, the parasitic effect of the passivation drain and source capacitances are equal for all channels and a differential readout method of all channels in the array would be possible.

- There is an optimum choice of the parameter sets for highest changes of the spectra by changes of the input impedance of the SiNW FET surface. For this selection the model developed in this thesis will be very helpful.

- The solution resistance is the main influencing parasitic parameter for these experiments since the drain and source passivation capacitances are fixed from the fabrication and encapsulation. Therefore, the stimulation signal should be provided by a stimulation electrode in very close vicinity of the actual recording device.

- Although in a parallel thesis work the impedance method was utilized for detection experiments with DNA [200], the devices and the readout circuits are not optimized to fully utilize this novel readout mode. Nevertheless, the simulation done in this thesis work represent a good starting point for future theoretical as well as practical works on the impedance recording with SiNW FETs.

8. Conclusions and Outlook

In this thesis, the following goals were achieved:

- A comparison of potentiometric and impedimetric modes in detecting non-charged biomolecules with SiNW FET sensors was obtained by an experimental approach. The experiments showed the high potential of the impedance method in detecting non-charged molecules in biosensing applications, which is not possible by the potentiometric method.

- For the understanding of potentiometric effects at the gate input, generic model PSPICE was implemented by combining a device part and an electrochemical part of the surface. By this the reactions of sensors with different gate oxide surfaces in pH sensitivity experiments was explained.

- A deeper understanding of the impedimetric readout mode with FET-based sensors was elaborated. It was found that the drain and source parasitic capacitances play an important role for the spectra, which was previously not considered in former models.

- A modelling approach of using the level7 PMOS SPICE model for SiNW FET based sensor simulation gave a hint to explain the advanced sensitivity of SiNW FETs in comparison to planar ISFET sensors as also reported in other works of the field.

Recent advances in micro/nano fabrication technology enabled ISFETs and SiNW FETs as the best platforms for label-free biosensing applications. However, both device types are facing one intrinsic problem in measuring the electric potential generated by charged molecules in liquid environments with the potentiometric mode. The biomolecule charges are screened by counterions in the liquid. For the potentiometric readout, it is necessary to implement experiments in low ionic strength solutions. As a result, realizing point-of-care applications is impossible with the potentiometric approach. The experiments with biotin-streptavidin in this work proved the capability of the impedimetric method in detecting uncharged molecules. Biotin in the measured solutions carries negligible charge and consequently it was not detectable in potentiometric readout. Nevertheless, it was clearly distinguishable in the impedance spectra recordings especially at a region, where a resonance effect happens. Although these measurements were carried out in a low ionic strength solution, the impedimetric method to detect non-charge molecules represents an alternative method to realize point-of-care devices for biosensing. Unfortunately, in this thesis work there were not enough devices available to draw robust, statistical conclusions for these experiments.

Previously, when implementing measurements in impedimetric mode with FET-based sensors only the same parameters for each sensor were considered as in the case of measurements in potentiometric mode. Parameters such as the drain and source passivation capacitances were not considered. In this work, it was shown that these parameters play an important role in impedance spectra recordings. The impedance spectra showed two pronounced frequency domains: a low-pass

characteristic at lower frequencies, and a resonance effect at higher frequencies. The former was interpreted as a contribution of the source and double layer capacitances. This was typically observed if the drain capacitance of the SiNW FET sensor was small enough. The latter can be interpreted as a coupling between the drain capacitance and the readout system (especially the first impedance converter). A simplified theoretical model to understand this resonance effect of the coupling between the SiNW FET chip and the readout system was suggested. The influence of the solution conductivity and the drain capacitance to the recorded impedance spectra were also confirmed by experimental data. This model will aid to optimize and simulate the next generation SiNW FET sensors and their related readout systems. In addition, the findings give a clearer view of impedance measurements utilizing SiNW FET sensors, not only for conductivity experiments, but also for many other bioelectronic applications. For instance, it is now possible to use this model to interpret the biosensor recordings for detection of DNA or immunoassays.

A behavioral PSPICE model for SiNW FET-based biosensors in both potentiometric and impedimetric measurement mode was also developed in this study. The simulation model included a double layer electrochemical model to describe the oxide/liquid interface and a PSPICE PMOS level2 or level7 (BSIM 3v3) model for the electrical properties of the SiNW FET sensors. The utilization of the level7 version gave a hint to explain the advanced sensitivity of SiNW FET sensors in the comparison to planar ISFET sensors as reported by others in the field. The smallest SiNW FET examined had a width of 200 nm and a length of 10 µm (length width ratio of about 500), which is approaching the critical dimensions, where quantum confinement effects should occur (width maximum of 100 nm and the ratio of the length to width greater than 1000 [217]). A change in the transfer characteristics steepness upon DNA binding to the SiNW FET was observed with narrower sensors (200 nm width), but not with wider ones (from 400 nm above). This effect was modelled by varying the bulk charge effect coefficient, that is only accessible in the level7 MOSFET model. This phenomenon can be explained by an artificial increase in carrier density in the structure. The utilization of this parameter however, was only explaining the effects in a qualitative way. From this part it was concluded that in future a full SOI model should be used for the SiNW FET sensors.

In addition, to obtain the goals in this thesis, the development of two readout systems was necessary. The first one enabled 32-channel multiplexing measurements and the second one a battery power handheld device was utilized for point-of-care tests [218]. Therefore, the thesis work created a groundwork for further research with SiNW FET devices. At the beginning of this thesis work, FET-based sensors were measured by a commercial, high resolution parameter analyzer (Agilent 4156C) and/or a dedicated 16-channel system called Transistor Transfer Function box (TTF box) from a former project [99]. In this thesis work, the following readout setups were developed and tested:

- A 32-channel readout device: the system has different amplifier options that can be used in measuring different sensors with different current ranges. The design utilized a multiplexer

and switching between channels, which can reduce the cost of amplifiers while maintaining the accuracy of the experiments. A readout software in LabVIEW was also developed in this work. The AC measurements were made with a commercial Lock-In amplifier. An automatic acquiring software was also developed for AC measurements. Therefore, all the measurements with 32-channels devices in both potentiometric and impedimetric readout mode can now be done automatically at one time. The device provided a whole solution for measuring up to 32-channel, FET-based array sensors. The design provided a foundation for further setup development with more channels, more features, and less noise. The current system was proven to be more cost effective and more accurate in comparison with the previously developed TTF box. It is also able to implement noise spectrum characterization, that was previously not available with the system. The implemented software is based on the state-machine-programming method and provides a platform that could be easily extended for even larger sensors arrays.

- A handheld readout device: the device based on a 32-bit microcontroller was also designed such that it can measure 4-channel FET sensors simultaneously for label-free point-of-care applications. It is a stripped-down version of the 32-channel devices that are used for only 4 channels, simultaneously. However, it has a similar accuracy compared to the 32-channel setup (less than 5% tolerance in comparison to a commercial parameter analyzer). Because of the advantage in state-machine-programming with LabVIEW, the software for a 32-channel system needed only a minor change for the handheld devices. In this work, also a USB protocol was developed for communication and a firmware program was written for the microcontroller. The handheld device can be operated on mains supply line or with battery power, which enables also measurements in remote areas or in point-of-care applications.

- The realized readout system was utilized for pH sensing and DNA experiments. The pH sensitivity of the bare SiO_2 chips was 34 mV/pH. In addition, the gas phase treatment of the chip surface with APTES created a better sensitivity of 45 mV/pH and increased the linearity of sensor signal. The characteristic curves of the DNA experiments shifted to the right side upon the binding of negatively charged molecules (pDNA, BSA and cDNA) as expected from theory. The immobilization of 1µM pDNA induced a V_{TH} shift of 29 mV, while the hybridization with 1µM cDNA resulted in a shift of 13 mV in comparison with the curve after the blocking step. In real DNA experiments, this shift would be the DNA sensor response, which could be treated similarly to the fluorescence intensity in standard DNA microarrays.

- To prove the performance of the system for measuring in impedimetric mode, simple conductivity measurements were used with different PBS solutions having the same pH values and different conductivity values. With ISFET sensors, as the conductivity of the solution increased (higher the concentration of the PBS solutions), the cut-off frequency of

the spectra shifted to the right side (greater frequency region). This showed the low-pass filter response with resistance (combining resistance of reference electrode and the electrolyte) and capacitance (gate oxide, contact line insulator). It was found from the experiments that the cut-off frequency was linear with the concentration of the measurement buffer solutions. The response of the impedance spectra of the SiNW FET channels to the variation of solution conductivities was different from those of the ISFET sensors. The clear difference interestingly happened at a certain frequency and only a resonance peak in the spectra varied as the concentration changed. It was revealed that the coupling between the SiNW FET and the first amplifier stage of the transimpedance created this resonance at a certain resonance frequency, that did not depend on the conductivity of the buffer solution. The low pass-filter effect was still there in the spectrum; however, it was hidden and leaded to different amplitudes of the pitch point at the resonance frequency. At the end this work, an analytical model is available that can explain the basic phenomenon of AC measurement with SiNW FET sensors.

In this thesis work, also some novel effects were found and discussed. Unfortunately, for some of findings there were not enough devices available to fully elaborate on them and statistically proof the findings.

- There were not enough devices to statistically evaluate the sensors performances and relate them to the quality and reproducibility of the wafer scale fabrication. Several different sensor types and devices were used for the experiments presented here. Four ISFET chips (16 channels) and two ISFET sensors (8 channels) were utilized for pH and DNA experiments, respectively, and their evaluations were presented in chapter 6.1. More channels and more statistical analysis of DNA experiments were done in another work [200] in the framework of this project. The AC spectrum recording phenomenon with different solutions conductivities with SiNW FETs were only tested with five channels on a single chip. The AC and DC measurements with biotin-streptavidin presented here were resulting from a single experiment on one SiNW FET sensor. A repetition of this experiment was not possible because of the shortage of SiNW FET chips. The experiments with ISFETs, where more devices were available, did not generate the same results. The comparison between SiNW FET characteristics measurements and simulation in the chapter 7 for SiNW 2×10 (width 200 nm and length 10µm) was done for only three channels on one chip. In the appendix D different SiNW FET dimensions experiments and simulations are presented. In summary, the experiments with ISFET were done with different chips with many channels. However, the experiments with SiNW FETs were implemented mainly with different channels of a single available chip. However, a full statistical evaluation of the sensors that are fabricated on a whole wafer and on different wafers would be critical to realize these sensors as a biomedical device.

- The influence of the important parameter temperature could not be investigated as well. The temperature is important to appreciate the effects exhibited by ISFETs and SiNW FETs. The influence is the sum of four main factors: i) the thermal behavior of the reference electrode (liquid junction potential); ii) the thermal behavior of the measurement solutions (pH value vs. temperature as well as temperature dependence of the activity of analytes); iii) the temperature characteristics of the liquid/solid interface such as the Boltzmann distribution of ions; and iv) the thermal properties of the sensing FET structure. Among these factors the thermal properties of semiconductor silicon transistor are well known as the temperature increase induces a reduction in the amplitude of the threshold voltage. Very little work has been done on this highly complex topic and only some experimental works were found in the literature [219,220]. This research topic is very interesting to investigate, because it is crucial to understand the thermal behavior of ISFETs and SiNW in a theoretical and in an empirical approach.

- The aging effect caused by multiple uses of the sensors were not investigated systematically as well. ISFET and SiNW FET sensors used in this work can be reused after experiments by implementing proper cleaning procedures. However, these cleaning steps induced a sensitivity degradation after each use. The wearing out phenomenon is mainly dependent on the quality of the thermal growth gate oxide, cleaning procedures and encapsulation methods. Therefore, for the simulations and for precise experimental evaluations all experiments presented in this thesis were done with fresh devices. This also explains the low number of channels and devices but was found important to draw solid conclusions from the experiments.

Outlook

With the new finding in this thesis, the following aspects must be improved for future applications of SiNW FET sensors:

- With the help of the multi-channel readout system, that can implement both potentiometric and impedimetric approaches, more experiments should be carried out to confirm the capability of the impedimetric method in detecting uncharged molecules. The measurements should be done also in high ionic strength solutions such as in physiological conditions. Two questions remained unanswered in this work: (1) whether and how do charged molecules affect impedance spectra recordings? By measuring the biotin-streptavidin in a series of the same ionic strength solutions with different pH, effects of the charged molecules to the spectra could eventually be explained better. (2) After doing biotin-streptavidin experiments with both SiNW FETs and ISFETs, it seems that only the SiNW FETs can be used to detect the uncharged molecules. Experimental data with ISFET sensors generated unclear results. This phenomenon requires further investigation and are very interesting to understand.

- The BSIM 3v3 level7 model in PSPICE is still not the ideal model for SOI devices in general. It is necessary to employ an SOI device model such as BSIM-SOI to fully simulate the effects of the fabricated sensors. The model should be able to systematically vary the sensor dimensions in width and length to validate the hypothesis and examine the effects in potentiometric readout more precisely. Eventually, this effect could be used to explain the higher sensitivities of nanowire devices compared to micro-scale ISFET devices as observed in this thesis and reported by others before. Consequently, this model can be used to combine it with the ion-permeable model for the sensing layer to generate a complete picture of the sensing device and to interpret the biosensing experiments with SiNW FET in the impedimetric approach as well.

- An AC functionality should be accomplished for the handheld readout system as well such that the device can offer both potentiometric and impedimetric measurements. The system should still be small in size and be able to communicate with a cell phone via Bluetooth or Wi-Fi.

As a final remark, this thesis now fulfilled its mission in providing basic experimental work with SiNW FET devices in impedance readout. New amplifiers were built and optimized for these sensors. The SPICE model can be very valuable in future in two aspects. Firstly, it can be utilized to generate an optimized design of future SiNW FET devices. Secondly, it can also be used and eventually expanded with BSIM-SOI part to explain the recordings in biosensing experiments. Therefore, this thesis work can be regarded as an important step stone towards future point-of-care health care devices based on SiNW FETs.

9. Appendices

Appendix A: ISFET Fabrication

The fabrication of ISFET at the University of Applied Sciences Kaiserslautern was done in the other work [142]. A summary of the fabrication processes is described in the following:
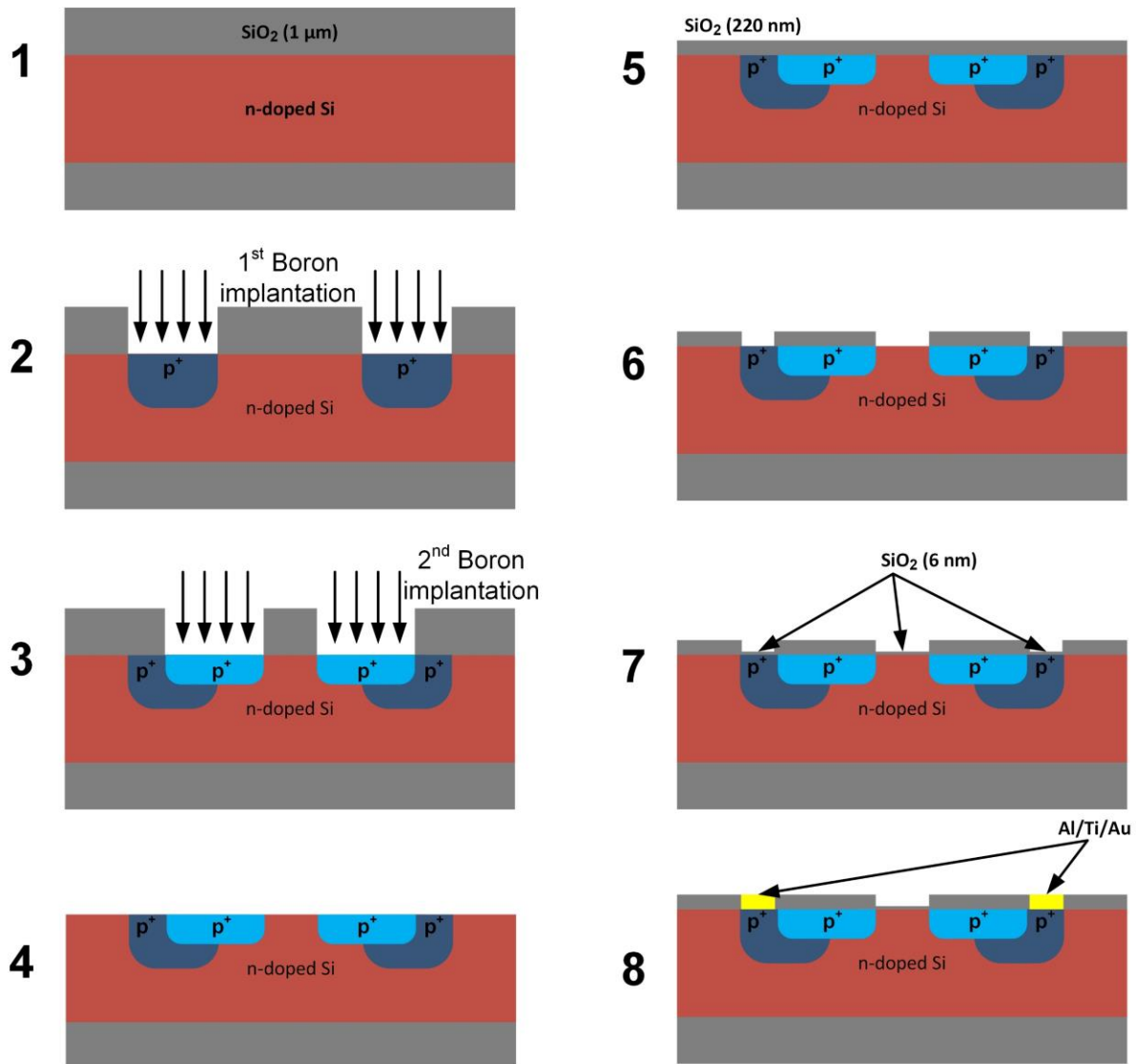
Figure 9-1 Cross-section of the ISFET fabrication process;

1) In the first step, a 4" n-doped both side polished silicon wafer was wet oxidized. The thickness of the oxide was adjusted to 1 µm and was used as a hard mask for next step implantation.

2) First lithography and a wet etching of the silicon oxide defined the contact lines of the source and drain electrodes. And then the contact lines were implanted with a boron dose of $D = 1*10^{16}$ ions/cm^2, 150 keV.

3) The second lithography step defines the source and drain areas. A shallow boron implantation ($1*10^{15}$ ions/cm^2, 80 keV) was implemented to define the source and drain electrode.

4) The implantation oxide mask was removed completely.

5) A wet oxidation process created a 220-nm layer of silicon dioxide overall wafer.

6) Next lithography step defined the drain and source contacts and the gate areas.

7) A thermally grown 6 nm dioxide (820°C) was constructed as the gate insulation layer.

8) The final step was a lift-off process that defined the drain and source contacts (layer stack of Al/Ti/Au). This step followed a preparation step of removing oxide on the source and drain contact by hydro fluoric acid solution (HF 1%).

Appendix B: SiNW FET Fabrication

The fabrication of SiNW FET employed in this thesis was accomplished and described in the other PhD thesis [64]. A summary of the fabrication process is described as follows:
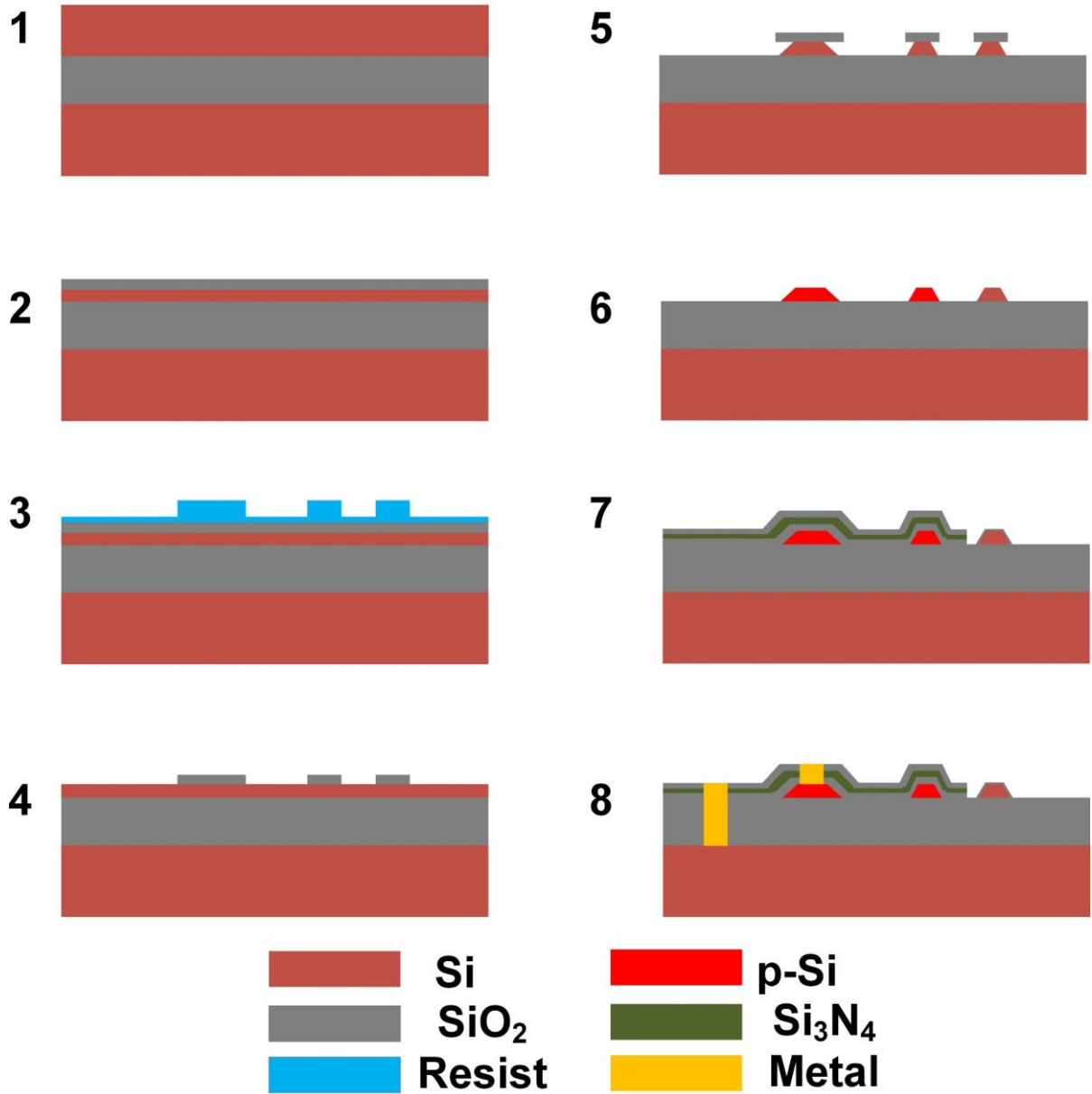
Figure 9-2 Fabrication process of SiNW

1) 4-inch Silicon-on-insulator (SOI) wafer (SOITEC, France): Si substrate, 400 nm buried oxide and 360 nm of top Si layer (device layer).

2) Thin out the top silicon layer to 50 -60 nm.

3) The structure of both contact lines and SiNW are defined by Nano imprint lithography.

4) Reactive ion etching (RIE) etches residue photoresist layer and SiO_2 between the contact lines.

5) Device structure was finally defined by wet tetramethylammonium hydroxide (TMAH 25%, 90°C) etching.

6) LPCVD process created a 100-nm layer of silicon oxide. This oxide was used as a mask for contact lines implantation (Boron ion $1*10^{14}$ ion/cm^2, 7 keV). Subsequently the wafer was annealed at 900°C for 30 min.

7) An oxide-nitride-oxide ONO structure covered the chip as passivation layer of contact lines.

8) The gate areas and the bond pads were re-opened. The gate insulator was a thermally grown silicon dioxide layer (8 nm). A lift-off process created contact to outside world.

Appendix C: PSPICE Simulation Model
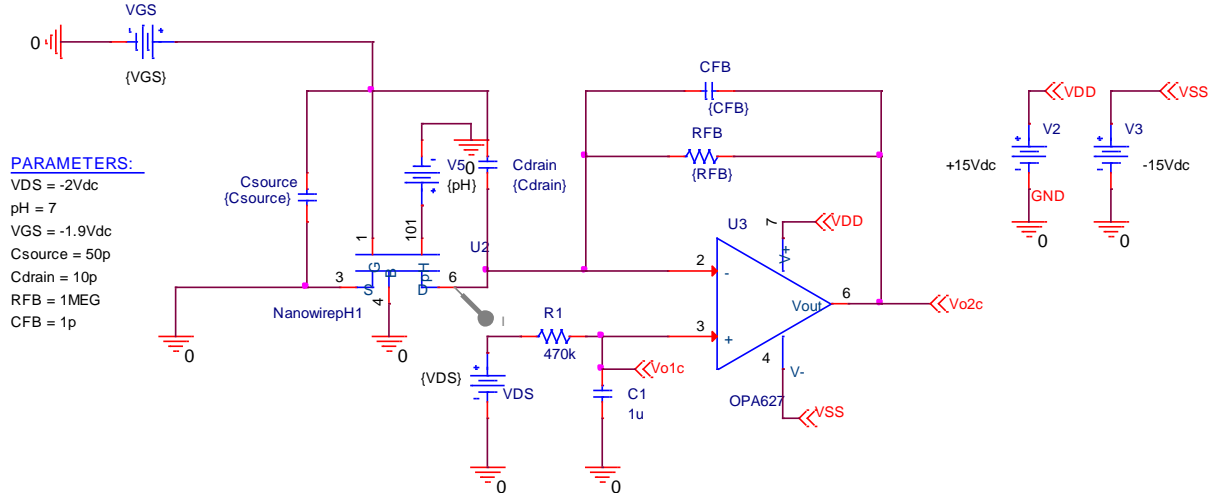

```
* Nanowire model based on Martinoia 1999
*drain|ref.el|source|bulk|pH input
.SUBCKT Nanowire_pH 6 1 3 4 101
* PARAMETERS LIST
* General constant:
* q = electronic charge [C]
.PARAM q=1.6e-19
* T = Absolute temperature
.PARAM T=293
* k = Boltzmann's constant [J/K]
.PARAM k=1.38e-23
* NAv = Avogadro's constant [1/mol]
.PARAM NAv={6.023e23*1e3}
* eps0=dielectric constant [F/m]
.PARAM eps0=8.85e-12
* epsw=relative permittivity of water
.PARAM epsw=78.5
* Ka=positive dissociation constant [mole/l]
*SiO2
.PARAM Ka=0.1
* Kb=negative dissociation constant [mole/l]
*SiO2
.PARAM Kb=63.1e-9
* Nsil=Silanol or oxide surface site density [#/m2]
.PARAM Nsil=5.0e18
* Cbulk = electrolyte concentration [1/moles]
.PARAM Cbulk=0.1
* epsihp = relative permittivity of the Inner Helmholtz layer
.PARAM epsihp = 32
* epsohp = relative permittivity of the Outer Helmholtz layer
.PARAM epsohp = 32
* dihp = distance between the Inner Helmholtz Plan IHP and the ISFET surface
[m]
.PARAM dihp = 0.1n
* dohp = distance between the Outer Helmholz Plane OHP the ISFET surface [m]
.PARAM dohp = 0.3n
* Reference electrode electrochemical parameters:
* Eabs = absolute potential of the standard hydrogen electrode[V]
```

```
.PARAM Eabs = 4.7
* Erel = potential of the ref. electrode Ag/AgCl relative to the hydrogen
electrode[V]
.PARAM Erel = 0.2
* Phim = work function of the metal back contact r electronic charge V
.PARAM Phim=4.7
* Chieo = surface dipole potential[V]
.PARAM Chieo = 3e-3
* Philj = liquid-junction potential difference between the ref. solution and
the electrolyte[V]
.PARAM Philj=1e-3
* Equations
.PARAM ET = {q/(k*T)}
* Effective Width
.PARAM Width= 0.370u
* Effective length
.PARAM Length= 10u
* parameter to calculate Gouy-Chapman Helmholtz capacitance
.PARAM Ch = {(eps0*epsihp*epsohp)/(epsohp*dihp+epsihp*dohp)}
* Number of particles
.PARAM Cb = {NAv*Cbulk}
.PARAM sq = {sqrt(8*eps0*epsw*k*T)}
.PARAM Cd = {sq*ET*0.5*sqrt(Cb)}
.PARAM KK = {Ka*Kb}
.PARAM Ceq={1/(1/Cd+1/Ch)}
*FET model for SiNW
************************************************************
*level7
.MODEL MISFET PMOS
* MODEL SELECTION FLAG
+Level= 7
+TNOM=20.0
+Mobmod= 1 binunit= 2
* CHANNEL GEOMETRY
+lmin=8.0e-7 lmax=1.5e-5 wmin=1.0e-7 wmax=5.0e-7
+wint= 40.0E-09 dev/gauss=25%
+lint=16.00E-09
* PROCESS RELATED PARAMETERS
+Tox= 6.00E-09 dev/gauss=8%
+Xj= 50.0000000E-09 dev/gauss=5%
+Nch= 1.0E+17
* THRESHOLD VOLTAGE PARAMETERS
+Vth0= -0.4 dev/gauss=8%
+K1= 0.5 K2= 0.5 K3= 80 K3B=0
+Dvt0= 2.2 Dvt1= 0.53 Dvt2= -0.032
+Nlx= 1.74E-7 W0= 2.5E-06
+K3b= 0.0
*Ngate= 1.0000000E+30
* MOBILITY PARAMETERS
+U0= 115 UA= 2.25E-09 UB= 5.87E-19 UC= -4.65E-11
*DRAIN CURRENT
+Vsat= 0.8000000E+05 A1= 0.23 A2= 1.08000000
+A0= -0.55 Ags= 0 Keta= -0.047 B0= 0.0000000 B1= 0.00
* SUBTHRESHOLD CURRENT PARAMETERS
+Voff= -0.11 NFactor= 1 Cit=0
+Cdsc= 2.4E-04 Cdscb=0 Cdscd=0
* DRAIN-SOURCE RESISTANCE
```

```
+Rdsw= 0.0E+02 Prwb= 0.00 Prwg= 0.00 Wr= 0
* ROUT PARAMETERS
+Pclm= 1.3 Pdiblc1= 0.39 Pdiblc2= 0.0086 Pdiblcb= 0.00 Drout= 0.56
+Pscbe1= 4.24E+08 Pscbe2= 1.0E-05 Pvag= 0
+Beta0= 30.0000000
***********************************************************
Eref 1 10 Value = {Eabs-Phim-Erel + Chieo + Philj}
Ceq 10 2  {1/(1/{Cd} + 1/{Ch})}
Ep1 46 0 Value = {log(KK) + 4.6*V(101)}
RP1 46 0 1G
Ep2 23 0 Value = {log(Ka) + 2.3*V(101)}
RP2 23 0 1G
EpH 2 10 Value = {(q/Ceq)*(Nsil*(exp(-2*V(2,10)*ET)-exp(V(46))))/(exp(-
2*V(2,10)*ET)+exp(V(23))*exp(-1*V(2, 10)*ET)+exp(V(46)))}
RpH 101 0 1K
M1 6 2 3 4 MISFET L={Length} W={Width}
.ENDS
```

Table 9-1 Level7 BSIM3v3 parameters explanation and default values

Parameter	Description	Default Value (NMOS/PMOS)	Unit
Threshold Voltage			
VTHO	Ideal threshold voltage	0.7/-0.7	V
K1	First-order body effect coefficient	0.5	$V^{0.5}$
K2	Second-order body effect coefficient	0.5	-
K3	Narrow width coefficient	80.0	-
K3B	Body effect coefficient of K3	0.0	1/V
W0	Narrow width parameter	2.5E-6	m
NLX	Lateral non-uniform doping coefficient	1.74E-7	m
VBM	Maximum applied body bias in VTH calculation	-5.0	V
DVT0	First coefficient of short-channel effect on VTH	2.2	-
DVT1	Second coefficient of short-channel effect on VTH	0.53	-
DVT2	Body-bias coefficient of short-channel effect on VTH	-0.032	1/V
DVT0W	First coefficient of narrow-channel effect on VTH	2.2	-
DVT1W	Second coefficient of narrow-channel effect on VTH	5.3E6	-
DVT2W	Body-bias coefficient of narrow-channel effect on VTH	-0.032	1/V
ETA0	DIBL coefficient in the subthreshold region	0.08	-
ETAB	Body-bias for the subthreshold DIBL effect	-0.07	1/V
DSUB	DIBL coefficient in subthreshold region	DROUT	-
Mobility			
U0	Mobility	670 / 250	$cm^2/(Vs)$
UA	First-order mobility degradation coefficient	2.25E-9	m/V
UB	Second-order mobility degradation coefficient	5.87E-19	$(m/V)^2$
UC	Body-effect of mobility degradation	-4.65E-11	$(m/V)^2$
Drain current			
VSAT	Saturation velocity	8.0E6	cm/s
A0	Bulk charge effect coefficient	1.0	-
A1	First non-saturation factor	0/0.23	1/V
A2	Second non-saturation factor	1.0/0.08	-
AGS	Gate-bias coefficient of Abulk	0.0	1/V
B0	Bulk charge effect coefficient for channel width	0.0	m
B1	Bulk charge effect width offset	0.0	m
KETA	Body-bias coefficient of the bulk charge effect.	-0.047	1/V
Subthreshold region			
VOFF	Offset voltage in the subthreshold region	-0.11	V
NFACTOR	Subthreshold swing factor	1.0	-
CIT	Interface trap density	0	F/m^2
CDSC	Drain-Source to channel coupling capacitance	2.4E-4	F/m^2
CDSCB	Body-bias coefficient of CDSC	0	F/Vm^2
CDSCD	Drain-bias coefficient of CDSC	0	F/Vm^2
Drain source resistance			
RDSW	Parasitic resistance per unit width	0	Ωμ m
WR	Width offset from Weff for RDS calculation	1.0	-
PRWB	Body effect coefficient of RDSW	0	$V^{-0.5}$
PRWG	Gate bias effect coefficient of RDSW	0	1/V
Channel geometry			

WINT	Channel width reduction on one side	0	m
WL	Coeff. of length dependence for width offset	0	m
WLN	Power of length dependence for width offset	1	-
WW	Coeff. of width dependence for width offset	0	m
WWN	Power of width dependence for width offset	1	-
WWL	Coeff. of length and width cross term for width offset	0	m
LINT	Channel length reduction on one side	0	m
LL	Coeff. of length dependence for length offset	0	m
LLN	Power of length dependence for length offset	1	-
LW	Coeff. of width dependence for length offset	0	m
LWN	Power of width dependence for length offset	1	-
LWL	Coeff. of length and width cross term for length offset	0	m
DWG	Coefficient of Weff's gate dependence	0	m/V
DWB	Coefficient of Weff's substrate dependence	0	$m/V^{0.5}$
Output resistance			
PCLM	Channel length modulation coefficient	1.3	-
PDIBLC1	First output resistance DIBL effect	0.39	-
PDIBLC2	Second output resistance DIBL effect	0.0086	-
PDIBLCB	Body effect coefficient of output resistance DIBL effect	0	1/V
DROUT	L dependent coefficient of the DIBL effect in output resistance	0.56	
PSCBE1	First substrate current body-effect coefficient	4.24E8	V/m
PSCBE2	Second substrate current body-effect coefficient	1.0E-5	m/V
PVAG	Gate dependence of Early voltage	0	-
ALPHA0	The first parameter of impact ionization	0	m/V
ALPHA1	Length dependent substrate current parameter	0	1/V
BETA0	The second parameter of impact ionization	30	
Diode characteristic			
JS	Source drain junction saturation density	1E-4	A/m^2
JSSW	Side wall saturation current density	0	A/m
NJ	Emission coefficient of junction	1	-
IJTH	Diode limiting current	0.1	A
Capacitance			
CJ	Source/drain bottom junction capacitance per unit area	5.0E-4	F/m^2
CJSW	Source/drain side junction capacitance per unit length	5.0E-10 F/m	
CJSWG	Source/drain gate side junction capacitance per unit length	CJSW	F/m
MJ	Bottom junction capacitance grading coefficient	0.5	-
MJSW	Source/drain side junction capacitance grading coefficient	0.33	-
MJSWG	Source/drain gate side junction cap. Grading coefficient	MJSW	-
PB	Bottom junction built-in potential	1.0	V
PBSW	Source/drain side junction built-in potential	1.0	V
PBSWG	Source/drain gate side junction built-in potential	PBSW	V
CGSO	Gate-source overlap capacitance per unit W	XJ*COX/2	F/m

CGDO	Gate-drain overlap capacitance per unit W	XJ*COX/2	F/m
GGBO	Gate-bulk overlap capacitance per unit W	0.0	F/m
CGSL	Light doped source-gate region overlap capacitance	0.0	F/m
CGDL	Light doped drain-gate region overlap capacitance	0.0	F/m
CKAPPA	Coefficient for lightly doped region overlap	0.6	F/m
CF	Fringing field capacitance	-	F/m
CLC	Constant term for the short channel model	0.1E-6	m
CLE	Exponential term for the short channel model	0.6	
DLC	Length offset fitting parameter from C-V	LINT	m
DWC	Width offset fitting parameter from C-V	WINT	m
NOFF	Subthreshold swing factor for CV model	1	-
VOFFCV	Offset voltage for CV model	0	V
Process Related Parameters			
TOXM	Gate oxide thickness at which parameters are extracted	15E-9	m
TOX	Gate oxide thickness	15E-9	m
XJ	Junction depth	150E-9 m	
NCH	Doping concentration near interface	1.7E17	$1/cm^3$
NSUB	Doping concentration away from interface	6E16	$1/cm^3$
NGATE	Poly gate doping concentration	0	$1/cm^3$
VTH	Flat-band voltage	-1.0	V
gamma1	Body-effect near interface	$\gamma_1 = \dfrac{\sqrt{2q\varepsilon_{Si}N_{Ch}}}{C_{ox}}$	$V^{1/2}$
gamma2	Body-effect far from interface	$\gamma_2 = \dfrac{\sqrt{2q\varepsilon_{Si}N_{Sub}}}{C_{ox}}$	$V^{1/2}$
XT	Doping depth	1.55E-7	V
RSH	Source/Drain Sheet resistance	0	$\dfrac{\Omega}{square}$

Appendix D: Additional Simulation Data

Monte Carlo simulation of SiNW 4×10
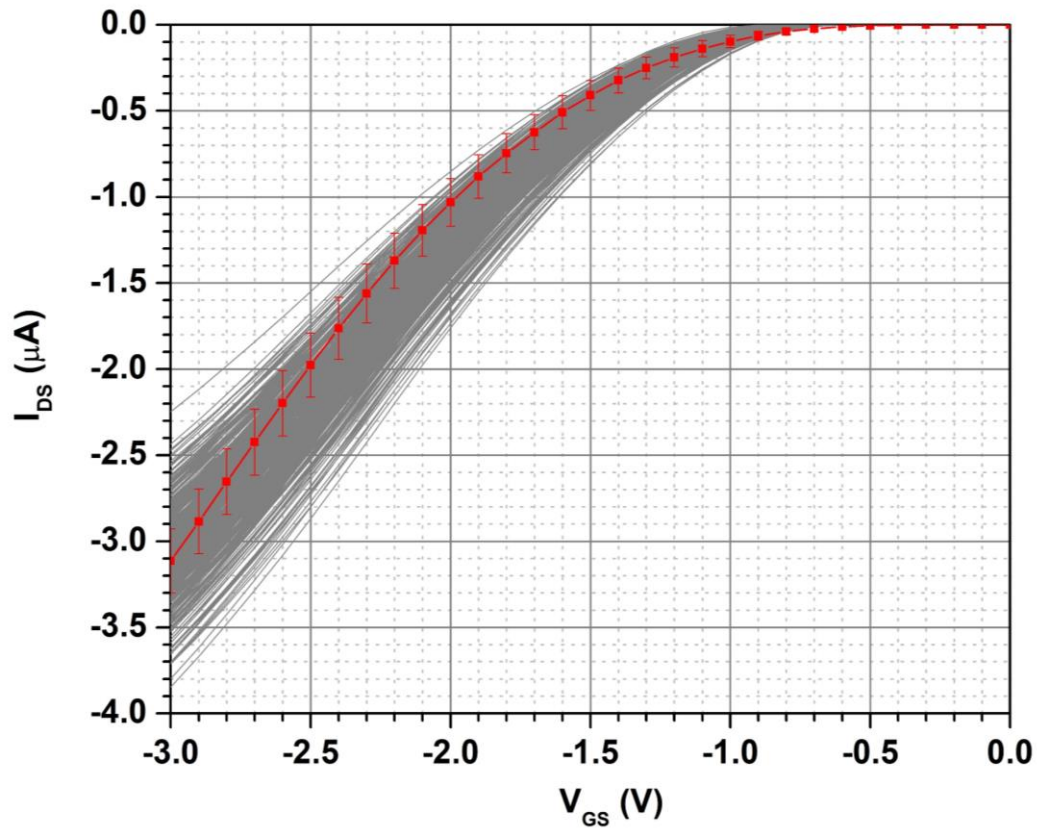
Figure 9-3 500 runs transfer characteristic curves Monte Carlo simulation (grey) when all four main parameters were varied within their tolerances and measurement results (n=8) of 4×10 SiNW chip (V_{DS} = -2 V)

Monte Carlo simulation of SiNW 2×40
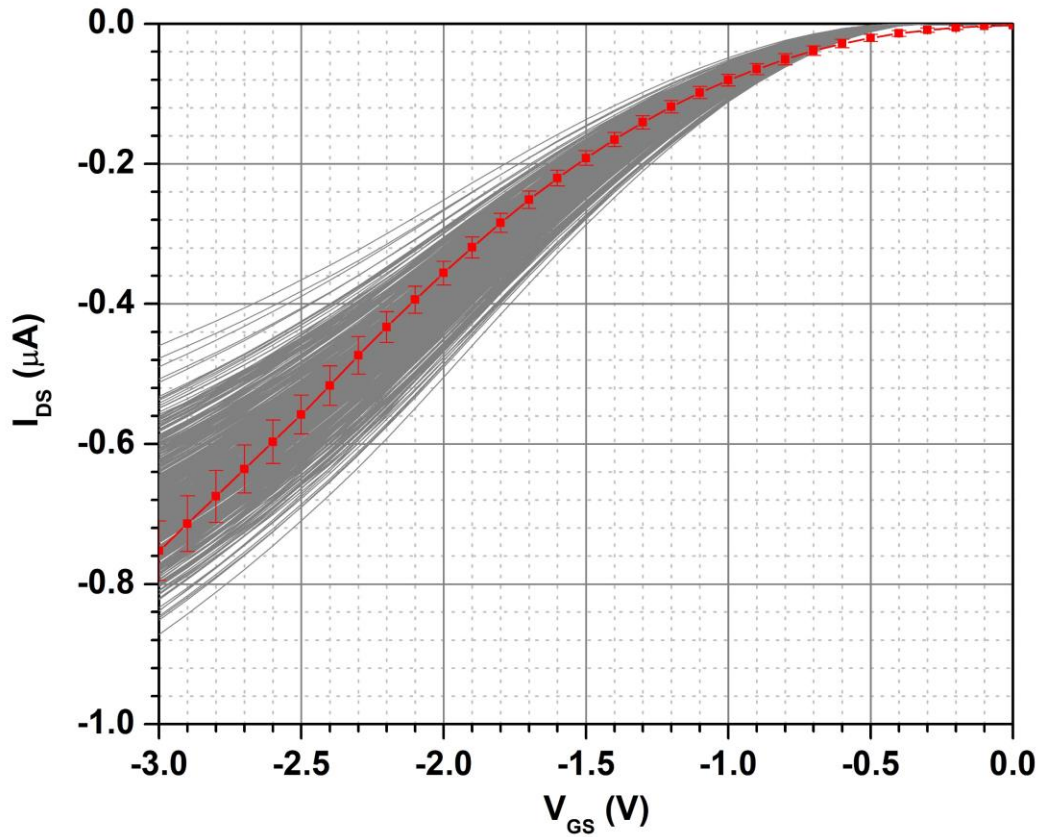
Figure 9-4 500 runs transfer characteristic curves Monte Carlo simulation (grey) when all four main parameters were varied within their tolerances and measurement results (n=4) of 2×40 SiNW chip (V_{DS} = -2 V)

Additional simulation and experimental results for testing the influence of the Solution Resistance

Above line: 2x10 channel (200 nm width and 10 um length)

Channel 05:
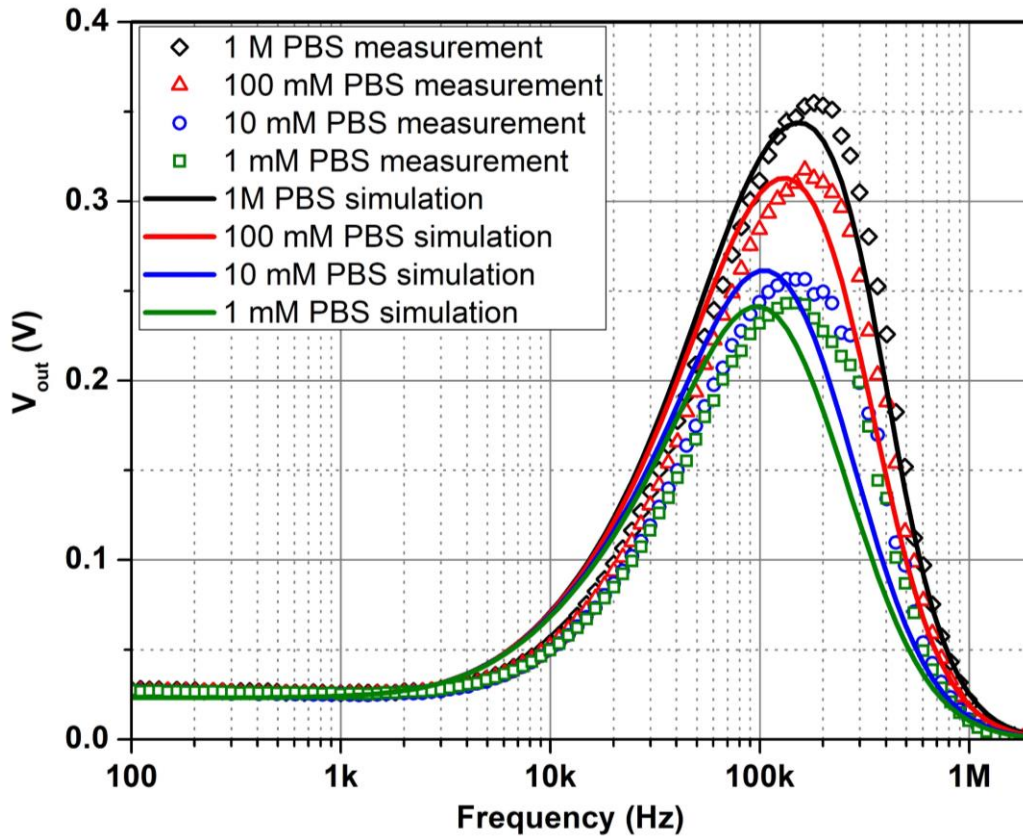
Figure 9-5 Conductivity measurements of different phosphate buffer solutions and corresponding simulation results (channel05A). Parameters of simulation: C_{PD}=30 pF, C_{soure}=50 pF.

Error: 21.7% (Channel05Above_Error.xlsx)

Channel 17Above:
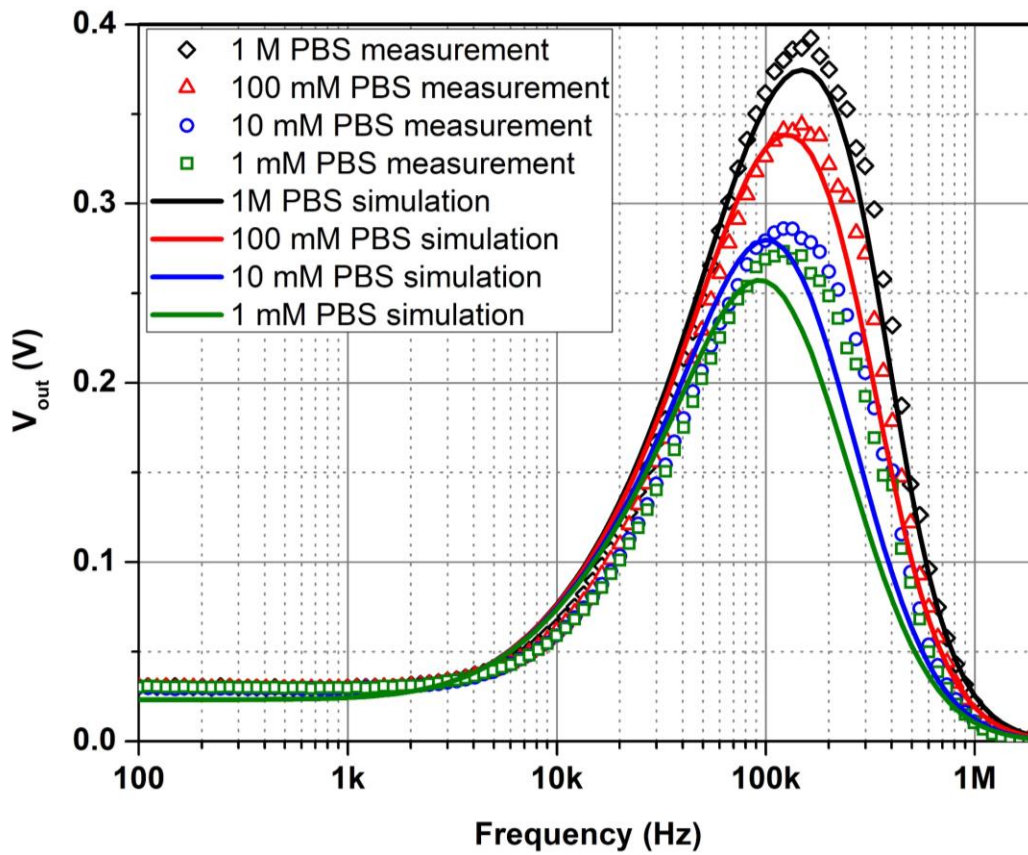
Figure 9-6 Conductivity measurements of different phosphate buffer solutions and corresponding simulation results (channel17A). Parameters of simulation: C_{PD}=33 pF, C_{soure}=50 pF.

Error: 21.3 % (Channel17Above_Error.xlsx)

Below line: 4x10 channel (400 nm width and 10 μm length)

Channel05Below
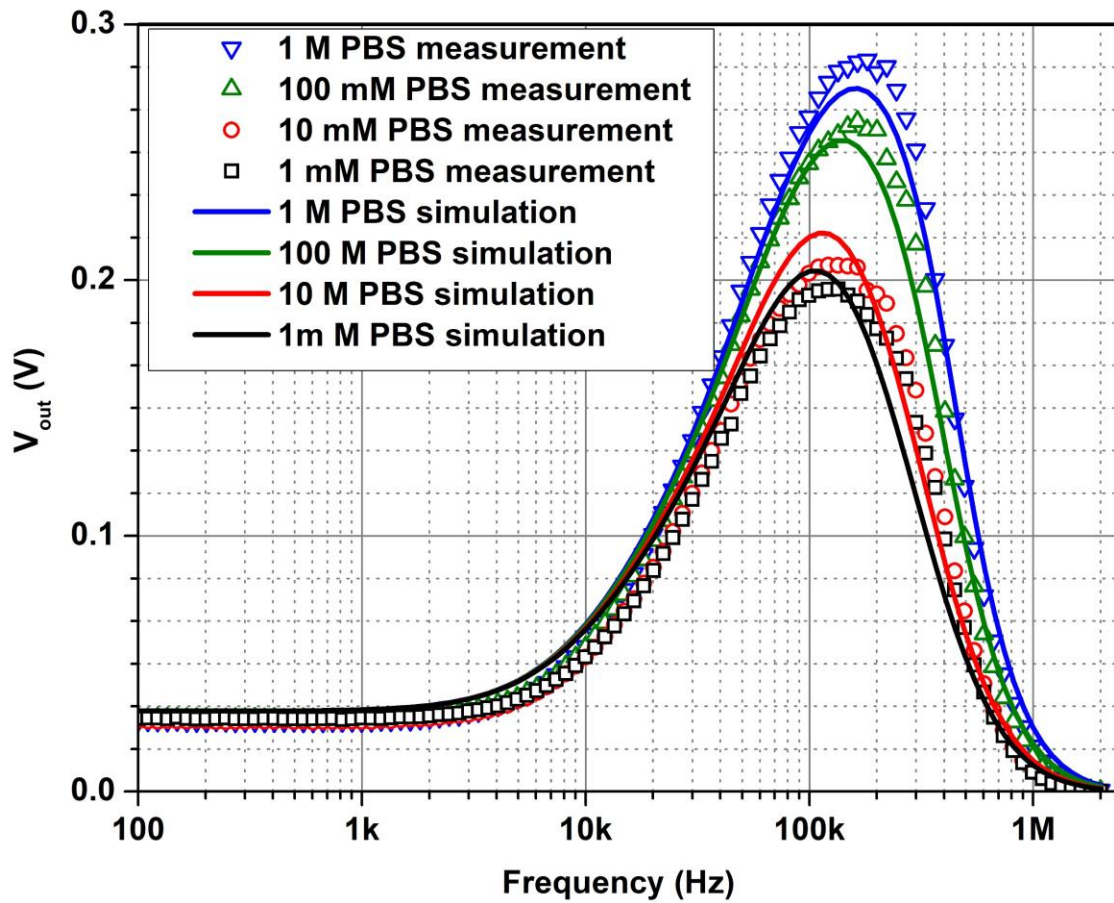
Figure 9-7 Conductivity measurements of different phosphate buffer solutions and corresponding simulation results (channel05B). Parameters of simulation: C_{PD}=23.5 pF, C_{soure}=50 pF.

Error: 18% (Channel05Below_Error.xlsx)

Channel14Below
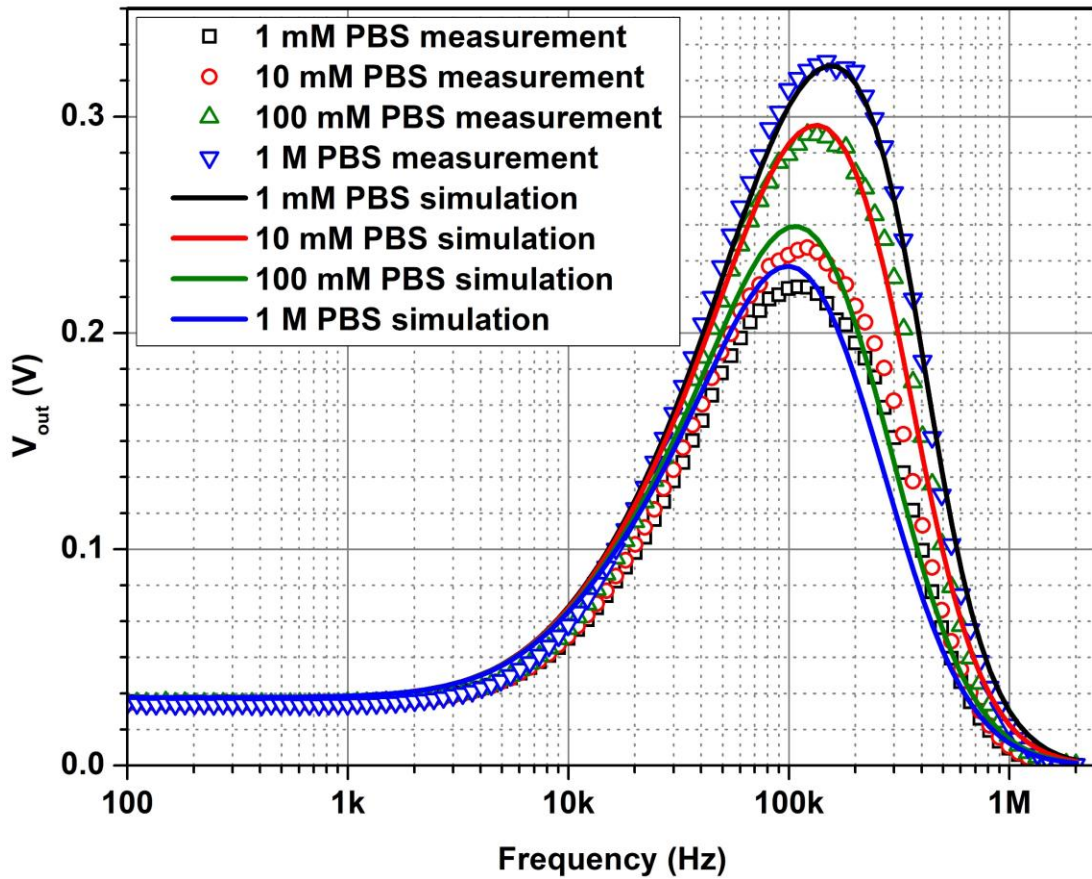
Figure 9-8 Conductivity measurements of different phosphate buffer solutions and corresponding simulation results (channel14B). Parameters of simulation: C_{PD}=28 pF, C_{soure}=50 pF.

Error: 16% (Channel14Below_Error.xlsx)

Channel17Below Line
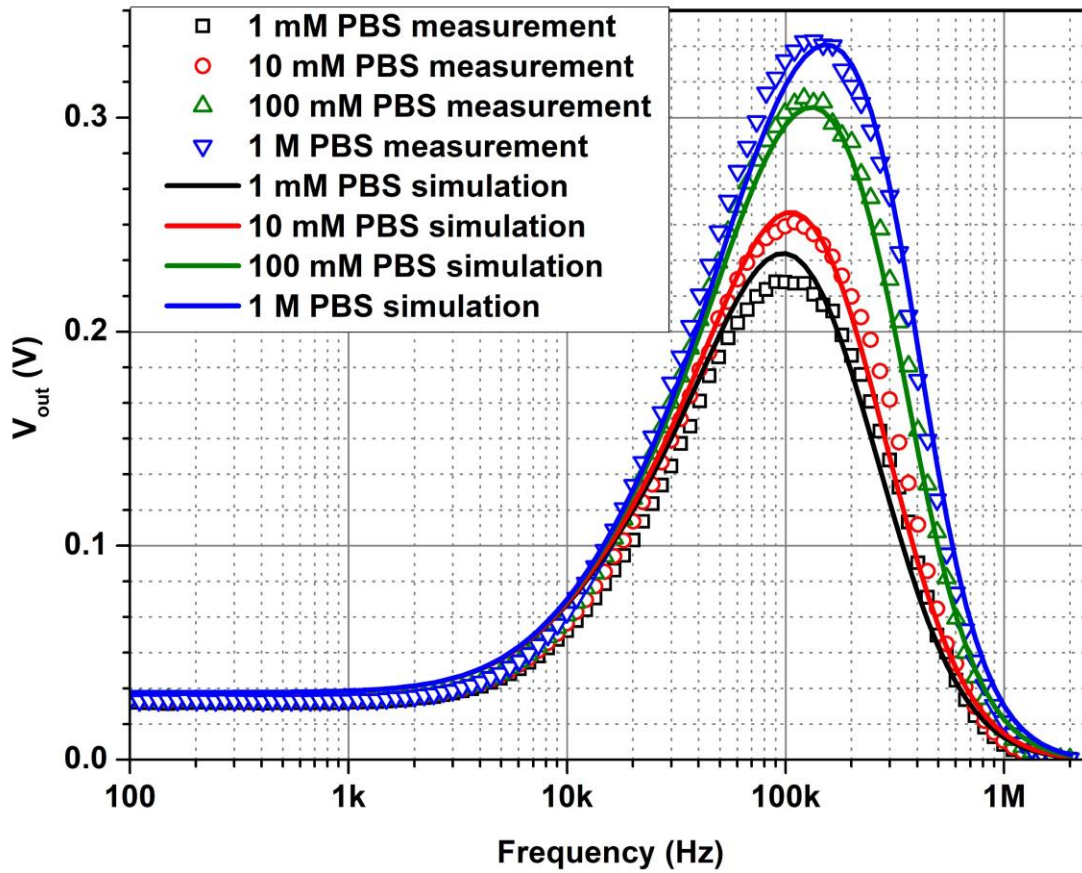
Figure 9-9 Conductivity measurements of different phosphate buffer solutions and corresponding simulation results (channel17 B). Parameters of simulation: C_{PD}=29 pF, C_{soure}=50 pF.

Error: 17.8 % (Channel17Below_Error.xlsx)

Effect of pH on the spectrum recording
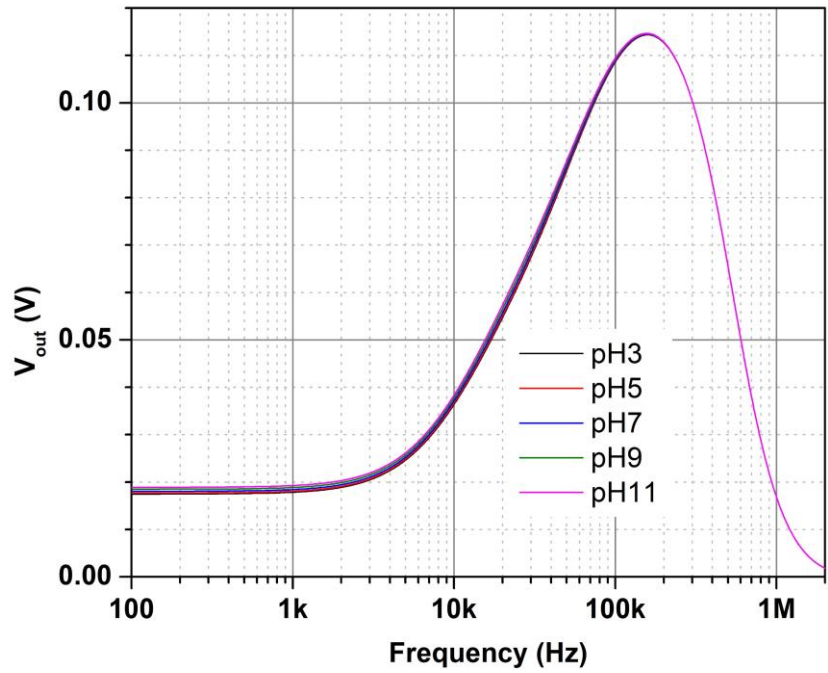
Figure 9-10 Effect of different pH on the spectrum recording
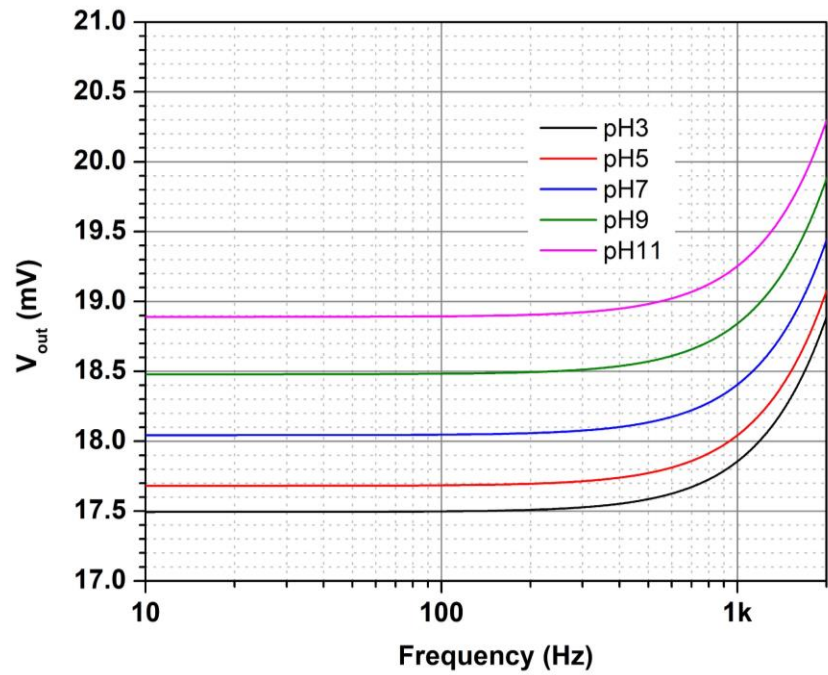
Figure 9-11 Zoom-in pH effect at low frequency component

Effect of SiNW width on the spectrum recording
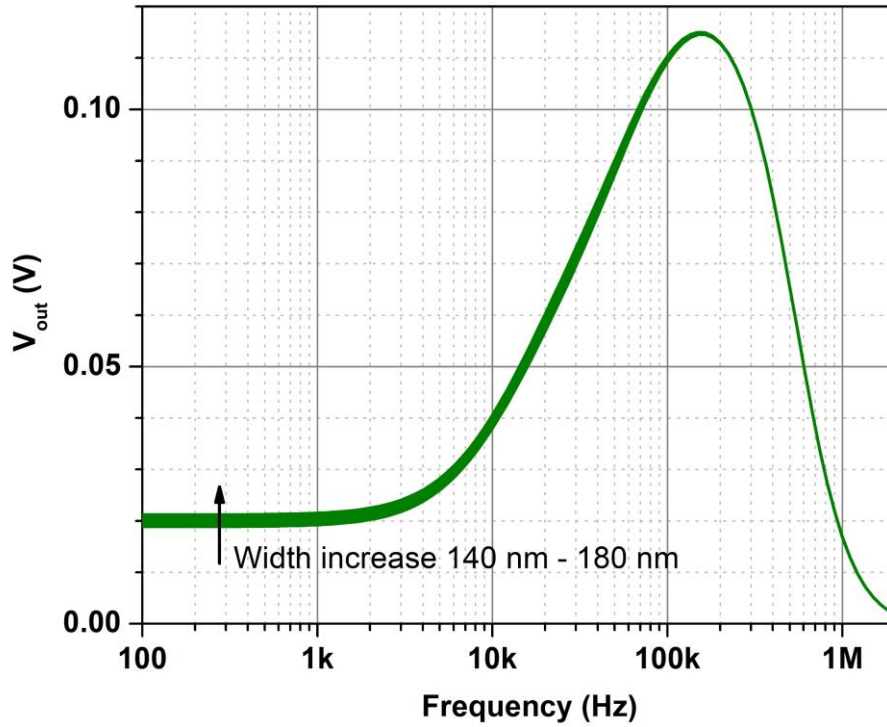
Figure 9-12 Effect of SiNW width on the spectrum recording (SiNW 2×10)

Effect of silicon oxide thickness at the gate surface of SiNW on the spectrum recording
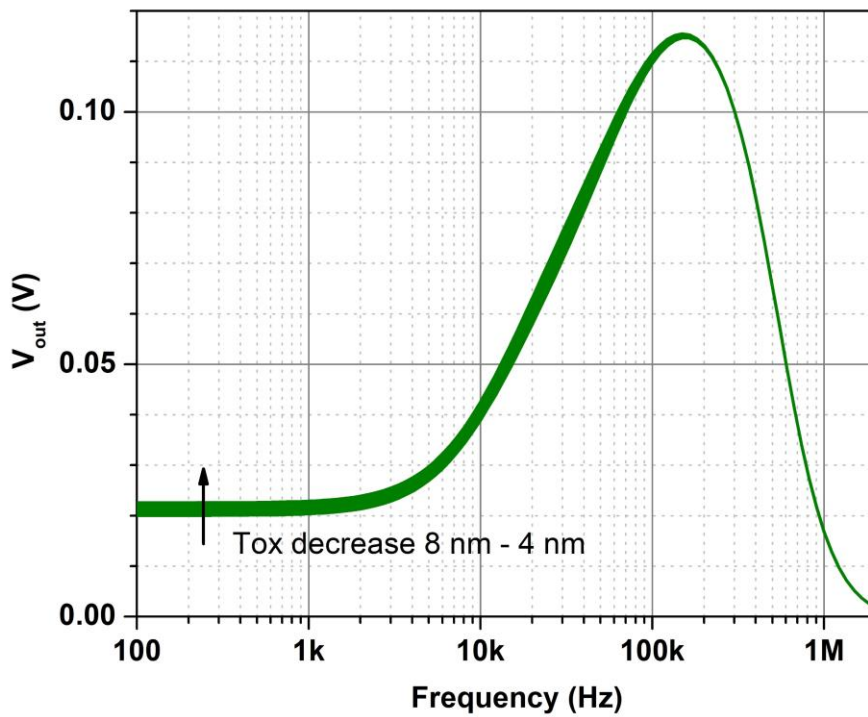
Figure 9-13 Effect of oxide thickness Tox on the spectrum recording (SiNW 2×10)

Effect of threshold voltage on the spectrum recording
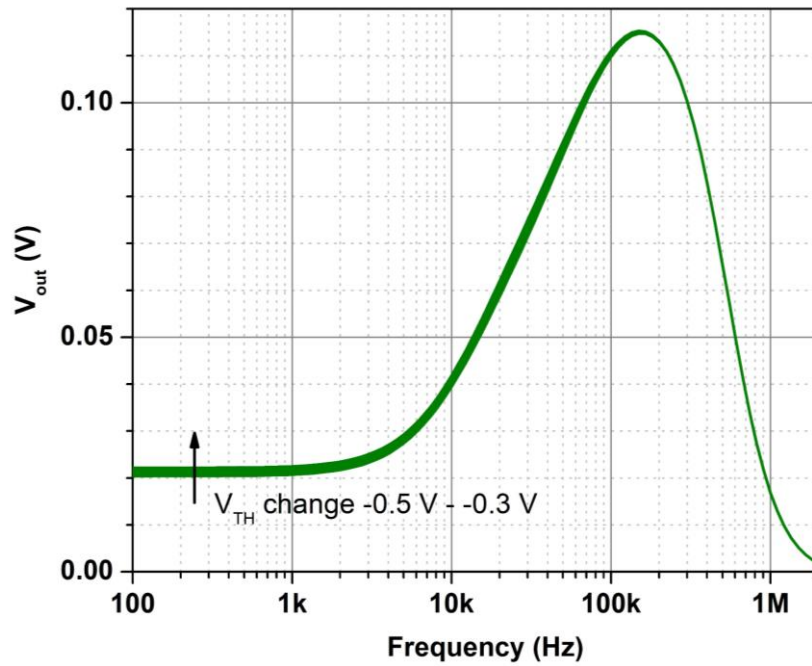
Figure 9-14 Effect of V_{TH} on the spectrum recording

All parameters were varied: width, SiNW thickness, threshold voltage and oxide thickness
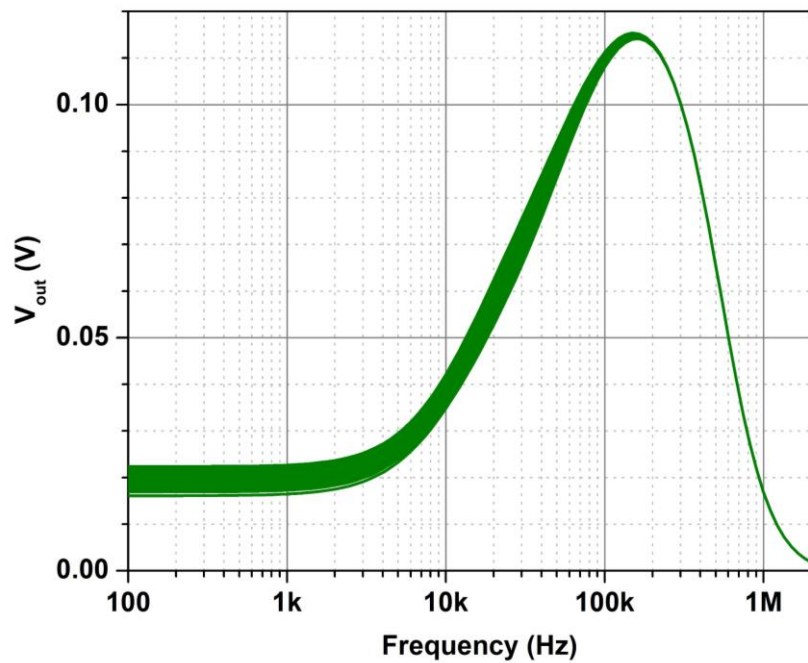
Figure 9-15 Effect of all four main parameters on the spectrum recording

Appendix E: Chips used in the presented results

Figure	Chips used	Layout (array)	Fabrication processes	No. Channels / no. Chip
Figure 4-5	ISFET 25 μm × 5 μm	4 × 4	[142]	1/1
Figure 4-6 Figure 4-7	SiNW 200 nm, 400 nm width; 10 μm, 20 μm, 40 μm length	28 × 2	[64]	1/1
Figure 4-9	SiNW 400 nm × 10 μm	28 × 2	[64]	1/1
Figure 5-10 (left)	ISFET 16 μm × 7 μm	4 × 4	[139]	16/1
Figure 5-10 (right)	SiNW 400 nm × 20 μm	28 × 2	[64]	32/1
Figure 5-11	ISFET 16 μm × 7 μm	4 × 4	[139]	1/1
Figure 5-13	ISFET 16 μm × 7 μm	4 × 4	[139]	16/1
Figure 5-16	ISFET 16 μm × 7 μm	4 × 4	[139]	4/1
Figure 5-17	ISFET 16 μm × 7 μm	4 × 4	[139]	4/1
Figure 5-20	ISFET 16 μm × 7 μm	4 × 4	[139]	7/2
Figure 5-23	ISFET 16 μm × 7 μm	4 × 4	[139]	1/1
Figure 6-1	ISFET 16 μm × 7 μm	4 × 4	[139]	8/2
Figure 6-2	ISFET 16 μm × 7 μm	4 × 4	[139]	8/2
Figure 6-5	ISFET 16 μm × 7 μm	4 × 4	[139]	1/1
	ISFET 12 μm × 4 μm		[142]	1/1
Figure 6-6	ISFET 16 μm × 7 μm	4 × 4	[139]	8/1
Figure 6-7	SiNW 400 nm × 10 μm	28 × 2	[64]	1/1
Figure 6-8	ISFET 16 μm × 7 μm	4 × 4	[139]	8/1
Figure 6-9	SiNW 400 nm × 10 μm	28 × 2	[64]	5/1
Figure 6-11	SiNW 200 nm × 10 μm	28 × 2	[64]	1/1
Figure 6-12	SiNW 200 nm × 10 μm	28 × 2	[64]	1/1
Figure 6-13	SiNW 200 nm × 10 μm	28 × 2	[64]	1/1
Figure 7-3	SiNW 200 nm × 10 μm	28 × 2	[64]	3/1
Figure 7-6	SiNW 200 nm × 10 μm	28 × 2	[64]	1/1
Figure 7-8	SiNW 200 nm × 10 μm	28 × 2	[64]	28/3
	SiNW 400 nm × 10 μm			13/2
Figure 7-26	SiNW 200 nm × 10 μm	28 × 2	[64]	2/1
	SiNW 400 nm × 10 μm	28 × 2	[64	3/1

Appendix F: Passivation Capacitance Measurements

CV Sweep: V_{GD}: -2 V to 2 V step -0.1 V

Frequency: 1MHz

AC voltage: 30 mV

Solution: 100 mM PBS, pH 7.5
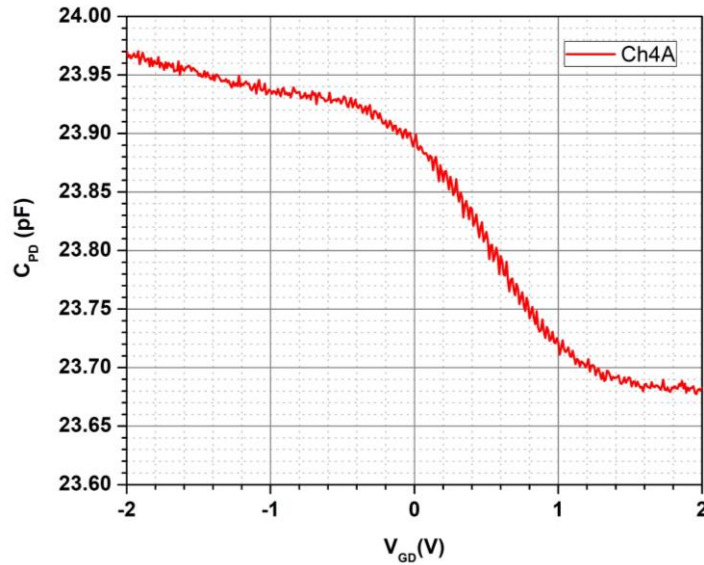
Figure 9-16 Capacitance vs. voltage measurement
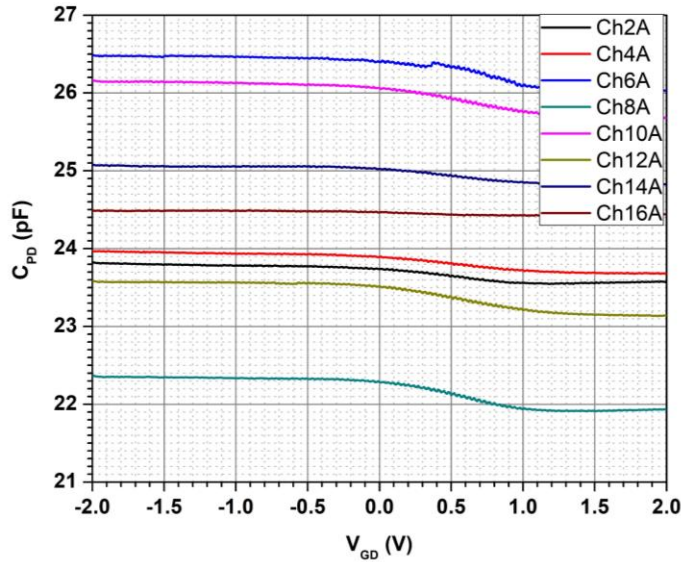
Figure 9-17 Capacitance measurements with different sensors channels on one 4×10 SiNW FET chip

Bibliography and Indices

Bibliography

[1]   Etzioni R, Urban N, Ramsey S, McIntosh M, Schwartz S, Reid B, Radich J, Anderson G, Hartwell L. Early detection: The case for early detection. *Nature Reviews Cancer*. 2003;3(4):243-252. doi:10.1038/nrc1041.

[2]   Hay Burgess DC, Wasserman J, Dahl CA. Global health diagnostics. *Nature*. 2006;444:1-2. doi:10.1038/nature05440.

[3]   Bohunicky B, Mousa SA. Biosensors: the new wave in cancer diagnosis. *Nanotechnology, science and applications*. 2010;4:1-10. doi:10.2147/NSA.S13465.

[4]   Narsaiah K, Jha SN, Bhardwaj R, Sharma R, Kumar R. Optical biosensors for food quality and safety assurance-a review. *Journal of food science and technology*. 2012;49(4):383-406. doi:10.1007/s13197-011-0437-6.

[5]   Farahi RH, Passian A, Tetard L, Thundat T. Critical issues in sensor science to aid food and water safety. *ACS Nano*. 2012;6(6):4548-4556. doi:10.1021/nn204999j.

[6]   Morris MC. Fluorescent biosensors — Probing protein kinase function in cancer and drug discovery. *Biochimica et Biophysica Acta (BBA) - Proteins and Proteomics*. 2013;1834(7):1387-1395. doi:10.1016/j.bbapap.2013.01.025.

[7]   Babington R, Matas S, Marco MP, Galve R. Current bioanalytical methods for detection of penicillins. *Analytical and Bioanalytical Chemistry*. 2012;403(6):1549-1566. doi:10.1007/s00216-012-5960-4.

[8]   Fraden J. *Handbook of Modern Sensors*. 3rd ed. New York, NY: Springer New York; 2010. doi:10.1007/978-1-4419-6466-3.

[9]   Li S, Singh J, Li H, Banerjee IA. *Biosensor Nanomaterials*. Weinheim, Germany: Wiley-VCH Verlag GmbH & Co. KGaA; 2011. doi:10.1002/9783527635160.

[10]   Wilson J. *Sensor Technology Handbook*. 1st ed. Newnes; 2004. http://store.elsevier.com/Sensor-Technology-Handbook/Jon-Wilson/isbn-9780750677295/. Accessed February 23, 2016.

[11]   Cooper MA. *Label-Free Biosensors Techniques and Application*. Cambridge University Press; 2009. http://www.cambridge.org/us/academic/subjects/life-sciences/molecular-biology-biochemistry-and-structural-biology/label-free-biosensors-techniques-and-applications. Accessed February 24, 2016.

[12]   Wang J. Electrochemical biosensors: Towards point-of-care cancer diagnostics. *Biosensors and Bioelectronics*. 2006;21(10):1887-1892. doi:10.1016/j.bios.2005.10.027.

[13]   Willner I, Willner B. Biomolecule-based nanomaterials and nanostructures. *Nano Letters*. 2010;10(10):3805-3815. doi:10.1021/nl102083j.

[14]   Yager P, Domingo GJ, Gerdes J. point-of-care diagnostics for global health. *Annual Review of Biomedical Engineering*. 2008;10(1):107-144. doi:10.1146/annurev.bioeng.10.061807.160524.

[15]   Iqbal SS, Mayo MW, Bruno JG, Bronk B V, Batt CA, Chambers JP. A review of molecular recognition technologies for detection of biological threat agents. *Biosensors and Bioelectronics*. 2000;15(11-12):549-578. doi:10.1016/S0956-5663(00)00108-1.

[16]   Caygill RL, Blair GE, Millner PA. A review on viral biosensors to detect human pathogens. *Analytica chimica acta*. 2010;681(1-2):8-15. doi:10.1016/j.aca.2010.09.038.

[17]   Ibraheem A, Campbell RE. Designs and applications of fluorescent protein-based biosensors. *Current Opinion in Chemical Biology*. 2010;14(1):30-36. doi:10.1016/j.cbpa.2009.09.033.

[18]   Cooper EB. *Silicon Field-Effect Sensors for Biomolecular Assays*. PhD Thesis, Dept. of Electrical Engineering and Computer Science, Massachusetts Institute of Technology; 2003. http://dspace.mit.edu/handle/1721.1/87450. Accessed April 7, 2015.

[19]   Sun YS, Landry JP, Fei YY, Zhu XD, Luo JT, Wang XB, Lam KS. Effect of fluorescently labeling protein probes on kinetics of protein−ligand reactions. *Langmuir*. 2008;24(23):13399-13405. doi:10.1021/la802097z.

[20]   Daniels JS, Pourmand N. Label-free impedance biosensors: opportunities and challenges. *Electroanalysis*. 2007;19(12):1239-1257. doi:10.1002/elan.200603855.

[21]   O'Sullivan CK, Guilbault GG. Commercial quartz crystal microbalances – theory and applications. *Biosensors and Bioelectronics*. 1999;14(8-9):663-670. doi:10.1016/S0956-5663(99)00040-8.

[22]   Speight RE, Cooper MA. A Survey of the 2010 Quartz crystal microbalance literature. *Journal of Molecular Recognition*. 2012;25(9):451-473. doi:10.1002/jmr.2209.

[23]   Homola J, Yee SS, Gauglitz G. Surface plasmon resonance sensors: review. *Sensors and Actuators B: Chemical*. 1999;54(1-2):3-15. doi:10.1016/S0925-4005(98)00321-9.

[24]   Köβlinger C, Uttenthaler E, Drost S, Aberl F, Wolf H, Brink G, Stanglmaier A, Sackmann E. Comparison of the QCM and the SPR method for surface studies and immunological applications. *Sensors and Actuators B: Chemical*. 1995;24(1-3):107-112. doi:10.1016/0925-4005(95)85023-6.

[25]   *Technical Note 103: Surface Plasmon Resonance v. Quartz Crystal Microbalance*. Biosensing Instrument Inc.; 2010. http://biosensingusa.com/technical-notes/technical-note-103-surface-plasmon-resonance-v-quartz-crystal-microbalance/. Accessed March 2, 2016.

[26]   Bergveld P. Development of an ion-sensitive solid-state device for neurophysiological measurements. *IEEE Transactions on Biomedical Engineering*. 1970;BME-17(1):70-71. doi:10.1109/TBME.1970.4502688.

[27]   Bergveld P. Development, operation, and application of the ion-sensitive field-effect transistor as a tool for electrophysiology. *IEEE Transactions on Biomedical Engineering*. 1972;BME-19(5):342-351. doi:10.1109/TBME.1972.324137.

[28]   Moss SD, Janata J, Johnson CC. Potassium ion-sensitive field effect transistor. *Analytical Chemistry*. 1975;47(13):2238-2243. doi:10.1021/ac60363a005.

[29]   Abe H, Esashi M, Matsuo T. ISFET's using inorganic gate thin films. *IEEE Transactions on Electron Devices*. 1979;26(12):1939-1944. doi:10.1109/T-ED.1979.19799.

[30] Bousse L, De Rooij NF, Bergveld P. Operation of chemically sensitive field-effect sensors as a function of the insulator-electrolyte interface. *IEEE Transactions on Electron Devices*. 1983;30(10):1263-1270. doi:10.1109/T-ED.1983.21284.

[31] Wolf B, Brischwein M, Baumann W, Ehret R, Henning T, Lehmann M, Schwinde A. Microsensor-aided measurements of cellular signalling and metabolism on tumor cells. *Tumor Biology*. 1998;19(5):374-383. doi:10.1159/000030030.

[32] Ehret R, Baumann W, Brischwein M, Lehmann M, Henning T, Freund I, Drechsler S, Friedrich U, Kob A, Palzer H, Motrescu E, Hubert M-L, Grothe H, Wolf B. Multiparametric microsensor chips for screening applications. *Fresenius' Journal of Analytical Chemistry*. 2001;369(1):30-35. doi:10.1007/s002160000628.

[33] Voelker M, Fromherz P. Signal transmission from individual mammalian nerve cell to field-effect transistor. *Small*. 2005;1(2):206-210. doi:10.1002/smll.200400077.

[34] Sprössler C, Denyer M, Britland S, Knoll W, Offenhäusser A. Electrical recordings from rat cardiac muscle cells using field-effect transistors. *Physical Review E*. 1999;60(2):2171-2176. doi:10.1103/PhysRevE.60.2171.

[35] Schöning MJ, Poghossian A. Recent advances in biologically sensitive field-effect transistors (BioFETs). *The Analyst*. 2002;127(9):1137-1151. doi:10.1039/B204444G.

[36] Straub B, Meyer E, Fromherz P. Recombinant maxi-K channels on transistor, a prototype of iono-electronic interfacing. *Nature Biotechnology*. 2001;19(2):121-124. doi:10.1038/84369.

[37] Kharitonov AB, Zayats M, Lichtenstein A, Katz E, Willner I. Enzyme monolayer-functionalized field-effect transistors for biosensor applications. *Sensors and Actuators B: Chemical*. 2000;70(1-3):222-231. doi:10.1016/S0925-4005(00)00573-6.

[38] Caras S, Janata J. Field effect transistor sensitive to penicillin. *Analytical Chemistry*. 1980;52(12):1935-1937. doi:10.1021/ac50062a035.

[39] Schasfoort RBM, Kooyman RPH, Bergveld P, Greve J. A new approach to immunoFET operation. *Biosensors and Bioelectronics*. 1990;5(2):103-124. doi:10.1016/0956-5663(90)80002-U.

[40] Souteyrand E, Cloarec JP, Martin JR, Wilson C, Lawrence I, Mikkelsen S, Lawrence MF. Direct detection of the hybridization of synthetic homo-oligomer DNA sequences by field effect. *The Journal of Physical Chemistry B*. 1997;101(15):2980-2985. doi:10.1021/jp963056h.

[41] Nair PR, Alam MA. Design considerations of silicon nanowire biosensors. *IEEE Transactions on Electron Devices*. 2007;54(12):3400-3408. doi:10.1109/TED.2007.909059.

[42] Cui Y, Lieber CM. Functional nanoscale electronic devices assembled using silicon nanowire building blocks. *Science*. 2001;291(5505):851-853. doi:10.1126/science.291.5505.851.

[43] Curreli M, Ishikawa FN, Cote RJ, Thompson ME. Real-time, label-free detection of biological entities using nanowire-based FETs. *IEEE Transactions on Nanotechnology*. 2008;7(6):651-667. doi:10.1109/TNANO.2008.2006165.

[44] Yang P, Yan R, Fardy M. Semiconductor nanowire: what's next? *Nano Letters*. 2010;10(5):1529-1536. doi:10.1021/nl100665r.

[45] Cui Y, Wei Q, Park H, Lieber CM. Nanowire nanosensors for highly sensitive and selective detection of biological and chemical species. *Science*. 2001;293(5533):1289-1292. doi:10.1126/science.1062711.

[46] Wang WU, Chen C, Lin K-H, Fang Y, Lieber CM. Label-free detection of small-molecule-protein interactions by using nanowire nanosensors. *Proceedings of the National Academy of Sciences*. 2005;102(9):3208-3212. doi:10.1073/pnas.0406368102.

[47] Zheng G, Patolsky F, Cui Y, Wang WU, Lieber CM. Multiplexed electrical detection of cancer markers with nanowire sensor arrays. *Nature Biotechnology*. 2005;23(10):1294-1301. doi:10.1038/nbt1138.

[48] Gao Z, Agarwal A, Trigg AD, Singh N, Fang C, Tung CH, Fan Y, Buddharaju KD, Kong J. Silicon nanowire arrays for label-free detection of DNA. *Analytical chemistry*. 2007;79(9):3291-3297. doi:10.1021/ac061808q.

[49] Gao A, Lu N, Dai P, Li T, Pei H, Gao X, Gong Y, Wang Y, Fan C. Silicon-nanowire-based CMOS-compatible field-effect transistor nanosensors for ultrasensitive electrical detection of nucleic acids. *Nano Letters*. 2011;11(9):3974-3978. doi:10.1021/nl202303y.

[50] Hahm J, Lieber CM. Direct ultrasensitive electrical detection of DNA and DNA sequence variations using nanowire nanosensors. *Nano Letters*. 2004;4(1):51-54. doi:10.1021/nl034853b.

[51] Zheng G, Patolsky F, Lieber CM. Multiplexed electrical detection of single viruses. *MRS Proceedings*. 2004;828:A2.2. doi:10.1557/PROC-828-A2.2.

[52] Eschermann JF, Stockmann R, Hueske M, Vu XT, Ingebrandt S, Offenhäusser A. Action potentials of HL-1 cells recorded with silicon nanowire transistors. *Applied Physics Letters*. 2009;95(83703):1-3. doi:10.1063/1.3194138.

[53] Patolsky F, Timko BP, Yu G, Fang Y, Greytak AB, Zheng G, Lieber CM. Detection, stimulation, and inhibition of neuronal signals with high-density nanowire transistor arrays. *Science*. 2006;313(5790):1100-1104. doi:10.1126/science.1128640.

[54] Cui Y, Lauhon LJ, Gudiksen MS, Wang J, Lieber CM. Diameter-controlled synthesis of single-crystal silicon nanowires. *Applied Physics Letters*. 2001;78(15):2214-2216. doi:10.1063/1.1363692.

[55] Lu W, Lieber CM. Nanoelectronics from the bottom up. *Nature Materials*. 2007;6(11):841-850. doi:10.1038/nmat2028.

[56] Stern E, Cheng G, Cimpoiasu E, Klie R, Guthrie S, Klemic J, Kretzschmar I, Steinlauf E, Turner-Evans DB, Broomfield E, Hyland J, Koudelka R, Boone T, Young M, Sanders A, Munden R, Lee T, Routenberg D, Reed MA. Electrical characterization of single GaN nanowires. *Nanotechnology*. 2005;16(12):2941-2953. doi:10.1088/0957-4484/16/12/037.

[57] Stern E, Klemic JF, Routenberg DA, Wyrembak PN, Turner-Evans DB, Hamilton AD, LaVan DA, Fahmy TM, Reed MA. Label-free immunodetection with CMOS-compatible semiconducting nanowires. *Nature*. 2007;445(7127):519-522. doi:10.1038/nature05498.

[58]   Martinez JA, Misra N, Wang Y, Stroeve P, Grigoropoulos CP, Noy A. Highly efficient biocompatible single silicon nanowire electrodes with functional biological pore channels. *Nano Letters*. 2009;9(3):1121-1126. doi:10.1021/nl8036504.

[59]   Vu XT, Stockmann R, Wolfrum B, Offenhäusser A, Ingebrandt S. Fabrication and application of a microfluidic-embedded silicon nanowire biosensor chip. *physica status solidi (a)*. 2010;207(4):850-857. doi:10.1002/pssa.200983316.

[60]   Vu XT, Eschermann JF, Stockmann R, GhoshMoulick R, Offenhäusser A, Ingebrandt S. Top-down processed silicon nanowire transistor arrays for biosensing. *physica status solidi (a)*. 2009;206(3):426-434. doi:10.1002/pssa.200880475.

[61]   Knopfmacher O, Tarasov A, Fu W, Wipf M, Niesen B, Calame M, Schönenberger C. Nernst limit in dual-gated Si-nanowire FET sensors. *Nano letters*. 2010;10(6):2268-2274. doi:10.1021/nl100892y.

[62]   Li Z, Chen Y, Li X, Kamins TI, Nauka K, Williams RS. Sequence-specific label-free DNA sensors based on silicon nanowires. *Nano Letters*. 2004;4(2):245-247. doi:10.1021/nl034958e.

[63]   Chen Y, Wang X, Erramilli S, Mohanty P, Kalinowski A. Silicon-based nanoelectronic field-effect pH sensor with local gate control. *Applied Physics Letters*. 2006;89(22):223512. doi:10.1063/1.2392828.

[64]   Vu XT. *Silicon Nanowire Transistor Arrays for Biomolecular Detection*. PhD Thesis, Faculty of Mathematics, Computer science, and Natural sciences, RWTH Aachen University; 2011. http://juser.fz-juelich.de/record/15536?ln=de. Accessed September 3, 2017.

[65]   Israelachvili JN. *Intermolecular and Surface Forces*. 3rd ed. Academic Press; 2011.

[66]   Butt HJ, Graf K, Kappl M. *Physics and Chemistry of Interfaces*. Weinheim, FRG: Wiley-VCH Verlag GmbH & Co. KGaA; 2003. doi:10.1002/3527602313.

[67]   Bergveld P. The future of biosensors. *Sensors and Actuators A: Physical*. 1996;56(1-2):65-73. doi:10.1016/0924-4247(96)01275-7.

[68]   Koch S, Woias P, Meixner LK, Drost S, Wolf H. Protein detection with a novel ISFET-based zeta potential analyzer. *Biosensors and Bioelectronics*. 1999;14(4):413-421. doi:10.1016/S0956-5663(99)00008-1.

[69]   Sørensen MH, Mortensen NA, Brandbyge M. Screening model for nanowire surface-charge sensors in liquid. *Applied Physics Letters*. 2007;91(102105):1-3. doi:10.1063/1.2779930.

[70]   Stern E, Wagner R, Sigworth FJ, Breaker R, Fahmy TM, Reed MA. Importance of the Debye screening length on nanowire field effect transistor Sensors. *Nano Letters*. 2007;7(11):3405-3409. doi:10.1021/nl071792z.

[71]   Nair PR, Alam MA. Screening-limited response of nanobiosensors. *Nano Letters*. 2008;8(5):1281-1285. doi:10.1021/nl072593i.

[72]   Antonisse MMG, Snellink-Ruël BHM, Lugtenberg RJW, Engbersen JFJ, van den Berg A, Reinhoudt DN. Membrane characterization of anion-selective CHEMFETs by impedance spectroscopy. *Analytical Chemistry*. 2000;72(2):343-348. doi:10.1021/ac990721k.

[73] Kharitonov AB, Wasserman J, Katz E, Willner I. The use of impedance spectroscopy for the characterization of protein-modified ISFET devices: application of the method for the analysis of biorecognition processes. *The Journal of Physical Chemistry B*. 2001;105(19):4205-4213. doi:10.1021/jp0045383.

[74] Schäfer S, Eick S, Hofmann B, Dufaux T, Stockmann R, Wrobel G, Offenhäusser A, Ingebrandt S. Time-dependent observation of individual cellular binding events to field-effect transistors. *Biosensors and Bioelectronics*. 2009;24(5):1201-1208. doi:10.1016/j.bios.2008.07.003.

[75] Susloparova A, Koppenhöfer D, Vu XT, Weil M, Ingebrandt S. Impedance spectroscopy with field-effect transistor arrays for the analysis of anti-cancer drug action on individual cells. *Biosensors and Bioelectronics*. 2013;40(1):50-56. doi:10.1016/j.bios.2012.06.006.

[76] Ingebrandt S, Han Y, Nakamura F, Poghossian A, Schöning MJ, Offenhäusser A. Label-free detection of single nucleotide polymorphisms utilizing the differential transfer function of field-effect transistors. *Biosens Bioelectron*. 2007;22(12):2834-2840. doi:10.1016/j.bios.2006.11.019.

[77] Bratov A, Abramova N, Ipatov A. Recent trends in potentiometric sensor arrays—A review. *Analytica Chimica Acta*. 2010;678(2):149-159. doi:10.1016/j.aca.2010.08.035.

[78] Mamińska R, Dybko A, Wróblewski W. All-solid-state miniaturised planar reference electrodes based on ionic liquids. *Sensors and Actuators B: Chemical*. 2006;115(1):552-557. doi:10.1016/j.snb.2005.10.018.

[79] Polk BJ, Stelzenmuller A, Mijares G, MacCrehan W, Gaitan M. Ag/AgCl microelectrodes with improved stability for microfluidics. *Sensors and Actuators B: Chemical*. 2006;114(1):239-247. doi:10.1016/j.snb.2005.03.121.

[80] Johnson KW. Reproducible electrodeposition of biomolecules for the fabrication of miniature electroenzymatic biosensors. *Sensors and Actuators B: Chemical*. 1991;5(1):85-89. doi:10.1016/0925-4005(91)80225-9.

[81] Desmond D, Lane B, Alderman J, Glennon JD, Diamond D, Arrigan DW. Evaluation of miniaturised solid state reference electrodes on a silicon based component. *Sensors and Actuators B: Chemical*. 1997;44(1-3):389-396. doi:10.1016/S0925-4005(97)00231-1.

[82] Han Y, Offenhäusser A, Ingebrandt S. Detection of DNA hybridization by a field-effect transistor with covalently attached catcher molecules. *Surface and Interface Analysis*. 2006;38(4):176-181. doi:10.1002/sia.2157.

[83] Vu XT, GhoshMoulick R, Eschermann JF, Stockmann R, Offenhäusser A, Ingebrandt S. Fabrication and application of silicon nanowire transistor arrays for biomolecular detection. *Sensors and Actuators B: Chemical*. 2010;144(2):354-360. doi:10.1016/j.snb.2008.11.048.

[84] Nguyen TC, Vu XT, Freyler M, Ingebrandt S. PSPICE model for silicon nanowire field-effect transistor biosensors in impedimetric measurement mode. *physica status solidi (a)*. 2013;210(5):870-876. doi:10.1002/pssa.201200919.

[85] Katz E, Willner I. Probing biomolecular interactions at conductive and semiconductive surfaces by impedance spectroscopy: routes to impedimetric immunosensors, DNA-sensors, and enzyme biosensors. *Electroanalysis*. 2003;15(11):913-947.

doi:10.1002/elan.200390114.

[86]   *Autolab Application Note EIS01: Electrochemical Impedance Spectroscopy (EIS Part 1 – Basic Principles).* Metrohm AG; 2011. https://www.metrohm.com/en-gb/applications/%7BDC34407C-240D-4824-B5EE-FE179CD506D7%7D. Accessed November 21, 2016.

[87]   Rodriguez MC, Kawde A-N, Wang J, Hermann T, Patel DJ, Mukhopadhyay R, McGown LB, Joseph MJ, Pitner JB, Vonk GP, Linn CP, Baldrich E, Restrepo A, O'Sullivan CK, Merino EJ, Weeks KM, McCauley TG, Hamaguchi N, Stanton M, Liu J, Lu Y, Pavlov V, Xiao Y, Shlyabovsky B, Willner I, Nutio R, Li Y, Stojanovic MN, Kolpashchikov DM, Dijksma M, Kamp B, Hoogvliet JC, Bennekom WP van, Ruan C, Yang L, Li Y, Bardea A, Katz E, Willner I, Righetti PG, Tudor G, Ek K. Aptamer biosensor for label-free impedance spectroscopy detection of proteins based on recognition-induced switching of the surface charge. *Chemical Communications*. 2005;287(34):4267. doi:10.1039/b506571b.

[88]   Lisdat F, Schäfer D. The use of electrochemical impedance spectroscopy for biosensing. *Analytical and Bioanalytical Chemistry*. 2008;391(5):1555-1567. doi:10.1007/s00216-008-1970-7.

[89]   Athey D, Ball M, McNeil CJ, Armstrong RD. A study of enzyme-catalyzed product deposition on planar gold electrodes using electrical impedance measurement. *Electroanalysis*. 1995;7(3):270-273. doi:10.1002/elan.1140070313.

[90]   Manickam A. *Integrated Impedance Spectroscopy Biosensors*. PhD Thesis, Falculty of the Graduate School, University of Texas at Austin; 2012. https://repositories.lib.utexas.edu/handle/2152/ETD-UT-2012-05-4962. Accessed September 3, 2017.

[91]   *Autolab Application Note EIS02: Electrochemical Impedance Spectroscopy (EIS) Part 2 – Experimental Setup.* Metrohm AG; 2011. https://www.metrohm.com/en-gb/applications/%7B3557CFB6-539A-4CB7-BD78-EF117F1200EA%7D. Accessed November 22, 2016.

[92]   Vladikova D. The technique of the differential impedance analysis Part I: Basics of the impedance spectroscopy. *Proceedings of the International Workshop "Advanced Techniques for Energy Sources Investigation and Testing."* 2004:1-28.

[93]   *Autolab Application Note EIS03: Electrochemical Impedance Spectroscopy (EIS) Part 3 – Data Analysis.* Metrohm AG; 2011. https://www.metrohm.com/en-us/applications/%7BD6E132A9-E8A7-421B-82DD-5E4A9E3D92AE%7D. Accessed November 22, 2016.

[94]   Barsoukov E, Macdonal JR. *Impedance Spectroscopy*. 2nd ed. Hoboken, NJ, USA: John Wiley & Sons, Inc.; 2005. doi:10.1002/0471716243.

[95]   Schasfoort RBM, Streekstra GJ, Bergveld P, Kooyman RPH, Greve J. Influence of an immunological precipitate on D.C. and A.C. behaviour of an isfet. *Sensors and Actuators*. 1989;18(2):119-129. doi:10.1016/0250-6874(89)87012-X.

[96]   Bergveld P. A critical evaluation of direct electrical protein detection methods. *Biosensors and Bioelectronics*. 1991;6(1):55-72. doi:10.1016/0956-5663(91)85009-L.

[97]   Kruise J, Rispens JG, Bergveld P, Kremer FJB, Starmans D, Haak JR, Feijen J, Reinhoudt DN. Detection of charged proteins by means of impedance measurements. *Sensors and Actuators B: Chemical*. 1992;6(1-3):101-105. doi:10.1016/0925-4005(92)80039-Z.

[98]   Zayats M, Raitman OA, Chegel VI, Kharitonov AB, Willner I. Probing Antigen−Antibody binding processes by impedance measurements on ion-sensitive field-effect transistor devices and complementary surface plasmon resonance analyses: development of cholera toxin sensors. *Analytical Chemistry*. 2002;74(18):4763-4773. doi:10.1021/ac020312f.

[99]   Ingebrandt S, Han Y, Nakamura F, Poghossian A, Schöning MJ, Offenhäusser A. Label-free detection of single nucleotide polymorphisms utilizing the differential transfer function of field-effect transistors. *Biosensors and Bioelectronics*. 2007;22(12):2834-2840. doi:10.1016/j.bios.2006.11.019.

[100]   Susloparova A, Koppenhöfer D, Vu XT, Weil M, Ingebrandt S. Impedance spectroscopy with field-effect transistor arrays for the analysis of anti-cancer drug action on individual cells. *Biosensors and Bioelectronics*. 2013;40(1):50-56. doi:10.1016/j.bios.2012.06.006.

[101]   Law JKY, Susloparova A, Vu XT, Zhou X, Hempel F, Qu B, Hoth M, Ingebrandt S. Human T cells monitored by impedance spectrometry using field-effect transistor arrays: A novel tool for single-cell adhesion and migration studies. *Biosensors and Bioelectronics*. 2015;67:170-176. doi:10.1016/j.bios.2014.08.007.

[102]   Sedra AS. *Microelectronic Circuits*. 5th ed. Oxford University Press; 2004.

[103]   Sze SM, Ng KK. *Physics of Semiconductor Devices*. 3rd ed. Hoboken, NJ, USA: John Wiley & Sons, Inc.; 2006. doi:10.1002/0470068329.

[104]   Tarasov A. *Silicon Nanowire Field-Effect Transistors for Sensing Applications*. PhD Thesis, Department of Physics, University of Basel; 2012. http://edoc.unibas.ch/23881/1/Tarasov_PhD_thesis.pdf. Accessed December 28, 2015.

[105]   Bergveld P. Thirty years of ISFETOLOGY. *Sensors and Actuators B: Chemical*. 2003;88(1):1-20. doi:10.1016/S0925-4005(02)00301-5.

[106]   Gouy M. Sur la constitution de la charge électrique à la surface d'un électrolyte. *Journal de Physique Théorique et Appliquée*. 1910;9(1):457-468. doi:10.1051/jphystap:019100090045700.

[107]   Chapman DL. A contribution to the theory of electrocapillarity. *Philosophical Magazine Series 6*. 1913;25(148):475-481. doi:10.1080/14786440408634187.

[108]   Debye P, Hückel E. De la theorie des electrolytes. I. abaissement du point de congelation et phenomenes associes. *Physikalische Zeitschrift*. 1923;24(9):185-206.

[109]   Stern O. Zur theorie der elektrolytischen doppelschicht. *Zeitschrift für Elektrochemie und angewandte physikalische Chemie*. 1924;30(21-22):508-516. doi:10.1002/bbpc.192400182.

[110]   Deal BE, Helms CR. *The Physics and Chemistry of SiO2 and the Si-SiO2 Interface*. (Helms CR, Deal BE, eds.). Boston, MA: Springer US; 1988. doi:10.1007/978-1-4899-0774-5.

[111]   Yates DE, Levine S, Healy TW. Site-binding model of the electrical double layer at the oxide/water interface. *Journal of the Chemical Society, Faraday Transactions 1: Physical Chemistry in Condensed Phases*. 1974;70:1807-1818. doi:10.1039/f19747001807.

[112] Shinwari MW, Deen MJ, Landheer D. Study of the electrolyte-insulator-semiconductor field-effect transistor (EISFET) with applications in biosensor design. *Microelectronics Reliability*. 2007;47(12):2025-2057. doi:10.1016/j.microrel.2006.10.003.

[113] Chen S, Bomer JG, Carlen ET, van den Berg A. Al2O3/silicon nanoISFET with near ideal Nernstian response. *Nano Letters*. 2011;11(6):2334-2341. doi:10.1021/nl200623n.

[114] Knopfmacher O. *Sensing with Silicon Nanowire Field-Effect Transistors*. PhD Thesis, Faculty of Science, University of Basel; 2011. http://edoc.unibas.ch/1351/1/Diss_Knopfmacher.pdf. Accessed December 30, 2015.

[115] Stern E. *Label-Free Sensing with Semiconducting Nanowires*. PhD Thesis, Faculty of the Graduate School, Yale University; 2007. https://www.eng.yale.edu/reedlab/publications/Stern_PhDthesis_FINAL.pdf. Accessed September 3, 2017.

[116] Bunimovich YL, Shin YS, Yeo W-S, Amori M, Kwong G, Heath JR. Quantitative real-time measurements of DNA hybridization with alkylated nonoxidized silicon nanowires in electrolyte solution. *Journal of the American Chemical Society*. 2006;128(50):16323-16331. doi:10.1021/ja065923u.

[117] Bergveld P. ISFET, theory and practice. *Proceedings of the IEEE Sensor Conference, Toronto, Ontario, Oct*. 2003:1-26. http://www.ieee-sensors.org/files/2011/08/ISFET-Bergveld.pdf. Accessed October 12, 2014.

[118] van Hal REG, Eijkel JCT, Bergveld P. A general model to describe the electrostatic potential at electrolyte oxide interfaces. *Advances in Colloid and Interface Science*. 1996;69(1-3):31-62. doi:10.1016/S0001-8686(96)00307-7.

[119] Rajan NK. *Limit of Detection of Silicon BioFETs*. PhD Thesis, Faculty of the Graduate School, Yale University; 2013. https://www.eng.yale.edu/reedlab/publications/Rajan_Thesis.pdf. Accessed January 3, 2016.

[120] Schasfoort RBM, Bergveld P, Kooyman RPH, Greve J. Possibilities and limitations of direct detection of protein charges by means of an immunological field-effect transistor. *Analytica Chimica Acta*. 1990;238:323-329. doi:10.1016/S0003-2670(00)80554-1.

[121] Stern E, Wagner R, Sigworth FJ, Breaker R, Fahmy TM, Reed MA. Importance of the Debye screening length on nanowire field effect transistor sensors. *Nano Letters*. 2007;7(11):3405-3409. doi:10.1021/nl071792z.

[122] Clément N, Nishiguchi K, Dufreche JF, Guerin D, Fujiwara A, Vuillaume D. A silicon nanowire ion-sensitive field-effect transistor with elementary charge sensitivity. *Applied Physics Letters*. 2011;98(1):14104. doi:10.1063/1.3535958.

[123] Vacic A, Criscione JM, Rajan NK, Stern E, Fahmy TM, Reed MA. Determination of molecular configuration by Debye length modulation. *Journal of the American Chemical Society*. 2011;133(35):13886-13889. doi:10.1021/ja205684a.

[124] Kulkarni GS, Zhong Z. Detection beyond the Debye screening length in a high-frequency nanoelectronic biosensor. *Nano Letters*. 2012;12(2):719-723. doi:10.1021/nl203666a.

[125] Gao N, Zhou W, Jiang X, Hong G, Fu T-M, Lieber CM. General strategy for biodetection

in high ionic strength solutions using transistor-based nanoelectronic sensors. *Nano Letters*. 2015;15(3):2143-2148. doi:10.1021/acs.nanolett.5b00133.

[126] Fernandes PG, Stiegler HJ, Zhao M, Cantley KD, Obradovic B, Chapman RA, Wen H-C, Mahmud G, Vogel EM. SPICE macromodel of silicon-on-insulator-field-effect-transistor-based biological sensors. *Sensors and Actuators B: Chemical*. 2012;161(1):163-170. doi:10.1016/j.snb.2011.10.002.

[127] Landheer D, McKinnon WR, Aers G, Jiang W, Deen MJ, Shinwari MW. Calculation of the response of field-effect transistors to charged biological molecules. *IEEE Sensors Journal*. 2007;7(9):1233-1242. doi:10.1109/JSEN.2007.901047.

[128] Berggren C, Bjarnason B, Johansson G. Capacitive biosensors. *Electroanalysis*. 2001;13(3):173-180. doi:10.1002/1521-4109(200103)13:3<173::AID-ELAN173>3.0.CO;2-B.

[129] Berggren C, Stålhandske P, Brundell J, Johansson G. A feasibility study of a capacitive biosensor for direct detection of DNA hybridization. *Electroanalysis*. 1999;11(3):156-160. doi:10.1002/(SICI)1521-4109(199903)11:3<156::AID-ELAN156>3.0.CO;2-O.

[130] Schweiss R, Werner C, Knoll W. Impedance spectroscopy studies of interfacial acid–base reactions of self-assembled monolayers. *Journal of Electroanalytical Chemistry*. 2003;540:145-151. doi:10.1016/S0022-0728(02)01303-7.

[131] Ogata K. *Modern Control Engineering*. 5th ed. Prentice Hall; 2010.

[132] Kharitonov AB, Wasserman J, Katz E, Willner I. The use of impedance spectroscopy for the characterization of protein-modified ISFET devices: application of the method for the analysis of niorecognition processes. *J Phys Chem B*. 2001;105:4205-4213. doi:10.1021/jp0045383.

[133] Huang H. *Impedance Spectroscopy Systems Suitable for Biomedical Cell Impedance Measurement*. Master's thesis, Office of Graduate Studies, Texas A & M University; 2013. http://hdl.handle.net/1969.1/151036. Accessed January 28, 2016.

[134] *Application Note #3: About Lock-In Amplifiers*. Stanford Research Systems Inc. http://www.thinksrs.com/downloads/PDFs/ApplicationNotes/AboutLIAs.pdf. Accessed September 3, 2017.

[135] Dufaux T. *Design and Development of Amplifier Electronics for Silicon-Nanowire Biosensors*. Master's Thesis, Faculty of Electrical Engineering and Information Technology, RWTH Aachen University; 2008.

[136] Li N. *Development of Real-Time Cellular Impedance Analysis System*. PhD Thesis, School of Engineering and Informatics, University of Sussex; 2014. http://sro.sussex.ac.uk/49706/1/Li%2C_Nan.pdf. Accessed February 4, 2016.

[137] Tamiya K, Higashidate M, Kikkawa S. Technique with lock-in amplifier for real-time measurement of tricuspid valve annulus area. *American Journal of Physiology - Heart and Circulatory Physiology*. 1986;251(2):H236-241. http://ajpheart.physiology.org/content/251/2/H236.short. Accessed February 5, 2016.

[138] *HF2LI Lock-in Amplifier - User Manual*. Zurich Instruments AG; 2010. https://www.zhinst.com/products/hf2li. Accessed February 5, 2016.

[139] Offenhäusser A, Sprössler C, Matsuzawa M, Knoll W. Field-effect transistor array for monitoring electrical activity from mammalian neurons in culture. *Biosensors and Bioelectronics*. 1997;12(8):819-826. doi:10.1016/S0956-5663(97)00047-X.

[140] Sprössler C, Denyer M, Britland S, Knoll W, Offenhäusser A. Electrical recordings from rat cardiac muscle cells using field-effect transistors. *Physical Review E*. 1999;60(2):2171-2176. doi:10.1103/PhysRevE.60.2171.

[141] Ingebrandt S, Offenhäusser A. Label-free detection of DNA using field-effect transistors. *physica status solidi (a)*. 2006;203(14):3399-3411. doi:10.1002/pssa.200622465.

[142] Susloparova A, Vu XT, Koppenhöfer D, Law JK-Y, Ingebrandt S. Investigation of ISFET device parameters to optimize for impedimetric sensing of cellular adhesion. *physica status solidi (a)*. 2014;211(6):1395-1403. doi:10.1002/pssa.201330636.

[143] Ingebrandt S. *Characterisation of the Cell-Transistor Coupling*. PhD Thesis, Faculty of Chemistry, Pharmaceutical Sciences and Geoscience, Johannes Gutenberg University Mainz; 2001. http://ubm.opus.hbz-nrw.de/volltexte/2001/170/. Accessed September 3, 2017.

[144] Vu XT, Eschermann JF, Stockmann R, GhoshMoulick R, Offenhäusser A, Ingebrandt S. Top-down processed silicon nanowire transistor arrays for biosensing. *physica status solidi (a)*. 2009;206(3):426-434. doi:10.1002/pssa.200880475.

[145] Fan HJ, Werner P, Zacharias M. Semiconductor nanowires: from self-organization to patterned growth. *Small*. 2006;2(6):700-717. doi:10.1002/smll.200500495.

[146] Bergveld P, Sibbald A. *Analytical and Biomedical Applications of Ion-Selective Field-Effect Transistors*. Elsevier Science Publisher; 1988.

[147] Nguyen TC, Schwartz M, Vu XT, Blinn J, Ingebrandt S. Handheld readout system for field-effect transistor biosensor arrays for label-free detection of biomolecules. *physica status solidi (a)*. 2015;212(6):1313-1319. doi:10.1002/pssa.201431862.

[148] Bergveld P. Electronic-circuit-design principles for parameter control of i.s.f.e.t.s and related devices. *Medical & Biological Engineering & Computing*. 1979;17(5):655-661. doi:10.1007/BF02440912.

[149] Casans S, Navarro AE, Ramírez D, Pelegrí J, Baldi A, Abramova N. Novel constant current driver for ISFET/MEMFETs characterization. *Sensors and Actuators B: Chemical*. 2001;76(1-3):629-633. doi:10.1016/S0925-4005(01)00658-X.

[150] Völker M. Detektion von aktionspotentialen einzelner säugetierneurone mit rauscharmen feldeffekttransistoren nahe der thermodynamischen meßgrenze. https://mediatum.ub.tum.de/603082. Published 2005. Accessed September 3, 2017.

[151] Bragg LM, Stone G, Butler MK, Hugenholtz P, Tyson GW. Shining a light on dark sequencing: characterising errors in ion torrent PGM data. Beerenwinkel N, ed. *PLoS Computational Biology*. 2013;9(4):e1003031. doi:10.1371/journal.pcbi.1003031.

[152] Rothberg JM, Hinz W, Rearick TM, Schultz J, Mileski W, Davey M, Leamon JH, Johnson K, Milgrew MJ, Edwards M, Hoon J, Simons JF, Marran D, Myers JW, Davidson JF, Branting A, Nobile JR, Puc BP, Light D, Clark TA, Huber M, Branciforte JT, Stoner IB, Cawley SE, Lyons M, Fu Y, Homer N, Sedova M, Miao X, Reed B, Sabina J, Feierstein E,

Schorn M, Alanjary M, Dimalanta E, Dressman D, Kasinskas R, Sokolsky T, Fidanza JA, Namsaraev E, McKernan KJ, Williams A, Roth GT, Bustillo J. An integrated semiconductor device enabling non-optical genome sequencing. *Nature*. 2011;475(7356):348-352. doi:10.1038/nature10242.

[153] Ion Torrent (ThermoFisher) - AllSeq, Inc. http://allseq.com/knowledge-bank/sequencing-platforms/ion-torrent/. Published 2017. Accessed March 12, 2017.

[154] *Datasheet for Model SR570 Low-Noise Preamplifier*. Stanford Research Systems Inc.; 2015. http://www.thinksrs.com/products/SR570.htm. Accessed September 3, 2017.

[155] *OPA627 and OPA637 Precision High-Speed Difet ® Operational Amplifiers*. Texas Intruments Incorporated; 2015. http://www.ti.com/lit/ds/symlink/opa627.pdf. Accessed September 3, 2017.

[156] *NI 6255 Device Specifications*. National Instruments; 2015. http://www.ni.com/pdf/manuals/375213a.pdf. Accessed September 3, 2017.

[157] *LTC1451/LTC1452/LTC1453 - 12-Bit Rail-to-Rail Micropower DACs in SO-8*. Linear Technology Corporation; 1995. http://cds.linear.com/docs/en/datasheet/145123fs.pdf. Accessed September 3, 2017.

[158] *LTC1655/LTC1655L - 16-Bit Rail-to-Rail Micropower DACs inSO-8 Package*. Linear Technology Corporation; 1998. http://www.linear.com/product/LTC1655. Accessed September 3, 2017.

[159] *PIC32MX Family Reference Manual*. Microchip Technology Inc.; 2008. http://hades.mech.northwestern.edu/images/2/21/61132B_PIC32ReferenceManual.pdf. Accessed October 18, 2014.

[160] *AD5933 1 MSPS , 12-Bit Impedance Converter , Network Analyzer*. Analog Devices Inc.; 2012. http://www.analog.com/en/products/rf-microwave/direct-digital-synthesis/ad5933.html. Accessed September 3, 2017.

[161] Jakobson C, Bloom I, Nemirovsky Y. 1/f Noise in CMOS transistors for analog applications from subthreshold to saturation. *Solid-State Electronics*. 1998;42(10):1807-1817. doi:10.1016/S0038-1101(98)00162-2.

[162] Müller R. *Rauschen*. Vol 15. Springer Berlin, Heidelberg; 1990. doi:10.1007/978-3-642-61501-6.

[163] Marlow D. Physics 312 lecture notes on characterizing noise. http://phy-page-imac.princeton.edu/~page/phy312/. Published 2011. Accessed September 2, 2015.

[164] Bergveld P. Development, operation, and application of the ion-sensitive field-effect transistor as a tool for electrophysiology. *IEEE Transactions on Biomedical Engineering*. 1972;BME-19(5):342-351. doi:10.1109/TBME.1972.324137.

[165] van den Berg A, Bergveld P, Reinhoudt DN, Sudhölter EJ. Sensitivity control of ISFETs by chemical surface modification. *Sensors and Actuators*. 1985;8(2):129-148. doi:10.1016/0250-6874(85)87010-4.

[166] Bousse L. Single electrode potentials related to flat-band voltage measurements on EOS and MOS structures. *The Journal of Chemical Physics*. 1982;76(10):5128-5133.

doi:10.1063/1.442812.

[167] Kratz RF. *Molecular and Cell Biology For Dummies*. 2nd ed. Wiley Publishing, Inc.; 2009.

[168] Neil A. Campbell JBR. *Biology*. 7th ed. Benjamin Cummings; 2004.

[169] Pray LA. Discovery of DNA structure and function: Watson and Crick. *Nature Education*. 2008;1(1). https://www.nature.com/scitable/topicpage/discovery-of-dna-structure-and-function-watson-397. Accessed September 3, 2017.

[170] Eggins BR. *Analytical Techniques in the Sciences*. Chichester, UK: John Wiley & Sons, Ltd.; 2002. doi:10.1002/9780470511305.

[171] Poghossian A, Cherstvy A, Ingebrandt S, Offenhäusser A, Schöning MJ. Possibilities and limitations of label-free detection of DNA hybridization with field-effect-based devices. *Sensors and Actuators B: Chemical*. 2005;111-112:470-480. doi:10.1016/j.snb.2005.03.083.

[172] Han Y, Offenhäusser A, Ingebrandt S. Detection of DNA hybridization by a field-effect transistor with covalently attached catcher molecules. *Surface and Interface Analysis*. 2006;38(4):176-181. doi:10.1002/sia.2157.

[173] Hahm J, Lieber CM. Direct ultrasensitive electrical detection of DNA and DNA sequence variations using nanowire nanosensors. *Nano Letters*. 2004;4(1):51-54. doi:10.1021/nl034853b.

[174] Li Z, Chen Y, Li X, Kamins TI, Nauka K, Williams RS. Sequence-specific label-free DNA sensors based on silicon nanowires. *Nano Letters*. 2004;4(2):245-247. doi:10.1021/nl034958e.

[175] Li Z, Rajendran B, Kamins TI, Li X, Chen Y, Williams RS. Silicon nanowires for sequence-specific DNA sensing: device fabrication and simulation. *Applied Physics A*. 2005;80(6):1257-1263. doi:10.1007/s00339-004-3157-1.

[176] Gao Z, Agarwal A, Trigg AD, Singh N, Fang C, Tung CH, Fan Y, Buddharaju KD, Kong J. Silicon nanowire arrays for label-free detection of DNA. *Analytical Chemistry*. 2007;79(9):3291-3297. doi:10.1021/ac061808q.

[177] Wu CC, Ko FH, Yang YS, Hsia DL, Lee BS, Su TS. Label-free biosensing of a gene mutation using a silicon nanowire field-effect transistor. *Biosensors and Bioelectronics*. 2009;25(4):820-825. doi:10.1016/j.bios.2009.08.031.

[178] Uslu F, Ingebrandt S, Mayer D, Böcker-Meffert S, Odenthal M, Offenhäusser A. Labelfree fully electronic nucleic acid detection system based on a field-effect transistor device. *Biosensors and Bioelectronics*. 2004;19(12):1723-1731. doi:10.1016/j.bios.2004.01.019.

[179] Williams AP, Longfellow CE, Freier SM, Kierzek R, Turner DH. Laser temperature-jump, spectroscopic, and thermodynamic study of salt effects on duplex formation by dGCATGC. *Biochemistry*. 1989;28(10):4283-4291. doi:10.1021/bi00436a025.

[180] Wetmur JG, Davidson N. Kinetics of renaturation of DNA. *Journal of Molecular Biology*. 1968;31(3):349-370. doi:10.1016/0022-2836(68)90414-2.

[181] GhoshMoulick R, Vu XT, Gilles S, Mayer D, Offenhäusser A, Ingebrandt S. Impedimetric detection of covalently attached biomolecules on field-effect transistors. *physica status*

solidi (a). 2009;206(3):417-425. doi:10.1002/pssa.200880482.

[182] Landheer D, Aers G, McKinnon WR, Deen MJ, Ranuarez JC. Model for the field effect from layers of biological macromolecules on the gates of metal-oxide-semiconductor transistors. *Journal of Applied Physics*. 2005;98(4):44701. doi:10.1063/1.2008354.

[183] McKinnon WR, Landheer D, Aers G. Sensitivity of field-effect biosensors to charge, pH, and ion concentration in a membrane model. *Journal of Applied Physics*. 2008;104(12):124701. doi:10.1063/1.3050329.

[184] Chrisey L. Covalent attachment of synthetic DNA to self-assembled monolayer films. *Nucleic Acids Research*. 1996;24(15):3031-3039. doi:10.1093/nar/24.15.3031.

[185] Cloarec J, Martin J, Polychronakos C, Lawrence I, Lawrence M, Souteyrand E. Functionalization of Si/SiO2 substrates with homooligonucleotides for a DNA biosensor. *Sensors and Actuators B: Chemical*. 1999;58(1-3):394-398. doi:10.1016/S0925-4005(99)00102-1.

[186] Sakata T, Kamahori M, Miyahara Y. Immobilization of oligonucleotide probes on Si3N4 surface and its application to genetic field effect transistor. *Materials Science and Engineering: C*. 2004;24(6-8):827-832. doi:10.1016/j.msec.2004.08.042.

[187] Souriau C, Hudson PJ. Recombinant antibodies for cancer diagnosis and therapy. *Expert Opinion on Biological Therapy*. 2003;3(2):305-318. doi:10.1517/14712598.3.2.305.

[188] *Product Information: Streptavidin from Streptomyces Avidinii (Sigma-Aldrich)*. Sigma-Aldrich, Inc.; 2007. http://www.sigmaaldrich.com/catalog/substance/streptavidinfromstreptomycesavidinii123 45901320111?lang=de&region=DE. Accessed September 3, 2017.

[189] *Instructions: EZ-Link ® NHS-Biotin Reagents*. Vol 747. Thermo Fisher Scientific Inc.; 2011. https://www.thermofisher.com/order/catalog/product/20217. Accessed September 3, 2017.

[190] *The Streptavidin-Biotin Interaction*. Innova Biosciences Ltd.; 2017. https://www.innovabiosciences.com/guides/antibody-labeling-guides/biotin-streptavidin-interaction/. Accessed September 3, 2017.

[191] Massobrio G, Martinoia S, Grattarola M. Ion sensitive field effect transistor (ISFET) model implemented in Spice. In: *Simulation of Semiconductor Devices and Processes*. Vol 4. ; 1991:563-570. http://in4.iue.tuwien.ac.at/pdfs/sisdep1991/pdfs/Massobrio_62.pdf. Accessed September 3, 2017.

[192] Massobrio G, Martinoia S. Modelling the ISFET behaviour under temperature variations using BIOSPICE. *Electronics Letters*. 1996;32(10):936-938. doi:10.1049/el:19960577.

[193] Martinoia S, Massobrio G. A behavioral macromodel of the ISFET in SPICE. *Sensors and Actuators B: Chemical*. 2000;62(3):182-189. doi:10.1016/S0925-4005(99)00377-9.

[194] Martinoia S, Massobrio G, Lorenzelli L. Modeling ISFET microsensor and ISFET-based microsystems: a review. *Sensors and Actuators B: Chemical*. 2005;105(1):14-27. doi:10.1016/j.snb.2004.02.046.

[195] Tong HD, Chen S, van der Wiel WG, Carlen ET, van den Berg A. Novel top-down wafer-

scale fabrication of single crystal silicon nanowires. *Nano Letters*. 2009;9(3):1015-1022. doi:10.1021/nl803181x.

[196] Frohman-Bentchkowsky D, Grove AS. Conductance of MOS transistors in saturation. *IEEE Transactions on Electron Devices*. 1969;16(1):108-113. doi:10.1109/T-ED.1969.16571.

[197] Antognetti P, Massobrio G. *Semiconductor Device Modeling with Spice*. 2nd ed. McGraw-Hill, Inc.; 1993. http://dl.acm.org/citation.cfm?id=562745. Accessed October 30, 2015.

[198] Schindler M. *Design of a High Density CMOS Array for the Bidirectional Coupling With Electrogenic Cells*. PhD Thesis, Fakultät für Elektrotechnik und Informationstechnik. http://juser.fz-juelich.de/record/61365/. Published 2007. Accessed September 3, 2017.

[199] *IC-CAP 2013.01 MOSFET Models*. Agilent Technologies, Inc; 2013. http://www.keysight.com/en/pd-2226367/ic-cap-201211?cc=DE&lc=ger. Accessed September 3, 2017.

[200] Schwartz M. *Detection of Biomolecules Using Multivariant Data Analysis from Silicon Nanowire Field-Effect Transistor Arrays*. PhD Thesis, Faculty of Medicine and Life Sciences, Hasselt University, Belgium; 2017.

[201] Elfström N, Juhasz R, Sychugov I, Engfeldt T, Karlström AE, Linnros J. Surface charge Sensitivity of Silicon Nanowires: Size Dependence. *Nano Letters*. 2007;7(9):2608-2612. doi:10.1021/nl0709017.

[202] Patolsky F, Zheng G, Hayden O, Lakadamyali M, Zhuang X, Lieber CM. Electrical detection of single viruses. *Proceedings of the National Academy of Sciences*. 2004;101(39):14017-14022. doi:10.1073/pnas.0406159101.

[203] Zhang G-J, Zhang G, Chua JH, Chee R-E, Wong EH, Agarwal A, Buddharaju KD, Singh N, Gao Z, Balasubramanian N. DNA sensing by silicon nanowire: charge layer distance dependence. *Nano Letters*. 2008;8(4):1066-1070. doi:10.1021/nl0729911l.

[204] Schwartz M, Nguyen TC, Vu XT, Weil M, Wilhelm J, Wagner P, Thoelen R, Ingebrandt S. DNA detection with top-down fabricated silicon nanowire transistor arrays in linear operation regime. *physica status solidi (a)*. 2016;213(6):1510-1519. doi:10.1002/pssa.201532919.

[205] Ohshima H, Ohki S. Donnan potential and surface potential of a charged membrane. *Biophysical Journal*. 1985;47(5):673-678. doi:10.1016/S0006-3495(85)83963-1.

[206] Tikhonov AM. Ion-size effect at the surface of a silica hydrosol. *The Journal of Chemical Physics*. 2009;130(2):24512. doi:10.1063/1.3056663.

[207] Ara G, Mullen JG. Effect of ion size on diffusion in Alkali Halides. *Physical Review*. 1966;143(2):663-665. doi:10.1103/PhysRev.143.663.

[208] Landheer D, McKinnon WR, Jiang WH, Aers G. Effect of screening on the sensitivity of field-effect devices used to detect oligonucleotides. *Applied Physics Letters*. 2008;92(25):253901. doi:10.1063/1.2948906.

[209] Heitzinger C, Mauser NJ, Ringhofer C. Multiscale modeling of planar and nanowire field-effect biosensors. *SIAM Journal on Applied Mathematics*. 2010;70(5):1634-1654. doi:10.1137/080725027.

[210] Heitzinger C, Kennell R, Klimeck G, Mauser N, McLennan M, Ringhofer C. Modeling and simulation of field-effect biosensors (BioFETs) and their deployment on the nanoHUB. *Journal of Physics: Conference Series*. 2008;107:1-12. doi:10.1088/1742-6596/107/1/012004.

[211] Livi P, Bedner K, Tarasov A, Wipf M, Chen Y, Schönenberger C, Hierlemann A. A Verilog-A model for silicon nanowire biosensors: from theory to verification. *Sensors and Actuators B: Chemical*. 2013;179:293-300. doi:10.1016/j.snb.2012.09.026.

[212] Fung CD, Cheung PW, Ko WH. A generalized theory of an electrolyte-insulator-semiconductor field-effect transistor. *IEEE Transactions on Electron Devices*. 1986;33(1):8-18. doi:10.1109/T-ED.1986.22429.

[213] Vezenov D, Noy A, Rozsnyai LF, Lieber CM. Force titrations and Ionization state sensitive imaging of functional groups in aqueous solutions by chemical force microscopy. *Journal of the American Chemical Society*. 1997;119(8):2006-2015. doi:10.1021/ja963375m.

[214] Schwartz M, Vu XT, Nguyen TC, Wagner P, Ingebrandt S. Impedimetric sensing of DNA with silicon nanowire transistors can overcome the Debye screening limitation by an alternative transducer mechanism. *Physica Status Solidi (a)*. 2018; doi: 10.1002/pssa.201700740.

[215] Schäfer S, Eick S, Hofmann B, Dufaux T, Stockmann R, Wrobel G, Offenhäusser A, Ingebrandt S. Time-dependent observation of individual cellular binding events to field-effect transistors. *Biosensors and Bioelectronics*. 2009;24(5):1201-1208. doi:10.1016/j.bios.2008.07.003.

[216] Susloparova A, Vu XT, Koppenhöfer D, Law JK-Y, Ingebrandt S. Investigation of ISFET device parameters to optimize for impedimetric sensing of cellular adhesion. *Physica Status Solidi (a)*. 2014;211(6):1395-1403. doi:10.1002/pssa.201330636.

[217] Holmes JD. Control of thickness and orientation of solution-grown silicon nanowires. *Science*. 2000;287(5457):1471-1473. doi:10.1126/science.287.5457.1471.

[218] Rani D, Pachauri V, Mueller A, Vu XT, Nguyen TC, Ingebrandt S. On the use of scalable nanoISFET arrays of silicon with highly reproducible sensor performance for biosensor applications. *ACS Omega*. 2016;1(1):84-92. doi:10.1021/acsomega.6b00014.

[219] Leistiko O. The selectivity and temperature characteristics of ion sensitive field effect transistors. *Physica Scripta*. 1978;18(6):445-450. doi:10.1088/0031-8949/18/6/021.

[220] Martinoia S, Lorenzelli L, Massobrio G, Conci P, Lui A. Temperature effects on the ISFET behaviour: simulations and measurements. *Sensors and Actuators B: Chemical*. 1998;50(1):60-68. doi:10.1016/S0925-4005(98)00157-9.

Index of Tables

Index of Figures

161

List of Abbreviations

Abbreviation	Meaning
A	adenine
AC	alternating current
ADC	analog-to-digital converter
anti-DNP-Ab	anti-dinitrophenyl antibody
APTES	(3-aminopropyl)-triethoxysilane
ASIC	application specific integrated circuits
BOX	buried oxide
BSA	bovine serum albumin
BSIM	Berkeley short-channel IGFET model
BW	bandwidth
C	cytosine
CMOS	complementary metal-oxide-semiconductor
CPE	constant phase element
CT	cholera toxin
CV	capacitance-voltage
D	drain terminal
DAC	digital-to-analog converter
DAQ	data acquisition
DC	direct current
ddDTP	dideoxy ribonucleotide
DDS	direct digital synthesizer
DFT	discrete Fourier transform
DIC	Differential interference contrast
DNA	deoxyribonucleic acid
DNL	differential nonlinearity
DNP	dinitrophenyl
dNTP	nucleotide
DSP	digital signal processor
DUT	device under test
EIS	electrochemical impedance spectroscopy
ELISA	enzyme-linked immunosorbent assay
FET	field-effect transistor
FFT	fast Fourier transform
FMM	fully mismatch
FRA	frequency response analyzer
G	gate terminal
G	guanine
GND	ground
GPTES	(3-Glycidyloxypropyl) trimethoxysilane
H441	human lung adenocarcinoma epithelial

HEK293	human embryonic kidney
Hg	mercury
Hg_2Cl_2	Mercury chloride
HID	human interface device
HSA	human serum albumin
ICs	integrated circuits
IDE	integrated development environment
IHP	inner Helmholtz plane
INL	Integral nonlinearity
LPCVD	low-pressure chemical vapor deposition
LSB	Least significant bit
ISFET	ion-sensitive field-effect transistor
MIPS	Microprocessor without Interlocked Pipeline Stages
MM	mismatch
MOSFET	metal oxide semiconductor field-effect transistor
MS/s	Mega samples per second
NI	National Instruments
nM	nanomolar
OHP	outer Helmholtz plane
ONO-stack	silicon oxide / silicon nitride / silicon oxide stack
PBS	phosphate buffer solutions
PC	personal computer
PCB	printed circuit board
PCR	polymerase chain reaction
PDMS	polydimethylsiloxane
PGA	programmable gain amplifier
pI	isoelectric point
pH_{pzc}	point of zero charge
PLCC	plastic lead chip carrier
PM	perfect match
PMOS	P-type metal-oxide-semiconductor
PSD	phase-sensitive detection
PSPICE	personal computer simulation program with integrated circuit emphasis
QCM	quartz crystal microbalance
RC	resistor capacitor
RF	radio frequency
RIE	reactive-ion etching
RISC	reduced instruction set computer
RNA	ribonucleic acid
S	source terminal
SCSI	small computer system interface
SiNW	silicon nanowire
SiNW FET	silicon nanowire field-effect transistor
SNPs	single polymorphisms

SNR	signal-to-noise ratio
SOI	silicon-on-insulator
SPI	serial peripheral interface
SPICE	simulation program with integrated circuit emphasis
SPR	surface plasmon resonance
SSC	saline sodium citrate buffer
ssDNA	single-stranded deoxyribonucleic acid
T	thymine
TC	transfer characteristics
TE	Tris-EDTA
TEM	transmission electron microscopy
TMAH	tetramethylammonium hydroxide
USB	universal serial bus
UV	Ultraviolet

List of Symbols

Symbol	Meaning	Value/ unit
A	amplitude of reference voltage of Lock-in amplifier	V
A	area of passivation layer at the drain or source electrode	m^2
A_0	amplitude of resulting voltage	V
$\overline{A}$	average value of measuring data	V
A(t)	time-dependent measuring data	V
$A(\tau)$	auto-correlation Function	
C	capacitance	F
c	concentration of the electrolyte	particles/cm^3
C_{DL}	Double layer capacitance	F
C_{PD}	capacitances of passivation drain electrode	F
C_{FB}	feedback capacitance	F
c_i	ion concentration of ion i^{th}	particles/cm^3
C_{mem}	membrane capacitance	F
C_{ox}	capacitance per unit gate area	F/cm^2
C_{SC}	space-charge capacitance	F
C_{PS}	capacitances of passivation source electrode	F
C_{St}	Stern capacitance	F
C_{GC}	Gouy-Chapman capacitance	F
C_D	Drain capacitance	F
C_i	$C_i = C_{ox} + C_D$	F
C_{Helm}	Helmholtz capacitance	F
C_{Gouy}	Gouy-Chapman capacitance	F
D	diffusion coefficient	m^2/s
d_{IHP}	thickness of the inner Helmholtz plane	m
d_{OHP}	thickness of outer Helmholtz plane	m
f(jω)	dependence of applied gate voltage and effective gate voltage	
f_c	gain bandwidth product of the operation amplifier	Hz
f_{zf}	$f_{zf} = \dfrac{1}{2\pi R_{FB}(C_i + C_{FB})}$	Hz
f_{pf}	$f_{pf} = \dfrac{1}{2\pi R_{FB}C_{FB}}$	Hz
$[H^+]_s$	concentration of H+ ion on the chip surface	
$[H^+]$	concentration of H+ ion in bulk solutions	
I	amplitude of DC current	A
i_{DS}	AC drain-source current	A
I_{DS}	electrical current between the Drain and Source electrodes	A
k	Boltzmann constant	$1.38066 * 10^{-23}$ J K^{-1}
Ka, Kb	dimensionless equilibrium value	

L	inductance	H
L	channel length	m
$N(f)$	Fourier transform of a function	
N_A	Avogadro constant	$6.02214 * 10^{23}$ mol^{-1}
n_0	buffer ionic strength	
N_s	number of surface sites	
pH_{pzc}	point of zero charge	
$P(f)$	power spectral density	
Q_{ox}	sum of charges in the oxide	C
Q_{ss}	charge at the oxide-semiconductor interface	C
Q_D	silicon depletion charge	C
R_{CT}	Charge transfer resistance	Ω
R_{drain}	resistance values at the drain contact line	Ω
R_{FB}	feedback resistance	Ω
R_{ion}	radius of the hydrated ions (ions at Outer Helmholtz plane: OHP)	m
R_{mem}	membrane resistance	Ω
R_{Si}	silicon-electrode resistance	Ω
R_{sol}	Resistance of electrolyte solution	Ω
R_{source}	resistance values at the source contact line	Ω
R_S	resistance at source contact line	Ω
R_D	resistance at drain contact line	Ω
R_{SiNW}	$R_{SiNW} = 1/g_m$	Ω
R_{CL}	$R_{CL} = R_S + R_D$	Ω
$[SiO^-]$	density of SiO^- terminals	/m^2
$[SiOH]$	density of SiOH terminals	/m^2
$[SiOH_2^+]$	density of $[SiOH_2^+]$ terminals	/m^2
t	Celsius temperature	°C
T	Kelvin temperature	K
V_{ref}	reference voltage	V∠
v_{out}	AC part of output voltage after the amplifier	V∠
v_0	Voltage after amplifier/ resulting voltage	V∠
v_r	reference voltage of Lock-in amplifier	V∠
v_{psd1}	voltage of phase sensitive detector 1	V∠
v_{psd2}	voltage of phase sensitive detector 2	V∠
v_{flt1}	voltage after filter 1	V∠
v_{flt2}	voltage after filter 2	V∠
W	channel width	m
W	Warburg impedance	Ω∠
z	valance of the ions in the electrolyte	
Z_{FB}	feedback impedance	Ω∠

Z_i	valence of the ith ion	
T	Kelvin temperature	K
y_0	$$y_0 = \frac{q\Psi_0}{kT}$$	
Y_0	diffusion admittance	S
Z	complex impedance	$\Omega\angle$
Z_{CS}	impedance of capacitance of passivation layers	$\Omega\angle$
Z_{CO}	impedance of capacitance at gate oxide of SiNW	$\Omega\angle$
$\propto_0$	$$\propto_0 = \frac{\sigma_0}{qN_s}$$	
ε	relative dielectric permittivity of solvent	
ε_0	vacuum permittivity	
ε_{IHP}	relative permittivity of inner Helmholtz plane	
ε_{OHP}	relative permittivity of outer Helmholtz plane	
ε_{SiO_2}	relative permittivity of SiO_2	
ε_{St}	permittivity at the surface	
σ_{DNA}	surface charge density of DNA	C/m^2
τ_1, τ_2	time constant of transfer function	s
Φ_{ms}	work-function difference between the gate material (metal/polysilicon) and semiconductor	V
χ_{sol}	surface dipole potential of the solution	V
Ψ_0	surface potential	V
Ψ_s	working function of semiconductor	V
ω_c	$\omega_c = 2\pi f_c$	Rad·s^{-1}
ω_{pf}	$$\omega_{pf} = \frac{1}{R_{FB}C_{FB}}$$	Rad·s^{-1}
ω_r	reference angular frequency	Rad·s^{-1}
ω_{zf}	$$\omega_{zf} = \frac{1}{R_{FB}(C_i + C_{FB})}$$	Rad·s^{-1}
$2\Psi_B$	sum of voltages across the semiconductor	C
β	$$\beta = \frac{q^2 N_s \delta}{C_{eq}kT}$$	
δ	diffusion layer thickness	m
δ	$\delta = 2\sqrt{K_a K_b}$	
$\Delta\Psi_0$	change of surface potential	V
ε_0	vacuum permittivity	$8.85419 * 10^{-12}$ A s $V^{-1}m^{-1}$
ζ	damping factor	
θ	phase of the resulting voltage output	rad
λ_D	Debye length	m

ω   angular frequency $Rad \cdot s^{-1}$

Curricula Vitae

Thanh Chien Nguyen

Education

04.2014 – 12.2017	PhD Student, Institute of Integrated Sensor Systems (Prof. Dr. – Ing. Andreas König), Kaiserslautern University of Technology, Germany
10.2011 – 03.2015	PhD student, Biomedical Instrumentation working group (Prof. Dr. rer. nat. Sven Ingebrandt), University of Applied Science Kaiserslautern, Germany
09.2007 – 07.2009	Master of Science, Department of Power Mechanical Engineering, National Tsing Hua University, Taiwan
09.2001 – 07.2006	Bachelor, School of Mechanical Engineering, Hanoi University of Science and Technology (previously: Hanoi University of Technology), Vietnam

Experience

04. 2015 – now	Hardware and Software developer, Ram Group DE GmbH, Germany
01.2010-12. 2011	Researcher, Laboratory of Nanotechnology, Vietnam National University- Ho Chi Minh City, Vietnam
09.2006-08. 2007	Engineer, DENSO Manufacturing Vietnam Co., Ltd., Vietnam

Publications

Patents

1. A. RAM, A. Lichtenstein, X. T. VU, J. K. Y. Law, M. Schwartz, J. WILHELM, and **T. C. NGUYEN**, "Nanoelectronic sensor pixel," U.S. Patent US20160290957 A1, 2016.
2. A. RAM, A. Lichtenstein, X. T. VU, J. K. Y. Law, D. P. TRAN, J. WILHELM, and **T. C. NGUYEN**, "Optoelectronic pixel sensor," U.S. Patent US20160290958 A1, 2016.

Publications

1. **T. C. Nguyen**, X. T. Vu, M. Freyler, and S. Ingebrandt, "PSPICE model for silicon nanowire field-effect transistor based biosensors in impedimetric measurement mode," *Phys. status solidi*, vol. 210, no. 5, pp. 870–876, May 2013.
2. **T. C. Nguyen**, M. Schwartz, X. T. Vu, J. Blinn, and S. Ingebrandt, "Handheld readout system for field-effect transistor biosensor arrays for label-free detection of biomolecules," *Phys. status solidi*, vol. 212, no. 6, pp. 1313–1319, Jun. 2015.
3. M. Schwartz, **T. C. Nguyen**, X. T. Vu, M. Weil, J. Wilhelm, P. Wagner, R. Thoelen, and S. Ingebrandt, "DNA detection with top-down fabricated silicon nanowire transistor arrays in linear operation regime," *Phys. status solidi*, vol. 213, no. 6, pp. 1510–1519, Jun. 2016. **(co-first author)**
4. F. Hempel, **T. C. Nguyen**, J. K. Y. Law, and S. Ingebrandt, "The influence of medium conductivity on ECIS measurements with field-effect transistor arrays," *Phys. status solidi*, vol. 212, no. 6, pp. 1260–1265, Jun. 2015.
5. M. Schwartz, **T. C. Nguyen**, X. T. Vu, P. Wagner, and S. Ingebrandt, "Impedimetric sensing of DNA with silicon nanowire transistors can overcome the Debye screening limitation by an alternative transducer mechanism," *Phys. status solidi A*, 1700740, 2018.
6. F. Hempel, J. K.-Y. Law, **T. C. Nguyen**, W. Munief, X. Lu, V. Pachauri, A. Susloparova, X. T. Vu, and S. Ingebrandt, "PEDOT:PSS organic electrochemical transistor arrays for extracellular electrophysiological sensing of cardiac cells," *Biosens. Bioelectron.*, vol. 93, pp. 132–138, Jul. 2017.
7. D. Rani, V. Pachauri, A. Mueller, X. T. Vu, **T. C. Nguyen**, and S. Ingebrandt, "On the Use of Scalable NanoISFET Arrays of Silicon with Highly Reproducible Sensor Performance for Biosensor Applications," *ACS Omega*, vol. 1, no. 1, pp. 84–92, Jul. 2016.
8. **T. C. Nguyen**, M. Schwartz, X. T. Vu, and S. Ingebrandt, "PSPICE Simulation Model for Biomolecule Detection with Silicon Nanowire Bio- sensors in both Potentiometric and Impedimetric Readout Mode," in *International Conference on Solid State Devices and Materials*, Tsukuba, pp. 280–281, 2014.
9. T. N. Khoa Phan, T. C. Tu, T. T. Nguyen, **T. C. Nguyen**, and M. C. Dang, "Development and application investigation of an ICSHG 532 nm diode-pumped solid-state laser system," *Adv. Nat. Sci. Nanosci. Nanotechnol.*, vol. 2, no. 4, p. 45008, Nov. 2011.

10. V. B. Pham, X. T. Tung Pham, N. T. Duong Dang, T. T. Tuyen Le, P. D. Tran, **T. C. Nguyen**, V. Q. Nguyen, M. C. Dang, C. J. M. van Rijn, and D. H. Tong, "Detection of DNA of genetically modified maize by a silicon nanowire field-effect transistor," *Adv. Nat. Sci. Nanosci. Nanotechnol.*, vol. 2, no. 2, p. 25010, May 2011.

Presentations

1. Thanh Chien Nguyen, "Readout circuit for FET silicon nanowire biosensor," PhD Seminar, University of Applied Science Kaiserslautern, Germany, 05.2012
2. Thanh Chien Nguyen, Miriam Freyler, Xuan Thang Vu, Sven Ingebrandt, "Large bandwith readout system for SiNW biosensor, "EnFI 2012 Engineering of Functional Interfaces, University of Applied Sciences Kaiserslautern, Germany, 07. 2012
3. Thanh Chien Nguyen, Miriam, Xuan Thang Vu, Miriam Schwartz, Sven Ingebrandt, "Impedimetric detection of biomolecules with silicon nanowire sensors, "EnFI 2013 Engineering of Functional Interfaces, University of Hasselt, Belgium, 07. 2013
4. Thanh Chien Nguyen, "Impedimetric measurement for SiNW biosensor and readout development," PhD Seminar, University of Applied Science Kaiserslautern, Germany, 05.2013
5. Thanh Chien Nguyen, Miriam, Xuan Thang Vu, Miriam Schwartz, Sven Ingebrandt, "Multifunctional 32-channel amplifier system for FET biosensors in potentiometric and impedimetric readout mode, "EnFI 2014 Engineering of Functional Interfaces, Aachen University of Applied Sciences, 07. 2014
6. Thanh Chien Nguyen, Miriam, Xuan Thang Vu, Miriam Schwartz, Sven Ingebrandt, "PSPICE Simulation Model for Biomolecule detection with Silicon Nanowire Biosensors in both potentiometric and impedimetric readout mode, "International Conference on Solid State Devices and Materials, Tsukuba, Japan, 09. 2014

Poster

1. Thanh Chien Nguyen, Miriam Freyler, Xuan Thang Vu, Sven Ingebrandt, "Design of readout electronics for large bandwidth sensing with silicon nanowire biosensors, "Nano workshop, University of Hasselt, Belgium, 04. 2012
2. Thanh Chien Nguyen, Xuan Thang Vu, Miriam Freyler, Sven Ingebrandt, "A new biasing technique to stabilize the measurement of SiNW FETs for label-free biosensor applications, "Label Free Technology Conference, Amsterdam, The Netherlands, 11. 2012
3. Thanh Chien Nguyen, Miriam Freyler, Xuan Thang Vu, Sven Ingebrandt, "Large bandwith readout system for SiNW biosensor, "EnFI 2012 Engineering of Functional Interfaces, University of Applied Sciences Kaiserslautern, Germany, 07. 2012
4. Thanh Chien Nguyen, Miriam, Xuan Thang Vu, Miriam Schwartz, Sven Ingebrandt, "Multifunctional 32-channel amplifier system for FET biosensors in potentiometric and impedimetric readout mode, "EnFI 2014 Engineering of Functional Interfaces, Aachen University of Applied Sciences, 07. 2014

5. Thanh Chien Nguyen, Miriam, Xuan Thang Vu, Miriam Schwartz, Sven Ingebrandt, "PSPICE Simulation Model for Biomolecule detection with Silicon Nanowire Biosensors in both potentiometric and impedimetric readout mode, "International Conference on Solid State Devices and Materials, Tsukuba, Japan, 09. 2014